# TOWARDS REVERSIBLE MECHANOCHEMICALLY TRIGGERED STRENGTHENING, TOUGHENING AND ASSEMBLY OF SOFT MATERIALS

BY

ERIC EPSTEIN

DISSERTATION

Submitted in partial fulfillment of the requirements
for the degree of Doctor of Philosophy in Materials Science and Engineering
in the Graduate College of the
University of Illinois at Urbana-Champaign, 2018

Urbana, Illinois

Doctoral Committee:

Professor Paul V. Braun, Chair and Director of Research
Professor Jeffrey S. Moore
Assistant Professor Christopher Evans
Associate Professor Andrew Ferguson

## ABSTRACT

The field of mechanochemistry is on many levels inspired by biology, which harnesses mechanical energy to trigger a variety of chemical functions including regulating the flux of ions through channels, generating electrochemical impulses, and activating the rearrangement of protein complexes. A key attribute of many biochemical reactions is reversibility, as this enables the molecular machinery of cells to perform their functions repeatedly for many cycles. With the exception of color switching mechanophores, the majority of mechanochemical reactions developed in the lab are completely irreversible, thus limiting their function to a one time use. Spiropyran (SP) is a unique mechanophore that reversibly switches from a ring-closed state to a ring-open, merocyanine (MC) state in response to a variety of stimuli, including UV light, heat, and mechanical force. Herein, a strategy is proposed to reversibly crosslink polymer chains using SP's well documented ability to bind to metal cations in its MC state.

A proof of concept is demonstrated, whereby viscous solutions containing transition metal ions and a SP functionalized polymer spontaneously switch from a viscous fluid to a viscoelastic gel in response to heat. Exposure to visible light dissociates polymer crosslinks, switching the gel back to a viscous fluid state. Rheological studies using small amplitude oscillatory shear demonstrates reversible crosslinking over several cycles. The data strongly suggest that crosslinking is due to intermolecular bridging of MC units via coordination to divalent metal ions.

A methodology is developed for incorporating metal ions into spiropyran mechanophore linked poly(dimethylsiloxane) elastomers. By removing moieties that stabilize MC, as well as incorporating additives that competitively solvate metal ions in PDMS, force-triggered MC-

metal complexation is demonstrated for the first time with autonomous dissociation of the metal complexes after removal of the applied stress. Force-triggered complexation is demonstrated over many cycles without any sign of hysteresis. Though spontaneous activation is not completely inhibited, it is well controlled. An inverse relationship between the thermodynamic stability of MC-metal complexes measured in solution and the ratio of mechanochemical to thermal activation in the SP-PDMS/metal ion composite is revealed. Though force-triggered crosslinking is not demonstrated in this system, these results are a significant step towards engineering systems with reversible mechanochemical functionalities that extend beyond color indication.

2D diffusion NMR is employed to gain a deeper understanding of the molecular mechanisms that result in metal-ion-mediated gelation of SP polymer solutions. A number of complexities are revealed, and a method for decoupling the effects of shape, size, solvation and charge on the relative diffusivity of MC and SP is proposed.

Implications of our findings towards the possibility of engineering SP polymers that mechanochemical strengthen and toughen are heavily emphasized. This dissertation concludes with two rational strategies for the engineer or chemist who wishes to pursue these ideas further.

## ACKNOWLEDGEMENTS

First and foremost I would like to thank my friends and family who have continually lifted my spirits over the past several years. You were the charge that kept me going. Tisha, I can't thank you enough for your love, patience, support, and the delicious food. Mom and Grandma, thank you for always being there, no matter what. Craig and Jillian, thanks for giving me something to look forward to on holidays and vacations.

I would like to acknowledge all of my mentors and my collaborators who have encouraged me and supported me in my development as a scientist. Professor John Cumings, thank you for taking me in without question and pushing me to excel in my field. You were an extraordinary mentor, sparked my passion for research and provided me with an excellent foundation to succeed. Khim Karki and Kamal Baloch, you were the best role models I could have asked for as an undergrad.

Professor Paul Braun, thank you for always keeping an open mind, for your extraordinary patience, and for always being there for me throughout all the ups and the downs of my PhD. Professor Randy Ewoldt, I can't thank you enough for letting me use your lab and more or less treating me like a member of your group. Your ability to galvanize others as you teach them is something I strive for as a mentor. Dr. Luca Martinetti, thank you for so many thoughtful discussions. You really elevated the quality of my PhD work.

Professor Jeff Moore, every time we conversed I felt like I grew as a person. Thank you for all the great advice and keeping your door open to me. Professor Nancy Sottos, thank you for enabling a great collaboration. Tae Ann, thank you for taking a big break from your thesis work to help me with mine. I couldn't have gotten this far without you.

I'd like to thank all of the undergraduate, graduate, and post-doc colleagues who I've worked with over the years. Kali Miller, thank you not only for being a great friend but always being there to bounce ideas off of. Shuqi Lai, I consider you my first real chemistry teacher. Thanks for letting me ask a million and one questions. Jerome Davis and Dr. Ravichandran Kollarigowda, thanks for teaching me how real chemists get the job done.

Thanks to all the staff who keep things running behind the scenes, and a big thanks to Erica Malloch for being the glue that holds our group together. Finally, thank you so much to Dr. Dean Olsen and Dr. Lingyang Zhu for teaching me everything I know about 1D and 2D NMR.

To Tish, my love, you give me joy, purpose, and have made me a better man.
To Mom, thank you for your unconditional love and support.
For Autumn and Winter…

## TABLE OF CONTENTS

# CHAPTER 1: ORIGIN OF THESIS: EARLY WORK ON SHAPE-SWITCHING MICROPARTICLES

## 1.1 Background and summary of work on shape-switching microparticles

The motivation for the work in the subsequent chapters of this thesis stems from an early project on stimuli-responsive, shape shifting colloidal particles [1]. The goal of this project was to design particles that store and release mechanical energy by switching between two mechanically bistable shapes. Of particular interest to us were self-assembled colloidal systems whereby the constituent colloidal particles change shape at rates that significantly exceed that of their Brownian motion. It is well known that the structure of any colloidal assembly must reflect the geometry and interaction potentials of the particles comprising it. We speculated that by drastically modifying individual particle shapes on timescales that far exceed that of their collective motion, it may be possible to attain metastable colloidal structures that are inaccessible via equilibrium self-assembly.

As a first step toward exploring these dynamic colloidal systems, we designed and fabricated snap-buckling colloidal particles that rapidly switch shape (measured to be less than 200ms) in response to an external stimulus. In contrast to previously reported methods for triggering particle shape transformations, which include solvent- or temperature-induced polymer softening [2], thermally induced reorientation of liquid crystalline moieties[3, 4], and solvent induced swelling of polymer gels [5], a snap buckling approach provides rapid kinetics even under a slowly varying stimulus (e.g. temperature or pH change). These snap-buckling particles also exhibit full shape reversibility, which is not the case for many other systems. The discontinuous,

snap-actuated shape-change derives from the particles' geometry which is that of an open, spherically curved shell. These were the first colloidal particles to be programmed with mechanical bistability, and as expected, they change shape on a timescale that is decoupled from the diffusion-limited stimulus.

Mechanically bistable microparticles (illustrated on the left side of Figure 1.1) are composed of a diepoxide crosslinked p(acrylic acid) (PAA) hydrogel (pKa ~4.7) layer, which expands (or contracts as pH is increased (or decreased) and a p(vinyl cinnamate) PVCi organogel layer, which is chemo-mechanically inactive and provides the elastic energy for actuation as membrane forces are applied to it by the swelling PAA. The detailed fabrication methods can be found in our published work [1] and are illustrated in Figure 1.2. Hybrid particles with polymer bilayers tethered to silica microspheres and standalone polymer particles were fabricated. For both types of particles, swelling of PAA at ~pH 6 and above causes the particles to invert. As the pH is reduced to ≤5, PAA contracts and the particles revert back to their original shapes. Remarkably, the polymer caps tend to remain partly adhered to the silica microspheres throughout the inversion process. The adhesion may be attributed to a combination of Van der Waals bonding, hydrogen bonding, and diepoxide-mediated covalent bonding between acrylic acid units of PAA and OH groups on the microsphere surface.

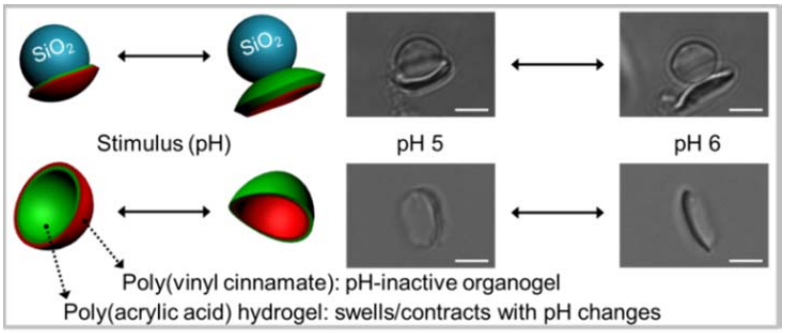


**Figure 1.1.** Schematic (left) and optical microscopy images (right) of snap-buckling colloidal particles. Particles consist of a PAA hydrogel (green) and PVCi organogel (red), either freestanding (bottom) or tethered to silica spheres (top). Particles are observed in their original conformations at pH 5 and in inverted conformations at pH 6. Scale bars = 4μm.

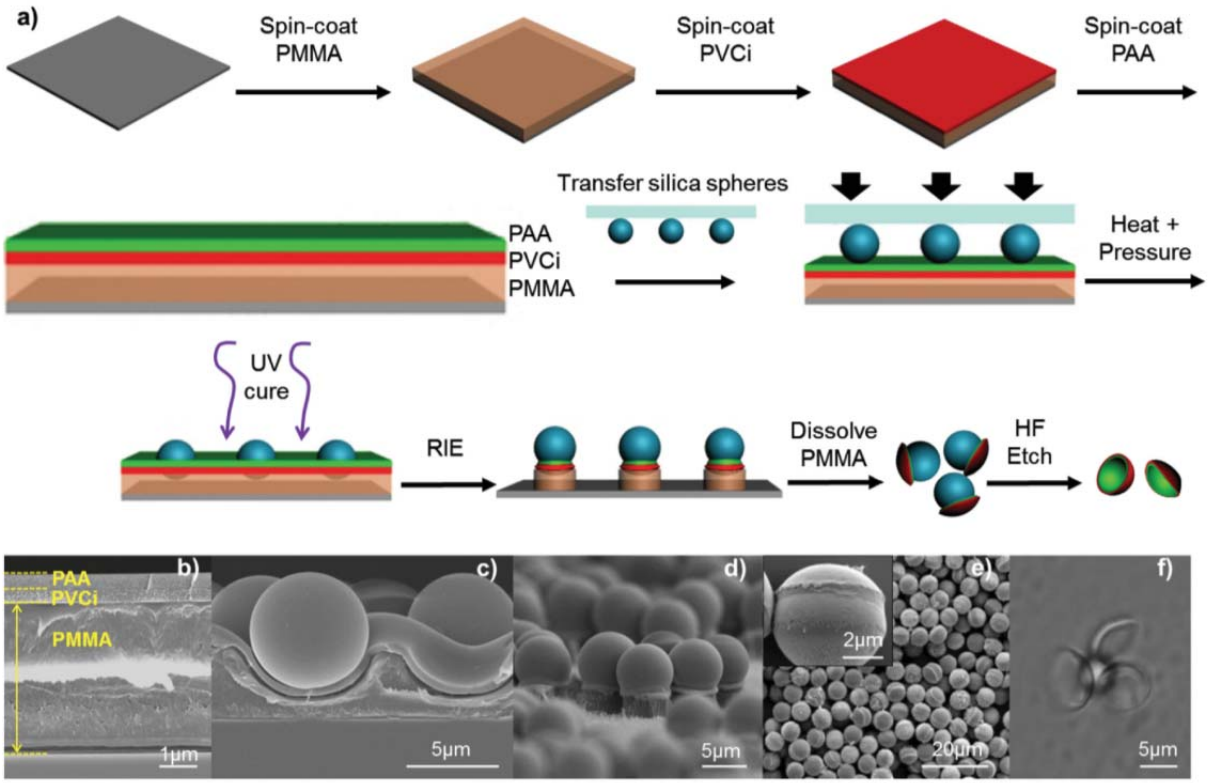


**Figure 1.2.** a) Schematic of process for fabricating silica-tethered and untethered particles. b) SEM cross-section of PMMA/PVCi/PAA multilayer spin cast on silicon substrate. c) Cross-sectional SEM image of silica spheres embedded in polymer multilayer after hot-press and polymer curing. d) SEM of sample after RIE. e) SEM of released particles after dissolving PMMA sacrificial layer. Inset is zoomed in image of silica microsphere with tethered PAA–PVCi spherical shell cap. f) Optical microscopy of untethered particles immersed in pH2 buffer after etching the silica spheres in 10% HF.

The pH-triggered buckling inversion of PAA-PVCi particles was studied using optical microscopy (Figure 1.3). At pH 4, all particles are in their original conformations. At pH 8, particles with inverted shapes are observed. When the pH is returned to 4 the particles return to their original shape. To investigate the hysteresis of the shape inversion process, two particles (Figure 1.3b)—one silica-tethered and one silica-free were followed as the pH was changed between 5 and 6. Decreasing the pH from 5.95 (where particles are in their inverted forms), the curvature of both tethered and untethered particles remains roughly unchanged until pH = 5.25, at which both particles are observed to invert back to the original conformations. Sweeping the pH up from 5.25, the shapes remain unchanged until pH ≥ 5.75 when the particles once again invert their shapes. Figure 1.3c illustrates these conformational changes by plotting the observed direction of curvature vs. pH, where increasing pH correlates with increasing mismatch strain as shown by Figure 1.3. The key observation is hysteresis in particle shape as a function of pH. This hysteresis is clear evidence of mechanical bistability.

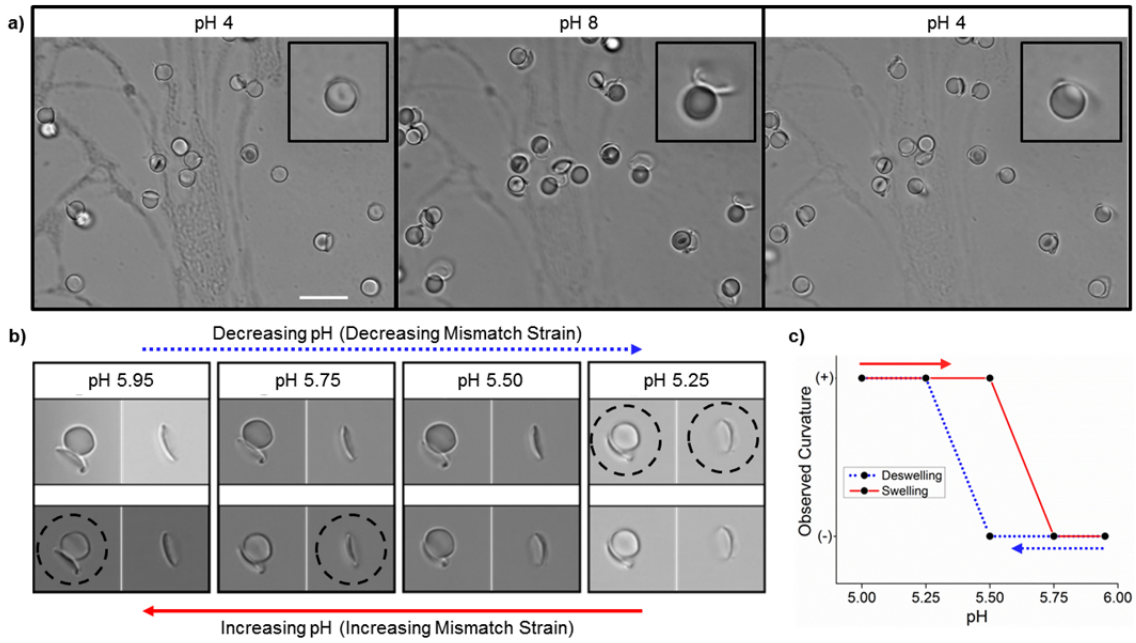


**Figure 1.3.** a) Optical microscopy images showing reversible actuation of PAA-PVCi-tethered silica microspheres. Scale bar = 10 µm and applies to all 3 images. Frame widths of insets = 10 µm. b) The hysteretic response of silica-tethered and silica-free particles in response to pH between 5 and 6. Dashed circles highlight frames in which particles invert. Each image frame is 15 µm across. c) The observed curvature hysteresis of the particles of Figures 1.2b and S2 of reference 1 (starting from their initial orientation at pH 5.95) as a function of pH.

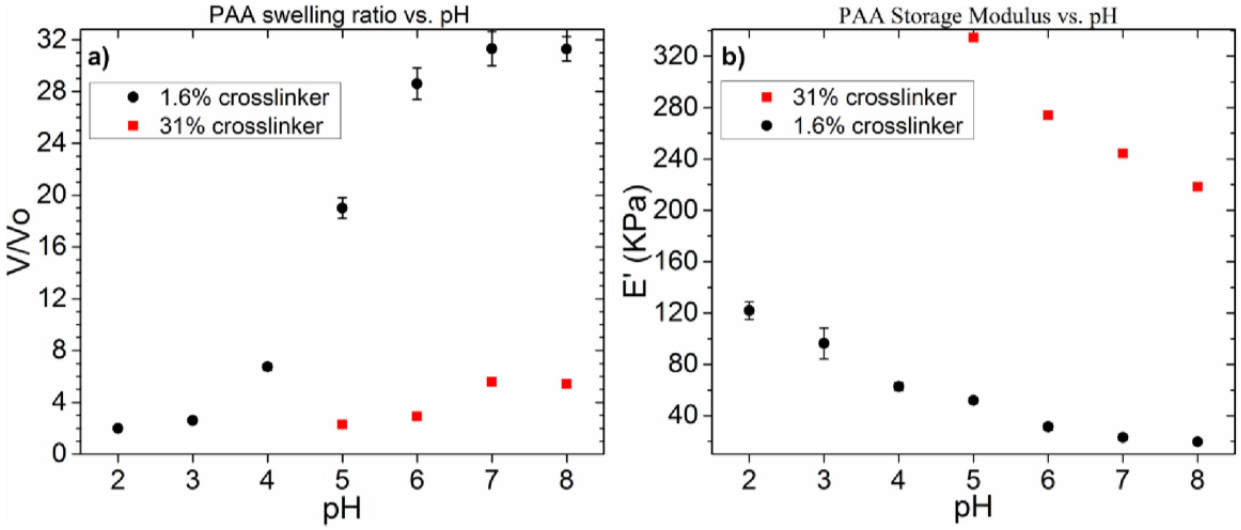


**Figure 1.4.** (a) Volumetric swelling ratio (hydrated volume/dry volume) vs. pH of freestanding PAA hydrogel prepared with two different concentrations of diepoxide crosslinker. V/Vo for freely suspended, bulk PAA with 1.6mol% crosslinker.. (b) Storage modulus vs. pH of freestanding PAA discs. Both swelling ratio and storage modulus changes were identical with increasing and with decreasing pH, indicating no hysteresis in the mechanical properties of freely suspended PAA films.

A 2D finite element model generated using ABAQUS qualitatively shows that this hysteresis is an inherent property of the spherical dome geometry of the particles (Figure 1.5). A plot of curvature vs. mismatch strain generated in a model particle (Figure 1.5a) reveals three actuation regimes: (1) upon swelling PAA, there is an initial actuation characterized by continuous deformation of the bilayer. (2) At a critical mismatch strain there is a jump from positive to negative curvature, signifying the buckling inversion of the shell. Due to the quasi-static nature of our simulations, the snap-through buckling does not appear as a discontinuous process as it does experimentally, but instead is characterized by a shift to negative global stiffness and a concomitant release of mismatch strain, which is necessary in order to maintain a quasi-static equilibrium. (3) Finally, there is a post-buckling regime whereby further deformation is once again continuous. Most notably, there is a similar hysteresis trend observed experimentally, whereby the buckling inversion upon swelling occurs at a larger mismatch strain (~0.15) than upon deswelling PAA (~0.10). This model confirms that the experimentally observed hysteresis is an inherent property of the particle geometry, existing independently of any effects due to viscoelasticity or plastic deformation, as these effects were not considered in our FEA. A plot of global strain energy of the bilayer structure vs. mismatch strain (Figure 1.5b) shows two local energy minima, indicating that these particles are mechanically bistable, having two energetically favorable conformations.

The discontinuous shape inversion of PAA-PVCi colloids was recorded in real-time movies. Representative snapshots taken during one of the movies is shown in Figure 1.6. The key observation is that there are three time regimes associated with particle actuation: first is the initial swelling/contracting of the PAA layer in response to pH changes; the second is the

buckling inversion whereby the most drastic shape changes are observed; the third is a post-buckling regime whereby further swelling of PAA may cause the particle to continue to deform gradually and continuously. In the first time regime, the swelling/contracting of PAA occurs continuously and strongly depends on the flux of water and ions into or out of the PAA hydrogel. When diffusion distances are very short and concentration gradients very large, the swelling response time may be on the order of ~0.5 s to 5 s; but when diffusion distances are longer (e.g. Figure 1.6a), the swelling response can occur on time scales ranging from ~30 s to several minutes. The second time regime occurs at a critical instability point whereby a discontinuous buckling inversion takes place, at which the rate of shape change is independent of the rate of diffusion of the aqueous buffer used to trigger the actuation. In all experiments, this buckling inversion takes place on a timescale, $\tau \leq 200$ ms (the inequality is due to the limited frame rate of the camera used: 5 fps). As a metric for comparison, we estimate the Brownian timescale to be the time for a spherical particle to diffuse its own radius: $\tau_{Brownian} = a^3(6\pi\eta)/k_BT$, where a is the particle radius, $\eta$ is the viscosity of the suspending liquid, and $k_BT$ is the thermal energy. For 1-6 μm diameter colloidal spheres in water near room temperature, $\tau_{Brownian}$ ranges from ~600 ms to ~120 s. Thus, it appears these bistable particles can switch their shapes on a significantly faster timescale than that of their Brownian motion. A careful analysis (presented in detail in Section 2.3 of Reference 1) and the data of Figure 1.6b indicate that the timescale of snap-buckling is ultimately limited by viscoelastic energy dissipation intrinsic to the polymers comprising the particles.

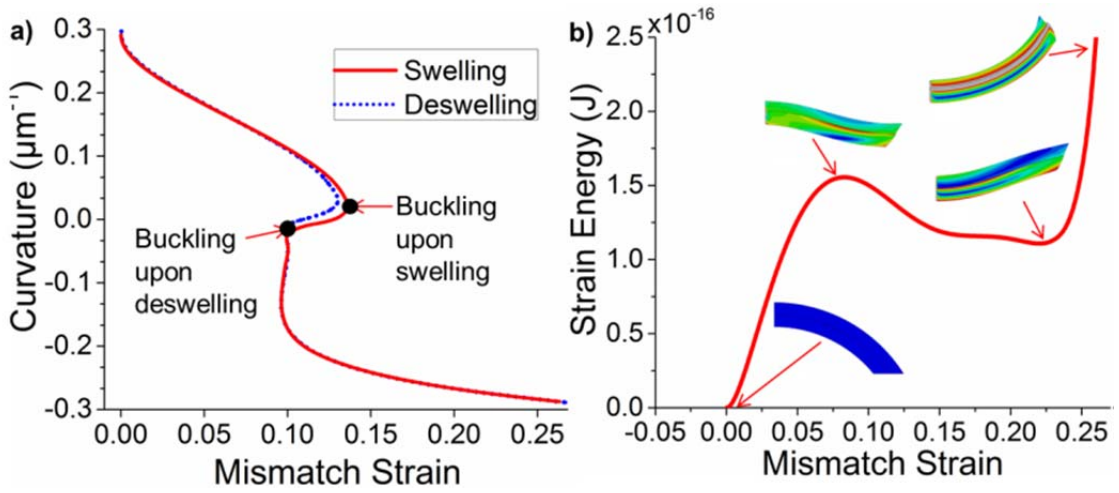


**Figure 1.5.** FEA simulations of PAA-PVCi bilayer shells with initial size and curvature similar to those of experimentally fabricated particles. a) Plot of curvature vs. mismatch strain of a model particle with conditions $h_{PVCi}/h_{PAA} = 1$ and $E_{PVCi}/E_{PAA} = 2$ where h and E represent thicknesses and elastic moduli. Hysteresis is exhibited as buckling upon swelling and deswelling occurring at two very different mismatch strains. b) Plot of elastic strain energy vs. mismatch strain of a bilayer colloid with swelling PAA. Arrows highlight shape changes during various stages of actuation.

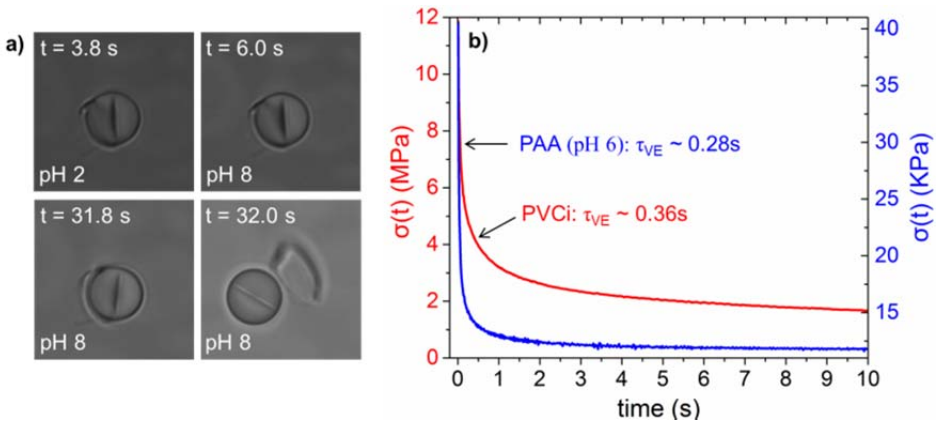


**Figure 1.6.** a) Sequential snapshots extracted from Movie S1 showing actuation of a tethered particle. The swelling time of PAA is limited by diffusion of the pH buffer, but upon reaching a point of mechanical instability (at ~31.8 s) the particle inverts in ≤ 200 ms. Frame widths = 20 μm. Frame rate of corresponding video is 5 fps. b) Typical stress relaxation curves for (b) dry PVCi gel (1% applied strain), showing non-negligible viscoelastic relaxation timescales.

## 1.2 Motivation for thesis work

We have shown that mechanical bistability can be a clever trick to overcome sluggish kinetics in shape-switching objects based on expanding and contracting hydrogels. However, in working

on this project we have become distinctly aware that the mechanistic toolbox for imparting stimuli-responsive function to synthetic materials is at present very limited. Though we often draw inspiration from biology when designing stimuli-responsive systems, the sophistication, and consequently the practical utility, of synthetic stimuli-responsive materials pales in comparison to what is observed in nature.

In nature, there exists an intimate link between mechanical forces and biochemical processes. Stretch-activation of ion channels (perhaps in response to changes in tension or curvature of the lipid bilayer) is one mechanism believed to regulate the flux of ions into or out of components of living cells (Figure 1.7a) [6]. Mechanical stretching has too been shown to play a direct role in protein chemistry, as for example, stretch-induced exposure of binding sites on Talin proteins leads to strong binding between Talin and Vinculin (Figure 1.7b) [7]. Other notable examples are ATP-driven molecular motors responsible for muscle contraction [8, 9] and the transduction of mechanical energy by hair cells within the inner ear, ultimately enabling us and other organisms to detect sound and fluid motion [10].

Force-induced transport and reactions of molecular species are ubiquitous in biology. Furthermore, these processes are often reversible (therefore cyclic in nature) and serve to trigger further (downstream) biochemical processes. No doubt inspired in large part by biological systems, mechanically-triggered chemistry (*mechanochemistry)* is an emerging, but currently very limited motif for synthetic materials. The primary purpose of the work discussed herein is to extend the functionality of a well-characterized mechanophore, spiropyran, to generate noncovalent associations in polymeric materials in response to mechanical force. Our aim is to engineer soft materials that produce a constructive response (e.g. formation of new bonds leading to strengthening, toughening or a phase transformation) from potentially destructive mechanical

stresses. Most importantly, we aim for this mechanochemistry to be reversible, thus potentially allowing for cyclic behavior.

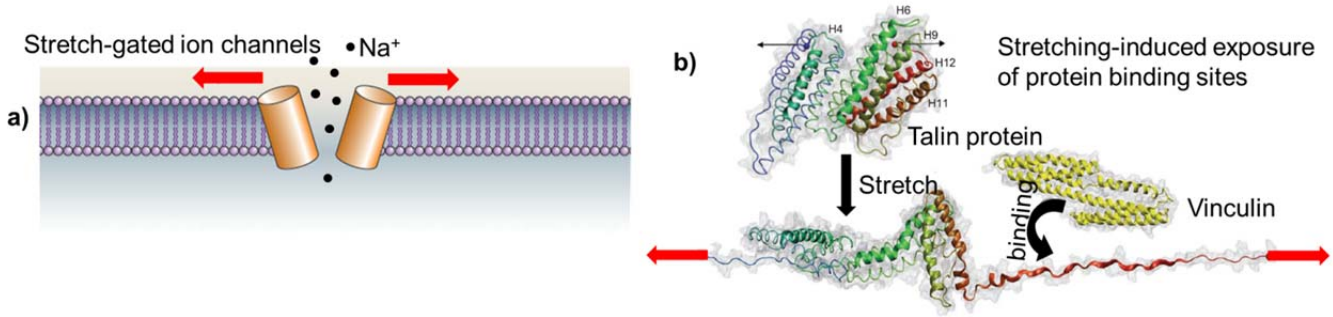


**Figure 1.7.** a) Illustration of a stretch-gated ion channel [6]. b) Illustration of stretch-induced binding of talin to vinculin [7].

## 1.3 REFERENCES


1. Epstein, E., Yoon, J., Madhukar, A., Hsia, K. J. and Braun, P. V. *Small* **2015**, *11*, 6051.
2. Yoo, J. W. and Mitragotri, S. *Proc Natl Acad Sci U S A* **2010**, *107*, 11205.
3. Buguin, A., Li, M.-H., Silberzan, P., Ladoux, B. and Keller, P. *Journal of the American Chemical Society* **2006**, *128*, 1088.
4. Marshall, J. E., Gallagher, S., Terentjev, E. M. and Smoukov, S. K. *Journal of the American Chemical Society* **2014**, *136*, 474.
5. Lee, K. J., Yoon, J., Rahmani, S., Hwang, S., Bhaskar, S., Mitragotri, S. and Lahann, J. *Proc Natl Acad Sci U S A* **2012**, *109*, 16057.
6. Lumpkin, E. A. and Caterina, M. J. *Nature* **2007**, *445*, 858.
7. Rio, A. d., Perez-Jimenez, R., Liu, R., Roca-Cusachs, P., Fernandez, J. M. and Sheetz, M. P. *Science* **2009**, *323*, 638.
8. Yu, J., Ha, T. and Schulten, K. *Biophys J* **2006**, *91*, 2097.
9. Vale, R. D. and Milligan, R. A. *Science* **2000**, *288*, 88.
10. Gillespie, P. G. and Muller, U. *Cell* **2009**, *139*, 33.

# CHAPTER 2: INTRODUCTION, PROJECT VISION, AND OVERVIEW OF THESIS

## 2.1 Mechanochemistry

The progression of a chemical reaction is often depicted on an energy landscape, whereby one or more potential barriers separate reactant from product. In the classical perspective of chemistry, reactions are triggered and energy landscapes traversed by means of thermal, electrical or electromagnetic energy. *Mechano*chemistry describes the coupling of mechanical energy to chemical transformations. In both hard and soft materials researchers are pursuing ways to trigger chemical reactions and manipulate energy surfaces using mechanical force. In hard matter, this is commonly referred to as "strain engineering", whereby mechanical strain is used to alter electronic band structures of materials [1] or the catalytic activity of surfaces [2, 3]. In the realm of soft matter, we often take inspiration from nature, where mechanical force is used as a stimulus to produce a deterministic response, such as an electrochemical impulse or the rearrangement of a protein complex. One of the earliest published attempts to understand the chemical response of soft, polymeric systems to mechanical force is credited to Staundinger who in the 1930s interpreted the decrease in molecular weight of polymers under mastication as rupture of polymer chains [4-6]. Early pioneers established our understanding of the physicochemical link between viscous flow and polymer chain scission [7-10], and the modern era of mechanochemistry was initiated upon the realization that certain bonds cleave more easily than others. For example Encina and co-workers demonstrated that random incorporation of peroxide (O—O) linkages in a poly(vinylpyrrolidone) backbone, led to a five thousand-fold increase in the rate of polymer chain scission in response to ultrasonication [11]. Most recent

work seeks to design polymer-bound molecules that break or respond in a predictable manner. These molecules, called **mechanophores**, possess strategically weakened bonds so as to produce a deterministic (and in the best cases, useful!) response under stress. The linkage of the mechanophore to a polymer chain enables effective transduction of mechanical energy to the weakened bond through tension, compression or shear.

Li, Nagamani and Moore provide an outstanding perspective including many types of mechanochemical reactions that have been reported to date [12]. Most mechanophores contain a weak bond or strained ring that can be selectively cleaved or isomerized under stress (Figure 2.1). The list of mechanophores highlighted by Li, Nagamani and Moore is extensive, but by no means exhaustive, as researchers are continually introducing new examples of mechanochemical reactions, resulting in a more and more diverse list of variants.

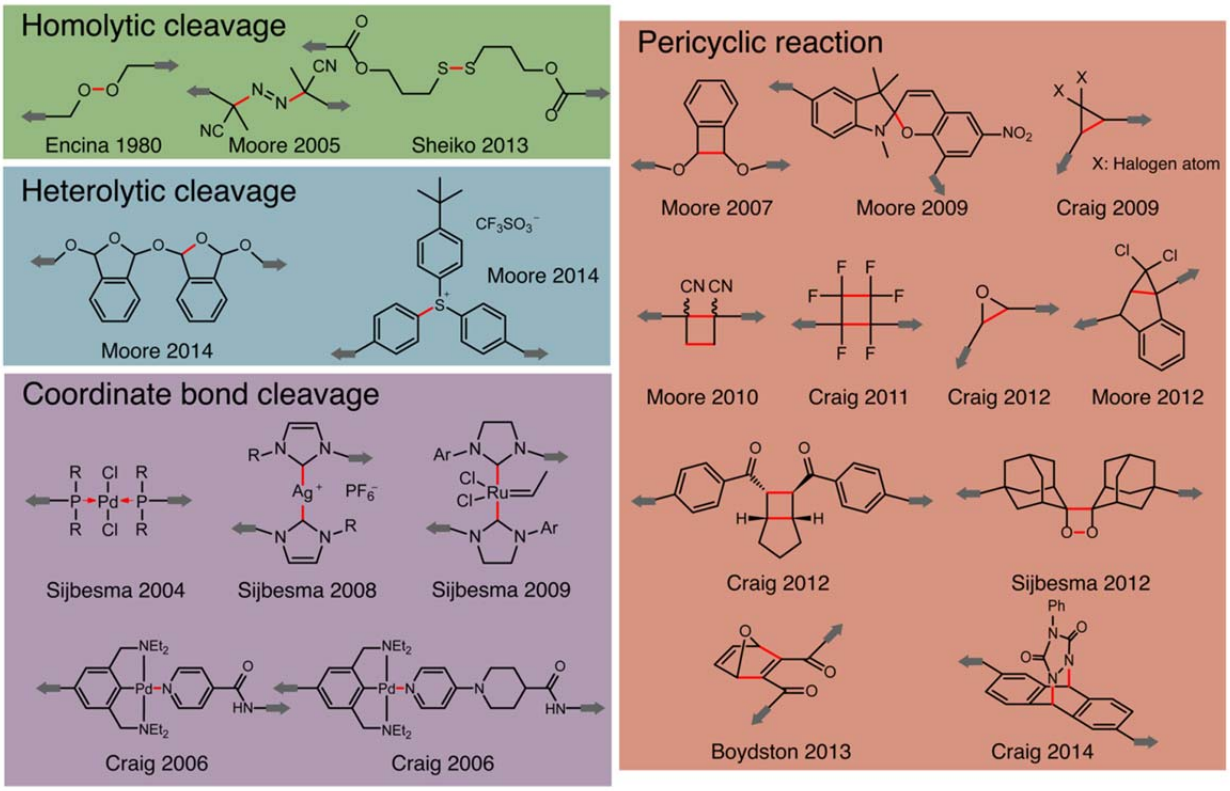


**Figure 2.1.** List of mechanophore structures highlighted by Li, Nagamani and Moore in 2015. Figure adapted with permission from [12].

For example, Imato and co-workers have reported a diarylbibenzofuranone-based mechanophore that undergoes hemolytic bond cleavage to produce blue colored, air-stable radical species (Figure 2.2a) [13]. Li and coworkers recently introduced a 2,6-pyridinedicarboxamide-Fe(III) coordination complex built into a PDMS backbone (Figure 2.2b) [14]. These metal-ligand coordination bonds contain a hierarchy of three different coordination bond strengths resulting in multimodal rupture under mechanical stress. Metal-ligand coordination complexes need not be the only non-covalent mechanophores. In 2014 Chung et al. reported a polymer linked 2-ureido-4-[1H]-pyrimidinone (UPy)-based hydrogen bonded complex that unfolds upon stretching in a way that mimics the behavior of titin proteins (Figure 2.2c) [15]. Though the authors did not advertise their system as a mechanophore, it possesses the same characteristics, as the hydrogen bonds of the UPy dimers selectively break in response to mechanical stress. Finally, Sagara and co-workers recently reported a mechanochromic rotaxane, which contains a macrocycle that translates along a mechanically interlocked shaft in response to an externally applied stress (Figure 2.2d) [16].

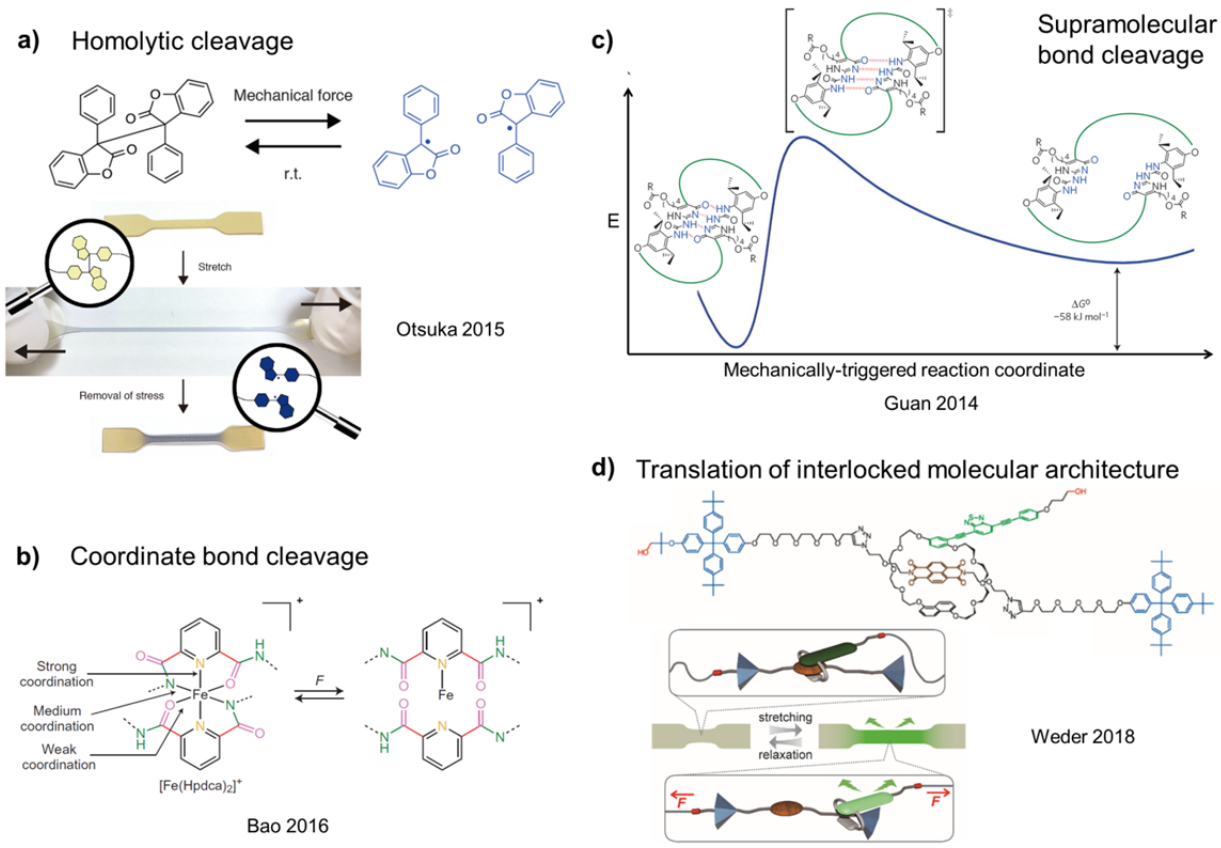


**Figure 2.2.** Notable examples of mechanophores not shown in Figure 2.1. a) Diarylbibenzofuranone-based mechanophore built into a polyurethane backbone undergoes reversible changes in color due to hemolytic bond cleavage and reformation. Figure adapted from [13]. b) 2,6-pyridinedicarboxamide-Fe(III) coordination complex undergoes multimodal bond rupture. Figure adapted from [14]. c) UPy-based dimers undergo mechanically-triggered unfolding. Figure adapted from [15]. d) Rotaxane-based mechanophore switches from non-fluorescent to fluorescent state in response to mechanical stress. Figure adapted from [16].

## 2.2 Getting more out of a mechanophore: how to trigger a useful response?

Although the diversity of mechanochemical reactions is growing, mechanochemistry is still considered to be in a nascent stage of research. The challenge lies not only in designing mechanically-triggered reactions, but in designing systems with a useful or constructive response to mechanical stress. Issues that inhibit advancement towards this goal include difficult, time consuming and/or low yielding organic synthesis procedures, complications with polymer formulation, and undesirable side reactions often associated with the weak bond(s) of the mechanophore.

Ultrasonication is a commonly used method for screening molecules, demonstrating mechanochemical activity for the first time, and doing fundamental studies; however, many mechanophores have not made it past this "ultrasonication phase" of research. A major milestone for any mechanophore is its demonstrated use in a solid-state polymer or gel where it may be subjected to more common modes of tension, compression or shear. This section highlights the practical uses of mechanophores in solid state systems. These can be divided into 4 categories: sacrificial bonds, mechanochromic dyes, mechanocatalysis, and generation of reactive species (Figure 2.3).

*2.2.1. Sacrificial bonds*

Metal-ligand complexes and supramolecular complexes are generally weaker than covalent bonds, and can sacrificially rupture, thereby dissipating mechanical energy under an applied load. These bonds are also reversible, meaning they can reform after they break. Researchers have harnessed the inherent "weakness" and reversibility of non-covalent bonds to toughen polymers and impart materials with the ability to self-repair. Li and co-workers have demonstrated a notable example of a metal-coordination ligand containing three coordination sites possessing different bond association strengths with Fe(III) [14]. Using single molecule force microscopy, the researchers demonstrated a sequence of three different rupture strains of the Fe(III)-bridged complex. The bond energy of the Fe(III)-pyridyl coordination site was shown to be 145 kCal/mol, which is on par with the Si—O bond strength of the PDMS chains these complexes crosslinked. The researchers suggested this "strong" coordination site led to enhanced strength of the crosslinked elastomer, whereas the other two coordination sites (bond strengths of 82.7 and 40.7 kCal/mol, respectively), led to enhanced material toughness and an extraordinary 10,000% strain at failure [14]. The key function of these types of non-covalent mechanophores is

to act as self-healing, sacrificial bonds and break instead of their parent polymer chains. This dual functionality of toughening and self-healing has been imparted to both solid state polymers and gels using a variety of metal coordination ligands including alginate [17], imidazoles [18] and catechols [19]. In addition, this same type of targeted, sacrificial bond breaking has also been demonstrated in a number of solid-state supramolecular polymers (an example of which is shown in Figure 2.2c) [15, 20, 21].

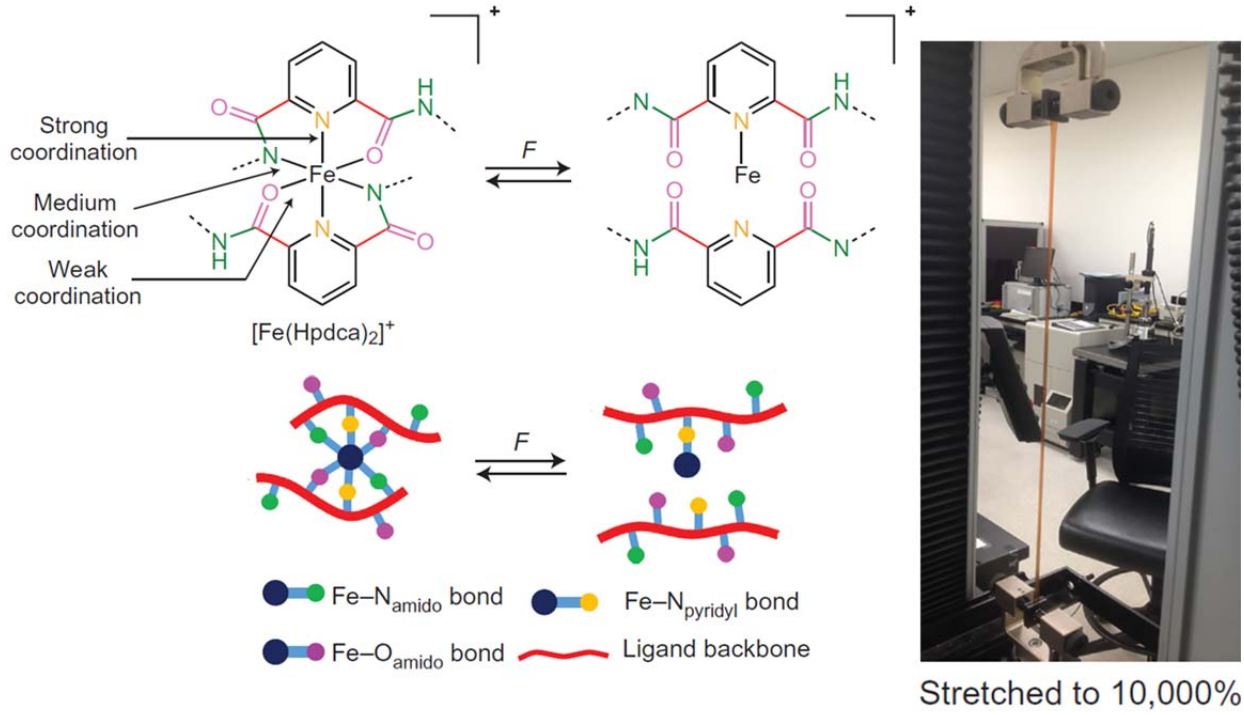


**Figure 2.3.** Metal-ligand coordination crosslinks built into a PDMS backbone are used as sacrificial bonds to dissipate mechanical energy. The elastomer exhibits extraordinary stretchability as well as the ability to self-repair after metal-ligand bond rupture. Figure adapted from [14].

### *2.2.2. Mechanochromic dyes*

Force activated absorbance, fluorescence and chemiluminescence has been investigated by a number of researchers. These "force probes" provide a visible cue of mechanical stress, making them particularly attractive for engineering applications [22, 23] as well as fundamental studies

of polymer mechanics [24]. In addition, their emission or absorption of light makes them particularly convenient for studying the mechanisms of force-activated transformations of the mechanophore itself.

The first deliberately designed mechanochromic dye was reported by Kim and Reneker who introduced an azobenzene dye into a polyurethane backbone and studied their transformations from *cis* to *trans* isomers in response to mechanical stretching [25]. If azobenzenes could reliably switch from *cis* to *trans* under mechanical stress, they would provide a fantastic platform for some of the ideas presented in this dissertation; but unfortunately, azobenzenes have the pesky issue of being far more stable in their *trans* conformation than their *cis* state. In order to study the mechanical transformation of *cis* to *trans*, Kim and Reneker provided some kinetic stability to the *cis* form using intramolecular hydrogen bonding, and also cheated a little by using UV light to transform the thermodynamically stable *trans* azobenzene to its *cis* state immediately prior to stretching.

One example of a mechanochromic dye that has found success in the lab is bis(adamantyl) dioxetane, which emits visible light when the 1,2-dioxetane bond is irreversibly cracked open (Figure 2.4a) [24, 26] . Another broadly used class of mechanochromic dyes, introduced by Moore, Sottos, White, Braun and others are spiropyrans [27-29] and naphthopyrans [30]. These molecular switches are particularly attractive due to their reversibility, enabling multiple force-triggered “on”/“off” cycles to occur [31].

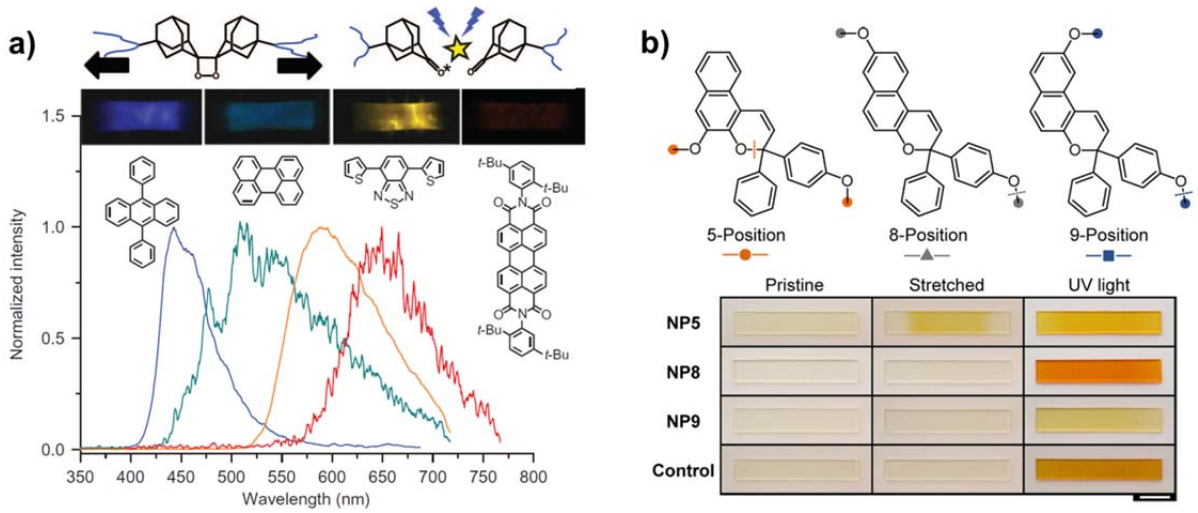


**Figure 2.4.** Examples of mechanochromic dyes. a) chemiluminescent mechanophore: bis(adamantyl) dioxetane. Top schematic adapted from [24]. Bottom images and fluorescence plot, adapted from [26], shows different mechanically-triggered chemiluminescent wavelengths when mechanophore is coupled with different electron acceptors. b) Naphthopyrans absorb visible light after exposure to UV light. Only by connecting to a polymer backbone at specific locations does the molecule become mechanochromic. Figure adapted from [30].

### *2.2.3. Mechanocatalysts*

Force-triggered catalysis is an intriguing concept that could enable new classes of self-healing materials. Several different reports have shown the release of metal catalysts via ultrasonication [32]; however, just two systems to date has been demonstrated in solid state polymers [33, 34]. One, reported by Sijbesma and co-workers, consists of a polymer-bound ruthenium-N-heterocyclic carbine complex, which is activated by subjecting the polymer to compression (Figure 2.5a) [33]. After compression-triggered release, the catalyst initiates ring-opening metathesis polymerization and crosslinking within the polymer matrix, thereby demonstrating the potential use of this system for self-strengthening and repair. The other example, reported by Moore and co-workers, is a *gem*-dichlorocyclopropane mechanophore linked to a poly(methyl acrylate) backbone, which releases HCl under compression (Figure 2.5b) [34]. In theory, the

hydrochloric acid produced could go on to catalyze productive (or destructive) chemistry; however, this has not yet been demonstrated.

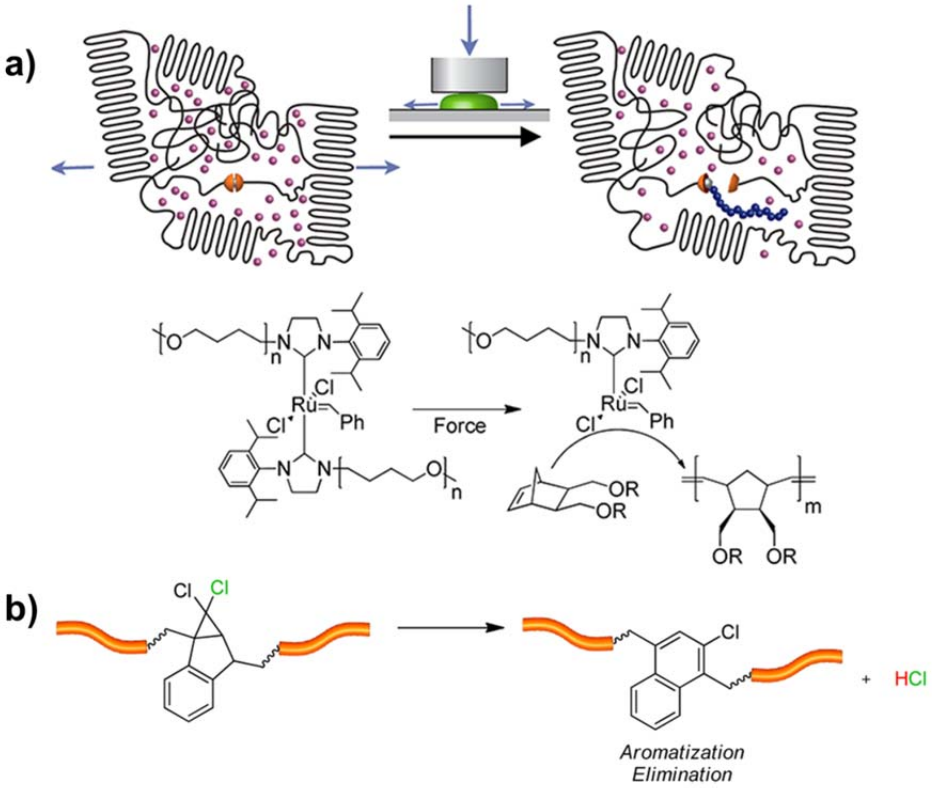


**Figure 2.5.** Force-triggered catalysis. a) Release of ruthenium catalyst under compression triggers ring-opening metathesis polymerization and crosslinking in a solid polymer matrix. Figure adapted from [33]. b) Activation of polymer-bound *gem*-dichlorocyclopropanated indene under compression releases hydrochloric acid. Figure adapted from [34].

### *2.2.4. Generation of reactive species*

Another strategy for triggering productive chemistry using mechanical force is to switch a mechanophore from an unreactive state to a reactive state. Recently, Craig and co-workers demonstrated mechanically-triggered polymer crosslinking using dibromocyclopropane mechanophores (Figure 2.6) [35]. Under mechanical shear, the strained rings of the mechanophores undergo bond scission, generating allylic bromides that become crosslinked in situ via nucleophilic substitution by di- or poly-carboxylates. The authors were the first to demonstrate mechanochemical strengthening of a polymer via formation of new bonds in direct

response to mechanical forces. This mechanism led to gelation of a polymer solution in response to ultrasonication. This mechanism was also demonstrated in the solid-state, but required extrusion of the polymer at elevated temperature, suggesting limited applicability to self-healing systems other than under extreme conditions. Another downside of this system is that mechanochemical activation is irreversible, which prevents its applicability to situations that demand cyclic responses to mechanical stimuli.

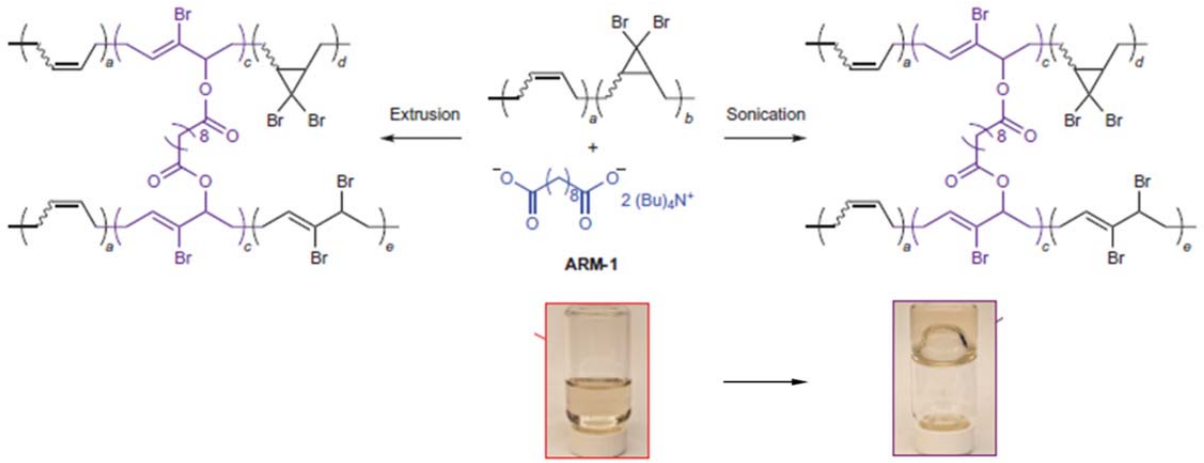


**Figure 2.6.** Dibromocyclopropane-linked poly(butadiene) undergoes mechanically-triggered ring-opening, producing an alkyl bromide species that is crosslinked via nucleophilic substitution. Images show permanent gelation of dissolved polymer after ultrasonication. Figure adapted from [35].

## 2.3 Spiropyran

Spiropyran (SP), the mechanophore used in this dissertation, is a class of heterocyclic molecules that have been used for many years as photochromic, thermochromic and metallochromic dyes [36]. When exposed to UV light many SPs switch from a visibly transparent, ring closed conformation (generally called the SP state) to a ring-open, merocyanine (MC) conformation, which strongly absorbs visible light. Upon removal of UV or exposure to visible light, the dynamic equilibrium shifts, and MC reverts back to SP (Figure 2.7a). In addition to UV and visible light, the reversible isomerization between SP and MC has been

shown to be modulated by thermal energy [37], changes in solvent polarity [38, 39] as well as interactions with chemical species including acids and bases [40], and metal ions [41-44]. As we and others have shown, when SP molecules are appropriately linked to a polymer backbone, mechanical force also triggers MC isomerization, making this molecule mechanochromic (Figure 2.7b) [27-29]. The large number of potential stimuli for modulating the dynamic equilibrium between SP and MC makes this molecular switch particularly attractive for programming materials with stimuli-responsive behavior [45]. Moreover, the ability of the spiropyran to switch reversibly between ring-open and ring-closed states opens up the possibility to mimic cyclic, force-activated functions in biology such as the stretch-gated opening and closing of ion channels [46].

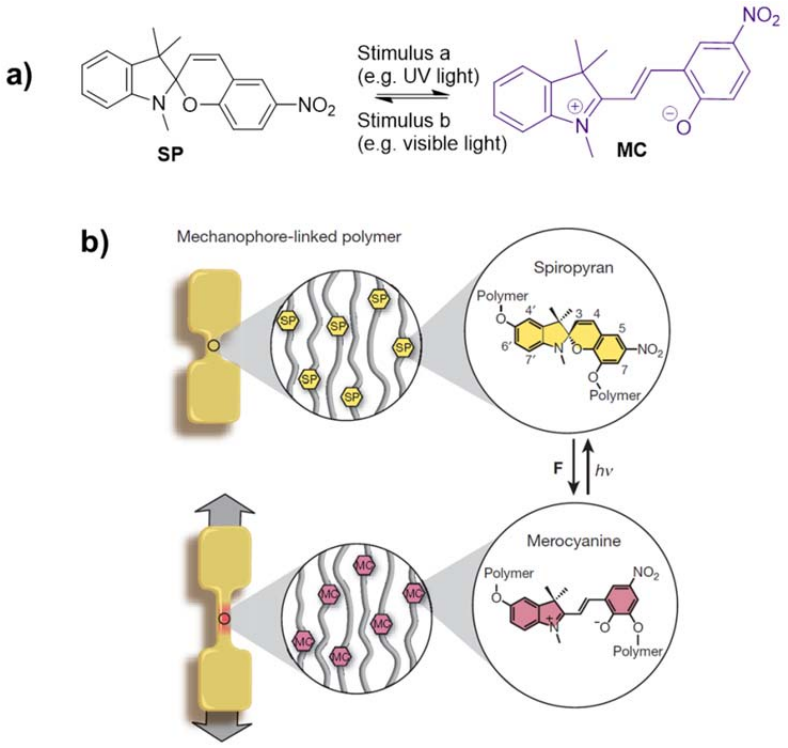


**Figure 2.7.** Spiropyran as a multifunctional molecular switch. a) Stimuli-triggered reversible isomerization between SP and MC. b) Spiropyran mechanophore switches between transparent and colored state in response to mechanical force. Figure adapted from [28].

*2.3.1. Merocyanine-metal complexes*

A central theme to the ideas and data presented in this dissertation is the reversible formation of coordination complexes of MC with metal cations. In general, when SP is in its closed form it does not interact with metal cations (except perhaps very weakly), but when SP switches to its ring open conformation, metal ions coordinate to the phenolate anion of MC. Depending on the MC-metal interaction strength, some number of SP molecules may open spontaneously in the presence of metal ions. In extreme cases, this spontaneous complexation is irreversible (except by addition of a stronger chelating agent to the solution [47]). If the MC-complex is weak enough, the equilibrium can be manipulated using UV and visible light: UV pushes the equilibrium towards greater formation of MC-metal complexes, whereas irradiation with visible light dissociates the complexes and shifts the equilibrium towards greater concentrations of ring-closed SP [48]. This phenomenon has been shown to take place in solution as well as in solid-state polymers [49-51].

The metallochromism of SP has been studied for decades [41, 42]. The focus of reports varies between understanding the kinetics of formation and dissociation of MC-metal complexes [43, 44], designing SP chelators with new functional groups and modeling their behavior [52, 53], tuning for selectivity of specific metal cations [47, 54] and balancing thermodynamic stability with photo-reversibility [55, 56]. The emphasis, in most cases, is on optical sensing. This dissertation introduces the idea of using MC-metal coordination complexes to reversibly crosslink SP-functionalized polymer chains, and therefore, stoichiometry and reversibility play the most critical roles. Specifically, we intend to design systems with 2:1 MC-metal stoichiometry, so that metal ions can bridge polymer chains.

Figure 2.8 lists a number of SP molecules along with the reported stoichiometries of their MC-metal complexes and whether or not complex formation can be reversed either thermally or by exposure to visible light. In this discussion it is important to make the distinction between thermal reversal of MC-metal complexes back to dissociated SP, and the intrinsic, thermodynamic reversibility of metal-ligand complexes. Here, "thermally reversible" is strictly intended to mean thermal relaxation of MC back to the ring closed state after activation by UV light (or some other stimulus). It is evident from Figure 2.8 that adding certain chelating groups adjacent to the spirocyclic oxygen can guarantee the formation of 2:1 complexes with certain cations. However, addition of chelating groups leads to much higher stability of complexes, which in the case of SP molecules d-f), leads to total loss of reversibility. SPs g-h) are unique cases where the complexes have very high stability constants yet remain reversible.

It is important to note that the methodologies used to determine the stoichiometries of MC-metal complexes varies. Some researchers simply use the method of continuous variations (commonly referred to as Job's plots) [57], whereas others include stoichiometry in a full, quantitative analysis of thermodynamic stability [53, 58]. The stoichiometry of SP a), which is of particular interest, as SP a) is one of (if not the) most commonly reported form of the SP molecular switch, is particularly challenging to analyze, as the stability of its complexes is about 10 orders of magnitude weaker than for example, that of SP c). By brute force, Kubinyi and co-workers were able to obtain quantitative results: first they isolated the MC conformation of SP a) as a dry powder. Then they dissolved the MC powder in DMSO and monitored its thermal relaxation back to SP. By introducing metal salts at a precise time at which the concentration of MC was known, they were able to construct titration curves. Using this method, they determined that SP a) forms 1:1 complexes with Li(I) and divalent alkaline metal salts in DMSO.

Unfortunately, their methodology only worked using DMSO and they did not screen the properties of SP a) with transition metal salts. Others have reported 2:1 complexes of SP a) with transition metals such as Co(II) and Cu(II), but their methodologies were less robust than that of Kubinyi [48, 59, 60]. Unfortunately, the truth of the matter is the stoichiometry of SP a) with multivalent metal salts, and how it relates to solvent environment and concentration, remains unclear.

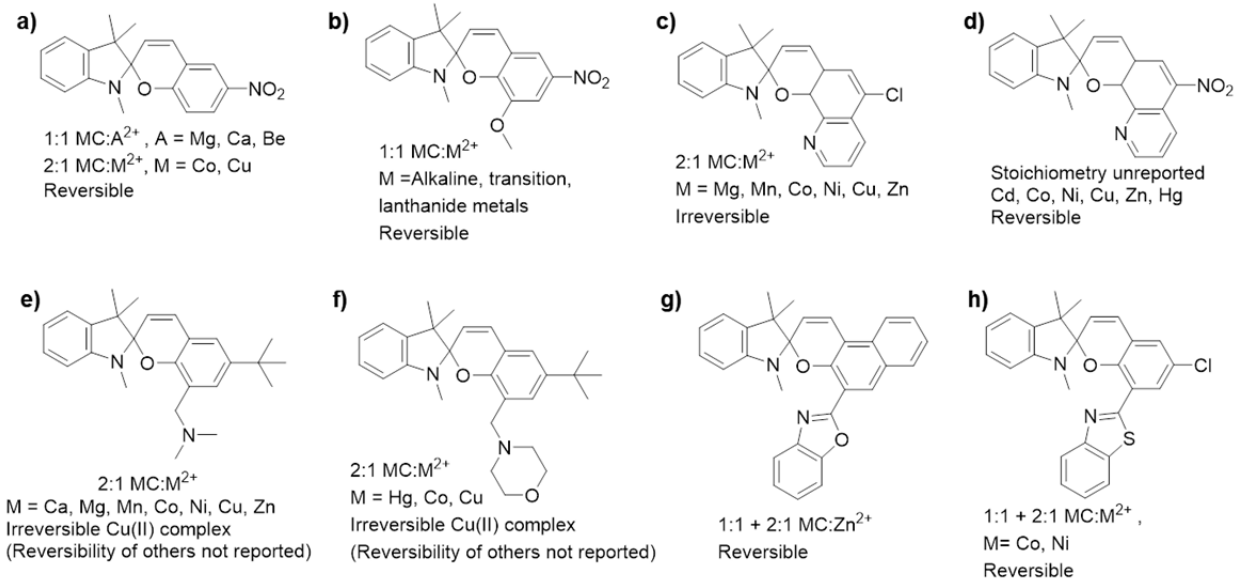


**Figure 2.8.** Examples of SP molecules that form metal complexes in their MC conformation. The reported stoichiometry of each complex as well as whether or not the complex is photo- or thermally-reversible is written underneath each SP molecule. a) Stoichiometry with alkaline metals reported by [58]. Stoichiometry with Co(II) or Cu(II) reported by [48, 59, 60]. b) Reported by [43, 44], c) reported by [55], d) reported by [56], e) reported by [47], f) reported by [54], g) reported by [52], h) reported by [53].

## 2.4 Project vision

With the exception of color switching mechanophores, the majority of mechanochemical reactions reported are completely irreversible. The vision that motivates this dissertation is the design of polymers that crosslink reversibly in response to applied mechanical forces. We proposed that SP-functionalized polymers interspersed with multivalent metal ions may form

MC-metal coordination crosslinks upon mechanochemical activation of MC. Removal of the applied stress would shift the equilibrium back to a more thermodynamically favorable un-crosslinked state. We hypothesized that force-triggered, reversible crosslinking is possible so long as at least two merocyanine molecules coordinate to each metal ion (Figure 2.9).

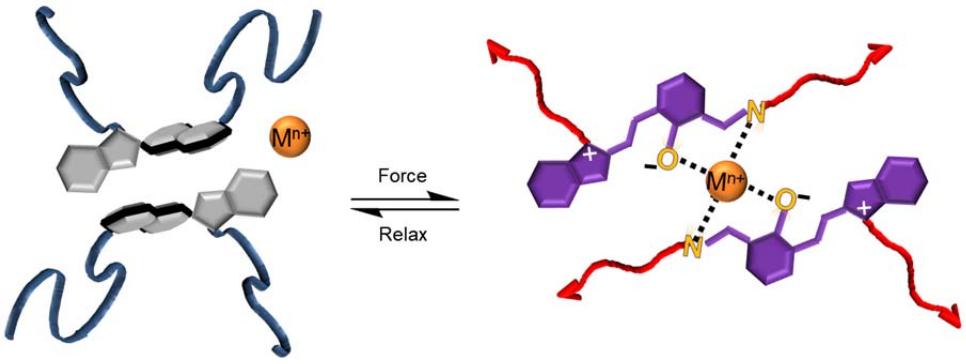


**Figure 2.9.** Proposed scheme for force-triggered, reversible crosslinking of SP-mechanophore functionalized polymer with multivalent metal ions.

Previously reported polymers that undergo mechanochemically triggered crosslinking do so irreversibly [35, 61]. Introducing an element of reversibility could open up opportunities to mimic cyclic processes in biology that are triggered by external force, such as stretch-gated opening and closing of ion channels [46] and force-triggered associations between natural proteins such as Vinculin and Talin [62, 63]. Our proposed mechanism may also introduce new classes of self-reinforcing materials that generate bonds in response to otherwise damaging events, and recover their original properties after removal of the applied stress. Furthermore, the dynamic bond of SP itelf is similar to metal-ligand and supramolecular bonds, which can selectively and sacrificially rupture, and subsequently heal after they are broken. Therefore, we anticipate that energy dissipation through rupturing spirocyclic bonds may enable polymers containing high concentrations of SP to become tougher (increasing their resistance to fracture) as they become stronger (via formation of MC-metal crosslinks). This dissertation takes the first

steps towards achieving our overarching vision, and provides guidance to the material scientist or chemist who wishes to pursue these ideas further.

### 2.5 Overview of thesis

As a first step towards achieving our vision of reversible, mechanochemically triggered polymer strengthening and toughening, two critical questions are addressed in my dissertation: first, can spiropyran molecules reversibly crosslink polymer chains? Second, can mechanical force be used as an effective stimulus for generating MC-metal coordination bonds? If the answer to both questions is yes, then it follows that mechanochemically-triggered, reversible crosslinking using SP mechanophores is at least feasible. In addition, effects of both the electronic structure of the SP mechanopohore and of metal-ion interactions on the rupture strength of the spirocyclic bond are explored. Recognizing the challenges of characterizing stoichiometry in cases where MC-metal complexes are very weak, diffusion NMR is introduced as a technique to characterize MC associations. To conclude I provide logical next steps for either the polymer scientist or synthetic chemist interested in pushing this project forward. The progression of this dissertation is as follows:

**Chapter 3** presents a set of proof-of-concept rheological experiments, where reversible modulation of metal-ligand crosslinks in a spiropyran-functionalized polymer is demonstrated for the first time. Here, reversible crosslinking is not triggered by mechanical force. Instead, MC-metal crosslinks are modulated using heat and light as independent stimuli (Figure 2.10).

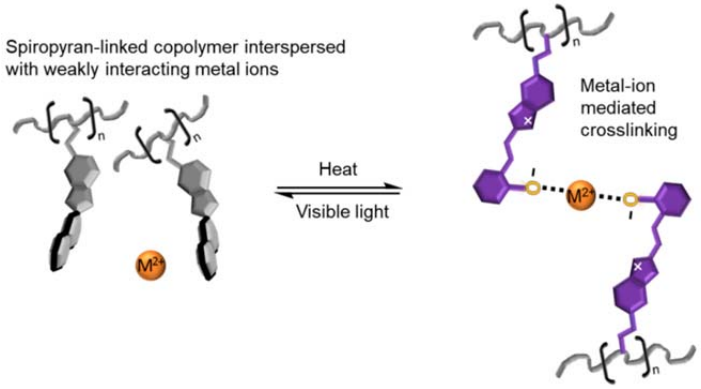


**Figure 2.10.** Schematic of the proposed mechanism for heat-triggered crosslinking and light-triggered un-crosslinking of SP-linked polymers. This work is presented in Chapter 3.

Activation of MC-metal complexes happens spontaneously in the polymer system presented in Chapter 3 (heat is merely used to accelerate the reaction). In order for mechanical force to be an effective stimulus for non-covalent bond formation, it is important to first understand and control spontaneous activation. **Chapter 4** presents the first demonstration and in-depth study of fully reversible, force-triggered MC-metal complexation in a solid-state elastomer (Figure 2.11). The primary focus is to demonstrate reversibility and elucidate mechanisms that reduce spontaneous activation and increase mechanochemical activation of SP mechanophores in the presence of metal ions. In Chapter 4 we also presents DFT simulations that reveal different mechanochemical behavior of SP mechanophores depending on both the electronic structure of SP and the presence or absence of metal ions.

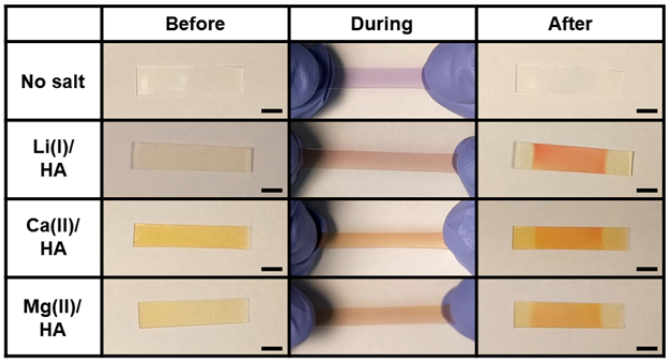


**Figure 2.11.** Photos highlighting the work presented in Chapter 4. Here, we demonstrate force-triggered MC-metal complexation in PDMS elastomers.

In **Chapter 5**, diffusion ordered spectroscopy (DOSY) is introduced as a method for evaluating the stoichiometry of MC-metal complexes (Figure 2.12). In **Chapter 6**, we summarize what we have accomplished, discuss ongoing work and challenges towards developing high SP-content polymers, and present synthesis schemes and preliminary analyses towards developing mechanophores with moieties that inhibit spontaneous MC-metal coordination and that reliably produce 2:1 MC-metal complexes in single-molecule studies.

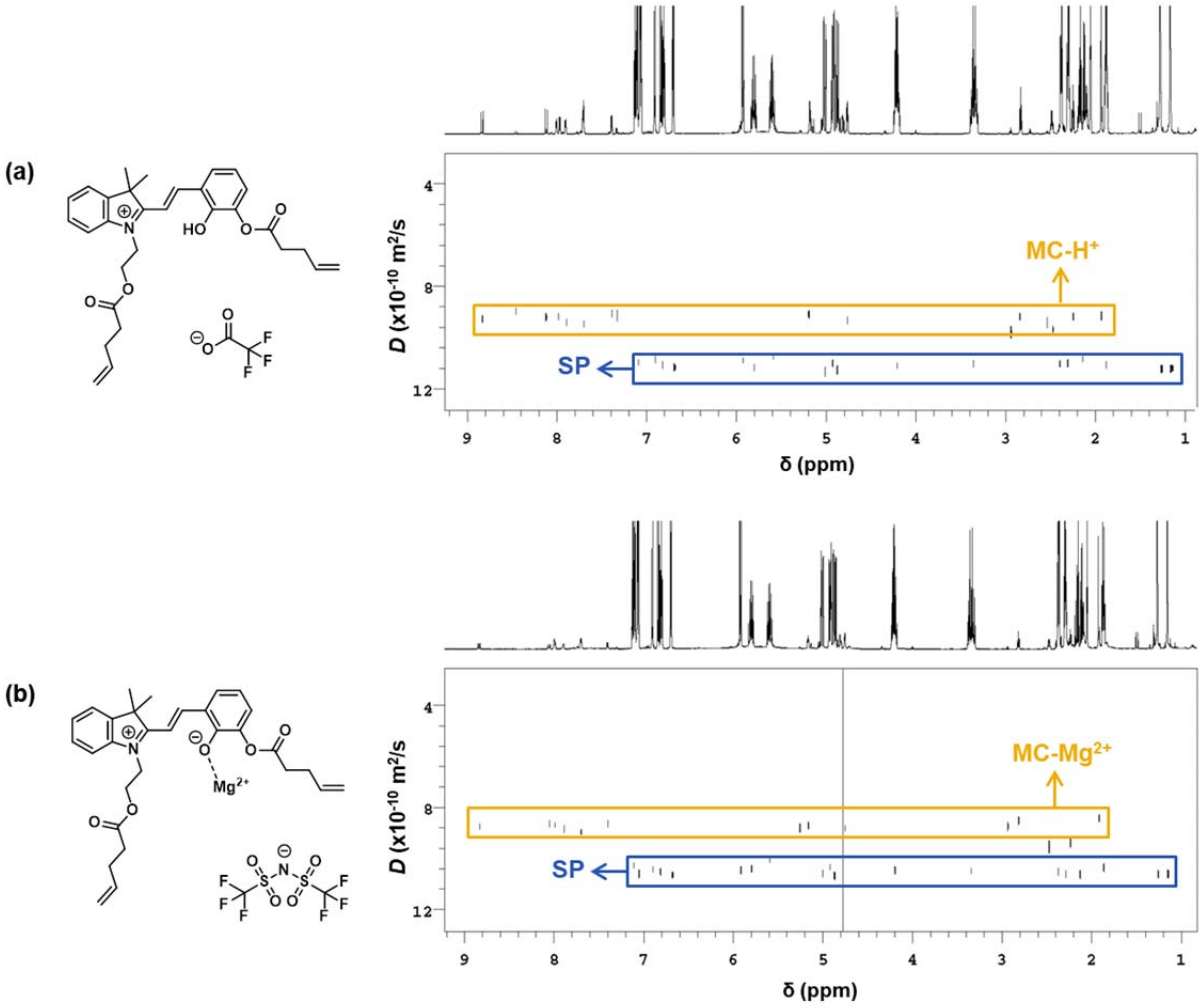


**Figure 2.12.** DOSY NMR spectrum of SP with $Cu(NTf_2)_2$ in acetone-$d_6$. Work presented in detail in Chapter 5.

## 2.6 REFERENCES


1. Schlom, D. G., Chen, L.-Q., Fennie, C. J., Gopalan, V., Muller, D. A., Pan, X., Ramesh, R. and Uecker, R. *MRS Bulletin* **2014**, *39*, 118.
2. Mavrikakis, M., Hammer, B. and Nørskov, J. K. *Physical Review Letters* **1998**, *81*, 2819.
3. Wang, H., Xu, S., Tsai, C., Li, Y., Liu, C., Zhao, J., Liu, Y., Yuan, H., Abild-Pedersen, F., Prinz, F. B., et al. *Science* **2016**, *354*, 1031.
4. Staudinger, H. and Bondy, H. F. *Berichte der deutschen chemischen Gesellschaft (A and B Series)* **1930**, *63*, 734.
5. Staudinger, H. and Leupold, E. O. *Berichte der deutschen chemischen Gesellschaft (A and B Series)* **1930**, *63*, 730.
6. Staudinger, H. and Heuer, W. *Berichte der deutschen chemischen Gesellschaft (A and B Series)* **1934**, *67*, 1159.
7. Kauzmann, W. and Eyring, H. *Journal of the American Chemical Society* **1940**, *62*, 3113.
8. Porter, R. S. and Johnson, J. F. *The Journal of Physical Chemistry* **1959**, *63*, 202.
9. Keller, A. and Odell, J. A. *Colloid and Polymer Science* **1985**, *263*, 181.
10. Odell, J. A. and Keller, A. *Journal of Polymer Science Part B: Polymer Physics* **1986**, *24*, 1889.
11. Encina, M. V., Lissi, E., Sarasúa, M., Gargallo, L. and Radic, D. *Journal of Polymer Science: Polymer Letters Edition* **1980**, *18*, 757.
12. Li, J., Nagamani, C. and Moore, J. S. *Accounts of Chemical Research* **2015**, *48*, 2181.
13. Imato, K., Kanehara, T., Ohishi, T., Nishihara, M., Yajima, H., Ito, M., Takahara, A. and Otsuka, H. *ACS Macro Letters* **2015**, *4*, 1307.
14. Li, C. H., Wang, C., Keplinger, C., Zuo, J. L., Jin, L., Sun, Y., Zheng, P., Cao, Y., Lissel, F., Linder, C., et al. *Nat Chem* **2016**, *8*, 618.
15. Chung, J., Kushner, A. M., Weisman, A. C. and Guan, Z. *Nature Materials* **2014**, *13*, 1055.
16. Sagara, Y., Karman, M., Verde-Sesto, E., Matsuo, K., Kim, Y., Tamaoki, N. and Weder, C. *Journal of the American Chemical Society* **2018**, *140*, 1584.
17. Sun, J. Y., Zhao, X., Illeperuma, W. R., Chaudhuri, O., Oh, K. H., Mooney, D. J., Vlassak, J. J. and Suo, Z. *Nature* **2012**, *489*, 133.
18. Mozhdehi, D., Neal, J. A., Grindy, S. C., Cordeau, Y., Ayala, S., Holten-Andersen, N. and Guan, Z. *Macromolecules* **2016**, *49*, 6310.
19. Filippidi, E., Cristiani, T. R., Eisenbach, C. D., Waite, J. H., Israelachvili, J. N., Ahn, B. K. and Valentine, M. T. *Science* **2017**, *358*, 502.
20. Neal, J. A., Mozhdehi, D. and Guan, Z. *J Am Chem Soc* **2015**, *137*, 4846.
21. Chen, Y., Kushner, A. M., Williams, G. A. and Guan, Z. *Nat Chem* **2012**, *4*, 467.
22. Gossweiler, G. R., Brown, C. L., Hewage, G. B., Sapiro-Gheiler, E., Trautman, W. J., Welshofer, G. W. and Craig, S. L. *ACS Applied Materials & Interfaces* **2015**, *7*, 22431.
23. Peterson, G. I., Larsen, M. B., Ganter, M. A., Storti, D. W. and Boydston, A. J. *ACS Applied Materials & Interfaces* **2015**, *7*, 577.
24. Ducrot, E., Chen, Y., Bulters, M., Sijbesma, R. P. and Creton, C. *Science* **2014**, *344*, 186.
25. Kim, S.-J. and Reneker, D. H. *Polymer Bulletin* **1993**, *31*, 367.
26. Chen, Y., Spiering, A. J. H., Karthikeyan, S., Peters, G. W. M., Meijer, E. W. and Sijbesma, R. P. *Nature Chemistry* **2012**, *4*, 559.
27. Potisek, S. L., Davis, D. A., Sottos, N. R., White, S. R. and Moore, J. S. *Journal of the American Chemical Society* **2007**, *129*, 13808.

28. Davis, D. A., Hamilton, A., Yang, J., Cremar, L. D., Van Gough, D., Potisek, S. L., Ong, M. T., Braun, P. V., Martinez, T. J., White, S. R., et al. *Nature* **2009**, *459*, 68.
29. Lee, C. K., Davis, D. A., White, S. R., Moore, J. S., Sottos, N., R. and Braun, P. V. *Journal of the American Chemical Society* **2010**, *132*, 16107.
30. Robb, M. J., Kim, T. A., Halmes, A. J., White, S. R., Sottos, N. R. and Moore, J. S. *Journal of the American Chemical Society* **2016**, *138*, 12328.
31. Gossweiler, G. R., Hewage, G. B., Soriano, G., Wang, Q., Welshofer, G. W., Zhao, X. and Craig, S. L. *ACS Macro Letters* **2014**, *3*, 216.
32. Brantley, J. N., Wiggins, K. M. and Bielawski, C. W. *Polymer International* **2013**, *62*, 2.
33. Jakobs, R. T. M., Ma, S. and Sijbesma, R. P. *ACS Macro Letters* **2013**, *2*, 613.
34. Diesendruck, C. E., Steinberg, B. D., Sugai, N., Silberstein, M. N., Sottos, N. R., White, S. R., Braun, P. V. and Moore, J. S. *Journal of the American Chemical Society* **2012**, *134*, 12446.
35. Ramirez, A. L., Kean, Z. S., Orlicki, J. A., Champhekar, M., Elsakr, S. M., Krause, W. E. and Craig, S. L. *Nat Chem* **2013**, *5*, 757.
36. Guglielmetti, R. In *Photochromism (Revised Edition)*; Bouas-Laurent, H., Ed.; Elsevier Science: Amsterdam, 2003, p 314.
37. Keum, S.-R., Ma, S.-Y., Lim, H.-W., Han, T.-H. and Choi, K.-H. *Bulletin of the Korean Chemical Society* **2012**, *33*, 2683.
38. Murugan, N. A., Chakrabarti, S. and Agren, H. *J Phys Chem B* **2011**, *115*, 4025.
39. Metelitsa, A. V., Lokshin, V., Micheau, J. C., Samat, A., Guglielmetti, R. and Minkin, V. I. *Phys. Chem. Chem. Phys.* **2002**, *4*, 4340.
40. Wojtyk, J. T. C., Wasey, A., Xiao, N.-N., Kazmaier, P. M., Hoz, S., Yu, C., Lemieux, R. P. and Buncel, E. *Journal of Physical Chemistry* **2007**, *111*, 2511.
41. Taylor, L. D., Nicholson, J. and Davis, R. B. *Tetrahedron Letters* **1967**, *17*, 1585.
42. Phillips, J. P., Mueller, A. and Przystal, F. *Journal of the American Chemical Society* **1965**, *87*, 4020.
43. Gorner, H. and Chibisov, A. K. *Journal of the Chemical Society, Faraday Transactions* **1998**, *94*, 2557.
44. Chibisov, A. K. and Görner, H. *Chemical Physics* **1998**, *237*, 425.
45. Klajn, R. *Chem Soc Rev* **2014**, *43*, 148.
46. Perozo, E., Cortes, D. M., Sompornpisut, P., Kloda, A. and Martinac, B. *Nature* **2002**, *418*, 942.
47. Shao, N., Zhang, Y., Cheung, S., Yang, R., Chan, W., Mo, T., Li, K. and Liu, F. *Analytical Chemistry* **2005**, *77*, 7294.
48. Byrne, R. J., Stitzel, S. E. and Diamond, D. *Journal of Materials Chemistry* **2006**, *16*, 1332.
49. Fries, K., Samanta, S., Orski, S. and Locklin, J. *Chem Commun (Camb)* **2008**, 6288.
50. Fries, K. H., Driskell, J. D., Samanta, S. and Locklin, J. *Analytical Chemistry* **2010**, *82*, 3306.
51. Fries, K. H., Driskell, J. D., Sheppard, G. R. and Locklin, J. *Langmuir* **2011**, *27*, 12253.
52. Chernyshev, A. V., Voloshin, N. A., Metelitsa, A. V., Tkachev, V. V., Aldoshin, S. M., Solov'eva, E., Rostovtseva, I. A. and Minkin, V. I. *Journal of Photochemistry and Photobiology A: Chemistry* **2013**, *265*, 1.
53. Zakharova, M. I., Coudret, C., Pimienta, V., Micheau, J. C., Delbaere, S., Vermeersch, G., Metelitsa, A. V., Voloshin, N. and Minkin, V. I. *Photochemical & Photobiological Sciences* **2010**, *9*, 199.

54. Shao, N., Jin, J. Y., Wang, H., Zhang, Y., Yang, R. H. and Chan, W. H. *Analytical Chemistry* **2008**, *80*, 3466.
55. Chernyshev, A. V., Metelitsa, A. V., Gaeva, E. B., Voloshin, N. A., Borodkin, G. S. and Minkin, V. I. *Journal of Physical Organic Chemistry* **2007**, *20*, 908.
56. Evans, L., Collins, G. E., Shaffer, R. E., Michelet, V. and Winkler, J. D. *Analytical Chemistry* **1999**, *71*, 5322.
57. Byrne, R., Ventura, C., Benito Lopez, F., Walther, A., Heise, A. and Diamond, D. *Biosens Bioelectron* **2010**, *26*, 1392.
58. Kubinyi, M., Varga, O., Baranyai, P., Kállay, M., Mizsei, R., Tárkányi, G. and Vidóczy, T. *Journal of Molecular Structure* **2011**, *1000*, 77.
59. Kundu, P. K., Olsen, G. L., Kiss, V. and Klajn, R. *Nat Commun* **2014**, *5*, 3588.
60. Aleksandar, R., Silvia, S., Robert, B., Conor, S., King Tong, L. and Dermot, D. *Journal of Physics D: Applied Physics* **2007**, *40*, 7238.
61. Kean, Z. S. and Craig, S. L. *Polymer* **2012**, *53*, 1035.
62. Rio, A. d., Perez-Jimenez, R., Liu, R., Roca-Cusachs, P., Fernandez, J. M. and Sheetz, M. P. *Science* **2009**, *323*, 638.
63. Yao, M., Goult, B. T., Chen, H., Cong, P., Sheetz, M. P. and Yan, J. *Sci Rep* **2014**, *4*, 4610.

# CHAPTER 3: MODULATING NON-COVALENT CROSSLINKS WITH MOLECULAR SWITCHES

## 3.1 Introduction

Metal-ligand (M-L) coordination complexes have been shown to add unique mechanical functionalities to polymers through their dynamic bonding nature. An important distinction between M-L complexes and covalent bonds is that M-L complexes are both generally weaker than covalent bonds, and more likely to participate in reversible bond formation. As such, when incorporated in a polymer, M-L complexes can act as sacrificial bonds that dissipate mechanical energy, increasing the polymer's toughness [1-3], while their reversibility means that broken bonds can reform, enabling material repair after a damage event [3-6]. Though M-L bonds are intrinsically reversible, few M-L systems have been shown to reversibly associate and dissociate in response to external stimuli, other than by mechanically breaking bonds or adding reagents. Here we introduce molecular switches as a motif for toggling the formation and dissociation of M-L coordination crosslinks in polymers. Specifically, we demonstrate that M-L coordination crosslinks in a spiropyran (SP) functionalized polymer solution are modulated using both light and heat as independent stimuli, resulting in reversible transformations between fluid and gel states.

Using SP as a switchable, M-L crosslinker enables a variety of opportunities to impart stimuli-responsive behavior to soft materials. SP has been used for many years as a photochromic dye [7]. When exposed to UV light many SPs switch from a visibly transparent, ring closed constitution (generally called the SP state) to a ring-open, merocyanine (MC) form, which strongly absorbs visible light. Upon removal of UV or exposure to visible light, the dynamic equilibrium shifts, and MC reverts back to SP (Figure 1A). In addition to UV and

visible light, the reversible isomerization between SP and MC is modulated by thermal energy [8], changes in solvent polarity [9, 10] as well as interactions with chemical species including acids and bases [11], and metal ions [12-15]. As we and others have shown, when SP molecules are appropriately linked to a polymer backbone, mechanical force also triggers MC isomerization [16-18]. The large number of potential stimuli for modulating the dynamic equilibrium between SP and MC makes this molecular switch particularly attractive for programming materials with stimuli-responsive behavior [19].

Based on previous reports that showed 2:1 coordination between MC and transition metal ions [19-22], we hypothesize that metal salts such as Co(II) and Cu(II) mediate reversible crosslinks between SP functionalized polymer chains. As a proof of concept, a concentrated solution of a spiropyran containing methacrylate copolymer (Fig. S1), in a high boiling point solvent, propylene carbonate (PC), was reversibly crosslinked by externally triggering MC complexation with transition metal ions. As illustrated by the schematic of Figure 1B, heat triggers polymer crosslinking via ring opening of SP, yielding MC-metal coordination complexes. Crosslinking is reversed by irradiating the polymer network with visible light, causing MC to release ions and revert to its ring-closed SP state.

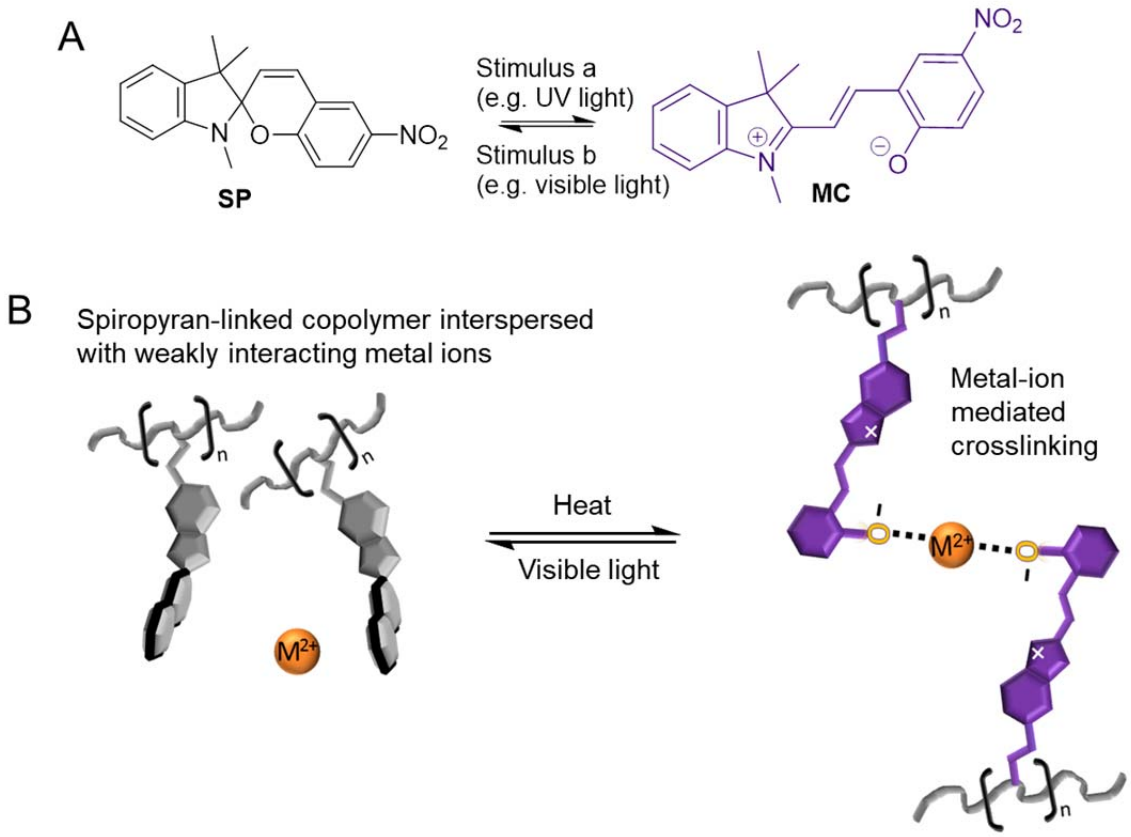


**Figure 3.1.** Spiropyran as a multifunctional molecular switch. (A) Stimuli-triggered reversible isomerization between SP and MC. (B) Schematic of the proposed mechanism for heat-triggered crosslinking and light-triggered un-crosslinking of SP-linked polymers.

## 3.2 Experimental Methods

### *3.2.1 General Information*

5-methoxy-2,3,3-trimethyl-3H-indole was purchased from Biosynth. Cobalt bis(trifluoromethylsulfonyl)imide ($Co(NTf_2)_2$) and copper bis(trifluoromethylsulfonyl)imide ($Cu(NTf_2)_2$) were purchased from TCI Chemicals. Sodium bis(trifluoromethylsulfonyl)imide was purchased from Alfa Aesar. All other chemicals and solvents were purchased from either Sigma Aldrich or Alfa Aesar. All chemicals and solvents were used without further purification. NMR spectra were taken on a 500 MHz Carver B500 spectrometer. Gel permeation chromatography (GPC) was performed with a Waters 515 HPLC pump and recorded with

Waters 2414 refractive index and Waters 2998 UV absorption detectors. GPC traces were taken of polymer samples dissolved in THF using monodisperse polystyrene as calibration standards.

*3.2.2 Synthetic procedures*

*2,3,3-trimethyl-3H-indol-5-ol:* 20 g (105.67 mmol) of 5-methoxy-2,3,3-trimethyl-3H-indole was dissolved in 48% aqueous HBr and refluxed at 140 °C for 2.5 hours under argon. After cooling to room temperature, the solution was added to 600 ml of DI water, partially neutralized with $Na_2CO_3$ and brought to pH ~7-8 with $NaHCO_3$. Extracted with $CH_2Cl_2$ (3 x 200 ml). The combined organics were washed twice with 100 ml of DI water, and concentrated *in vacuo* to yield the product as an off-white solid (16.42 g, 93.7 mmoles, 88.7%). The material was pure by NMR and mass spec, and was used without further purification.

$^1$H NMR (500 MHz, DMSO-$d_6$) δ 9.27 (s, 1H), 7.18 (d, $J$ = 8.2 Hz, 1H), 6.77 (d, $J$ = 2.4 Hz, 1H), 6.64 (dd, $J$ = 8.2, 2.4 Hz, 1H), 2.12 (s, 3H), 1.18 (s, 6H). $^{13}$C NMR (126 MHz, DMSO-$d_6$) δ 183.93, 155.31, 147.48, 145.85, 119.49, 113.45, 109.17, 53.02, 22.76, 14.81.

*Compound* **1**: *5-hydroxy-1,2,3,3-tetramethyl-3H-indol-1-ium iodide*. 16.39 g (93.52 mmol) of *2,3,3-trimethyl-3H-indol-5-ol* was dissolved in 400 ml of 1:1 toluene/acetonitrile in a one-necked round bottom flask. 26.5 g (186.7 mmol, 2 equiv) of iodomethane was added and the solution was refluxed at 90 °C for 14 hours. The precipitated solid was filtered and washed copiously with ethanol and diethyl ether to yield **1** as a white, sand-textured powder (28.914 g, 91.16 mmol, 97.48%). Product was used without further purification.

$^1$H NMR (500 MHz, DMSO-$d_6$) δ 7.69 (d, $J$ = 8.7 Hz, 1H), 7.12 (d, $J$ = 2.4 Hz, 1H), 6.93 (dd, $J$ = 8.7, 2.4 Hz, 1H), 3.91 (d, $J$ = 1.2 Hz, 3H), 2.70 (d, $J$ = 1.3 Hz, 3H), 1.47 (s, 6H). $^{13}$C NMR

(126 MHz, DMSO-$d_6$) δ 191.89, 158.94, 143.72, 134.15, 116.14, 115.01, 110.31, 53.47, 34.79, 21.91, 13.98.

*Compound* **2**: *1',3',3'-trimethyl-6-nitrospiro[chromene-2,2'-indolin]-5'-ol*. A solution of **1** (4.44 g, 14 mmol), 2-hydroxy-5-nitrobenzaldehyde (2.342, 14 mmol, 1 equiv), and piperidine (2.385 g, ~28 mmol, ~2 equiv) was refluxed in 38 ml of absolute ethanol for 5 hours in an oil bath set to 100 °C. After 5 hours, the solution slowly cooled to room temperature in the oil bath for several hours. The precipitate was filtered, washed with ethanol, diethyl ether and hexanes to yield **2** as dark green crystals (4.25 g, 12.56 mmol, 89.7%). Characterization matched literature values [23].

**SPMA:** *1',3',3'-trimethyl-6-nitrospiro[chromene-2,2'-indolin]-5'-yl methacrylate*. 4.23 g (12.5 mmol) of compound **2** and 2 g of DMAP (16.37 mmol, 1.3 equiv) were dissolved in 67 ml of THF. 2.83 g (18.357 mmol, 1.47 equiv) of methacryloyl anhydride was added and the solution stirred at room temperature for 6 hours. A small amount of methanol was then added to quench the reaction. THF was removed *in vacuo* and the crude mixture was redissolved in $CH_2Cl_2$ and the product purified by flash chromatography through a silica followed by flash chromatography through basic alumina gel. $CH_2Cl_2$ was then removed *in vacuo* to yield the product as a brown solid (5.595 g, 11.3 mmol, 90.5%).

$^1$H NMR (500 MHz, DMSO-$d_6$) δ 8.23 (d, $J$ = 2.9 Hz, 1H), 8.01 (dd, $J$ = 9.0, 2.8 Hz, 1H), 7.24 (d, $J$ = 10.4 Hz, 1H), 6.99 (d, $J$ = 2.3 Hz, 1H), 6.96 (d, $J$ = 8.9 Hz, 1H), 6.92 – 6.90 (m, 1H), 6.63 (d, $J$ = 8.4 Hz, 1H), 6.25 (t, $J$ = 1.3 Hz, 1H), 6.00 (d, $J$ = 10.4 Hz, 1H), 5.87 (t, $J$ = 1.6 Hz, 1H), 2.94 (s, 3H), 2.68 (s, 3H), 1.17 (d, $J$ = 39.2 Hz, 6H). $^{13}$C NMR (126 MHz, DMSO-$d_6$) δ

165.91, 159.29, 145.15, 143.86, 140.57, 137.04, 135.52, 128.38, 127.31, 125.75, 122.85, 121.18, 120.41, 118.88, 115.84, 115.44, 107.05, 106.40, 79.18, 51.95, 38.60, 28.69, 25.49, 19.50, 18.12.

HRMS-ESI (m/z): $[M + H]^+$ calcd for $C_{23}H_{23}N_2O_5$, 407.1602; found 407.1607

**P(DEGMEMA–SPMA):** Synthesized by RAFT polymerization. 3.709 g (9.13 mmol) of **SPMA**, 11.394 g (60.54 mmol) of diethylene glycol methyl ether methacrylate (DEGMEMA), 0.181 g (0.09 mmol) of 4-Cyano-4-[(dodecylsulfanylthiocarbonyl) sulfanyl]pentanoic acid (RAFT agent), and 0.0117 g (.071 mmol) of AIBN was dissolved in 12.5 ml of anhydrous DMF. Solution was purged with $N_2$ for 45 minutes and polymerized at 80 °C for 24 hours. Polymer was precipitated directly into diethyl ether, redissolved in $CH_2Cl_2$ and precipitated a second time in diethyl ether to yield red colored polymer flakes (10.92 g, 71.4%). $M_n$ = 26.2 kDa, $M_w$ = 38.4 kDa (PDI = 1.47) by GPC. $^1$H NMR spectrum shown in Fig. 3.2.

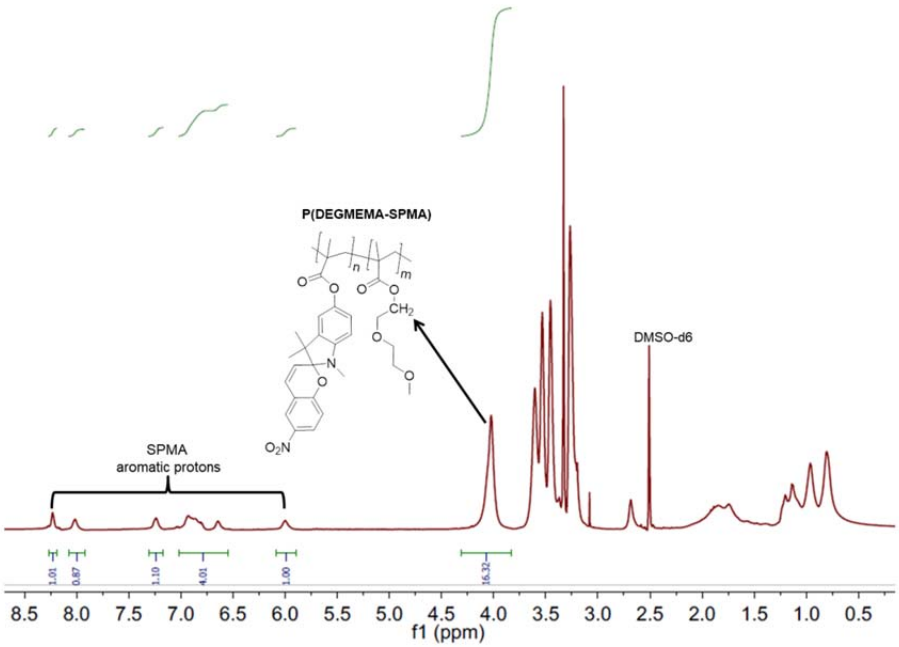


**Figure 3.2.** $^1$H NMR spectrum of P(DEGMEMA–SPMA) in DMSO-d6. SPMA concentration (~ 10.5 mol%) quantified by comparing integrals of aromatic peaks to peak at 4.02 ppm.

*3.2.3 Preparation of polymer solutions for rheology*

A stock solution of 27.5 wt% P(DEGMEMA–SPMA) in PC was prepared. Stock solutions of $Co(NTf_2)_2$, $Cu(NTf_2)_2$ and $Na(NTf_2)$ in PC were prepared in separate vials. For each experiment a particular salt solution and the 27.5 wt% P(DEGMEMA–SPMA) solution were combined to achieve a targeted SPMA:metal stoichiometric ratio. In all cases the polymer solution was diluted to 21 wt% P(DEGMEMA–SPMA) after addition of the metal salt solution. The viscous mixture was vortexed until the solution became homogeneous and then held under high vacuum (50-80 mTorr) for approximately two hours until a final concentration of 24.5 ± 0.3 wt% P(DEGMEMA–SPMA) was attained. Polymer solutions at different concentrations were prepared in a similar manner.

*3.2.4 UV-Vis absorption spectroscopy*

For UV-Vis absorption spectra of concentrated polymer solutions, 24.5 wt% solutions of P(DEGMEMA-SPMA) with and with $Co(NTf_2)_2$ in a ratio of 2:1 SP: $Co(NTf_2)_2$ were prepared in the manner described above. Polymer solutions were sandwiched between glass coverslips using an epoxy-adhered, ~100 μm thick washer as a spacer. The absorption spectra of Fig. 2 were measured using an Axio Observer D1 inverted microscope with a Halogen illumination light source, coupled via multi-mode fiber optic cables to a Control Development 2DMPP, thermoelectrically-cooled optical spectrometer ($\lambda$ = 420-779 nm detection range). Heating was conducted in the dark using a standard hot plate. Samples were heated to 80 °C for 1 hour and immediately transferred to the spectrometer for measurements. UV exposure was conducted using a 100 W, 365 nm peak wavelength UV light source positioned approximately 6 inches from the sample surface. 3 minutes of UV exposure was used for all UV excitation experiments,

as this was determined to maximize the conversion of SP to MC under these conditions. The solution was exposed to visible light using a high current white LED spotlight (Advanced Illumination SL073), which was positioned ~ 6 cm from the surface of the sample. According to the specifications of the manufacturer, the LED spotlight emits wavelengths between approximately 420 to 750 nm, and the irradiance at normal incidence 10 cm from the source varies from 79.6 to 93.7 W/m$^2$.

Absorption spectra of dilute solutions (total concentration [SP] + [$Co(NTf_2)_2$] = 0.5 mM) were measured in 1 mm path length glass cuvettes using a Shimadzu UV-2401 PC UV-Vis spectrophotometer. Samples were irradiated with a 100 W, 365 nm peak wavelength UV lamp positioned approximately 10 inches from the cuvette. 90 seconds of UV exposure was used for all UV excitation experiments, as this was determined to maximize the conversion of SP to MC under these conditions.

*3.2.5 Rheology*

Experiments were performed on a stress-controlled (single-head) rotational rheometer (Discovery Series Hybrid Rheometer (DHR), model HR-3, TA Instruments). The instrument has an oscillatory minimum torque $T_{min}$ = 0.5 nN·m and inertia $I_{inst}$ = 21.0044 $\mu$N·m·s$^2$. A custom made, glass parallel plate geometry of 25 mm diameter was used. The measured geometry inertia was $I_{geom}$ = 5.1747 $\mu$N·m·s$^2$. In all oscillatory experiments the resolution was limited by inertia of the instrument and geometry. The inertial limit may be approximated as [24]:

$$G_{min} > \frac{\left(I_{inst} + I_{geom}\right)F_{\tau}}{F_{\gamma}}\omega^2 \tag{3.1}$$

where $G_{min}$ is the minimum dynamic modulus (Pa) that can be resolved by the instrument, $F_{\tau}$ and $F_{\gamma}$ are the stress and strain constants of the geometry, which equal 40743.7 m$^{-3}$ and 74.6269,

respectively, and $\omega$ is the angular frequency of oscillation (rad·s$^{-1}$). The inertial limit is plotted as grey regions in plots in which data points approach or fall below the limit. The initial gap height at the start of each experiment was ~ 410 ± 15 $\mu$m. Temperature was controlled using a Peltier plate bottom geometry, and three high current, white LED spotlights (Advanced Illumination SL073) were positioned ~ 6 cm from the surface of the top plate and were maintained at approximately the same distance for each experiment. According to the specifications of the manufacturer, the LED spotlight emits wavelengths between approximately 420 to 750 nm, and the irradiance at normal incidence 10 cm from the source varies from 79.6 to 93.7 W/m$^2$. Thermal expansion of the geometry was accounted for automatically by the software by performing a calibration prior to all measurements. During the "lights off" stages of experiments (e.g. during crosslinking), the LEDs were turned off and an opaque solvent trap was placed around the geometry to further reduce light exposure.

*3.2.6 Modeling the linear viscoelastic responses*

The linear viscoelastic responses are fit to a three-parameter model of a continuous relaxation spectrum, $H(\tau)$ (a viscosity density on relaxation time, with dimensions of Pa·s/s in SI units), derived from a log-normal distribution of relaxation times [25]

$$H(\tau) = H_p \cdot e^{-\frac{1}{2}\left[\frac{\ln(\tau)-\ln(\tau_p)}{\sigma}\right]^2} \tag{3.2}$$

where $\tau_p$ is the log-median relaxation timescale, $H_p$ is the peak of the spectrum, and $\sigma$ is the standard deviation of the log-normal distribution. The viscoelastic moduli are related to the spectrum through the equations [26]

$$G'(\omega) = \int_0^\infty \frac{H(\tau)}{\tau} \cdot \frac{(\omega\tau)^2}{1+(\omega\tau)^2} d\tau$$
$$G''(\omega) = \int_0^\infty H(\tau) \cdot \frac{\omega}{1+(\omega\tau)^2} d\tau \tag{3.3}$$

The apparent plateau modulus, $G_0$, is related to the spectrum as

$$G_0 = \lim_{\omega\to\infty} G'(\omega) = \int_0^\infty \frac{H(\tau)}{\tau} d\tau = H_p \sigma\sqrt{2\pi} \tag{3.4}$$

which we use to estimate the crosslink density of the networks. The spectrum is also used to calculate the so-called "number-average" relaxation time [26], $\tau_n$,

$$\tau_n = \frac{\int_0^\infty H(\tau) d\tau}{\int_0^\infty \frac{H(\tau)}{\tau} d\tau} = \tau_p e^{\frac{1}{2}\sigma^2} \tag{3.5}$$

and the so-called "weight-average" relaxation time [26], or longest characteristic timescale for viscoelastic liquids [27-29], $\tau_w$,

$$\tau_w = \frac{\int_0^\infty \tau H(\tau) d\tau}{\int_0^\infty H(\tau) d\tau} = \tau_p e^{\frac{3}{2}\sigma^2} . \tag{3.6}$$

Considering the frequency range over which experimental data have been collected, and the decay of the relaxation spectrum (Eq. 3.2) at short time scales, the calculated $\tau_n$ and $\tau_w$ are to be interpreted as characteristic times of the terminal dispersion of the gels [30]. A measure of the spread of this terminal dispersion is given by the so-called polydispersity index (PDI) of relaxation times [30],

$$\text{PDI} = \frac{\tau_w}{\tau_n} = e^{\sigma^2} . \tag{3.7}$$

The three-parameter model is fit numerically to the data using Eq. (3.3) with a custom-written non-linear regression routine in MATLAB. The fit routine minimizes the difference between data and the model using a residual sum of squares (RSS) defined as

$$\mathrm{RSS} = \sum_i \left( \log_{10}\left( \left| Y_i^{\mathrm{model}} \right| \right) - \log_{10}\left( \left| Y_i^{\mathrm{exp}} \right| \right) \right)^2 . \tag{3.8}$$

The elements of the variance-covariance matrix (in linear space), $\sigma^2_{x_i x_j}$ (where $x_i = \{\tau_p, H_p, \sigma\}$), are used to estimate the error, $\sigma_z^2$ (where $z = f(x_i)$), on the spectrum $H(\tau)$ and related quantities ($G_0$, $\tau_n$, $\tau_w$, PDI) through the following error propagation equation [31],

$$\sigma_z^2 = \sum_{m=1}^{P} \sigma^2_{x_m} \left( \frac{\partial z}{\partial x_m} \right)^2 + 2 \sum_{m=1}^{P} \sum_{n=m+1}^{P} \sigma^2_{x_m x_n} \frac{\partial z}{\partial x_m} \frac{\partial z}{\partial x_n} \tag{3.9}$$

where $P = 3$ is the number of fit parameters. The fit parameters are given in Table 3.1. Based on these fit parameters, the number-average relaxation time, the longest characteristic relaxation time, the polydispersity index of relaxation times, the plateau modulus, and the crosslink density are calculated, as given in Table 3.2.

### 3.3 Polymer synthesis, UV-Vis characterization and gelation

To demonstrate switchable crosslinking, we synthesized a SP-functionalized copolymer using reversible addition-fragmentation chain-transfer (RAFT) polymerization. Synthesis details are included in the Supporting Information (Figure 3.3). Di(ethylene glycol) methyl ether methacrylate (DEGMEMA) was chosen as a co-monomer to generate a polymer that is highly soluble in a variety of polar organic solvents. The random copolymer poly(DEGMEMA–SPMA) contains ~10.5 mol% SPMA, as determined from its $^1$H NMR spectrum (Fig. S3), and has number-average molecular weight $M_n \approx 26$ kDa and PDI = 1.47, as determined by gel permeation chromatography.

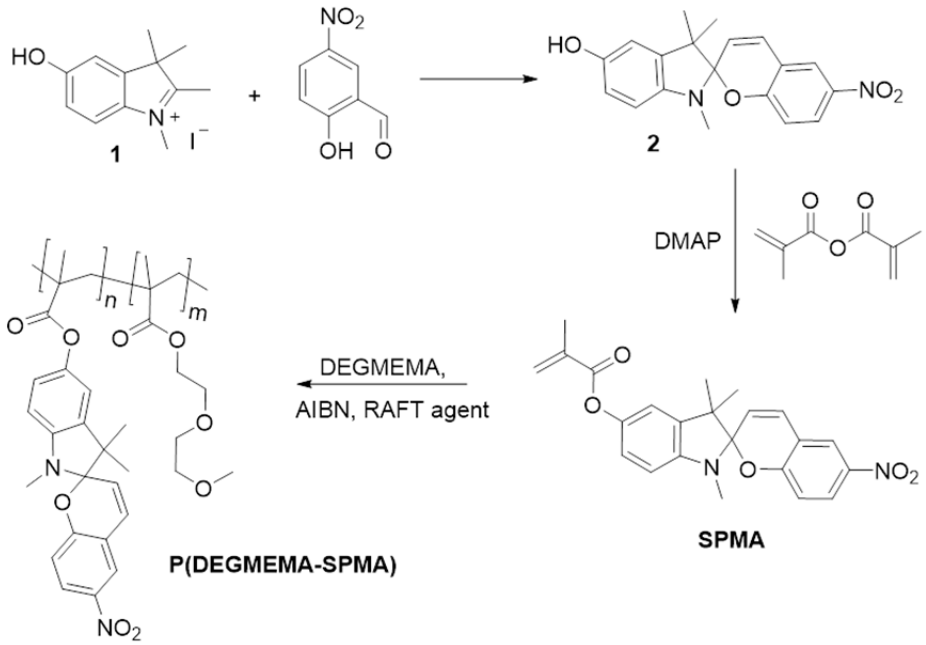


**Figure. 3.3.** Synthesis of SPMA and P(DEGMEMA–SPMA).

The reversible complexation of poly(DEGMEMA-SPMA) with $Co(NTf_2)_2$ was probed using UV-Vis absorption spectroscopy. Figure 3.4A shows UV-Vis absorption spectra of dilute solutions of poly(DEGMEMA-SPMA) in PC containing varying ratios of SP to $Co(NTf_2)_2$. UV light exposure of metal-salt free solutions generates a large absorption band centered at $\lambda$ = 564 nm, corresponding to the UV-triggered MC conformation. In the presence of $Co(NTf_2)_2$ UV light exposure results in a broad absorption band centered at $\lambda$ = 506 nm, which is characteristic of the of *trans*-MC-metal complexes [32, 33]. Importantly, these MC-Co complexes not only form via UV excitation, but also via thermal isomerization, a process which is accelerated by applying heat. The extent of thermal isomerization of MC-Co is strongly dependent on the concentration of poly(DEGMEMA-SPMA): whereas thermal equilibration of dilute solutions ([SP] + $[Co(NTf_2)_2]$ = 0.5 mM) results in a very small degree of MC-Co activation (Figure 3.4B), concentrated solutions heavily favor the formation of MC-Co complexes (Figure 3.5). As shown in Figure 3.5A, heating a 24.5 wt% polymer solution containing a 2:1 molar ratio of

SP:Co($NTf_2$)$_2$, results in two distinct absorption peaks centered at ~450nm and 506nm, respectively. The presence of two distinct peaks, both significantly blue shifted from the un-complexed MC absorption peak (inset of Figure 3.5B), indicates that multiple MC-Co isomers coexist under these conditions. Several studies speculate that when multiple MC complex peaks are present, the more blue-shifted peak corresponds to a *cis*-MC-metal conformation [32, 34, 35]; however, in the present case, we suggest further studies will be necessary to elucidate the true nature of both isomers, especially with respect to their precise stoichiometry and stability. Both peaks gradually decay under the low intensity light of the spectrometer, and exposure of the solution to high intensity white LEDs (~80-90 W/m$^2$ irradiance) results in rapid release of Co(II) ions and a dramatic shift of the equilibrium of SP back to its ring closed state (inset of Figure 3.5A). After heating a second time, a nearly identical distribution of MC-Co isomers is produced (Figure 3.5C), indicating that this process is reversible. As a rudimentary test of the degree to which complexes form under these conditions, the solution is immediately exposed to UV light. A comparison of the relative magnitudes of the deconvolved peaks of the thermally-activated MC-Co complex peaks of Figure 3.5C to the UV-generated peak, indicates that while UV light shifts the *distribution* of MC-Co isomers (as suggested by the disappearance of the 506 nm peak), the concentration of MC-Co complexes does not increase from those that were generated via thermal equilibration (as it does in Figure 3.4B). Thus, we deduce from this experiment that in the absence of visible light, equilibrium heavily favors MC-Co complexation in concentrated polymer solutions (that is, we expect near quantitative conversion of SP to MC-Co isomers under these conditions).

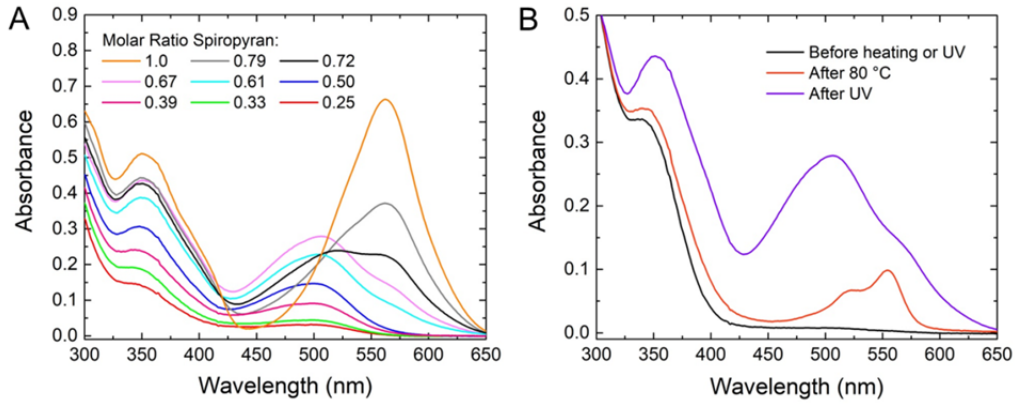


**Figure 3.4.** UV-Vis absorption spectra of P(DEGMEMA-SPMA)/$Co(NTf_2)_2$ solutions in PC. Total concentration [SP] + [$Co(NTf_2)_2$] = 0.5 mM. (A) Spectra of solutions containing varying ratios of SP/$Co(NTf_2)_2$. As more $Co(NTf_2)_2$ is added, the peak centered at λ = 564 nm, (characteristic of MC) gives way to a new peak centered at λ = 506 nm, corresponding to MC-Co complexes. The broad, asymmetric shape of the MC-Co peak suggests that multiple MC-Co isomers may be present. (B) Absorption spectra of solution containing approximately 2:1 molar ratio of SP:$Co(NTf_2)_2$ before heating, after heating to 80 °C for 4 hours, and after 90 seconds of exposure to UV light at room temperature.

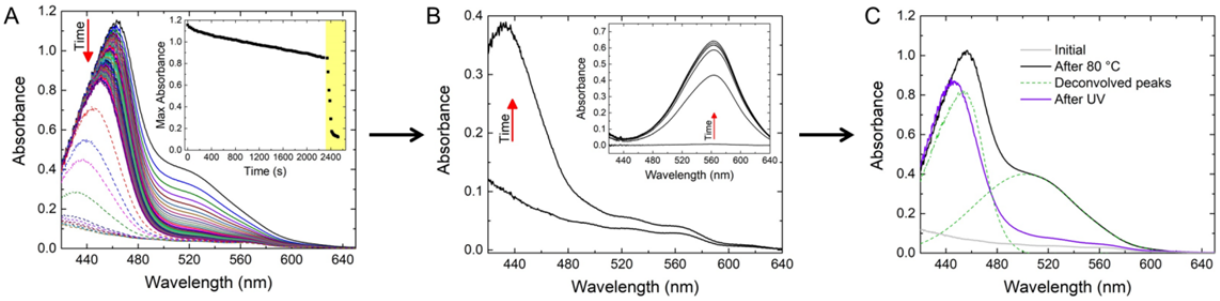


**Figure 3.5.** UV-Vis absorption spectra of 24.5 wt% poly(DEGMEMA-SPMA) solution in PC containing 2:1 ratio of SP:$Co(NTf_2)_2$. Blue arrows indicate these experiments were conducted in sequence. (A) Absorption spectra recorded immediately after heating solution at 80 °C in the dark for 1 hour. Solid curves recorded in 60 s intervals show gradual absorption d\ecay under low intensity light from the spectrometer light source. Dashed curves recorded in 15 s intervals show rapid absorption decay under high intensity white LEDs. Inset shows this decay as a function of time (yellow shaded region indicates exposure to high intensity LEDs: ~80-90 $W/m^2$ irradiance). (B) Spectra taken before and after 180 s UV exposure (100 $W/m^2$ irradiance at sample surface using $\lambda$ = 365 nm peak wavelength light source). Inset shows absorption curves (recorded in 36 s intervals) during UV exposure of poly(DEGMEMA-SPMA) in PC without metal salt. (C) Absorption spectra after heating again to 80 °C (black curve) and subsequent exposure for 180s to UV light (purple curve). The dashed green curves are the deconvolved "After 80 °C" spectrum.

Vial inversion tests show spontaneous gelation of concentrated (25 wt%) solutions of poly(DEGMEMA-SPMA) in PC containing 2:1 stoichiometric ratios of SP to transition metal salts (either ($Co(NTf_2)_2$ or $Cu(NTf_2)_2$) (Fig. 3.6). Initially viscous fluids, these polymer solutions gel after heating on a hot plate nominally set to 90 °C for 1 hour. Fluid-to-gel transformations also occur at room temperature over the course of several days in the dark or under low intensity ambient light. When exposed to intense white light, these gels revert to a viscous fluid. Although the word 'gel' can have a narrow definition related to power-law relaxation spectra with infinite viscosity [36, 37], here we use it in the broader sense for a structured viscoelastic network with a finite (large) viscosity, which we observe due to non-covalent bonding. Notably, gelation does not occur with monovalent salts, such as $Na(NTf_2)$, and evidently requires the presence of multivalent ions. Herein, we demonstrate that this reversible fluid to gel transition is due to thermally-triggered association and light-triggered dissociation of M-L crosslinks between SP-functionalized polymer chains.

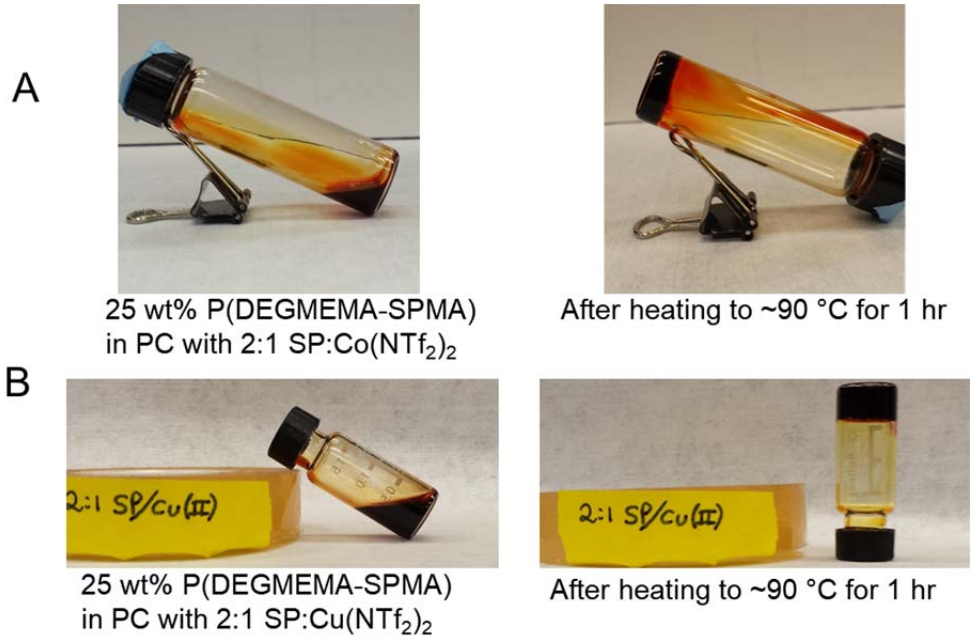


**Figure 3.6.** Vial inversion tests demonstrate gelation of P(DEGMEMA–SPMA) polymer solutions crosslinked with (A) $Co(NTf_2)_2$ and (B) $Cu(NTf_2)_2$. Heating to ~90 °C causes gelation in under an hour. Gelation also occurs when leaving vials in the dark for several days.

### 3.4 Reversible crosslinking modulated by heat and light

Reversible crosslinking was monitored under small-amplitude oscillatory shear deformations (Figure 3.7). Temperature was controlled using a Peltier bottom plate while a parallel glass disk upper geometry enabled light irradiation from above using white light (Figure 3.7A). Figure 3.7B shows the dynamic moduli of a 24.5 wt% solution of poly(DEGMEMA–SPMA) and a 2:1 ratio of SP:Co$(NTf_2)_2$ in PC tracked in real time at a constant angular frequency ($\omega$ = 0.5 rad·s$^{-1}$) and strain amplitude ($\gamma_0$ = 5%). Prior to gelation, the freshly prepared solution was exposed to white light to remove any residual MC-Co complexes formed during preparation. In its initial state under white light irradiation, the solution has a loss modulus $G''$ ($\omega$ = 0.5 rad·s$^{-1}$) ≈ 0.1 Pa and a storage modulus ($G'$) that falls below the detection limit of the rheometer due to instrument inertia (indicated by the grey region of the plot) [24]. Therefore, at 0.5 rad·s$^{-1}$ the solution is completely dominated by viscous flow. Gelation was initiated by heating the solution to 80 °C for 1 hour. During this heating stage, the solution switches from a viscous to a viscoelastic state, characterized by a >10-fold enhancement of both $G'$ and $G''$. Upon cooling to 20 °C, both moduli jump by roughly another order of magnitude. At this stage, $G'$ and $G''$ exhibit a slow decay, indicating that the concentration of MC-Co complexes activated at 80 °C slowly declines when cooled to 20 °C. Although heat here is used primarily to increase the kinetics of MC-Co complexation, this dark decay suggests that the equilibrium shifts toward higher concentrations of MC-Co complexes at elevated temperatures. Exposing the solution to white light causes the polymer network to rapidly dissociate, as indicated by the rapid decay of $G'$ and $G''$ to their original magnitudes prior to crosslinking. This process is modulated in a cyclic manner by crosslinking and dissociating crosslinks multiple times. However, hysteresis is observed with each heating and cooling cycle, as $G'$ increases from ~0.6 Pa to ~40 Pa and $G''$ from ~9 Pa to

~100 Pa after the first and third crosslinking sequences, respectively. In addition to elevated dynamic moduli, the gel state appears to become more kinetically stable after the first cycle, as the decay of $G''$ and $G'$ at 20 °C in the dark is much less pronounced after the second and third gelation sequences. The precise origin of this hysteretic behavior is unclear at this time, but the result of dissociating and re-associating crosslinks is restructuring of polymer chains into a network with different relaxation dynamics (as revealed by our relaxation spectrum model discussed in detail below). One potential source of this hysteretic restructuring of the polymer network is residual crosslinks after light exposure that leads to enhanced association of polymer chains in the subsequent heating step. Additionally, despite our use of a very low volatility of solvent, solvent evaporation is evident in our experiments as ~3% contractions in volume, corresponding to ≤ 1 wt% increases in polymer concentration, after each cycle. These two effects will have to be decoupled in future studies that seek to fully understand the origin of the observed hysteresis.

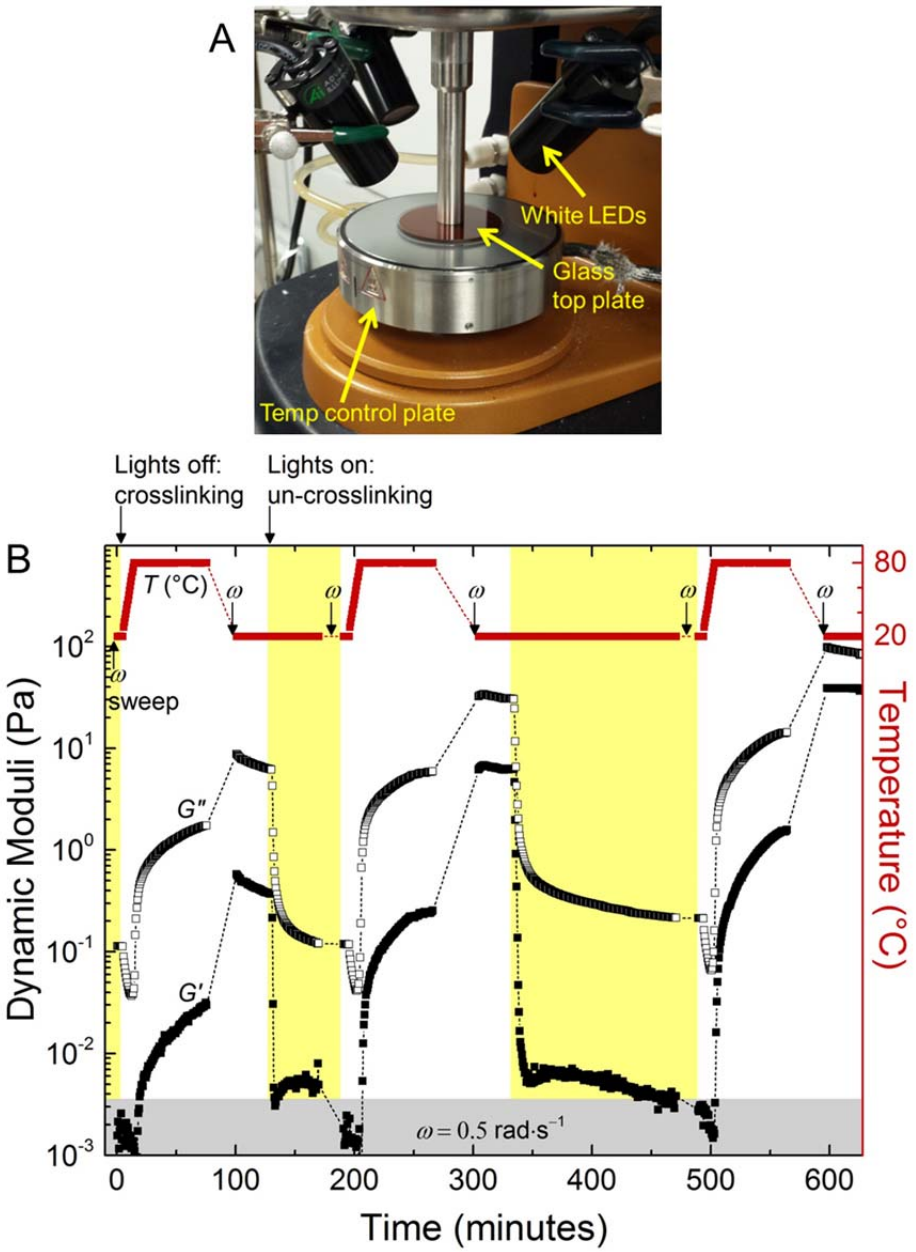


**Figure 3.7.** Reversible crosslinking of 24.5 wt% poly(DEGMEMA–SPMA) in PC with 2:1 SP:$Co(NTf_2)_2$. (A) Rheology cell contains Peltier bottom plate for temperature control and glass top plate and white LEDs for visible light exposure. (B) Storage ($G'$, closed squares) and loss moduli ($G''$, open squares) tracked at constant angular frequency ($\omega$ = 0.5 rad·$s^{-1}$) and strain amplitude ($\gamma_0$ = 5%) during heat-triggered crosslinking and light-triggered un-crosslinking. Temperature indicated by red squares (crosslinking induced by 80 °C holds). Visible light triggered un-crosslinking denoted by yellow shaded regions. Frequency sweeps were conducted periodically (denoted by $\omega$) prior to heating, after crosslinking, and after light exposure. Grey region of plot represents the estimated inertial limit of the rheometer [24]. Dashed lines connecting data points after lapses in data acquisition represent periods during which the gap size of the parallel plates was manually adjusted to maintain a constant fill.

Three control experiments were performed to confirm that reversible gelation is indeed due to MC-metal crosslinking and not a different mechanism. When the experiment shown in Figure 3.7 was repeated without any metal salt, no reversible changes in viscoelasticity were observed (Figure 3.8). Second, $Co(NTf_2)_2$ was replaced with monovalent $Na(NTf_2)$. Figure 3.9 shows that the poly(DEGMEMA–SPMA) solution with monovalent salt exhibits no observable change in elasticity (i.e. storage modulus) after heating at 80 °C for 2 hours (twice as long as the experiment shown in Figure 3.7B). Despite that M-L coordination crosslinks are not expected to be formed with Na(I) ions, a small increase in $G''$ was observed after heating. Part of this is attributed to solvent evaporation, but a significant fraction of the increase in $G''$ was recovered upon exposing the solution to visible light. Heat does result in conversion of SP to MC, and one possible explanation for this reversible shift in $G''$ is stacking of MC through π-π or dipole-dipole interactions. Molecular stacking has been observed spectroscopically in systems containing SP immobilized on inorganic surfaces [38], dissolved in polymer matrices [39], and linked to polymer backbones [40]. However, for this to occur in PC, a highly polar solvent, would be surprising as it has until now been assumed to take place exclusively in non-polar media [19]. An alternative explanation is that the affinity between polymer and solvent shifts when pendant SP groups on the polymer are converted to MC-Na complexes. A change in solvent affinity would change the radius of gyration of the polymer chains and consequently the viscosity of the polymer solution (30, 31). Determination if the observed small reversible viscosity change is due to a change in solvent quality will require further study.

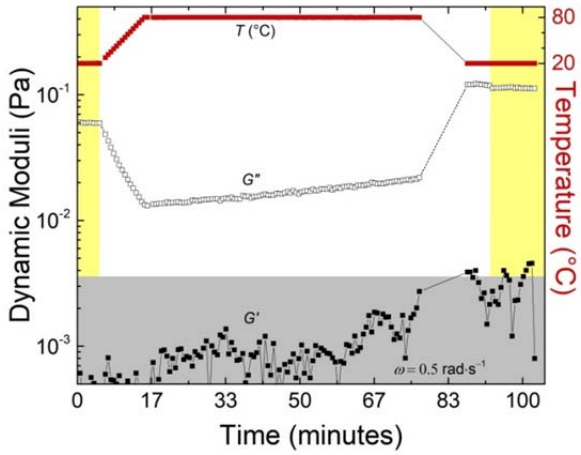


**Figure 3.8**. Control experiment showing rheological changes of a 24.5 wt% solution of P(DEGMEMA-SPMA) in PC without any metal salt. No measurable changes in elasticity were observed as the storage modulus remains below the inertial limit. The small change in $G''$ after heating and cooling is primarily attributed to solvent evaporation.

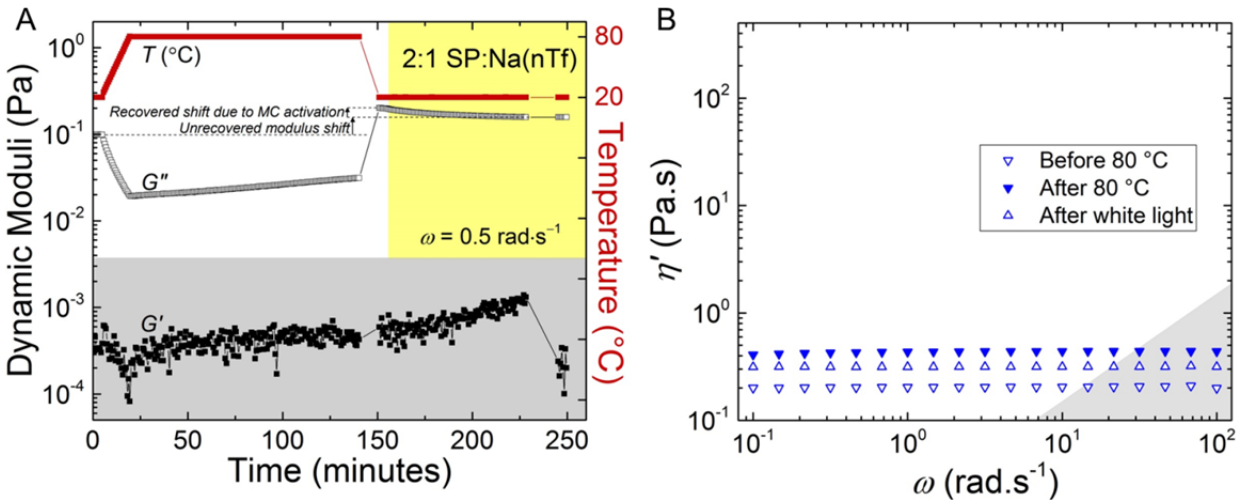


**Figure 3.9.** Reversible changes in dynamic moduli of P(DEGMEMA–SPMA) with Na($NTf_2$) salt. (A) Reversible changes of $G''$ at $\omega$ = 0.5 rad·$s^{-1}$ upon heat treatment and subsequent exposure to visible light. The polymer solution exhibits no measurable change in elasticity, indicating that crosslinks do not form in the presence of monovalent salt. (B) Frequency sweeps showing Newtonian behavior at all observed deformation timescales both before and after activation of MC-Na. This data should be compared to the frequency sweeps of Fig. 5A in the main text. Heating at 80 °C results in a > 2-fold increase of $\eta'$. After visible light irradiation, $\eta'$ decreases. The irreversible viscosity shift is attributed to solvent evaporation, and the reversible viscosity change is speculated to be attributed to changes in polymer-solvent affinity due to activation and deactivation of MC-Na complexes.

Based on the near-quantitative conversion of SP to MC-Co complexes in poly(DEGMEMA-SPMA) solutions with $Co(NTf_2)_2$, we hypothesized that the ratio of SP to divalent salt in solution plays a critical role in the formation or suppression of M-L crosslinks. Specifically, we expected that an excess of metal salt would favor the formation of 1:1 MC-Co complexes and thus inhibit the formation of metal-ion-mediated crosslinks. To test this hypothesis, the rheological properties of solutions containing 3:1, 2:1 and 1:1 SP:$Co(NTf_2)_2$ were compared (Figure 3.10). The 3:1 system exhibits very similar frequency-dependent behavior as the 2:1 system after heating and cooling, though the dynamic moduli after gelation appear to be somewhat diminished (Figure 3.10 and Figure 3.11). The behavior of the 1:1 system, on the other hand, differs drastically, and strongly supports our hypothesis, as $G'$ remains below the inertial limit of the instrument during the entire course of the experiment, and changes in $G''$ are 1 to 2 orders of magnitude smaller than those observed in the 2:1 and 3:1 SP:$Co(NTf_2)_2$ samples. In this regard, the behavior of the system with 1:1 SP:$Co(NTf_2)_2$ is strikingly similar to the $Na(NTf_2)$ control case, as both solutions remain viscous fluids after heating. Furthermore, the decay of $G''$ during light exposure for both samples fits very well to a bi-exponential kinetic model (Figure 3.12), whereas both the growth and decay of $G''$ with 2:1 and 3:1 SPMA:$Co(NTf_2)_2$ deviate significantly from simple first-order kinetics (Figure 3.13), suggesting that the same general mechanism accounts for the reversible $G''$ shift for both the $Na(NTf_2)$ and 1:1 SP:$Co(NTf_2)_2$ systems. With $Na(NTf_2)$ only 1:1 complexes form due to the monovalent nature of the salt, whereas with 1:1 $Co(NTf_2)_2$, the formation of 2:1 $(MC)_2Co$ coordination crosslinks is suppressed. We have thus differentiated two mechanisms at play for reversible changes in viscoelasticity of poly(DEGMEMA-SPMA)/metal ion solutions. Whether the reversible changes in viscoelasticity of concentrated solutions of poly(DEGMEMA-SPMA) and metal salts are

dominated by moderate shifts in polymer-solvent affinity or metal-ion-mediated crosslinking, depends both on the valence of the ion and the SP to metal salt molar ratio.

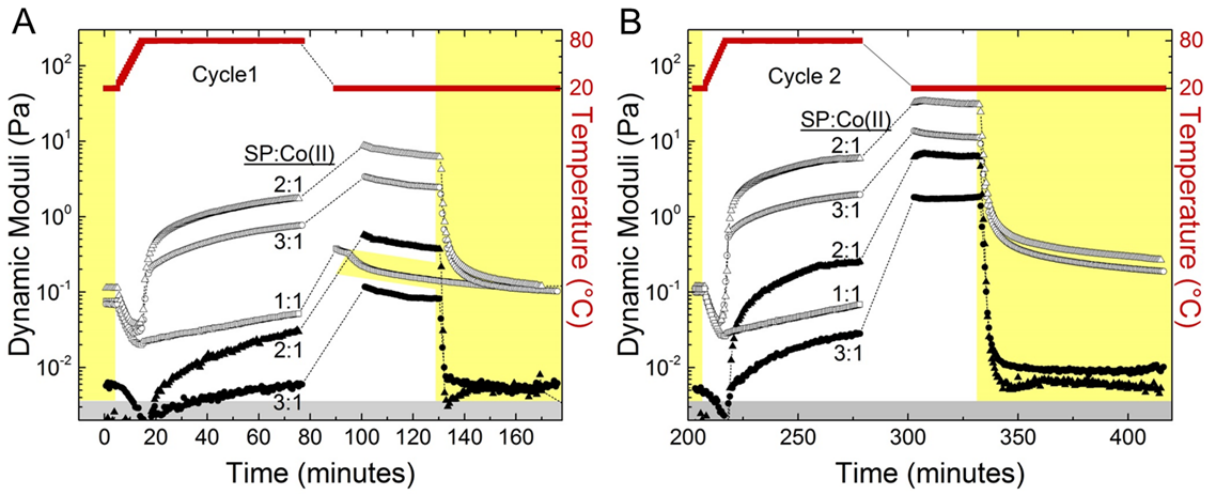


**Figure 3.10.** Comparison of first (A) and second (B) cycles for 1:1, 2:1 and 3:1 SP:Co(II). Whereas drastic, reversible changes in viscoelasticity were observed with 2:1 and 3:1 SP:Co(II), no measurable change in elasticity was observed with 1:1 stoichiometry ($G'$ remained well below the inertial limit during the entire experiment). It is hypothesized that few if any MC-Co(II) crosslinks form in the 1:1 solution. The small, reversible change in $G''$ is suggested to be due to molecular stacking of MC molecules rather than metal coordination. The data acquisition times of the 2:1 and 1:1 data are adjusted slightly to directly overlap the 3:1 sample data. Yellow shaded regions represent times at which solutions were exposed to visible light. Grey shaded regions represent the inertial limit of the instrument. All polymer solutions are 24.5 ± 0.3 wt% poly(DEGMEMA–SPMA) in PC.

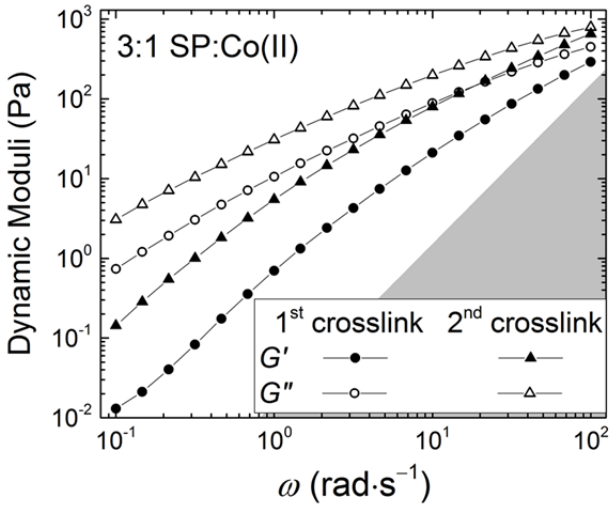


**Figure 3.11.** (A) Frequency sweeps of 3:1 SP:Co(II) comparing the dynamic moduli after the first and second crosslinking events. This data should be compared to the frequency sweeps of Figure 3.14. Grey region of plot represents the estimated inertial limit of the rheometer.

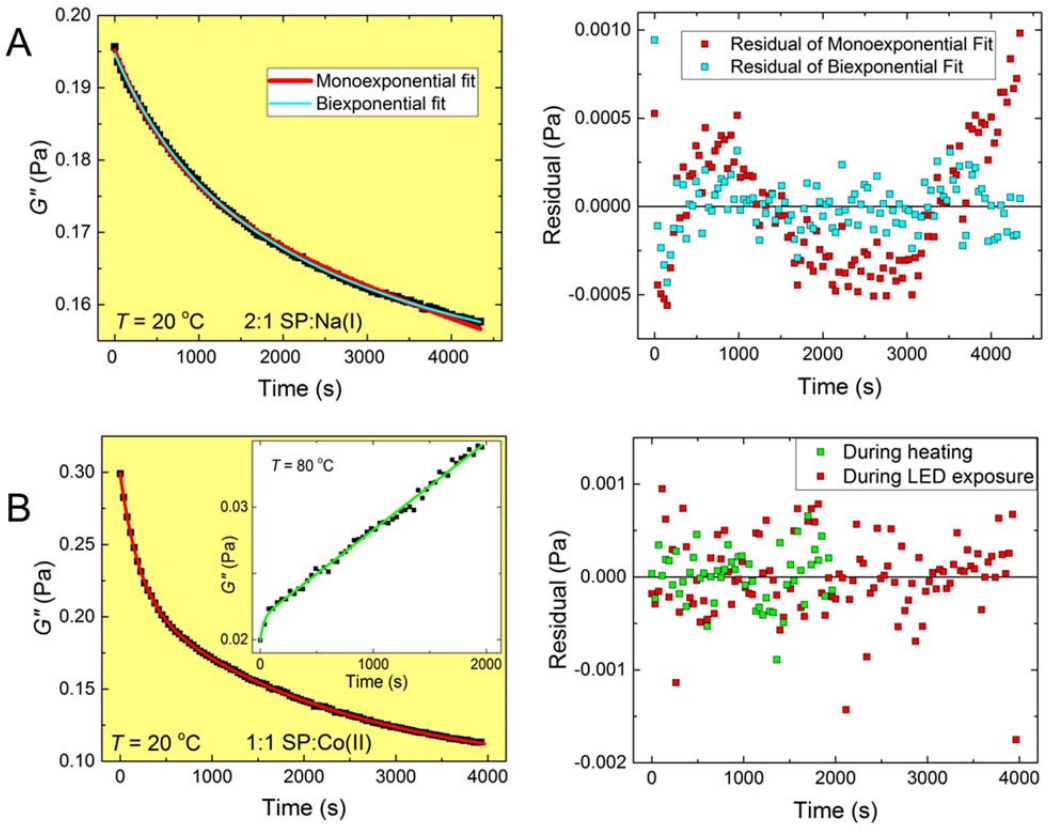


**Figure 3.12.** (A) Kinetics of light-triggered MC deactivation measured by the decay of *G″*. Residuals (right plot) of bi-exponential data fit show significantly reduced systematic error compared to a mono-exponential fit. (B) Kinetics of heat-triggered growth (inset), and light-triggered decay, of *G″* with 1:1 SP:Co(II). Both growth and decay of *G″* fit well with a bi-exponential kinetic model, as judged by the randomly distributed residuals of the data fits (right plot). The behavior of P(DEGMEMA–SPMA) with 2:1 SP:Na(I) and 1:1 SP:Co(II) are strikingly similar. Both samples exhibit a small increase in *G″* and no observable change in *G′*, and upon exposure to white light, *G″* in both samples undergoes bi-exponential decay. The similarities between the two samples suggests that the reversible *G″* shift is due to the same underlying chemical mechanism, namely molecular stacking of MC. Yellow shaded area indicates data acquired during visible light exposure.

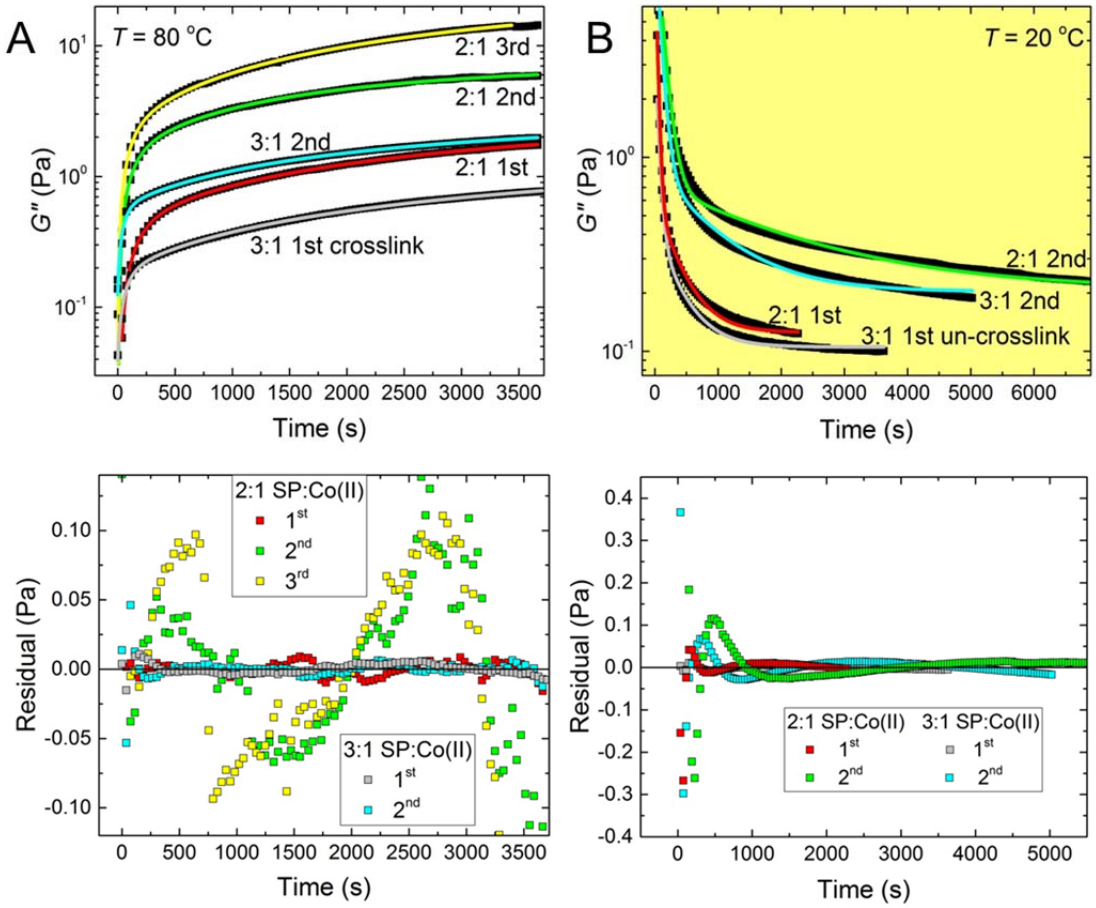


**Figure 3.13.** (A) Comparison of $G''$ responses during crosslinking with 3:1 and 2:1 SP:Co(II). (B) Comparison of $G''$ responses during un-crosslinking. Residuals of bi-exponential fits (bottom plots) in (A) and (B) show systematic error, indicating that the changes in $G''$ due to activation and deactivation of a structured, MC-metal coordinated polymer network is governed by different kinetics than the changes in $G''$ due to molecular stacking of MC in the presence of metal salts (Fig. S10).

### 3.5 Estimating the degree of crosslinking

To reveal a more complete picture of the viscoelastic properties during polymer network formation and dissociation, frequency sweeps were performed prior to heating, after gelation, and after gel dissociation of the polymer solution containing 2:1 SP:Co$(NTf_2)_2$ (Figure 3.12). The specific times at which these frequency sweeps were acquired are denoted by "$\omega$" in the plot of Figure 3.7B. Figure 3.12A shows that the solution in its initial state is a viscous fluid over the

entire experimental range of deformation timescales, having a dynamic viscosity ($\eta'$) of ~ 0.23 Pa·s. After crosslinking and cooling back to 20°C, the material clearly exhibits viscoelastic behavior. Upon exposure to visible light, the solution returns to a purely viscous state with a dynamic viscosity that is nearly identical to its original value. However, $\eta'$ nearly doubles after the solution is subject to a second round of gelation/un-crosslinking. Fig. 3.12B–D show the frequency-dependent dynamic moduli at 20 °C after the first, second and third crosslinking sequences, respectively. After crosslinking, the material behaves as a dissipative gel, exhibiting liquid-like terminal behavior in all three cycles. Hysteresis is also evident in the frequency sweeps. In each successive cycle the dynamic moduli shift to higher values at all frequencies, $G''$ becomes less dominant (i.e. the material response becomes more elastic), and the crossover of $G'$ and $G''$ occurs at lower frequencies (i.e. the network exhibits slower terminal relaxation dynamics). In order to estimate the percentage of SP units that are elastically active after each crosslinking cycle, the data of Figure 3.12 B–D are modeled using a continuous, log-normal distribution of relaxation times [25]. This model reasonably describes the behavior of crosslinked poly(DEGMEMA–SPMA) gels with the fewest adjustable parameters: $H_p$, the peak of the relaxation spectrum, $\tau_p$, the relaxation time at $H_p$, and $\sigma$, the standard deviation of the log-normal distribution of relaxation times (Table 3.1). The log-normal relaxation time model provides an estimate of both the plateau modulus, $G_0$, and the longest characteristic timescale of the gel, $\tau_w$ [26, 30]. Table 3.2 shows the $G_0$ and $\tau_w$ values computed for the Co(II)-crosslinked gel after each of the three curing cycles. The estimated $G_0$ increases dramatically between the first and second cycles, and remains essentially unaltered after the third curing cycle. The terminal relaxation dynamics become increasingly slower, as indicated by a twenty-fold increase of $\tau_w$ after the second cycle, and a thirty-fold increase after the third cycle. Longer relaxation times and larger

plateau moduli suggest greater connectivity of the polymer network (e.g. fewer dangling chains) after M-L crosslinks undergo light-triggered dissociation followed by re-association.

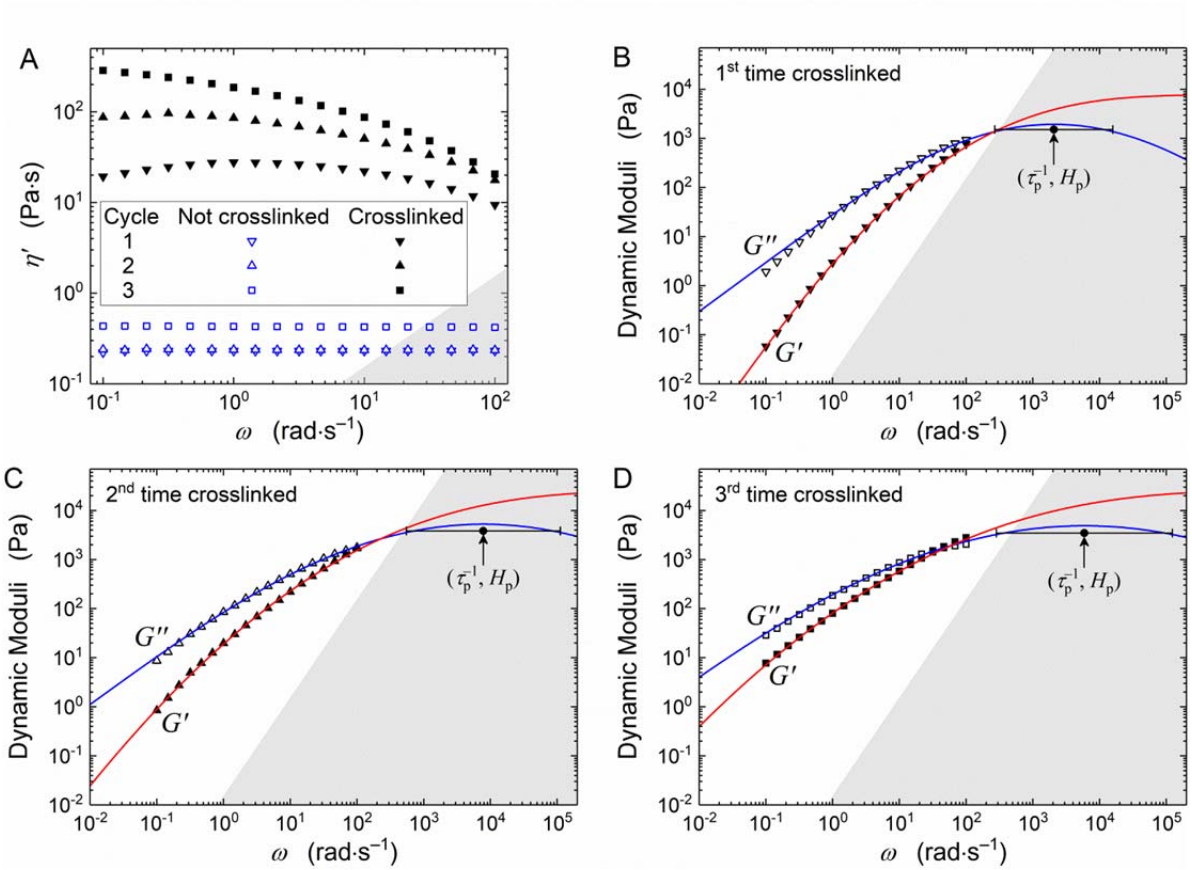


**Figure 3.14.** (A) Frequency sweeps show reversible changes in dynamic viscosity ($\eta'$) of poly(DEGMEMA–SPMA) with 2:1 SP:$Co(NTf_2)_2$ during the three crosslinking and un-crosslinking cycles shown in Fig. 3. Dynamic moduli of crosslinked gels at 20 °C after the (B) first, (C) second, and (D) third crosslinking sequences. Blue and red lines are numerical fits of a log-normal distribution of relaxation times with parameters ($\tau_p$, $H_p$, $\sigma$); values indicated by black circles, horizontal bar is $\tau_p^{-1}e^{\pm\sigma}$. Grey regions of plots denote the estimated inertial limit of the rheometer.

**Table 3.1.** Values of the parameters of the relaxation spectrum obtained by numerically fitting the frequency sweep data of Fig. 4 B–D in the main text.

| | $\tau_p$ [ms] | $H_p$ [kPa] | $\sigma$ [–] |
|---|---|---|---|
| 1st time crosslinked | 0.5 ± 0.2 | 1.5 ± 0.3 | 2.0 ± 0.07 |
| 2nd time crosslinked | 0.17 ± 0.03 | 3.8 ± 0.4 | 2.7 ± 0.05 |
| 3rd time crosslinked | 0.13 ± 0.06 | 3.5 ± 0.4 | 3.0 ± 0.07 |

**Table 3.2.** Number-average relaxation time ($\tau_n$), longest characteristic relaxation time ($\tau_w$), polydispersity index of relaxation times (PDI = $\tau_w/\tau_n$), plateau modulus ($G_0$), crosslink density, and estimated percentage of SP molecules in P(DEGMEMA–SPMA) that actively form an elastic polymer network after each crosslinking cycle. Values computed from nonlinear least squares fits of frequency sweep data of Fig. 3.14 B–D.

| | $\tau_n$ [ms] | $\tau_w$ [s] | PDI·$10^{-3}$ [–] | $G_0$ [kPa] | $\mu \cdot 10^{-24}$ [$m^{-3}$] | Elastically active SP [%] |
|---|---|---|---|---|---|---|
| 1st time crosslinked | 3.9 ± 0.8 | 0.2 ± 0.03 | 0.06 ± 0.02 | 7.8 ± 1.6 | 1.9 ± 0.4 | 4.3 ± 0.9 |
| 2nd time crosslinked | 4.4 ± 0.6 | 5.2 ± 0.8 | 1.2 ± 0.3 | 25.6 ± 3.5 | 6.3 ± 0.9 | 14.3 ± 2 |
| 3rd time crosslinked | 16.9 ± 2.1 | 169 ± 56 | 10 ± 4.4 | 26.4 ± 3.6 | 6.5 ± 0.9 | 14.8 ± 2 |

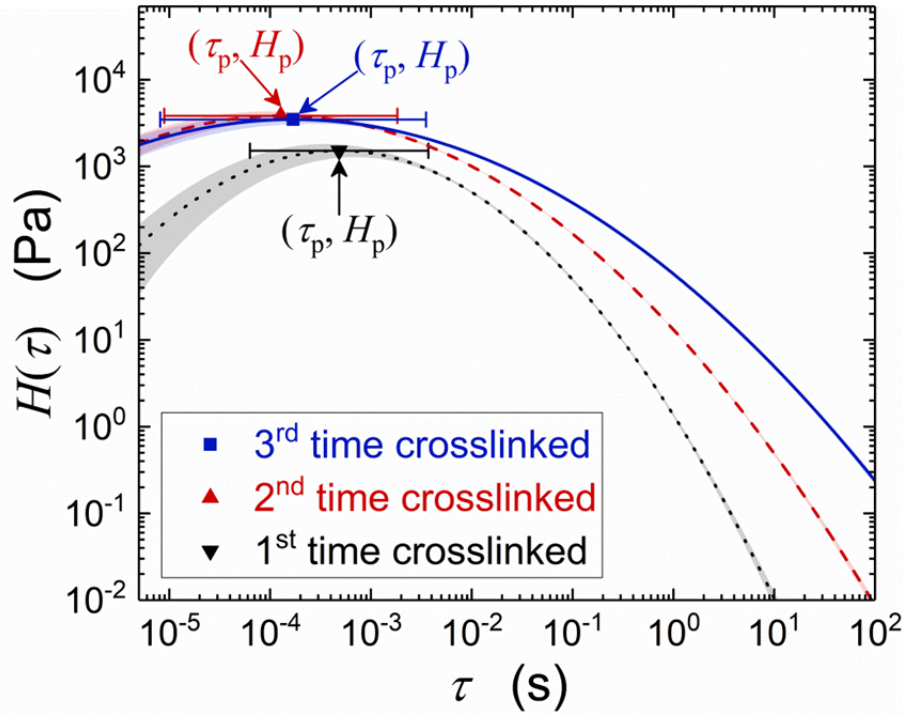


**Figure 3.15.** Relaxation spectra of crosslinked gels at 20 °C after the first (black), second (red), and third (blue) crosslinking sequences. Lines are numerical fits to the experimental data of Fig. 4 B–D of a log-normal distribution of relaxation times with parameters ($\tau_p$, $H_p$, $\sigma$); values indicated by symbols, horizontal bars are $\tau_p^{-1}e^{\pm\sigma}$. Shaded areas denote the error on the spectra estimated through error propagation, according to Eq. 3.9.

The computed values of $G_0$ provide a means to estimate the number density of SP monomer units that actively contribute to the elasticity of the polymer network. The degree of polymerization ($DP_e$) of the SPMA copolymer ($DP_e \approx 124$) is significantly smaller than the entanglement $DP_e$ of methacrylate-based polymers containing either aliphatic side groups of similar length as DEGMEMA (e.g. poly(n-hexyl methacrylate), $DP_e \approx 200$) or aromatic side groups (e.g. poly(4-*tert*-butylphenyl methacrylate), $DP_e \approx 320$) [41]. Therefore, we assume that elasticity arises primarily due to M-L crosslinks rather than physical entanglements of poly(DEGMEMA–SPMA) polymer chains. Using the phantom model of rubber elasticity [42, 43] and assuming a network functionality $f = 4$ (as expected for a 2:1 MC:metal complex), the

plateau modulus $G_0$ and the number density of elastically active crosslinks ($\mu$) are related by [44-47]:

$$G_0 = \left(\nu - \mu\right) k_B T = \mu k_B T \tag{3.10}$$

where $\nu$ (= $\mu f/2$) is the number density of elastically active network strands, and $k_B T$ is the thermal energy. As shown in Table 3.2, ~14.8% of SPMA in the polymer solution actively contributes to the elasticity of the polymer network after the third crosslinking sequence. We have preliminary evidence that the degree of crosslinking can be increased by enhancing the MC-cation interaction strength by changing the metal ion. Previous work has shown that MC coordinates to Cu(II) ions much more strongly than Co(II) ions [48]. As we show in the Figure 3.14, $Cu(NTf_2)_2$ crosslinked poly(DEGMEMA–SPMA) exhibits significantly higher dynamic moduli at elevated temperature than $Co(NTf_2)_2$ crosslinked networks. Unfortunately, $Cu(NTf_2)_2$ crosslinked gels phase separate when cooled to room temperature (Fig. S12B), preventing rigorous analysis. Similar to the $Co(NTf_2)_2$ crosslinked system, $Cu(NTf_2)_2$ network formation is reversed by visible light and a uniform viscous solution was formed by exposing the phase separated gel to visible light while mixing continuously with the rheometer plates. Finally, to help guide future work, we suggest a complementary strategy for improving the density of switchable crosslinks may be to tune the structure of the SP molecule itself. For example, adding certain chelating groups adjacent to the phenolate anion of MC has been shown to lead to highly stable 2:1 MC-metal complexes in dark conditions without sacrificing reversibility under visible light [49, 50].

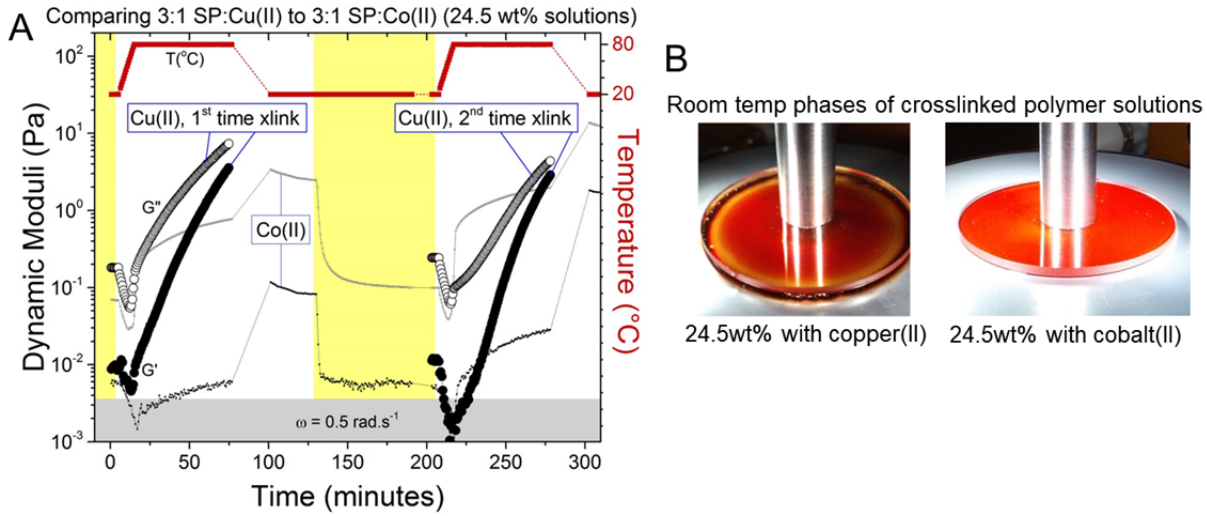


**Figure 3.16.** Crosslinking with $Cu(NTf_2)_2$. (A) Crosslinking of 24.5 wt% P(DEGMEMA–SPMA) solution with 3:1 SP:Cu(II). Cu(II) data (circles) overlays the data of 3:1 SP:Co(II) for comparison. (B) Phase separation (left image) prevented meaningful evaluation of the crosslinked Cu(II) solution at room temperature. However, mixing during visible light irradiation enabled re-dissolution of the polymer back into PC. Right image shows a homogeneous crosslinked Co(II) solution for comparison.

### 3.6 Conclusions

We have demonstrated a molecular switch leading to the reversible formation of crosslinked polymer networks in response to heat and light. As shown by UV-Vis spectroscopy, when poly(DEGMEMA–SPMA) is mixed with Co(II) ions, MC-metal complexes form spontaneously at room temperature in the dark, a process which is accelerated by applying heat. Exposure to visible light results in the rapid release of metal ions and ring closure of SP. The viscoelastic properties of poly(DEGMEMA-SPMA) solutions were probed under small-amplitude oscillatory shear during heat activated crosslinking and light activated un-crosslinking. This enabled us to capture both relatively large changes in viscoelasticity due to M-L crosslinks, as well as relatively small changes due to weaker interactions, which we propose are due to shifts in affinity between polymer and the solvent. The use of molecular switches to toggle M-L bond formation and dissociation may enable greater control over both the processing and self-healing capabilities of M-L coordination polymers. For example, light may be utilized to locally

transform damaged regions of a solid polymer or gel to a more fluid state in order to facilitate the dynamics of self-healing.

### 3.7 Opportunities for improvement

The results presented in this chapter have positive implications towards our ultimate goal of triggering reversible crosslinking of SP mechanophores using mechanical force. However, the data also reveal a critical challenge that must be addressed before applying these principles to solid-state and self-reinforcing systems. In poly(DEGMEMA-SPMA), crosslinking with Co(II) and Cu(II) occurs spontaneously, even at room temperature. In order for mechanical stress to be used as an effective stimulus, a sufficient number of SP molecules must remain in the ring-closed state prior to mechanical activation. Therefore, measures must be taken to limit the degree of spontaneous MC-metal bond formation. One strategy is to reduce the interaction strength of association between MC and metal ions. We apply this strategy in Chapter 4 when we use alkali and alkaline metal salts instead of transition metals. Another is to modify the SP structure in a way that reduces the lability of the spiro-bond. Specifically, we hypothesize that the simplest way to reduce spontaneous formation of MC is to remove the nitro electron withdrawing group para to the spirocyclic oxygen. Therefore, a major focus in the chapters that follow is on designing and characterizing SP molecules and mechanophores without a nitro electron withdrawing group. An excellent way to improve upon the material presented in this chapter is to demonstrate a SP-based system that is stable in an un-crosslinked state until it is triggered by a specific stimulus.

### 3.8 REFERENCES

1. Sun, J. Y., Zhao, X., Illeperuma, W. R., Chaudhuri, O., Oh, K. H., Mooney, D. J., Vlassak, J. J. and Suo, Z. *Nature* **2012**, *489*, 133.
2. Li, J., Illeperuma, W. R. K., Suo, Z. and Vlassak, J. J. *ACS Macro Letters* **2014**, *3*, 520.

3. Li, C. H., Wang, C., Keplinger, C., Zuo, J. L., Jin, L., Sun, Y., Zheng, P., Cao, Y., Lissel, F., Linder, C., et al. *Nat Chem* **2016**, *8*, 618.
4. Mozhdehi, D., Ayala, S., Cromwell, O. R. and Guan, Z. *Journal of the American Chemical Society* **2014**, *136*, 16128.
5. Holten-Andersen, N., Harrington, M. J., Birkedal, H., Lee, B. P., Messersmith, P. B., Lee, K. Y. and Waite, J. H. *Proc Natl Acad Sci U S A* **2011**, *108*, 2651.
6. Chen, Y., Kushner, A. M., Williams, G. A. and Guan, Z. *Nat Chem* **2012**, *4*, 467.
7. Guglielmetti, R. In *Photochromism (Revised Edition)*; Bouas-Laurent, H., Ed.; Elsevier Science: Amsterdam, 2003, p 314.
8. Keum, S.-R., Ma, S.-Y., Lim, H.-W., Han, T.-H. and Choi, K.-H. *Bulletin of the Korean Chemical Society* **2012**, *33*, 2683.
9. Murugan, N. A., Chakrabarti, S. and Agren, H. *J Phys Chem B* **2011**, *115*, 4025.
10. Metelitsa, A. V., Lokshin, V., Micheau, J. C., Samat, A., Guglielmetti, R. and Minkin, V. I. *Phys. Chem. Chem. Phys.* **2002**, *4*, 4340.
11. Wojtyk, J. T. C., Wasey, A., Xiao, N.-N., Kazmaier, P. M., Hoz, S., Yu, C., Lemieux, R. P. and Buncel, E. *Journal of Physical Chemistry* **2007**, *111*, 2511.
12. Taylor, L. D., Nicholson, J. and Davis, R. B. *Tetrahedron Letters* **1967**, *17*, 1585.
13. Phillips, J. P., Mueller, A. and Przystal, F. *Journal of the American Chemical Society* **1965**, *87*, 4020.
14. Gorner, H. and Chibisov, A. K. *Journal of the Chemical Society, Faraday Transactions* **1998**, *94*, 2557.
15. Chibisov, A. K. and Görner, H. *Chemical Physics* **1998**, *237*, 425.
16. Potisek, S. L., Davis, D. A., Sottos, N. R., White, S. R. and Moore, J. S. *Journal of the American Chemical Society* **2007**, *129*, 13808.
17. Davis, D. A., Hamilton, A., Yang, J., Cremar, L. D., Van Gough, D., Potisek, S. L., Ong, M. T., Braun, P. V., Martinez, T. J., White, S. R., et al. *Nature* **2009**, *459*, 68.
18. Lee, C. K., Davis, D. A., White, S. R., Moore, J. S., Sottos, N., R. and Braun, P. V. *Journal of the American Chemical Society* **2010**, *132*, 16107.
19. Klajn, R. *Chem Soc Rev* **2014**, *43*, 148.
20. Kundu, P. K., Olsen, G. L., Kiss, V. and Klajn, R. *Nat Commun* **2014**, *5*, 3588.
21. Byrne, R. J., Stitzel, S. E. and Diamond, D. *Journal of Materials Chemistry* **2006**, *16*, 1332.
22. Aleksandar, R., Silvia, S., Robert, B., Conor, S., King Tong, L. and Dermot, D. *Journal of Physics D: Applied Physics* **2007**, *40*, 7238.
23. Tomasulo, M., Kaanumal, S. L., Sortino, S. and Raymo, F. M. *The Journal of Organic Chemistry* **2007**, *72*, 595.
24. Ewoldt, R. H., Johnston, M. T. and Caretta, L. M. In *Complex Fluids in Biological Systems: Experiment, Theory, and Computation*; Spagnolie, S. E., Ed.; Springer New York: New York, NY, 2015, p 207.
25. Wiechert, E. *Annalen der Physik* **1893**, *286*, 335.
26. Tschoegl, N. W. *The Phenomenological Theory of Linear Viscoelastic Behavior: An Introduction*; 1 ed.; Springer-Verlag: Berlin, Germany, 1989.
27. Plazek, D. J. and O'Rourke, V. M. *Journal of Polymer Science Part A-2: Polymer Physics* **1971**, *9*, 209.
28. Graessley, W. W. and Roovers, J. *Macromolecules* **1979**, *12*, 959.
29. Roovers, J. and Graessley, W. W. *Macromolecules* **1981**, *14*, 766.

30. Graessley, W. W. *Polymeric Liquids and Networks: Dynamics and Rheology*; 1 ed.; Garland Science: New York, 2008.
31. Bevington, P. R. and Robinson, D. K. *Data Reduction and Error Analysis for the Physical Sciences*; 3 ed.; McGraw-Hill: New York, 2003.
32. Wojtyk, J. T. C., Kazmaier, P. M. and Buncel, E. *Chemistry of Materials* **2001**, *13*, 2547.
33. Natali, M., Aakeroy, C., Desper, J. and Giordani, S. *Dalton Trans* **2010**, *39*, 8269.
34. Fries, K. H., Driskell, J. D., Samanta, S. and Locklin, J. *Analytical Chemistry* **2010**, *82*, 3306.
35. Tian, Z., Stairs, R. A., Wyer, M., Mosey, N., Dust, J. M., Kraft, T. M. and Buncel, E. *The Journal of Physical Chemistry A* **2010**, *114*, 11900.
36. Winter, H. H. and Chambon, F. *Journal of Rheology* **1986**, *30*, 367.
37. Chambon, F. and Winter, H. H. *Journal of Rheology* **1987**, *31*, 683.
38. Ueda, M., Kudo, K. and Ichimura, K. *Journal of Materials Chemistry* **1995**, *5*, 1007.
39. Eckhardt, H., Bose, A. and Krongauz, V. A. *Polymer* **1987**, *28*, 1959.
40. Goldburt, E., Shvartsman, F., Fishman, S. and Krongauz, V. *Macromolecules* **1984**, *17*, 1225.
41. Tsukahara, Y., Namba, S.-i., Iwasa, J., Nakano, Y., Kaeriyama, K. and Takahashi, M. *Macromolecules* **2001**, *34*, 2624.
42. James, H. M. and Guth, E. *The Journal of Chemical Physics* **1943**, *11*, 455.
43. Flory, P. J. and Jr., J. R. *The Journal of Chemical Physics* **1943**, *11*, 512.
44. Chompff, A. J. and Duiser, J. A. *The Journal of Chemical Physics* **1966**, *45*, 1505.
45. Graessley, W. W. *Macromolecules* **1975**, *8*, 186.
46. Graessley, W. W. *Polymeric Liquids and Networks: Structure and Properties*; 1 ed.; Garland Science: New York, 2004.
47. Rubinstein, M. and Colby, R. H. *Polymer Physics*; 1 ed.; Oxford University Press: New York, 2003.
48. Fries, K. H., Driskell, J. D., Sheppard, G. R. and Locklin, J. *Langmuir* **2011**, *27*, 12253.
49. Zakharova, M. I., Coudret, C., Pimienta, V., Micheau, J. C., Delbaere, S., Vermeersch, G., Metelitsa, A. V., Voloshin, N. and Minkin, V. I. *Photochemical & Photobiological Sciences* **2010**, *9*, 199.
50. Chernyshev, A. V., Voloshin, N. A., Raskita, I. M., Metelitsa, A. V. and Minkin, V. I. *Journal of Photochemistry and Photobiology A: Chemistry* **2006**, *184*, 289.

# CHAPTER 4: FORCE-TRIGGERED METAL COMPLEXATION OF SPIROPYRAN

## 4.1 Introduction

Spiropyran mechanophores switch between a ring-closed (SP) state and a ring-open, merocyanine (MC) state in response to mechanical force. Under a mechanical load, the covalent, spirocyclic bond ruptures and the visibly transparent SP switches to a blue or purple colored MC conformation. When the stress is removed, MC relaxes back to its SP ground state, making this process reversible (though the reverse process sometimes requires the aid of visible light). Since SP mechanophores were first introduced by Moore and co-workers [1, 2], they have primarily been used as mechanochromic force probes providing a visual cue of applied mechanical stresses and strains. Our lab has been exploring ways to use SP mechanophores to generate useful chemical reactions that extend beyond color indication. Recently, Boulatov and co-workers demonstrated that polyurethanes containing a similar mechanophore, spirothiopyran, undergo mechanically-triggered covalent crosslinking via click reaction of the thiolate moiety of thiomerocyanine with a difunctional maleimide [3], thus proving that spirocyclic mechanophores can generate constructive of bonds in response to mechanical force. Unfortunately, reversibility of the spirothiopyran/thiomerocyanine is lost after the thiol-ene reaction takes place.

We hypothesized that mechanochemically triggered generation of *reversible* bonds can be realized by taking advantage of the reversible coordination of merocyanines to metal ions [4-8]. We envision this mechanism could open new avenues to mimic reversible, force-triggered reactions in biology, and to engineer self-reinforcing materials that crosslink in response to mechanical stress and soften when the stress is removed. Before such visions can be realized, it is important to address the critical issue that in the presence of complexing species, spiropyrans

often *spontaneously* switch to their open MC conformation. If mechanical force is to be used effectively as a stimulus for non-covalent bond formation, it is important to first understand and control spontaneous activation.

Gossweiler and co-workers demonstrated a simple methodology to covalently incorporate SP mechanophores into a PDMS elastomeric composite. They demonstrated PDMS as a convenient and effective system for studying repeatable mechanochemical transformations [9]. Here we introduce this PDMS-mechanophore elastomeric system as a platform for studying the competing effects of spontaneous versus mechanochemical activation of reversible, MC-metal complexes in the solid state.

We begin our study by investigating the stabilities of two different SP mechanophores in the absence of metal salts. The most commonly studied spiropyran mechanophore contains a nitro group oriented at the para-position from the spirocyclic oxygen (see SP-NO2 in Figure 4.1a). The nitro group enhances the efficiency of MC activation by UV excitation as well as the lifetime of the MC isomer. An unfortunate consequence of the enhanced stability MC is spontaneous isomerization of SP to its ring-open state. To mitigate this issue when studying mechanochromic systems, researchers often photo-bleach specimens with intense white light prior to mechanical testing so as to minimize the concentration of thermally activated MC [10-12]. Though this methodology solves the problem in laboratory studies, it does not address the issue head on.

Here, we directly address the issue of spontaneous activation of SP mechanophores. Combining DFT calculations and in situ mechanical/UV-Vis spectroscopy tests, we investigate the effect of the electron withdrawing group (EWG) on the mechanochemical behavior and stability of SP mechanophores with and without a nitro group (denoted SP-NO2 and SP0,

respectively). We then present a methodology for incorporating metal salts into a PDMS elastomeric matrix and demonstrate fully reversible, force-triggered complexation of SP with $Li(NTf_2)$, $Ca(NTf_2)_2$ and $Mg(NTf_2)_2$ ions in the solid state. Finally, combining NMR spectroscopy with *in situ* UV-Vis/mechanical measurements, we observe an inverse relationship between the stability of the MC-metal complex in solution and the ratio of mechanochemical to thermal activation in the solid state.

## 4.2 Experimental Methods

### *4.2.1 General Information*

A two-part polydimethylsiloxane (PDMS) elastomer kit (Dow Corning Sylgard® 184) was purchased from Fisher Scientific. Magnesium bis(trifluoromethanesulfonyl)imide ($Mg(NTf_2)_2$) and calcium bis(trifluoromethanesulfonyl)imide ($Ca(NTf_2)_2$) were purchased from TCI Chemicals. Lithium bis(trifluoromethanesulfonyl)imide ($Li(NTf_2)$) was purchased from Alfa Aesar. All other chemicals and reagents were purchased from either Sigma Aldrich or Alfa Aesar and used without further purification. $^{1}H$ and $^{13}C$ 1D NMR spectra were taken on a 500 MHz Carver B500 spectrometer. 2D Diffusion ordered spectroscopy and 1D NOESY NMR experiments were measured on a Varian 750 MHz spectrometer. All $^{1}H$ NMR experiments are reported in δ units, in parts per million (ppm), and were measured relative to the signals of residual acetone (2.05 ppm), DMSO (2.50 ppm), or chloroform (7.24 ppm) in deuterated S3 solvent. All $^{13}C$ NMR spectra were measured in deuterated solvents and are reported in ppm relative to the signals for residual acetone (206.26 and 29.84 ppm), DMSO (39.52 ppm), or chloroform (77.23 ppm).

### *4.2.2 Synthetic procedures*

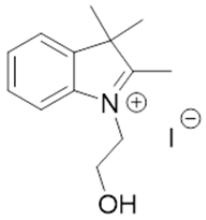


*1-(2-hydroxyethyl)-2,3,3-trimethyl-3H-indol-1-ium iodide*. 42.14 g (263 mmol) of 2,3,3-trimethyl-3H-indole and 63.6 g (369.8 mmol) of iodoethanol were dissolved in 100 ml of THF. The solution was bubbled with argon for 15 minutes and refluxed at 88 °C for 24 hours. Precipitate was filtered and washed with THF and recrystallized from boiling ethanol, yielding the title compound as white needles (76.92 g, 232.25 mmol, 88.3%). $^{1}$H NMR (500 MHz, DMSO-$d_6$) δ 7.99 – 7.95 (m, 1H), 7.89 – 7.84 (m, 1H), 7.62 (dd, $J$ = 5.8, 3.1 Hz, 2H), 4.61 (t, $J$ = 5.2 Hz, 2H), 3.88 (t, $J$ = 5.1 Hz, 2H), 2.83 (s, 3H), 1.56 (s, 6H). $^{13}$C NMR (126 MHz, DMSO-$d_6$) δ 198.21, 142.28, 141.58, 129.79, 129.29, 123.96, 116.07, 58.29, 54.76, 50.81, 22.52, 15.03.

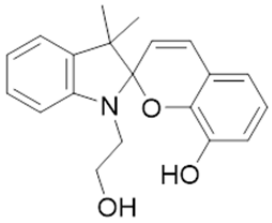


*1'-(2-hydroxyethyl)-3',3'-dimethylspiro[chromene-2,2'-indolin]-8-ol*. 24 g (72.46 mmol) of 1-(2-hydroxyethyl)-2,3,3-trimethyl-3H-indol-1-ium iodide, 10 g (72.4 mmol) of 2,3-dihydroxybenzaldehyde, and 8.86 g (87.5 mmol) of trimethylamine were dissolved in 270 ml of anhydrous ethanol. The solution was purged with bubbled with argon for 15 mins and refluxed at 100 °C for 8 hours. The solution was concentrated *in vacuo* and redissolved in 300 ml of chloroform. Combined organics were was with DI water (3 x 150 ml), saturated sodium bicarbonate (3 x 150 ml), saturated aqueous ammonium chloride (3 x 150 ml), brine (1 x 150 ml), dried over anhydrous $Na_2SO_4$, filtered and concentrated *in vacuo* to obtain the title compound as a pinkish-white powder (12.9 g, 40 mmol, 55.2%). $^{1}$H NMR (500 MHz,

Chloroform-*d*) δ 7.16 (td, *J* = 7.7, 1.3 Hz, 1H), 7.08 (dd, *J* = 7.4, 1.2 Hz, 1H), 6.90 – 6.82 (m, 2H), 6.82 – 6.72 (m, 2H), 6.64 (dd, *J* = 7.4, 1.4 Hz, 2H), 5.70 (d, *J* = 10.2 Hz, 1H), 5.48 (s, 1H), 3.81 – 3.73 (m, 1H), 3.68 (dt, *J* = 11.1, 5.6 Hz, 1H), 3.49 (ddd, *J* = 14.9, 7.3, 5.7 Hz, 1H), 3.30 (dt, *J* = 14.8, 5.3 Hz, 1H), 1.52 (s, 1H), 1.30 (s, 3H), 1.18 (s, 3H). $^{13}$C NMR (126 MHz, Chloroform-*d*) δ 147.33, 143.38, 140.51, 136.37, 129.77, 127.85, 122.10, 120.77, 119.78, 119.71, 118.88, 118.33, 115.99, 106.97, 105.77, 61.16, 52.30, 46.10, 26.08, 20.04.

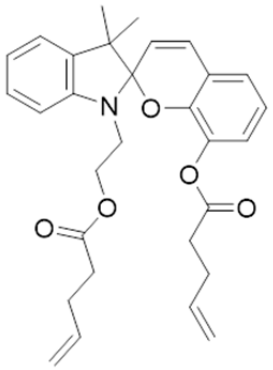


**SP0:** *3',3'-dimethyl-1'-(2-(pent-4-enoyloxy)ethyl)spiro[chromene-2,2'-indolin]-8-yl pent-4-enoate*. 3.3 g (10.2 mmol) of 1'-(2-hydroxyethyl)-3',3'-dimethylspiro[chromene-2,2'-indolin]-8-ol and 2.4 g (19.6 mmol) of DMAP were dissolved in 100 ml of anhydrous chloroform. 3 g (16.5 mmol) of pentenoic anhydride was added dropwise at room temperature and the reaction proceeded for 3 hours. Several drops of methanol were added, the solution was concentrated *in vacuo* and purified by column chromatography on silica using 3% EtOAc/hexanes, yielding 4.57 g (9.37 mmol, 91.9%) of the title compound as transparent, light blue oil, which gradually turns to a transparent, pale yellow color during storage. $^{1}$H NMR (500 MHz, Chloroform-*d*) δ 7.12 (td, *J* = 7.6, 1.3 Hz, 1H), 7.05 (dd, *J* = 7.2, 1.2 Hz, 1H), 6.95 (dd, *J* = 7.5, 1.6 Hz, 1H), 6.93 – 6.83 (m, 2H), 6.85 – 6.76 (m, 2H), 6.63 (d, *J* = 7.8 Hz, 1H), 5.88 – 5.78 (m, 0H), 5.79 (s, 1H), 5.80 – 5.72 (m, 1H), 5.57 (ddt, *J* = 17.6, 9.8, 6.4 Hz, 1H), 5.10 – 4.84 (m, 4H), 4.24 (dt, *J* = 11.0, 6.3

Hz, 1H), 4.20 – 4.10 (m, 1H), 3.44 – 3.27 (m, 2H), 2.44 – 2.28 (m, 4H), 2.24 – 2.09 (m, 2H), 1.86 (m, *J* = 9.0, 7.6, 6.1, 3.3, 1.6 Hz, 2H), 1.28 (s, 3H), 1.26 (d, *J* = 7.2 Hz, 0H), 1.16 (s, 3H). $^{13}$C NMR (126 MHz, Chloroform-*d*) δ 173.00, 171.10, 147.20, 145.01, 137.93, 136.87, 136.74, 136.46, 129.47, 127.58, 124.26, 122.97, 121.57, 119.91, 119.86, 119.60, 119.44, 115.64, 115.13, 106.86, 105.13, 63.01, 51.79, 42.54, 33.59, 33.23, 28.88, 28.64, 25.93, 19.64.

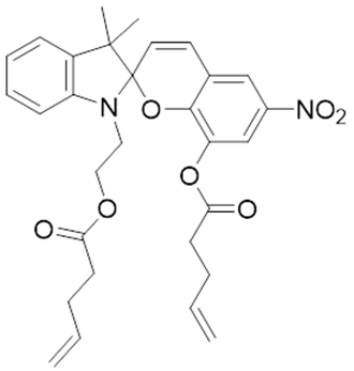


**SP-NO$_2$:** *3',3'-dimethyl-6-nitro-1'-(2-(pent-4-enoyloxy)ethyl)spiro[chromene-2,2'-indolin]-8-yl pent-4-enoate* was prepared as described previously [13] with slight modifications, namely 4-pentenoic anhydride was used instead of 6-heptenoic anhydride and the product was recrystallized in boiling hexanes instead of petroleum ether. Characterization matched literature values [13].

*4.2.3 Preparation of PDMS samples*

PDMS materials incorporating spiropyrans were prepared using two-part Sylgard® 184 elastomer kit (Dow Corning). Dogbone shaped specimens (gauge length: 5 mm; width: 2 mm; thickness: 0.7 mm) were used for *in situ* visible absorption measurements during mechanical testing with a custom uniaxial load frame.

**General procedure for preparation of dogbone and film specimens for mechanical characterization:** The molality of SP in all SP-PDMS specimens was 19.2 ± 0.2 μmol/g (~0.94 wt% of SP0 and ~1 wt% of SP-NO2). A representative procedure is provided as follows. 0.0408 g of 3',3'-dimethyl-1'-(2-(pent-4-enoyloxy)ethyl)spiro[chromene-2,2'-indolin]-8-yl pent-4-enoate (**SP0**) was dissolved in 0.26 mL toluene. Sylgard® 184 prepolymer base (3.924 g) and curing agent (0.393 mg) were added and the contents were thoroughly mixed for 20 min using a vortex mixer. The mixture was then poured into dogbone shaped delrin molds and cured under vacuum at 85 °C for 20 hours.

**General procedure for incorporating salts into SP-functionalized PDMS:** Metal salts were incorporated into the PDMS elastomers, by immersing PDMS samples in 1.38 wt% $Li(NTf_2)$, 2.80 wt% $Mg(NTf_2)_2$ or 2.88 wt% $Ca(NTf_2)_2$ solutions in either THF or a 10 vol% hexyl acetate/THF. The salt concentrations were selected to incorporate a three-fold excess of metal ions with respect to spiropyran in the swollen state. This was calculated by the volume change upon swelling, which increased by a factor of 2.3 ± 0.1 (corresponding to a ~2.2 X increase in mass) regardless of type of metal salt or the presence or absence of hexyl acetate. PDMS samples were immersed in salt solutions for 36 hours, removed, and dried under vacuum (~650 mTorr) at 22 °C for 12 hours. Dogbone specimens were tested within 24 hours after removing from vacuum.

*4.2.4 In-situ mechanical/UV-Vis absorption spectroscopy experiments*

In situ mechanical measurements were performed using the equipment described in [14] with some minor modifications. UV-Vis absorption spectra were acquired for dogbone shaped PDMS specimens using a custom uniaxial load frame (IMAC Motion Control Corp.). The specimens

were uniaxially stretched at a strain rate of 0.01 $s^{-1}$ by two opposing actuators and the load was monitored with a 50-lb capacity Honeywell Sensotec sensor. Absorption spectra of PDMS dogbones incorporating metal salts were acquired using an Ocean Optics D-2000 deuterium light source and an Ocean Optics HR2000+ spectrometer. Absorption spectra of PDMS samples without metal salts were acquired using an Ocean Optics HL-2000 halogen lamp. The irradiances at the sample surface from the two light sources at various wavelengths (measured using a Thorlabs PM100USB power and energy meter ) are listed in Table 4.1. Samples were "photo-bleached" with an Advanced Illumination SL073 white LED spotlight positioned about 10 mm from the sample surface. According to the manufacturer, this high power LED spotlight emits wavelengths between 420 to 750 nm at an irradiance of approximately 1000 $mW/cm^2$ at 100 mm distance. Therefore, irradiance of the sample during photo-bleaching is at least 2000 times the irradiance at the specimen surface during data acquisition. For specimens containing SP-$NO_2$, a 400 nm long-pass filter was placed between the sample and the light source to exclude UV light. The absorption spectra of specimens containing metal salts were baselined to a PDMS reference sample containing no SP or metal salt. All absorption spectra shown, except Figure 4.3, are of the samples in their pre-stretched or post-stretched states. For example, absorption kinetics data were acquired by stretching samples, releasing, and then monitoring the absorption immediately after release. Figure 4.3 shows absorption spectra of samples under a 4 N tensile strain.

**Table 4.1.** Irradiance of halogen and deuterium light sources measured at the sample surface (90 mm distance). The D-2000 source was used for measuring samples containing metal salts. For comparison, the irradiance on the specimen surface during photo-bleaching was ≥1000 mW/cm$^2$.

| Wavelength (nm) | HL-2000 Halogen Source (mW/cm$^2$) | D-2000 Deuterium Source (mW/cm$^2$) |
|---|---|---|
| 400 | 1.856807669 | 0.49121896 |
| 450 | 0.638584648 | 0.294731376 |
| 500 | 0.609111511 | 0.216136342 |
| 550 | 0.294731376 | 0.098243792 |
| 600 | 0.275082618 | 0.137541309 |
| 650 | 0.334028893 | 0.098243792 |

*4.2.5 Diffusion ordered spectroscopy (DOSY)*

DOSY experiments were performed on a Varian Unity Inova 750 MHz spectrometer capable of performing pulsed field gradient (PFG) spin-echo diffusion measurements. Solutions of SP0 (0.080 M) and either $Mg(NTf_2)_2$ or trifluoroacetic acid (0.040 M) was prepared in acetone-$d_6$ and thermally equilibrated at 25 ºC for 24 hours prior to data collection, and DOSY experiments were performed at 25 ºC. 90 degree pulse widths were set using the 1D $^1$H FID prior to performing experiments. DOSY was performed using a convection compensated gradient stimulated echo pulse sequence with a spectral width of 8992.8 Hz, d1 value of 2 s, diffusion gradient length of 2 ms, diffusion delay of 30.0 ms, and an 18 step array of gradients varying from 2.79-55.74 G/cm. The baselines and phases of all spectra were corrected prior to data processing. The data were processed and the diffusion coefficients extracted using the VNMR software without use of a reference.

*4.2.6 Determining cumulative stability constants*

Relative stability of MC-metal complexes of SP0 with $Li(NTf_2)$, $Ca(NTf_2)_2$, and $Mg(NTf_2)_2$ were measured by determining the ratio of MC to SP using $^1H$ NMR. This methodology works under the assumption that all MC in solution is coordinated to a metal ion. This assumption would be invalid for SP-NO2, which can form stable MC isomers in the absence of metal ions, but given the high instability of SP0 in its ring-open state, we deem this assumption to be valid. 80 mM SP0 solutions in acetone-$d_6$ were prepared and mixed with metal salts in ratios of 1:6 SP0:Li(I), 2:1 SP0:Ca(II) and 2:1 SP0:Mg(II). A much higher concentration of salt was required for Li(I) because no MC was measurable at lower salt concentrations. Solutions were equilibrated at 22 °C for 48 hours prior to measurement. NMR measurements were performed at 25 °C. The stability constants reported are cumulative stability constants for the 1:1 MC-metal complexes (further details on stoichiometry provided in Section 4.5).

*4.2.7 Density functional theory calculations*

CoGEF calculations were performed using Spartan ′16 according to previously reported methods [2, 14-16] with some modifications. Unless otherwise stated, ground state energies were computed using DFT at the B3LYP/6-31+G* level of theory. A diffuse function was added because this has been shown to improve the accuracy of energy calculations of metal complexes using Pople type basis sets [17, 18]. Though the systems being simulated here are not metal coordination complexes, the diffuse term has been added to account for delocalized charge effects from metal cation and counter-anion in cases where salt atoms are included. To maintain consistency, this term is kept for all computations, including those that do not have metal salts. In addition, unless otherwise stated, a conductor-like polarizable continuum model (C-PCM)

with an effective static dielectric constant of 7.43 was used to simulate electrostatic screening from a surrounding medium. In all cases, starting from the equilibrium geometry of the unconstrained molecules (energy = 0 kJ/mol), the distance between the terminal methyl groups of the spiropyran structures was increased in increments of 0.1 Å and the energy was minimized at each interval. The slope of the energy curve was calculated at each increment of elongation to estimate the applied force. Force versus elongation curves were evaluated to determine whether different mechanophores undergo similar degrees of motion during elongation, and the maximum force prior to bond rupture was used to evaluate the strength of the ruptured covalent bond.

### 4.3 Computational and experimental evaluation of the electron withdrawing effect on mechanochemical reactivity and thermal stability

DFT calculations using the constrained geometries simulate external force (CoGEF) methodology [15] were initially performed to compare the mechanochemical reactivity of SP0 and SP-NO2 (Figure 4.1b-f). To reduce the number of degrees of freedom and computational cost, methyl groups are used in place of the pentenoate moieties of SP-NO2 and SP0 (Figure 4.1b). Starting from the equilibrium geometries of each molecule the distance between the methyl groups was increased in 0.1 Å increments. Both SP-NO2 and SP0 exhibit cleavage of the spyrocyclic C—O bond, but cleavage occurs at two distinct energies (Figure 4.1c). To determine whether or not this energy difference signifies a true difference in bond dissociation energy, various modes of mechanical energy transduction throughout the spirocyclic molecule must be carefully taken into account. Because the SP molecule has many degrees of freedom, not all of the energy gets transduced directly to the C—O bond. Beyer's proposed solution to this problem

when he introduced the CoGEF technique was to extract the maximum gradient of the energy (i.e. the maximum force), $F_{max}$, immediately prior to bond rupture. Others have adopted this technique to evaluate mechanochemical bond strength [14, 19]. This methodology has been shown to suffice when the mechanophore has a small number of atoms and thus relatively few degrees of freedom in its constrained geometry [19]. However, the veracity of $F_{max}$ for comparing SP molecules is unclear. To address this issue, we plot the instantaneous gradient of the energy as well the lengths of the spirocyclic bond of interest at each increment of the CoGEF simulation. The instantaneous energy gradient curve constructs an effective force vs. elongation plot, revealing four different regions of differing linear slopes, resembling Hookean force curves with different spring constants (Figure 4.1d). Force vs. elongation curves suggest that in both mechanophores, mechanical energy is not effectively transduced to the spirocyclic bonds until about 30% elongation, where the curve takes on a constant, linear slope until bond cleavage. Further confirming this, the spirocyclic C—O and C—N bond lengths show significant changes only after about 30% elongation (Figure 4.1e & f). Our simulations predict a rupture force of 2.5 nN for SP-NO2, which is strikingly close to the experimental value of 2.4 nN measured by Gossweiler and coworkers using single molecule force spectroscopy [13]. In contrast, SP0 is predicted to rupture at 3.5 nN. Therefore, the electron withdrawing group has a significant impact on mechanochemical reactivity. A closer look at the relative lengths of the spirocylic oxygen bond in the unconstrained states (1.495 Å for SP-NO2 vs. 1.472 Å SP0) indicates that the nitro group makes the bond more chemically labile. These equilibrium bond lengths almost identically match values measured by X-ray crystallography for SPs with and without a nitro group (1.491 ±3 Å and 1.471 ±3 Å, respectively) [20, 21], further adding confidence to our calculations.

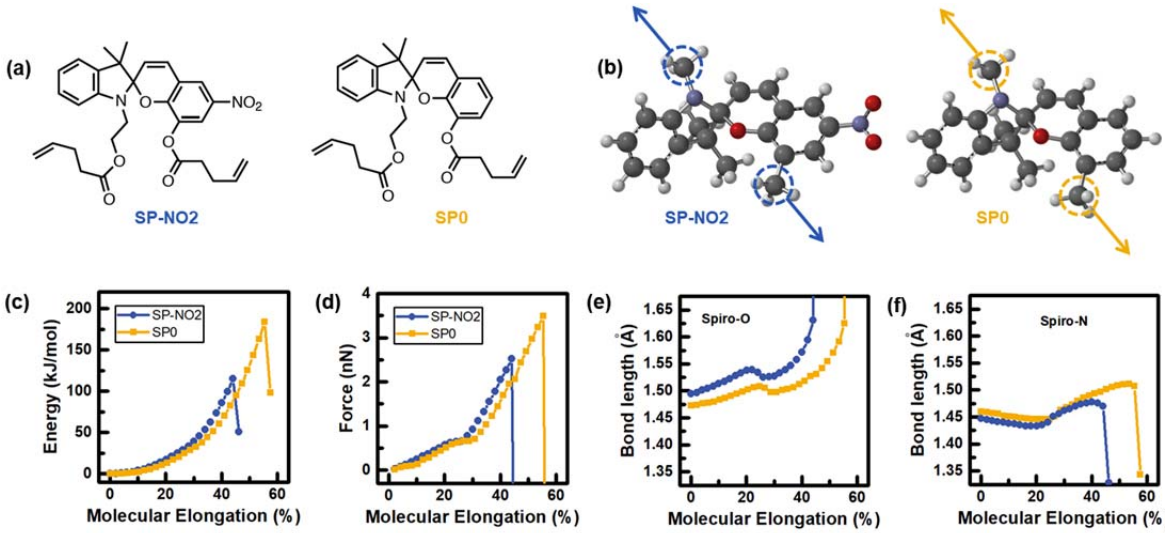


**Figure 4.1.** (a) DFT (CoGEF) calculations predict significantly different rupture forces for two mechanophores with and without a nitro electron withdrawing substituent. (a) The chemical structures of SP-NO2 and SP0 used in our experimental studies. (b) The structures of the simulating mechanophores in the transition states immediately before bond rupture. (c) Energy landscape and (d) effective force curves. (e) The length of the spirocyclic oxygen bond increases dramatically and (f) the length of the spirocyclic nitrogen bond begins to increase at about 30% elongation, marking this as the point at which maximum transduction of energy to the mechanochemically reactive bond begins. Calculations were performed at the B3LYP/6-31+G* level of theory using a C-PCM with an effective dielectric constant of 7.43.

To experimentally compare the behavior of SP0 and SP-NO2, the mechanophores were incorporated into PDMS elastomers at identical concentrations (19.2 μmol/g). The relative thermal stabilities of SP0 and SP-NO2 were compared by keeping samples in the dark for 24 hours and observing their color change. When kept in the dark for 24 hours at ~20 °C SP-NO2 specimens switch from a pale-yellow color to pink or purple (Figure 1a), indicating that SP-NO2 exists in a dynamic equilibrium having a finite concentration of MC without any external stimulus. Over periods of weeks to months, specimens typically become darker, suggesting relatively poor thermal stability of SP-NO2 in the solid state. SP0 does not exhibit this behavior, showing no color change after being kept in the dark for 24 hours (Figure 1a), and we find this stability is retained even after several months of storage in the dark. Qualitatively, this shows

that without a strong electron withdrawing group on the chromene side of the ring, SP heavily favors the ring-closed state. The electron withdrawing substituent (or lack thereof) also affects the color upon force activation. SP-NO2 turns blue when stretched and undergoes a secondary transition to a purple color after release. This secondary transition was first observed by Gossweiler and coworkers and is thought to be due to switching between different ring-open conformations of MC [9]. In contrast, SP0 turns purple under tensile strain, and remains purple immediately after release. Mechanochemical activation produces four distinct peaks in SP0 (a primary peak at $\lambda$ = 588 nm, and three additional peaks at approximately 515 nm, 546 nm, and 637 nm). In SP-NO2 only one main peak is observed under tensile strain ($\lambda$ = 598 nm with a subtle shoulder around 640 nm), suggesting that tensile strain produces a more complex distribution of isomers in SP0 than in SP-NO2 (Figure 4.3).

Experimental verification of the different rupture forces of SP0 and SP-NO2, which were predicted by DFT, has proven to be quite challenging. Therefore, to make a meaningful comparison of the two mechanophores, we focus on their kinetic behavior after release. Specimens were stretched under an applied tensile load of 4 N (true stress of 4.21 ± 0.09 MPa), and absorbance decay was monitored immediately after release (Figure 4.2b & c). Similar to the thermal decay of spiropyrans in polymeric matrices after UV excitation [22, 23], the absorbance decay of both SP-NO2 and SP0 after mechanochemical activation fits very well to a biexponential model; however, fitting the decay curves to a monoexponential function allows for a much simpler analysis of the relative rates of mechanophore deactivation. According to monoexponential fits, SP0 decays roughly 20 times faster than SP-NO2 (Figure 4.2 d). Thus, as expected, SP-NO2 exhibits much greater kinetic stability in its MC state than SP0.

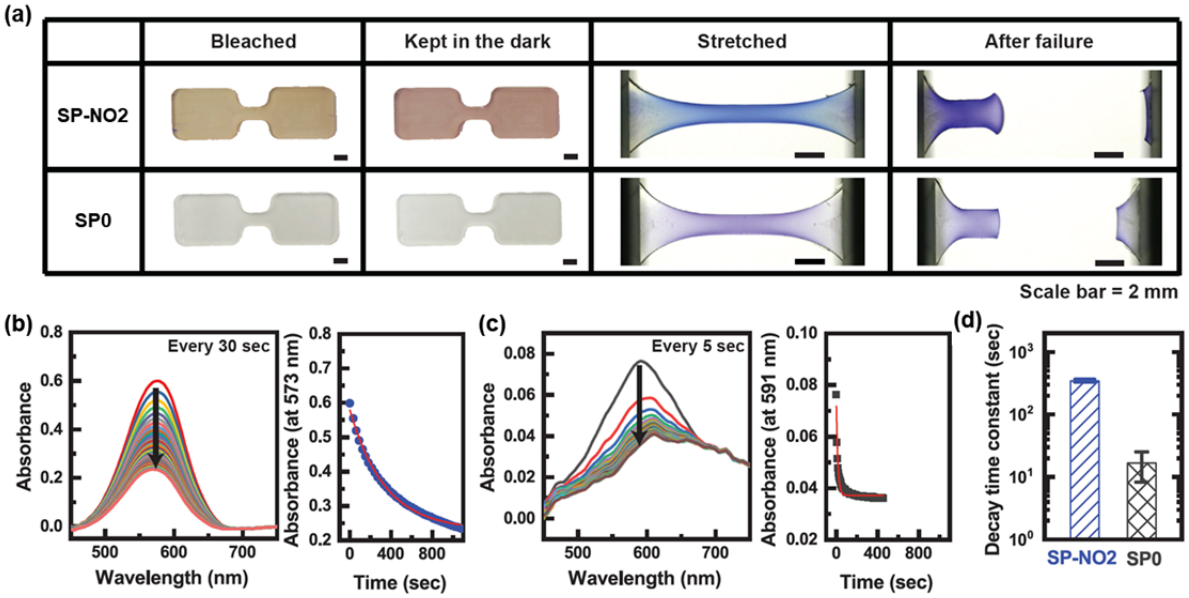


**Figure 4.2.** Comparing thermal stability and mechanochemical behavior of PDMS incorporating SP-NO2 and SP0. (a) Photos of SP-NO2 and SP0 PDMS specimens. When kept in the dark for 24 hours at ~20 °C, SP-NO2 exhibits spontaneous MC activation (PDMS gradually turns pink), while SP0 does not. Both materials exhibit mechanochromic behavior. SP-NO2 turns blue under tensile stress and turns purple color after the stress is removed. SP0 turns purple and does not exhibit any secondary transition after release. (b) Trace of absorbance decay of SP-NO2 and (c) SP0 after stretching at 4 N force (true stress of 4.21 ± 0.09 MPa) for 45 minutes and releasing. (d) First order exponential decay time constants of SP-NO2 and SP0.

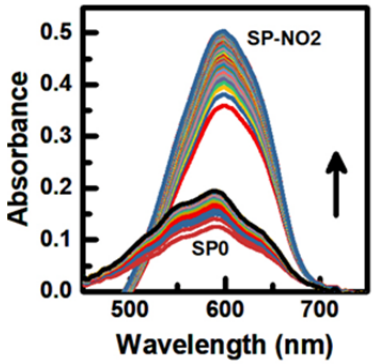


**Figure 4.3.** Absorbance spectra of SP0 and SP-NO2 under a 4 N applied load (true stress of 4.21 ± 0.09 MPa). Spectra were recorded in 60 s increments.

### 4.4 Force-triggered metal complexation in PDMS

Salts were incorporated by swelling PDMS-mechanophores specimens in solutions of Li(I), Ca(II), and Mg(II) bis(trifluoromethanesulfonyl)imide ($NTf_2$) salts in THF for 36 hours followed by evaporation of the solvent under high vacuum. Attempts to measure the uptake of salt based

on mass change of the dry polymer failed because PDMS samples tended to lose mass (most likely due to loss of un-polymerized material) upon swelling. Instead, based on the volume change of PDMS during swelling ($V_{swollen}/V_{dry}$ = 2.3) and concentration of salt in the THF solution, we approximate the uptake of metal ions to be ~57 μmoles/g or a 3x excess with respect to SP. Though clustering of ions in the low dielectric constant medium of PDMS is probable at the atomic level, optical clarity and uniform color of the dry PDMS samples indicates that the salts remain dissolved in the polymer matrix after drying and are evenly dispersed (at least on a macroscopic level) (Figures 4.4, 4.7 and 4.10a). As Mozhdehi and coworkers have surmised that metal salts containing the $NTf_2$ counter-anion have an exceptionally high solubility in solid-state matrices due to its delocalized charge and bulky size [24]. Our results indicate that this holds true even for matrices of very low dielectric constant ($\varepsilon_{PDMS} \approx 2.4$); however, further work is required to determine solubility limits as well as the extent of ion clustering in the nanometer to sub-nanometer regimes. The molar excess of metal salts, which we approximated by the volume uptake of salt solutions during swelling, is confirmed by the complete disappearance of the un-complexed MC peaks (550-600 nm range) in all mechanochemical measurements.

After drying, salt incorporated samples of SP0-PDMS retain similar mechanical properties of SP0-PDMS specimens without metal salts (Figure 4.6a). In contrast, SP-NO2 shows extreme embrittlement (Figure 4.10b). The cause of this drastic difference in mechanical behavior is unclear, but due to the brittle nature of SP-NO2-PDMS/metal salt specimens, we primarily focus our investigation on the SP0-PDMS/metal salt composite system.

Salt-incorporated samples show distinct coloration after drying (Figure 4.4). SP0 samples dried from THF/salt solutions exhibit a dramatic increase in absorption when kept in the dark for 24 hours at room temperature (Figure 4.4a), suggesting that equilibrium heavily favors MC

under these conditions. Scheme 4.1 illustrates the competing mechanisms of thermal activation and mechanochemical activation observed in the SP0-PDMS/salt system.

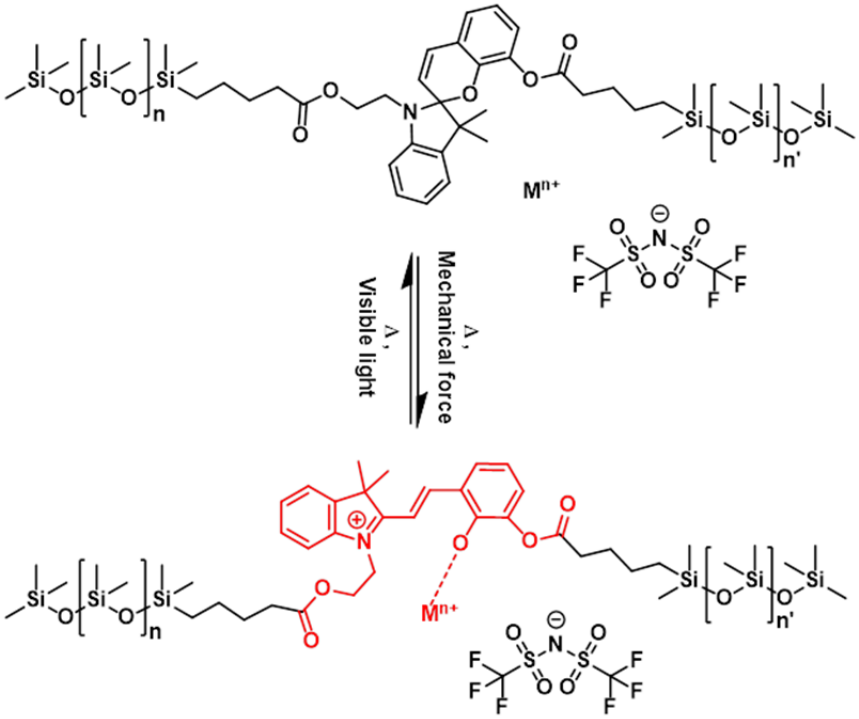


**Scheme 4.1.** Competition between spontaneous and force-triggered activation of MC-metal complexes in SP0-PDMS/metal salt composites. When designing SP-based systems that mechanochemically generate non-covalent bonds, it is critical to mitigate thermal activation.

We hypothesized that low polarity and poor electron donor ability of PDMS [25] promotes strong interactions between SP and metal cations. To mitigate this problem we added hexyl acetate (HA), a low vapor pressure solvent, to the salt solutions (10% by volume) and both qualitatively and quantitatively compared the thermal stabilities of the dried samples. In addition to being nonvolatile, HA was chosen because it is relatively benign, and it has the same density, and swells PDMS to the same degree, as THF. HA has a 2 order of magnitude lower vapor pressure than THF. Therefore, we assume that the majority of THF is removed while most of HA remains in the polymer after 12 hours at 650 mTorr//22 °C.

Qualitatively, the thermal stability of SP0 with metal salts appears to be dramatically improved with the HA additive (Figure 4.4b). Despite HA being a nonpolar solvent, its dielectric constant is almost twice that of PDMS ($\varepsilon_{HA}$ = 4.4 vs. $\varepsilon_{PDMS} \approx 2.4$). In addition, HA has greater Lewis basicity than PDMS, which we deduce by comparing the Kamlet-Taft parameters reported for dimethyl siloxane [25] and butyl acetate [26]. The greater polarity from the HA additive enhances solvation and electrostatic screening of metal cations in the polymer matrix, while the moderately increased electron-donating character of PDMS containing HA creates competition for ion interaction that would otherwise be absent. Furthermore, HA likely promotes mobility of ions, thus increasing solvent exchange kinetics. Together, these factors lead to greater thermal stability of SP0 in the presence of metal salts.

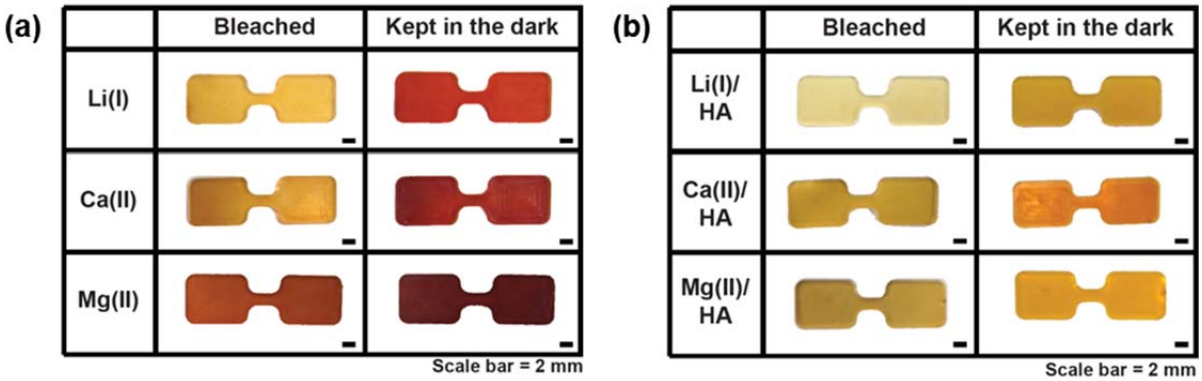


**Figure 4.4.** Qualitative comparison of thermal stabilities of SP0-PDMS containing various metal salts with and without HA. "Bleached" specimens were exposed to intense white light for 2 minutes and then kept in the dark for 24 hours. (a) Photos of dry samples after swelling in THF to incorporate metal salts. (b) Photos of samples with HA additive (10 vol% HA added to salt solutions during swelling).

The thermal stabilities of SP0 with Li(I), Ca(II), and Mg(II) were quantitatively compared by measuring the ratio of absorbance from mechanochemical activation to that from thermal activation (Figure 4.5 and 4.6b). In these experiments, samples were first bleached by exposure to intense visible light (~1000 mW/cm$^2$). The absorbance of specimens was then monitored for

45 minutes under the low intensity (0.22-0.49 mW/cm$^2$) light of the deuterium lamp, after which time the sample approaches equilibrium (blue curves of Figure 4.5). A representative curve showing an absorbance plateau during this equilibration period is shown Figure 4.9b. Although samples do not reach a *absolute* equilibrium in 45 minutes, all samples, regardless of the type of metal salt or presence/absence of HA, exhibit nearly identical thermal activation kinetics (Figure 4.9a). Therefore, we consider all samples to be in a similar, *quasi*-equilibrated state after 45 minutes.

Mechanochemical activation was triggered by applying a 4 N (4.08 ± 0.10 MPa true stress) tensile load. At this magnitude all SP0 specimens exhibited similar mechanical behavior regardless of incorporation of metal salt or inclusion/exclusion of HA (Figure 4.6a). Before mechanochemical equilibration a 4 N tensile load was applied for 30 seconds and immediately released to determine if samples have any appreciable mechanochemical response (yellow curves of Figure 4.5). A 4 N load was again applied, this time for 45 minutes, allowing samples to reach a mechanochemical equilibrium, after which they were released and their absorbance immediately measured (green curves of Figure 4.5). Using this methodology, the relative equilibria of three samples containing each metal salt, as well as those with and without HA, were tested and compared. The results are summarized in Figure 4.6b. From these measurements a clear trend is observed, which directly correlates with the stability constants of the MC-metal complexes in solution measured by NMR spectroscopy (Table 4.2). SP0 exhibits the smallest equilibrium concentration of MC-metal complexes in solution with Li($NTf_2$). Because the interaction of SP0 with Li($NTf_2$) is the weakest, PDMS-SP0 composites containing Li($NTf_2$) exhibit the greatest ratio of mechanochemical to thermal activation. Likewise, Mg($NTf_2$)$_2$ produces the highest degree of complexation in solution, and because it interacts much more

strongly with SP0, the smallest ratio of mechanochemical to thermal activation is observed in PDMS composites with $Mg(NTf_2)_2$. Therefore, there is an inverse relationship between the stability of the MC-metal complex in solution and the ratio of mechanochemical to thermal activation in the solid state. In addition, we observe a clear enhancement in mechanochemical activation when HA is added into the PDMS matrix. Because the mechanical properties of the composites with and without HA are roughly the same at the 4 N applied load, we conclude that the enhancement in mechanochemical activation is indeed due to suppression of spontaneous activation of the MC-metal complexes in the presence of HA. It is worth noting that the overall absorbance of the Mg(II) samples was reduced significantly in our HA samples—we interpret this as a reduction in the extinction coefficient of the MC-Mg complexes due to interaction with HA and not a decrease in the concentration of MC-Mg. It is unclear at this time why this occurs with Mg(II) samples, but this does not affect the overall trend that we observe in mechanochemical-to-thermal activation. Lastly, we note that the same mechanochemical activation to thermal stability trend was observed with SP-NO2-PDMS/HA composites (Figure 4.10c), but with nearly complete loss of reversibility after applying mechanical force. It appears combining complexing species with a nitro-functionalized SP provides too much stability to MC in the solid state. Introduction of competing ligands could potentially solve this issue, but this was not pursued further because of the poor mechanical properties of the SP-NO2/salt composites.

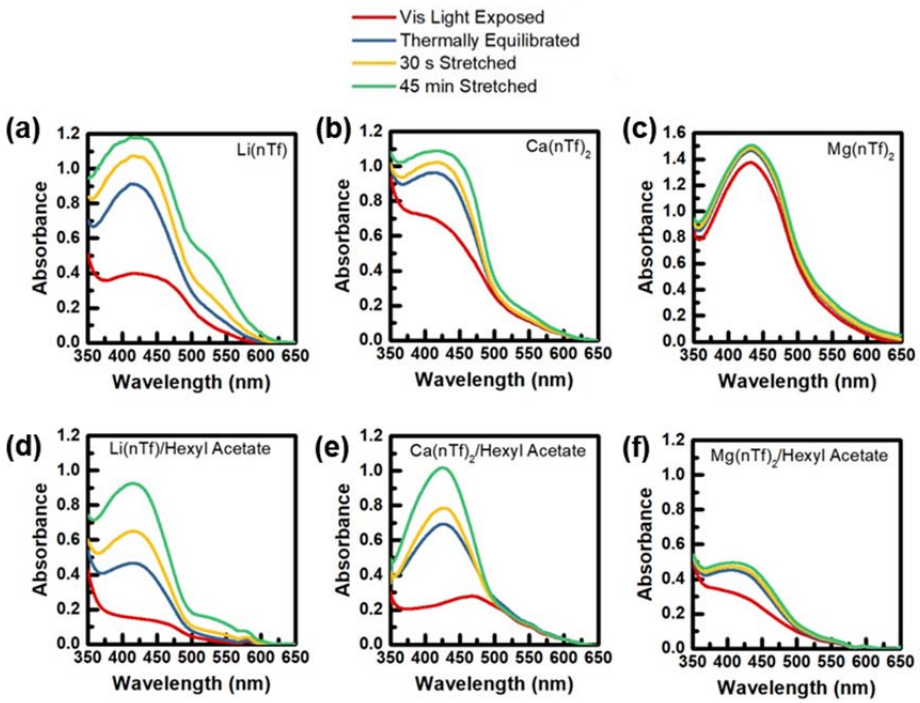


**Figure 4.5.** Absorbance spectra showing SP0-PDMS/metal ion composites after bleaching with high intensity (≥1000 mW/cm$^2$) visible light (red curves), thermally equilibrating under low intensity (0.22-0.49 mW/cm$^2$) light from the deuterium light source (blue curves), stretching at 4 N (true stress of 4.08 ± 0.10 MPa) for 30 s (yellow curves), and stretching at 4 N for 45 minutes (green curves). The ratio of green to blue curves are used to quantitatively compare mechanochemical to thermal activation under these conditions. The overall decrease in absorbance of Mg(II)/HA samples, while unclear at this time, does not affect the observed trend in mechanochemical-to-thermal activation.

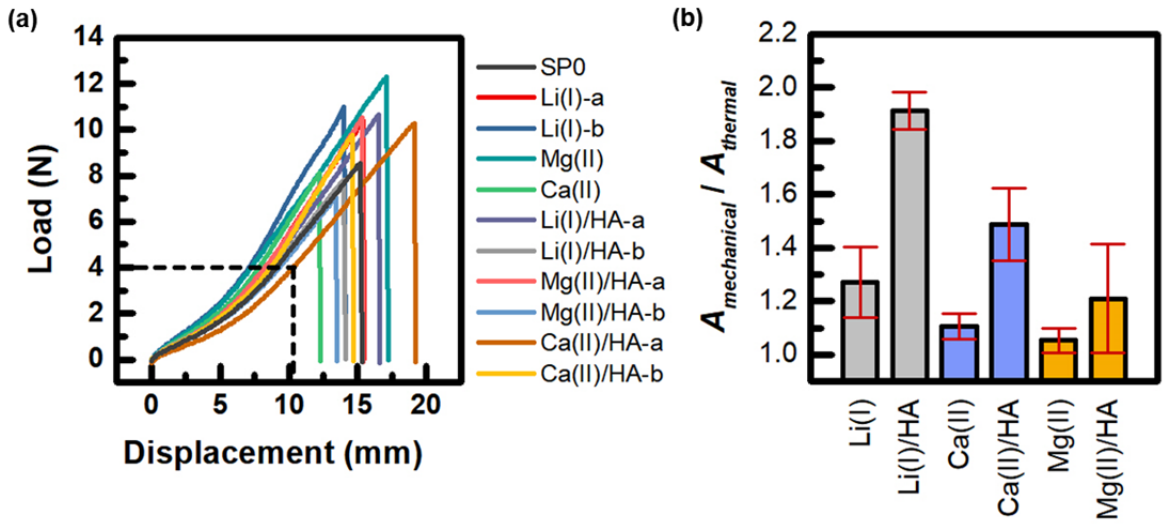


**Figure 4.6.** Summary of force-triggered metal complexation of SP0-PDMS. (a) Force vs. displacement curves show some spread in mechanical properties of specimens when tested to failure. Dashed lines highlight the 4 N load applied for testing mechanochemical reactivity. The magnitudes of true stress experienced by samples at this load were similar 4.08 ± 0.10 MPa. (b) Ratios of mechanochemical to thermal activation of MC-metal complexes in PDMS-SP0 composites measured by UV-Vis absorpance spectroscopy. Error bars show spread in data across 3 specimens of each sample type.

Our *in situ* tensile/UV-Vis measurements quantitatively verifies our hypothesis that HA suppresses spontaneous MC-metal coordination, thus enabling mechanical force to be a more effective stimulus. To demonstrate this visually, we prepared SP0-PDMS/HA composite films, which were more easily be manipulated by hand than the dogbone specimens (Figure 4.7). Prior to handling, the films were equilibrated for 24 hours at room temperature under ambient (fluorescent) light. Videos recorded the repeatable mechanochemical activation of MC with the various metal salts in real time as films were stretched and released. Snapshots taken before, during and after stretching are shown in Figure 4.7. Upon stretching, each sample exhibits a dramatic change in coloration along with a unique color signature. The kinetic stability afforded to MC by metal ion complexation is also evident. In the absence of metal ions, the force-induced coloration almost immediately switches off after release. With metal ions, the color fades gradually on a timescale of ~10 minutes. In our videos we triggered rapid release of metal ions

by briefly exposing the films to intense visible light (~1000 W/cm$^2$), thereby allowing us to demonstrate full repeatability of force-triggered ion complexation in a short timeframe.

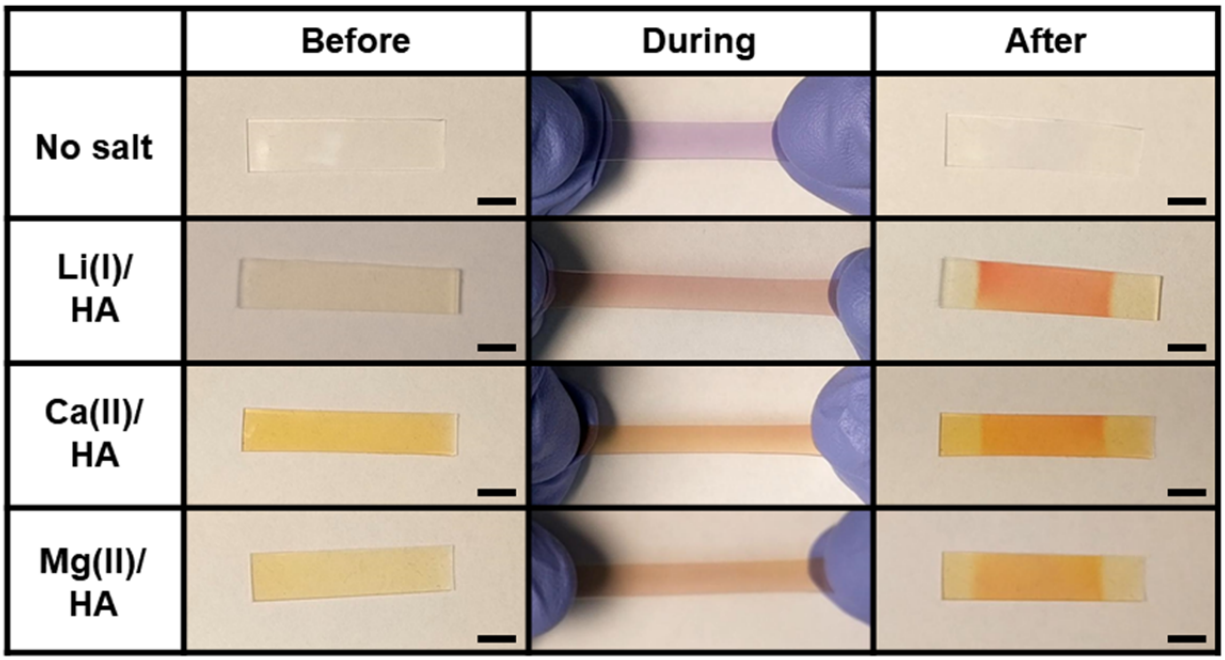


**Figure 4.7.** Photos of SP0-PDMS films incorporating HA and various metal salts. "Before" images show films after 24 hours equilibration at room temperature under ambient light. "During" images show films being stretched by hand. "After" images were recorded immediately after releasing films from the manually applied tensile strain. Scale bars are 7 mm.

*In situ* UV-Vis spectroscopy reveals full mechanochemical reversibility with all metal salts. As a representative example, a Li($NTf_2$)-incorporated SP0–PDMS composite was tested for multiple cycles (Figure 4.8). The specimen was first bleached with intense white light and then thermally equilibrated for 45 minutes under the low intensity deuterium source. After stretching at 4 N for 45 minutes the absorbance increases by nearly a factor of two. The absorbance decay upon release confirms the reversibility of the force activated MC-Li complex. This process of photobleaching, thermal equilibration, force activation, and thermal decay was repeated for multiple cycles showing little variability.

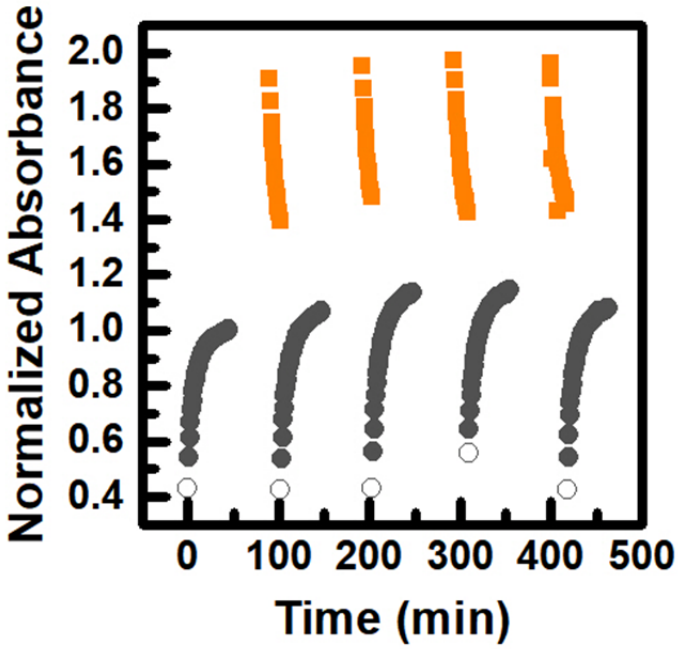


**Figure 4.8.** Reversible and repeatable force-triggered complexation in Li($NTf_2$)/SP0-PDMS composite. Open circles show absorbance immediately after photobleaching, closed grey circles show absorbance during thermal equilbration prior to stretching, orange squares show absorbance during thermal equilibration after applying a 4 N tensile load. Absorbance values shown are at $\lambda = 418.5$ nm, and are normalized to the maximum value recorded during the first cycle prior to stretching.

The kinetics of both spontaneous activation (prior to stretching) and thermal reversion (after stretching) of MC-metal complexes follow a biexponential rate law (red curves in Figure 4.9b & e); however, a monoexponential function (blue cuves in Figure 4.9b & e) provides a reasonable approximation for comparing general kinetic trends. Kinetic traces show no apparent differences in the activation rates of MC-metal complexes with Li(I), Ca(II) or Mg(II), nor between samples with and without HA (Figure 4.9c). To measure the kinetics of deactivation, a 4 N tensile load was applied for 45 minutes and released, and the subsequent absorbance decay was monitored. Using monoexponential approximations, we determine the rate of thermal deactivation to be ~1.5x faster with Li(I) ions than with Ca(II) and Mg(II). Addition of HA produces the most drastic difference, cutting the time constants for the thermal back reaction with all metal salts in

half (Figure 4.9f). As a final note, the reversibility and reversion kinetics appear far more superior with SP0 than with SP-NO2 (Figure 4.10d)

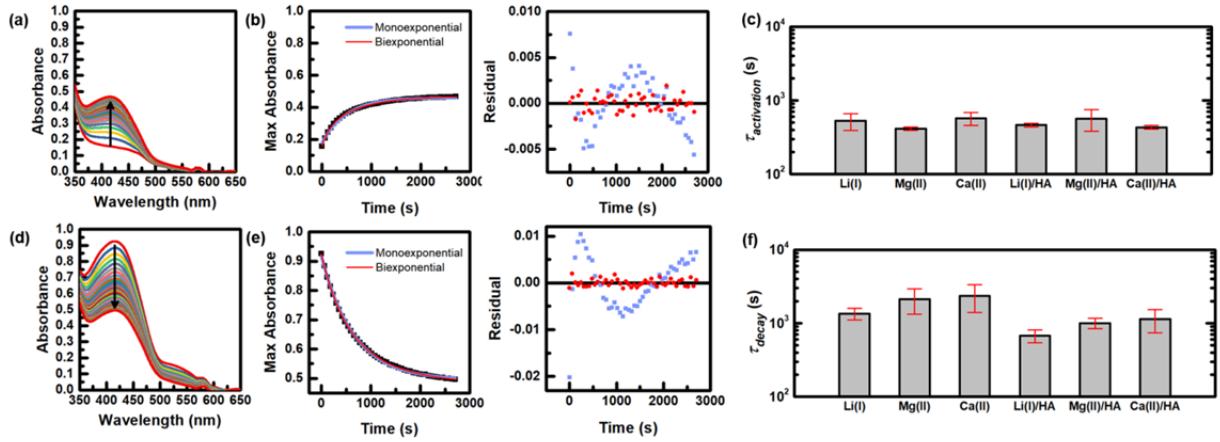


**Figure 4.9.** Kinetics of thermal activation prior to stretching and thermal deactivation after stretching. Spectra of a $Li(NTf_2)$/SP0-PDMS during (a) thermal activation and (d) thermal decay. Kinetic traces of (b) thermal activation and (e) thermal deactivation follow a biexponential rate law judging by the random distribution of the residuals from the data fits (plotted in red). A monoexponential function (plotted in blue) is found to be a reasonable approximation for comparing the kinetics of (c) thermal activation and (f) thermal deactivation of different samples. Addition of HA significantly affects the rate of thermal deactivation of MC-metal complexes but not the rate of thermal activation.

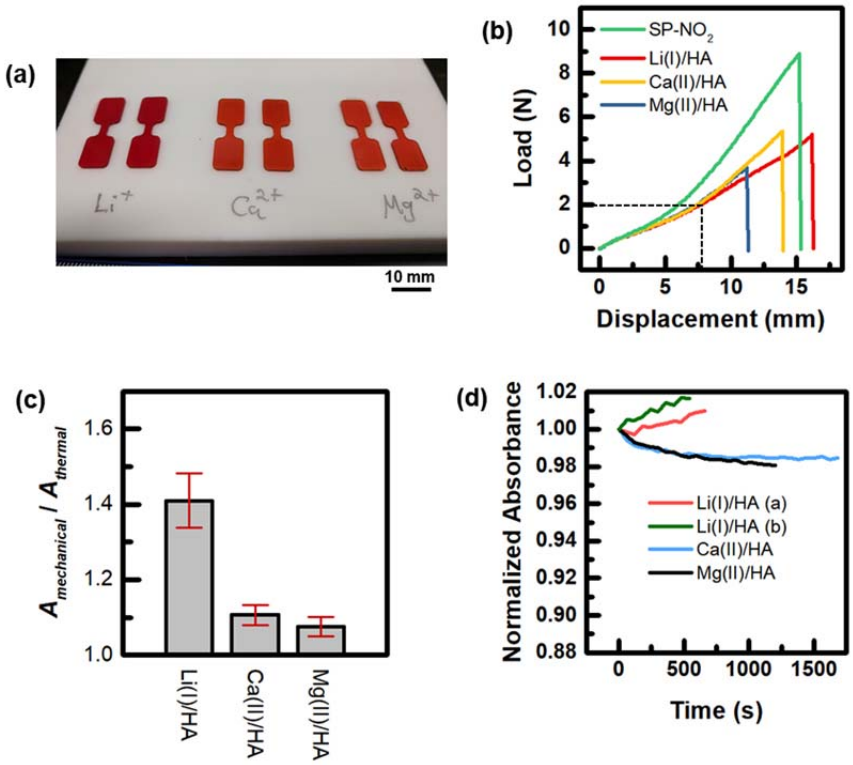


**Figure 4.10.** (a) Photos of SP-NO2-PDMS/metal salt/HA composites. (b) Addition of metal salts caused embrittlement of samples. The dashed line highlights the 2 N applied load for mechanochemical equilibrium tests. (c) A similar trend in relative ratios of mechanochemical activation to thermal activation is observed with SP-NO2 as with SP0, however, due to the high mechanical failure rate of specimens fewer SP-NO2 samples gave meaningful data (2 data points for each salt). (d) Kinetic traces of the absorbance maxima after release of the 2 N applied load. SP-NO2 samples show much higher kinetic stability than SP0 with metal salts.

### 4.5 Assessing stoichiometry and cumulative stability constants of complexes in solution

We obseinverse relationship between the stability of the MC-metal complex in solution and the ratio of mechanochemical to thermal activation in the solid state.

The observed trend in the ratio of mechanochemical activation to thermal activation of MC-metal complexes in PDMS-SP0 is indirectly proportional to the relative stability constants of the complexes measured in solution. Titrations are a common method for determining stability constants of metal-ligand complexes [27]; however, this method has proved exceedingly difficult

for spiropyrans such as SP0 that have very weak interactions with metal ions in solution. As a rudimentary analysis of the relative interaction strength of SP0 with Li(I), Ca(II) and Mg(II), we determined the equilibrium concentration of MC in the presence of the various metals using 1D NMR spectroscopy (Figure 4.11 and Table 4.2). For our analysis we used acetone-$d_6$, which provided good solubility to both SP0 and the metal salts.

Our analysis is based on two hypotheses: (1) all activated MC molecules coordinate to a metal ion, and (2) the stoichiometry of all complexes is the same in solution. The first hypothesis is based on the following logic: no measurable amount of SP0 exists in the merocyanine state unless metal ions are present to provide stability—therefore, it is reasonable to assume that the most, if not all, MC produced after thermal equilibration with metal salts is coordinated to a metal ion. Our second hypothesis is supported by DOSY NMR experiments. We use the following logic: first, it's reasonable to assume that Li(I) salts will produce 1:1 coordination complexes, as is expected for monovalent salts with MC [6]. However, because Ca(II) and Mg(II) are divalent ions, there is a possibility that two MC molecules coordinate to each ion (i.e. 2:1 complexes may be formed). The stoichiometry of MC0 with Mg(II) in acetone-$d_6$ was deduced by comparing 2D DOSY plots of SP0 solutions containing trifluoroacetic acid (Figure 4.12a) and $Mg(NTf_2)_2$ (Figure 4.12b). The ratios of diffusivities of the ring-open to ring-closed forms is identical in 4.12a and b. Therefore, we conclude that MC-Mg and protonated MC-$H^+$ have roughly the same molecular shape and size. Because MC-$H^+$ almost certainly does not form dimers, we conclude that MC-Mg also is not a dimeric species, and therefore, the stoichiometry of the complex in solution is 1:1. DOSY was not performed with Ca(II) because of the much lower activation of MC, but we assume a similar result would be observed. Therefore, we conclude that the stoichiometry of MC0 with Li(I), Ca(II) and Mg(II) in acetone-$d_6$ is 1:1.

Combining our deduction of stoichiometry with the relative ratios of MC0:SP0 measured from 1D $^{1}$H NMR (Figure 4.11), we estimate the cumulative stability constants, $\beta_{11}$ (Table 4.2):

$$\beta_{11} = \frac{[MC]}{[SP]} \cdot \frac{[MCM^{+}]}{[MC][M^{+}]} = \frac{[MCM^{+}]}{[SP][M^{+}]} \quad 4.1$$

**Table 4.2**. Cumulative stability constants ($\beta_{11}$) of SP0 with Li(nTf), Ca(nTf)$_2$ and Mg(nTf)$_2$ in acetone-$d_6$ at 25 °C determined by NMR spectroscopy. Peak wavelengths ($\lambda$) and extinction coefficients ($\varepsilon$) of the complexes were also estimated by taking UV-Vis absorption spectra of the solutions immediately after they were analyzed by NMR.

| Salt | $\lambda$ (nm) | $\varepsilon$ ($10^3$ cm$^{-1}$ M$^{-1}$)* | $\beta_{11}$ ($10^{-3}$ M$^{-1}$) |
|---|---|---|---|
| Li(NTf$_2$) | 408 | 5.1 | 3.1 |
| Ca(NTf$_2$)$_2$ | 420 | 3.4 | 360 |
| Mg(NTf$_2$)$_2$ | 414 | 2.6 | 1800 |

*It may be tempting to use these extinction coefficients in acetone to estimate the concentration of MC-metal species in PDMS, but caution must be taken, as extinction coefficients can change drastically in different media.

It is worth noting that acetone is a polar solvent with much stronger electron donor character than PDMS. Therefore, we expect MC-metal stability constants to be much higher in SP0-PDMS than for the free monomer in acetone. Nevertheless, the cumulative stability constants provided here reveal qualitative trends that we compare to our observations of the SP0-PDMS composites. Evidently, the thermal stability of the complex is the strongest with Mg(II) and by far the weakest with Li(I). This explains the much higher ratio of mechanochemical to thermal activation of SP0-PDMS with Li(I). These results clearly show an inverse relationship between the relative degrees of mechanochemical to thermal activation observed in SP0-PDMS and the stability of the metal complexes measured in solution.

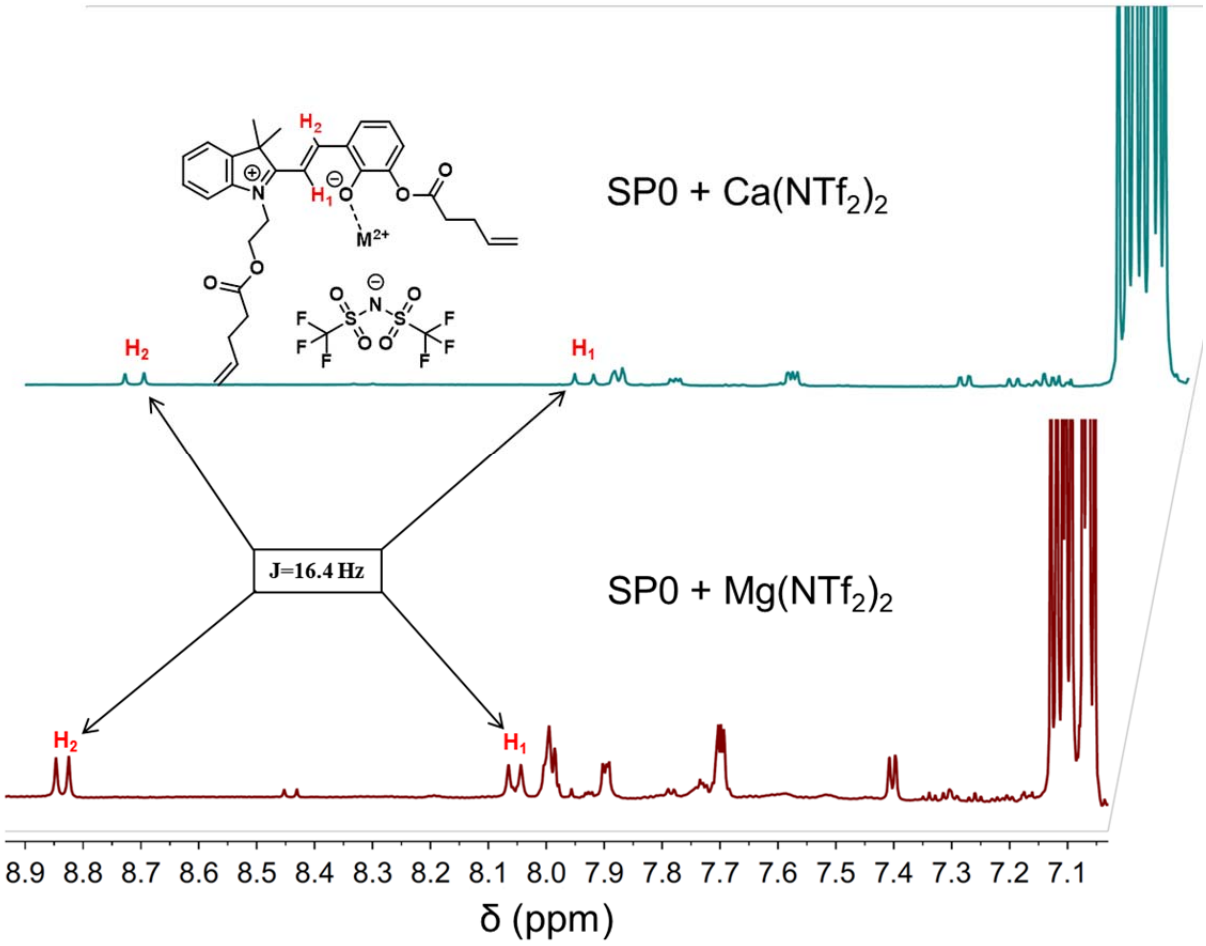


**Figure 4.11.** Stacked $^{1}$H NMR spectra highlighting MC-metal complex peaks with $Ca(NTf_2)_2$ and $Mg(NTf_2)_2$ in acetone-$d_6$. Arrows point to two doublets in each spectrum corresponding to the two protons highlighted in red in the schematic of the MC-$M^{2+}$ complex ($M^{2+}$ corresponds to either Ca(II) or Mg(II)). The ratio of MC to SP was determined by integrating the well-isolated peak at $\delta \approx 8.84$ ppm.

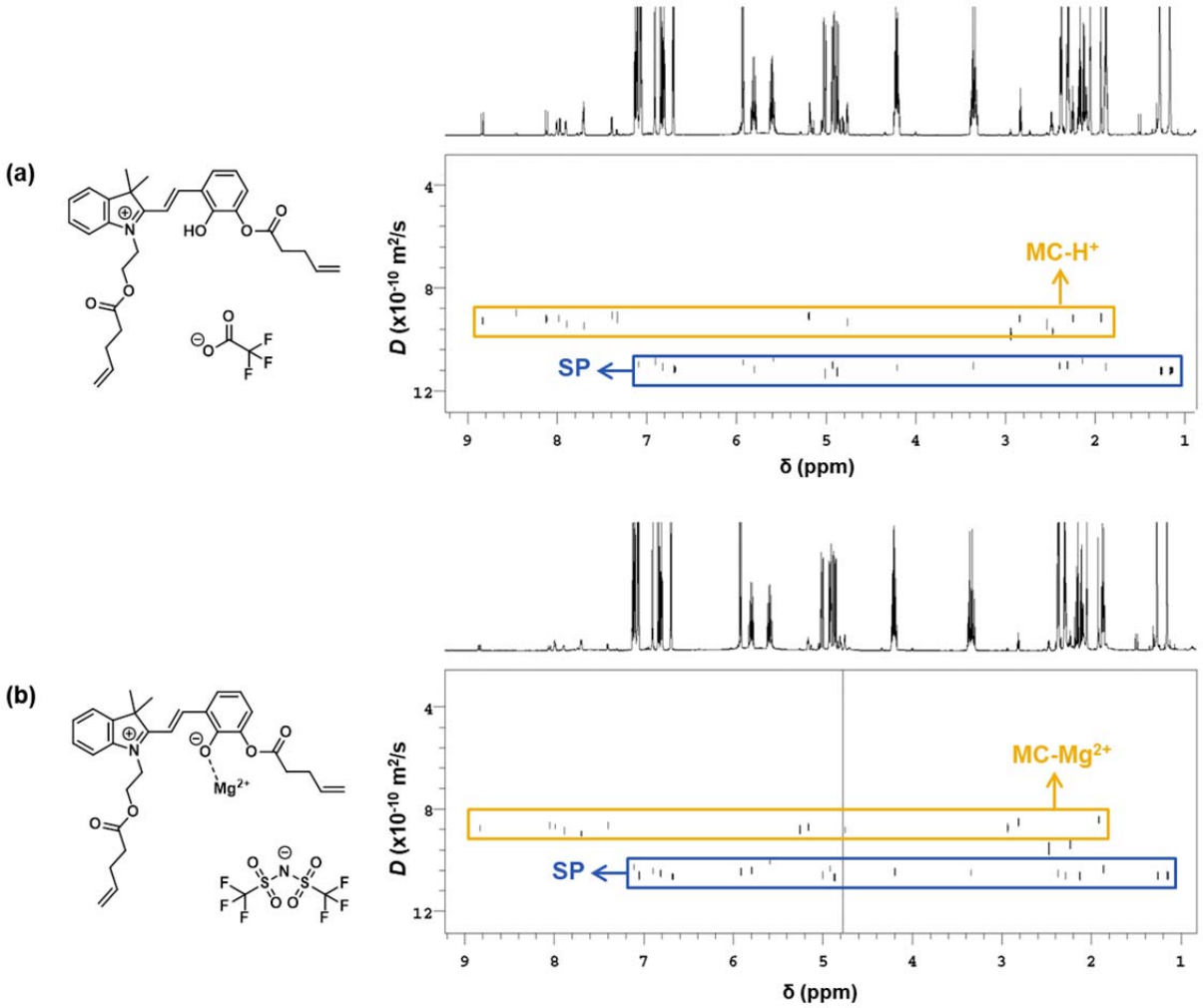


**Figure 4.12.** The stoichiometry of MC-metal complexes of SP0 with Mg(II) was deduced by comparing 2D DOSY plots of (a) SP0 with trifluoroacetic acid and (b) SP0 with $Mg(NTf_2)_2$ in acetone-$d_6$. The ratios of diffusivities of the ring-open to ring-closed forms is identical in (a) and (b). Therefore, we conclude that MC-Mg and MC-$H^+$ have roughly the same molecular shape and size. Because MC-$H^+$ almost certainly does not form dimers, we conclude that MC-Mg also is not a dimeric species, and therefore, the stoichiometry of the complex is 1:1.

### 4.6 Exploring the effect of non-covalent interactions on covalent bond rupture using DFT

Thus far, our study has focused on mitigating the spontaneous activation of merocyanine in the presence of metal ions. We posit that the driving force for this spontaneous activation derives from the metal ion interacting directly with the spirocyclic oxygen of SP in its ring-closed state. Generally, the association of metal ions with the ring-closed form is not taken into account in modeling or analyzing the thermal complexation MC-metal coordination [4, 28]; however, a

model recently reported by Ganesan and Remacle does predict that formation of protonated merocyanine is preceded by a protonated ring-closed transition state [29]. Here, we pose the following questions: do metal ions associate with SP in its ring-closed state? If so, do they lower the activation barrier for ring opening? Or rather in the context of mechanochemistry, does the presence of metal ions reduce the force required for bond rupture? DFT CoGEF simulations are a convenient tool to probe these questions. We begin our investigation by comparing the activation of SP0 in the presence and absence of a $Li^+$ ion (Figure 4.13a). To maintain charge neutrality, we include a bromide counterion. To include the possibility of chelation by the carbonyl moeity of SP0 (see Figure 4.1a). we include a methyl ester group directly adjacent to the spirocyclic oxygen. To account for electrostatic screening, calculations are performed using a polarizable continuum model with a dielectric constant of 7.43. a diffuse term is added to the basis set for all non-hydrogenic atoms to account for long-range effects.

The addition of a Li(I) ion has a significant effect on the unconstrained, equilibrium conformation of SP0 (Figure 4.13a). In the absence of any metal, the angle between the chromene ring, spirocyclic carbon and indoline nitrogen is 109.5°. With Li(I), this angle increases to 131.2° (angles of measurement are highlighted by yellow lines in Figure 4.13a). This unfolded structure is evidently due to the sandwiching of the Li(I) ion between the indoline nitrogen, spirocyclic oxygen and the carbonyl oxygen of SP0. In this equilibrium state, the interaction energy between Li(I) and SP0 ($E_{int} = E_{SP0\text{-}LiBr} - E_{SP0} - E_{LiBr}$) is computed to be 102.7 kJ/mol. This is about 57 kJ/mol less than the experimentally measured binding energy of Li(I) to dimethyl ether in the gas state, so it is reasonable to assume that the SP0-Li(I) interaction in our calculations is relatively weak.

Despite the relatively weak energetic interaction of Li(I) with SP0, the presence of Li(I) dramatically reduces both the energy and force of mechanophore bond rupture (Figure 4.13b & c). The position of the Li(I) ion in the unconstrained state suggests that it interacts both with the spirocyclic oxygen as well as the carbonyl oxygen of the alkyl ester moiety (Figure 4.13a). In this state, the Li(I) ion is about 0.2 Å closer to the carbonyl oxygen than the spirocyclic oxygen, suggesting a stronger interaction with the carbonyl group; however, the interaction with the spirocyclic oxygen appears to become stronger as the molecule is stretched (Figure 4.14d). In the unconstrained state, the length of the spirocyclic oxygen bond is no different when Li(I) is present than when Li(I) is absent. This indicates that the metal ion does not increase the lability of the spirocyclic bond, as we observed when SP is functionalized with a nitro group (Figure 4.1e). Furthermore, the displacement of the covalent bond upon rupture is not reduced when Li(I) is present. Therefore, while Li(I) interacts with the spirocyclic oxygen, it does not weaken the bond. We conclude that less work is required to rupture the mechanophore when Li(I) is present because Li(I) unfolds the SP rings, leaving the molecule in a more constrained state with fewer degrees of freedom. This results in more effective transduction of energy directly to the spirocyclic bond. Therefore, less work is ultimately required to break that bond.

Figure 4.13 shows that Li(I) has no effect on the actual strength of the spirocyclic bond even though it interacts with the spirocyclic oxygen. But what if the interaction was stronger? Shouldn't it be possible for such interactions to weaken the mechanochemically active bond? To explore this, we eliminate the electrostatic screening from the effective solvent medium and perform CoGEF simulations with three other salts: Na(I), Ca(II) and Mg(II) (Figure 4.14). The spirocyclic C—O bond becomes slightly longer with all three salts (0.011 Å, 0.008 Å and 0.009 Å for Na(I), Ca(II) and Mg(II), respectively). This bond lengthening is less dramatic than the

lengthening observed when adding a nitro group to SP (0.023 Å), but nevertheless, suggests that non-covalent interactions can increase the lability of the spirocyclic bond. Much more noticeably, there is a significant reduction in the C—O bond *displacement* required for total bond rupture (Figure 4.14d). In the absence of ions, the C—O bond displacement at break is 0.154 Å. With Na(I), Ca(II) and Mg(II), that value is reduced to 0.081 Å, 0.106 Å, and 0.061 Å, respectively. Clearly the effect is most drastic with Mg(II), which has the closest interaction with the spirocyclic oxygen (Figure 4.14c), and reduces the force at rupture to just 0.84 nN (Figure 4.14b). Though these simulations are just toy models, they have important implications for mechanochromic systems. If these results are experimentally verified, it may be possible to strategically tune the strength of mechanochemically active bonds by introducing certain ions. This would greatly enhance the versatility of mechanochromic dyes, as coupling different bond strengths with different colors produced via MC-metal coordination could enable polymers to display different colors at different applied loads. Moreover, strategically weakened covalent bonds could be applied as mechanism for toughening polymers.

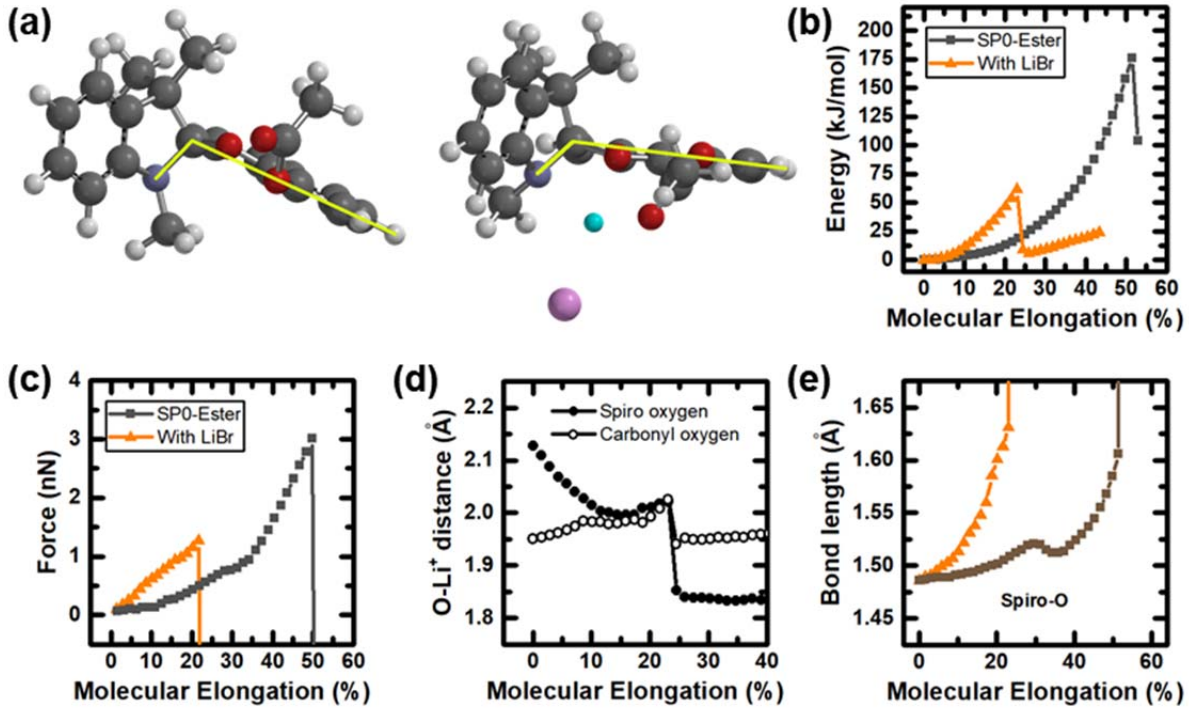


**Figure 4.13.** CoGEF simulations of SP0 with and without $Li^+$ + $Br^-$ ions. Calculations performed at the B3LYP/6-31+G* level of theory using a C-PCM with an effective dielectric constant of 7.43. (a) Snapshots of SP0-ester in the unconstrained, equilibrium state. Yellow lines highlight the difference in angle showing that interaction of the spirocyclic oxygen and carbonyl groups with $Li^+$ causes the equilibrium state of the molecule to take on an unfolded conformation. (b) Energy landscape, (c) gradient of energy, and (d) distance between $Li^+$ ion and the spirocyclic oxygen and carbonyl oxygen as a function of elongation. Closer distance suggests stronger interaction. (e) Length of spirocyclic oxygen bonds of SP0 with and without LiBr. Calculations were performed at the B3LYP/6-31+G* level of theory using a C-PCM with an effective dielectric constant of 7.43.

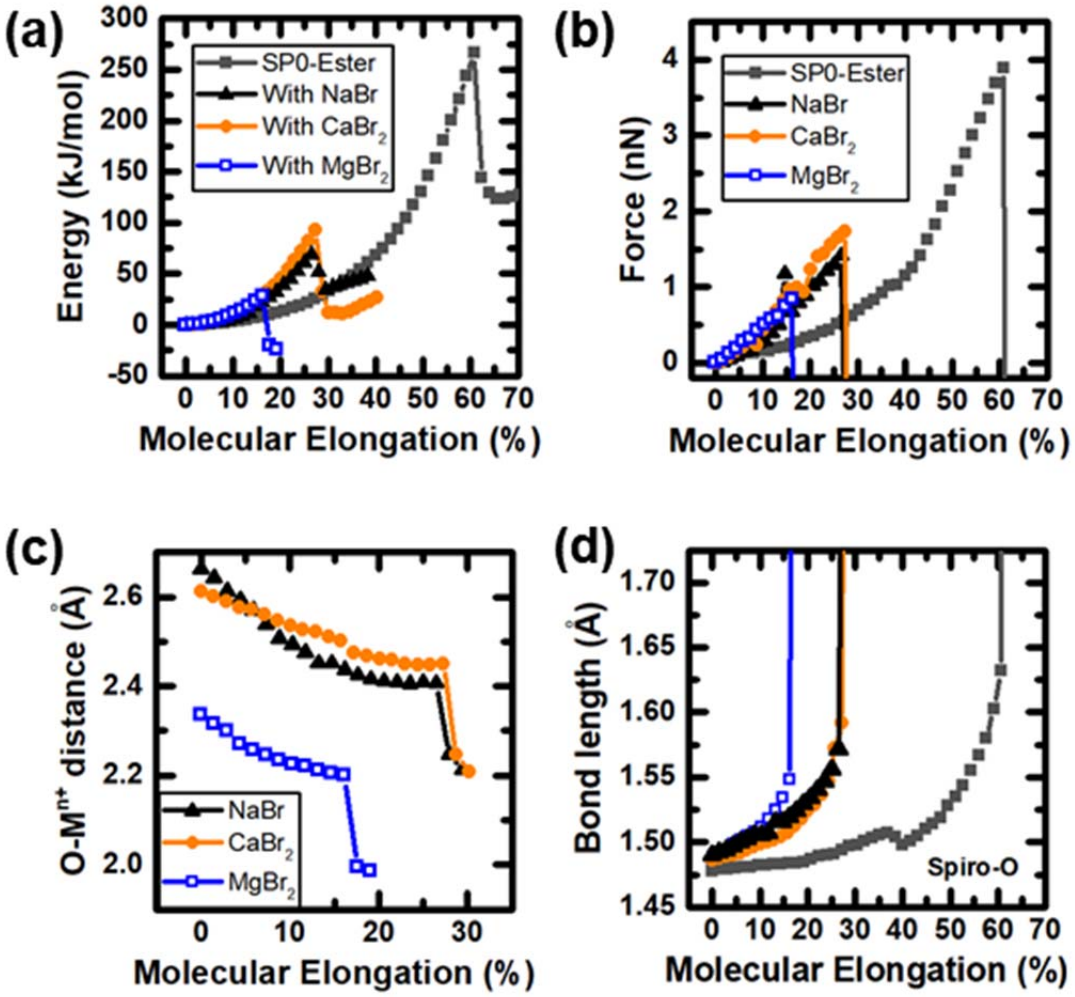


**Figure 4.14.** CoGEF calculations of SP0 with different metal salts in the absence of electrostatic screening. Calculations performed in the gas state at the B3LYP/6-31G* level of theory. The effective solvent medium was purposefully removed for these calculations so as to investigate the effect of ions when their interaction strength is maximized. The diffuse basis term used in Figure. 4.13 was dropped to reduce computation time. (a) Energy, (b) gradient of energy, (c) distance between spirocyclic oxygen and each metal ion, and (d) C—O (spirocyclic oxygen) bond length as a function of elongation with $MgBr_2$ (blue open squares), $CaBr_2$(orange circles), NaBr (black triangles) and without any salt (grey closed squares).

### 4.7 Conclusions

Reversible and repeatable force-triggered MC-metal coordination was demonstrated by incorporating metal salts in a SP-mechanophore linked PDMS elastomer. Spontaneous activation of SP to MC via ion interactions was effectively mitigated by selecting a SP mechanophore (SP0) that is very stable in its ring-closed state, and by incorporating hexyl acetate in the PDMS

matrix, which screened the interactions between SP and metal ions. The repeatability of this process is owed to a combination of the elasticity of the PDMS matrix and the reversible nature of the MC-metal complexes. A tradeoff between the thermodynamic stability of the MC-metal complex and the relative degree of mechanochemical to thermal activation was revealed. In addition, DFT simulations were used to explore the effects from electron withdrawing groups on the SP mechanophore and from metal ion interactions on the bond strength of the SP mechanophore. This work greatly expands the versatility of SP mechanophores and is an important step towards attaining our ultimate vision of engineering polymers that undergo reversible, force-triggered MC-metal crosslinking.

### 4.8 Opportunities for improvement

There are two immediate opportunities for improving the work discussed in this section. First, we evaluated stability, stoichiometry and extinction coefficients of MC0-metal complexes in acetone, but to draw a direct comparison between the solution behavior and behavior in SP0-PDMS, these NMR studies should be conducted in PDMS. Unfortunately, SP0 has extremely limited solubility in liquid PDMS. Covalently linking a monofunctional, Si-H terminated dimethylsiloxane oligomer to the alkene terminated groups of SP0 could solve this problem. If this is solved, NMR and UV-Vis spectroscopy can be used to precisely determine the extinction coefficients of MC0-metal complexes in 10% HA/PDMS. This would be a ***massive*** improvement because these values will tell us ***exactly*** how much MC-metal is activated at any given time. The second opportunity is to measure exactly how much salt is incorporated in the PDMS composites after drying. X-Ray fluorescence is the technique we recommend/plan to use, but these experiments have not yet been conducted.

## 4.9 REFERENCES


1. Potisek, S. L., Davis, D. A., Sottos, N. R., White, S. R. and Moore, J. S. *Journal of the American Chemical Society* **2007**, *129*, 13808.
2. Davis, D. A., Hamilton, A., Yang, J., Cremar, L. D., Van Gough, D., Potisek, S. L., Ong, M. T., Braun, P. V., Martinez, T. J., White, S. R., et al. *Nature* **2009**, *459*, 68.
3. Zhang, H., Gao, F., Cao, X., Li, Y., Xu, Y., Weng, W. and Boulatov, R. *Angew Chem Int Ed Engl* **2016**, *55*, 3040.
4. Chibisov, A. K. and Gorner, H. *Chemical Physics* **1998**, *237*, 425.
5. Gorner, H. and Chibisov, A. K. *Journal of the Chemical Society, Faraday Transactions* **1998**, *94*, 2557.
6. Kubinyi, M., Varga, O., Baranyai, P., Kállay, M., Mizsei, R., Tárkányi, G. and Vidóczy, T. *Journal of Molecular Structure* **2011**, *1000*, 77.
7. Fries, K., Samanta, S., Orski, S. and Locklin, J. *Chem Commun (Camb)* **2008**, 6288.
8. Fries, K. H., Driskell, J. D., Samanta, S. and Locklin, J. *Analytical Chemistry* **2010**, *82*, 3306.
9. Gossweiler, G. R., Hewage, G. B., Soriano, G., Wang, Q., Welshofer, G. W., Zhao, X. and Craig, S. L. *ACS Macro Letters* **2014**, *3*, 216.
10. Lee, C. K., Davis, D. A., White, S. R., Moore, J. S., Sottos, N., R. and Braun, P. V. *Journal of the American Chemical Society* **2010**, *132*, 16107.
11. Lee, C. K., Beiermann, B. A., Silberstein, M. N., Wang, J., Moore, J. S., Sottos, N. R. and Braun, P. V. *Macromolecules* **2013**, *46*, 3746.
12. Kingsbury, C. M., May, P. A., Davis, D. A., White, S. R., Moore, J. S. and Sottos, N. R. *Journal of Materials Chemistry* **2011**, *21*, 8381.
13. Gossweiler, G. R., Kouznetsova, T. B. and Craig, S. L. *J Am Chem Soc* **2015**, *137*, 6148.
14. Robb, M. J., Kim, T. A., Halmes, A. J., White, S. R., Sottos, N. R. and Moore, J. S. *Journal of the American Chemical Society* **2016**, *138*, 12328.
15. Beyer, M. K. *The Journal of Chemical Physics* **2000**, *112*, 7307.
16. Kryger, M. J., Munaretto, A. M. and Moore, J. S. *Journal of the American Chemical Society* **2011**, *133*, 18992.
17. Swart, M., Güell, M., Luis, J. M. and Solà, M. *The Journal of Physical Chemistry A* **2010**, *114*, 7191.
18. Kim, H., Park, J. and Lee, Y. S. *Journal of Computational Chemistry* **2013**, *34*, 2233.
19. Robb, M. J. and Moore, J. S. *J Am Chem Soc* **2015**, *137*, 10946.
20. Zou, W. X., Huang, H. M., Gao, Y., Matsuura, T. and Meng, J. B. *Structural Chemistry* **2004**, *15*, 317.
21. Crano, J. C., Guglielmetti, R. J., *Organic Photochromic and Thermochromic Compounds*; 1 ed.; Springer US, 2004.
22. Schaudel, B., Guermeur, C., Sanchez, C., Nakatani, K. and Delaire, J. A. *Journal of Materials Chemistry* **1997**, *7*, 61.
23. Evans, R. A., Hanley, T. L., Skidmore, M. A., Davis, T. P., Such, G. K., Yee, L. H., Ball, G. E. and Lewis, D. A. *Nature Materials* **2005**, *4*, 249.
24. Mozhdehi, D., Ayala, S., Cromwell, O. R. and Guan, Z. *J Am Chem Soc* **2014**, *136*, 16128.
25. Prause, S., Spange, S. and Barthel, H. *Macromolecular Chemistry and Physics* **2005**, *206*, 364.
26. Jessop, P. G., Jessop, D. A., Fu, D. and Phan, L. *Green Chemistry* **2012**, *14*, 1245.
27. Thordarson, P. *Chemical Society Reviews* **2011**, *40*, 1305.

28. Zakharova, M. I., Coudret, C., Pimienta, V., Micheau, J. C., Delbaere, S., Vermeersch, G., Metelitsa, A. V., Voloshin, N. and Minkin, V. I. *Photochemical & Photobiological Sciences* **2010**, *9*, 199.
29. Ganesan, R. and Remacle, F. In *Theoretical Chemistry in Belgium: A Topical Collection from Theoretical Chemistry Accounts*; Champagne, B., et al., Eds.; Springer Berlin Heidelberg: Berlin, Heidelberg, 2014, p 167.

# CHAPTER 5: EVALUATING MEROCYANINE-METAL COMPLEXES BY DIFFUSION NMR

## 5.1 Background: Challenges with measuring stoichiometry of weak MC complexes

Stoichiometry is critical to whether or not metal-ligand complexes crosslink polymer chains. In SP functionalized polymers, we assume that crosslinks form only if at least 2 MC molecules bind to a metal cation. Researchers have shown that 2:1 MC-metal complexes form when SP possesses certain chelating moieties (e.g. amines, thiazoles and oxazoles) directly adjacent to the spirocyclic oxygen [1-3], but the synthesis of these compounds involves many steps, and schemes for formulating mechanophore analogues to these derivatives are nonobvious. Hence, our investigations have primarily focused on SP molecules containing no nitrogenous chelating moieties. Previous studies posit that MC containing no chelating group forms 2:1 complexes with divalent transition metal salts [4-7]. However, as explained further below, the methodology used to determine stoichiometry in these studies has a major flaw.

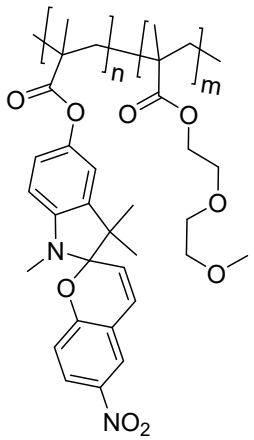


**Scheme 5.1.** Poly(DEGMEMA-SPMA)

In Chapter 3, we show that concentrated solutions of poly(DEGMEMA-SPMA) (Scheme 5.1) forms reversible crosslinks with Co(II) and Cu(II) ions. These results suggest that Co(II) and Cu(II) bridge MC-functionalized chains, and therefore, the MC:metal stoichiometry is ≥2:1.

However, thus far we failed to confirm the stoichiometry of MC-metal complexes spectroscopically. As a consequence of very weak MC-metal interaction strengths, we find the behavior of poly(PDEGMEMA-SPMA) with metal ions is highly dependent on the conditions of the surrounding medium. Figure 5.1 demonstrates this problem using UV-Vis spectroscopy. In dilute solutions of poly(DEGMEMA-SPMA) with 2:1 SP:$Co(NTf_2)_2$ (Figure 5.1a), thermal activation of MC (red curve) is significantly lower than activation by UV excitation (purple curve), indicating that the thermodynamic driving force for activating MC-metal complexes is extremely weak. Moreover, after both thermal and UV activation, there appears to be a significant amount of un-complexed MC in solution, as indicated by the peak centered at $\lambda \approx 560$ nm. In contrast, the concentrated poly(DEGMEMA-SPMA) solutions that form gels in our rheological experiments show near quantitative conversion of SP to MC-Co complexes (Figure 5.1b), indicating a much larger driving force for MC-metal activation. Furthermore, the absence of a peak at $\lambda \approx 560$ nm, indicates that all MC molecules coordinate to Co(II) ions, and therefore, the MC-metal interaction strength is much higher.

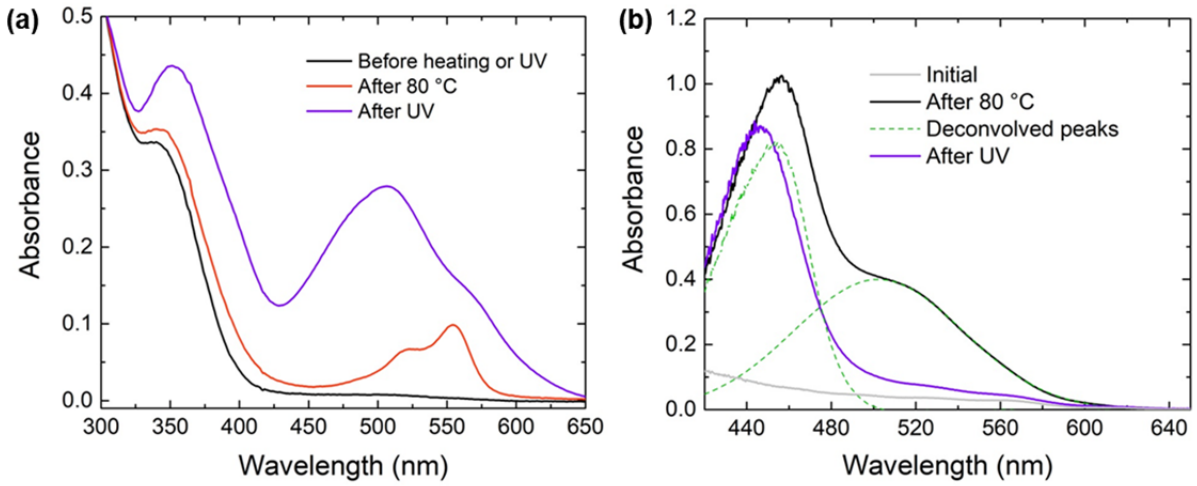


**Figure 5.1.** Significant difference between thermal activation of MC-Co complexes in dilute and concentrated poly(DEGMEMA-SPMA) solutions. (a) 0.08 wt% poly(DEGMEMA-SPMA) (0.333 mM SP) and (b) 24.5 wt% poly(DEGMEMA-SPMA) (~147 mM SP). Both solutions are in propylene carbonate and contain 2:1 SP:$Co(NTf_2)_2$. Experimental details provided in Chapter 3. In the dilute solution, UV excitation produces drastically more MC than thermal activation. In concentrated solutions, UV exposure changes the distribution of MC-Co complexes but does not appear to increase the overall concentration. Another clear difference is in the position(s) of the MC-Co complex peak(s), suggesting that the distribution of MC-Co isomers is concentration dependent.

The stoichiometry of metal-ligand complexes is often evaluated using the method of continuous variations, whereby the relative concentrations of ligand and metal ion are systematically varied while keeping the total concentration (ligand + metal) constant [8]. Ideally, all variables should be kept constant except the relative concentrations of ligand and metal ion. Unfortunately, in concentrated solutions of poly(DEGMEMA-SPMA), the conditions of the surrounding medium varies considerably as the ratio of SP:Co(II) changes. One highly dependent variable is the viscosity of the solution (as we show in Chapter 3). Another variable that is bound to change considerably at high concentrations of SP and metal salt is the effective dielectric constant of the solution. Thus, the problem becomes much more complicated.

We have attempted to use the method of continuous variations to evaluate MC-Co stoichiometry in dilute ([SP] + [Co(II)] = 0.5 mM) solutions of poly(DEGMEMA-SPMA) and $Co(NTf_2)_2$ (Figure 5.2). Here, we used UV excitation to activate MC. At low relative

concentrations of Co(II), we observe a large peak at $\lambda = 564$ nm, corresponding to free MC. As the salt concentration is increased, this peak decreases, and a new peak arises centered at $\lambda \approx 506$ nm, which corresponds to the MC-Co(II) complex (Figure 5.2a). To construct a Job plot, we evaluate the absorbance of the MC-Co complex at a wavelength far from the free MC peak (in this case we choose 450 nm). The Job plot of Figure 5.2b shows a maximum absorbance at a 2:1 SP:Co(II) ratio, which seemingly suggests that the stoichiometry of the MC-Co complex is 2:1. This exact methodology has been employed by others who arrived at the same conclusion [5]. However, this methodology has one major flaw, which is we do not know how much MC is actually produced upon UV activation. Though we are able to systematically vary the relative concentration of *SP* to metal salt, we are unable to systematically vary the relative concentration of *MC* to metal salt (which is actually the ratio we care about!). Therefore, this methodology is insufficient. To further complicate matters, the data presented in Figure 5.1 suggest that the nature of the MC-Co complexes in the dilute solution is very different than what we observe in our gels. Therefore, it is unwise to assume the Job plot of Figure 5.2b is representative of the complexes that cause gelation of poly(DEGMEMA-SPMA).

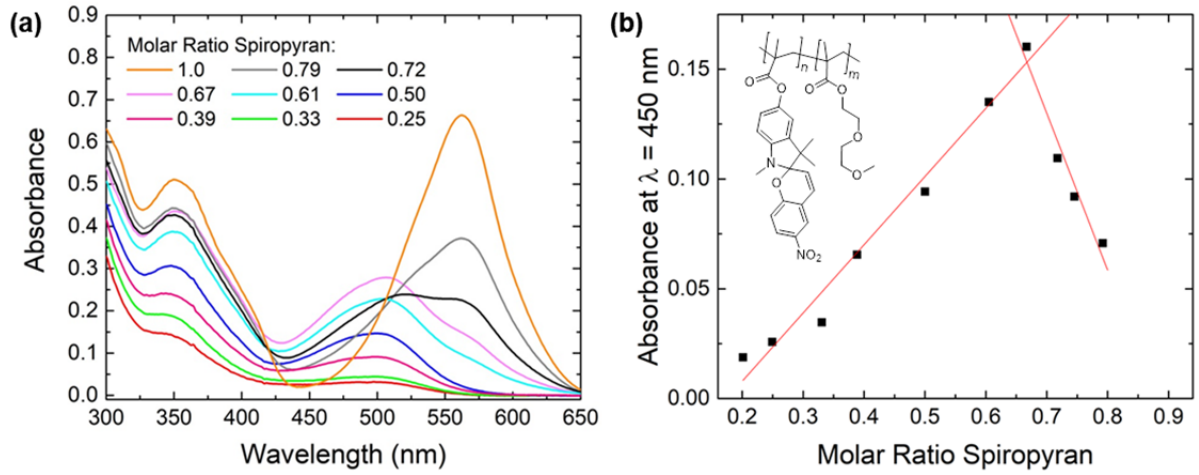


**Figure 5.2.** Evaluating stoichiometry of P(DEGMEMA-SPMA) with $Co(NTf_2)_2$ using the method of continuous variations (from Chapter 3). (a) UV-Vis absorption spectra of solutions containing varying ratios of SP/$Co(nTf)_2$. Each solution was exposed to 365 nm UV light for 2 minutes immediately prior to data acquisition to activate MC. (b) Job plot of the MC-Co complex evaluated at 450 nm.

In this chapter we explore diffusion ordered spectroscopy (DOSY) as an alternative technique for evaluating the stoichiometry of MC-metal complexes. For this study we focus our attention to SP compounds without a nitro electron withdrawing substituent on the chromene ring (SPs 2-5 in Scheme 5.2). SPs lacking a strong electron withdrawing group on the chromene ring are very unstable in their ring-open state when no coordinating species are present (as demonstrated in Chapter 4). Hence, we assume that all MC isomers produced when mixing SPs 2-5 with metal salts are coordinated to metal ions. The UV-Vis spectrum of Figure 5.3 strongly supports this hypothesis, as it shows only one peak corresponding to the MC-Co(II) of SP2. The absence of un-complexed MC greatly simplifies our analyses.

The purpose of this study is to determine the stoichiometry of transition metal complexes of MC without a chelating group. In this way, the data presented here is an extension to the rheological data presented in Chapter 3. SP2 and SP3 were chosen for this study because they are virtually identical in structure to SP1 (the monomer of poly(DEGMEMA-SPMA)), except for the absence of the nitro substituent. The assumption here is that SP2 and SP3 will produce

complexes of similar stoichiometry as SP1. Although SP4 and SP5 are not the primary focus of this study, their DOSY spectra provide useful information for our analyses of SP2 and SP3, and are also of interest moving forward because they are both mechanophores. Finally, in addition to DOSY spectroscopy, we determine the chemical shifts of all protons in SP3 using a combination of 2D COSY, NOESY, HSQC and HMBC, and we explore NOESY as a potentially complimentary method to detect associative interactions between two or more MC molecules.

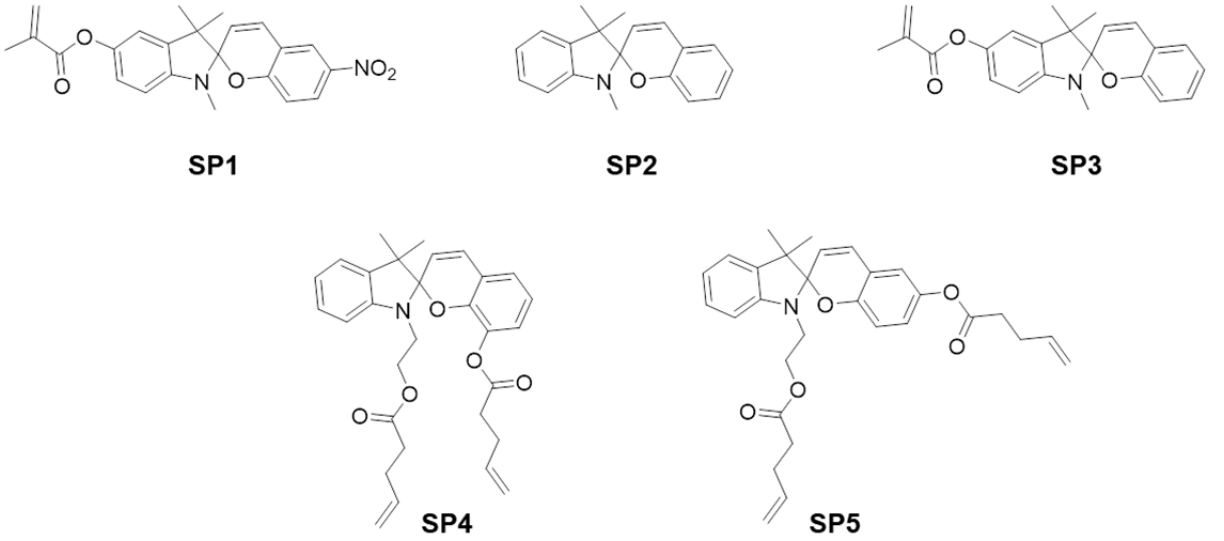


**Scheme 5.2.** Nomenclature for the different SP compounds discussed in this chapter

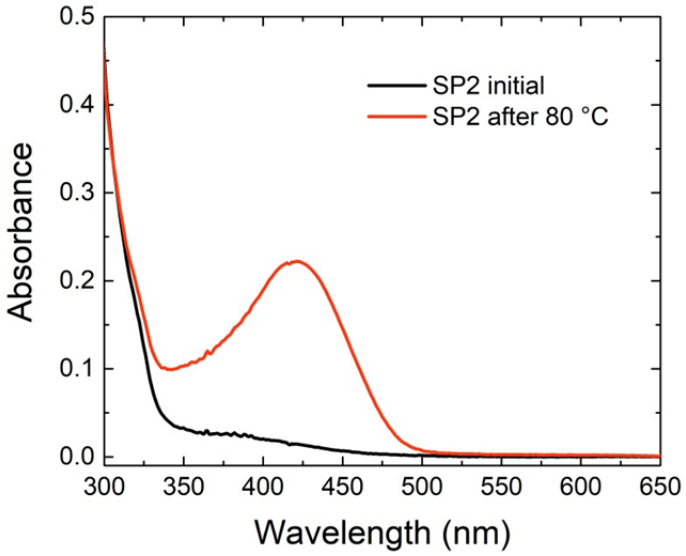


**Figure 5.3.** UV-Vis spectra before and after thermal equilibration of solution containing 0.333 mM SP2 and 0.166 mM $Co(NTf_2)_2$ (i.e. 2:1 SP:$Co(NTf_2)_2$) in propylene carbonate. Concentration, solvent and procedure for thermal equilibration are identical to those used in Figure 5.1a. Unlike SP1 in poly(DEGMEMA-SPMA), there is only one peak in the visible range after thermal activation of MC. The peak position ($\lambda \approx 420$ nm) is significantly blue-shifted from the 550-650 nm range typical for un-complexed MC, indicating that all MC in this solution is coordinated to Co(II) ions.

## 5.2 Inferring the stoichiometry of MC-metal complexes from their diffusivities

The diffusion coefficient is directly related to a compound's size and shape, and therefore, provides information about a compound's molecular weight and other physicochemical phenomena such as the formation of dimers or clusters. In dilute (~mM) solutions containing a solute of roughly spherical shape, the hydrodynamic radius of the solute can be estimated by:

$$D = \frac{k_B T}{f} \qquad 5.1$$

where $k_B$ is Boltzmann's constant, $T$ is the absolute temperature, and $f$ is the hydrodynamic friction factor. For a hard sphere diffusing in laminar flow, $f = 6\pi\eta r_s$, where $\eta$ is the solvent viscosity and $r_s$ is the hard sphere hydrodynamic radius. In cases where molecules are aspherical, researchers may use the modified Stokes-Einstein equation [9]:

$$D = \frac{k_B T}{c\pi\eta r_h f_h} \quad 5.2$$

where c is the size factor, which relates to the size of the diffusing species with respect to the solvent, and $f_h$ is the shape factor, which represents deviations from the spherical approximation. When the solute is greater than 5 times larger than the solvent (as is the case for SP in the solvents used in our experiments), the size factor, c has been shown to be roughly equal to 6. Furthermore, for certain ellipsoidally shaped supramolecular complexes, it has been found that the shape factor $f_h$ varies from about 1 to 1.14. In many cases, $f = 6\pi\eta r_s$ has been deemed a reasonable approximation for estimating molecular size [9], but for small molecules, any deviations from this quantity can produce significant errors.

Based on the dilute, hard-sphere approximation, the ratio of diffusivities of two compounds is inversely proportional to the cube root of their relative hydrodynamic volumes, which, as shown by Chapman and coworkers is directly proportional to their relative molecular weights [10]. Thus, we use the following relation to estimate the change in molecular weight when SP switches to a MC-metal complex:

$$\frac{MW_{MC}}{MW_{SP}} = \frac{V_{MC}}{V_{SP}} = \left(\frac{D_{SP}}{D_{MC}}\right)^3 \quad 5.3$$

This relation assumes that un-complexed MC is roughly the same shape and size as SP. In this chapter, we use the relative diffusivities of SP and MC to distinguish changes in molecular weight upon formation of MC-metal complexes. If the hard sphere model sufficiently approximates our system, then in theory, if a divalent metal ion bridges two MC molecules, the molecular weight should increase by roughly a factor of two.

## 5.3 Introduction to diffusion ordered spectroscopy (DOSY)

DOSY reports diffusion coefficients of individual resonances in a $^{1}$H NMR spectrum. The heart of DOSY is in a pair of gradient radio frequency pulses, but typically other pulses are added to compensate for convection or suppress solvent signals. The most basic DOSY pulse sequence is illustrated in Figure 5.4 [11]. The DOSY sequence begins with the standard 90° RF pulse, causing spins to align and precess as in a normal $^{1}$H NMR experiment. After the 90° pulse, a pulse possessing a gradient in its z-direction field strength twists the x-y magnetization into a corkscrew shape oriented along the z-direction. The degree of the corkscrew effect depends on the strength of the gradient (red shows the effect of a weak gradient and blue shows the effect of a strong gradient in Figure 5.4). This first pulse is called the "encoding" gradient pulse, as it encodes the spins into the corkscrew shape. The second gradient pulse is the "decoding" gradient pulse. If species do not diffuse at all between the encoding and decoding pulses, the decoding pulse realigns the spins exactly to their original positions, resulting in full recovery of the resonance signal. However, if sufficient time is allowed for species to diffuse (in NMR terminology this is called the "diffusion delay", $\Delta$), partial translation of species from their original positions in the z-direction results in imperfect realignment. Consequently, the resonance signal is attenuated. The amount of signal attenuation is a function of both the gradient strength and the diffusivities of the diffusing species. Higher gradient strengths create tighter corkscrews and increase the probability that the signals will be lost during mixing. The faster a molecule diffuses, the less magnetization will be recovered after the second gradient pulse, also resulting in a more attenuated signal. To differentiate signals based on their diffusion coefficients, an array of spectra are taken at different gradient pulse strengths. The intensity

change of the NMR signal is a function of the diffusion time, diffusivity, and gradient strength, according to the following relation [12]:

$$I = I_0 \exp(-D\gamma^2 g^2 \delta^2 (\Delta - \frac{\delta}{3}) \quad 5.4$$

where I is the observed intensity, $I_0$ is the unattenuated signal intensity, D is the diffusion coefficient, γ is the gyromagnetic ratio of the observed nucleus, g the gradient field strength, δ the length of the gradient, and Δ the diffusion delay time between the first and second gradient pulses. The intensity of signals are evaluated either by peak integration or peak height. In our study we evaluate signals based on their integration. To extract the diffusion coefficient for a particular resonance signal, a plot of I as a function of gradient strength is fit with equation 5.4.

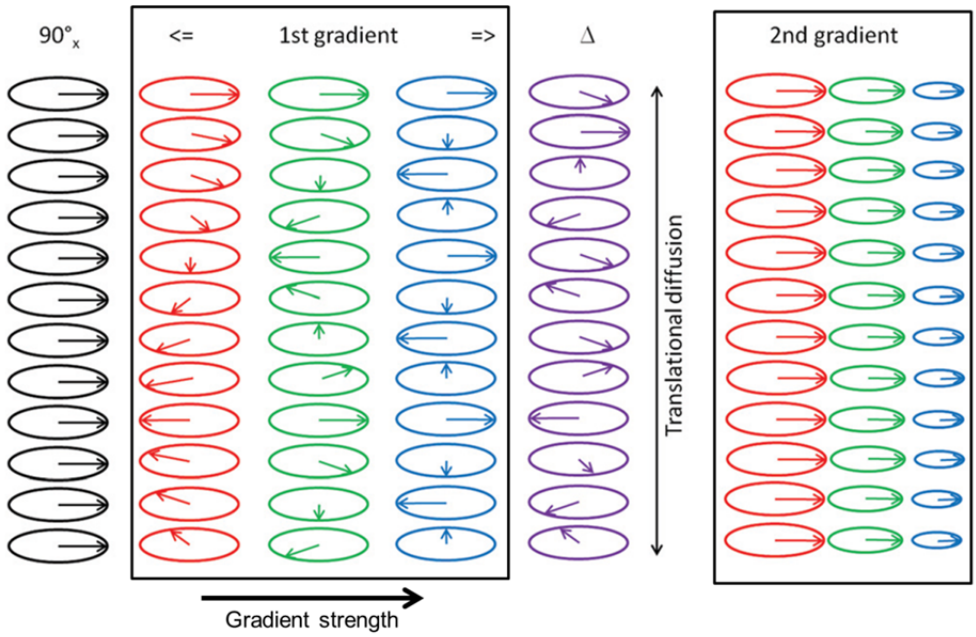


**Figure 5.4.** Schematic of a simple spin-echo DOSY pulse sequence. A standard 90° pulse aligns the magnetization in the x-y plane. The first gradient pulse encodes a corkscrew shape of the magnetization in the z-direction. The degree of the corkscrew effect depends on the gradient pulse strength (2% gradient red, 50% greenm 95% blue). The sample diffuses in the z-direction during a specified diffusion delay time, Δ, between the two gradient pulses. Finally, a second gradient pulse decodes the corkscrew orientation of the magnetizations back to their original alignments, but diffusion of the spins means that only part of the original signal is recovered. The amount of signal attenuation is dependent on both the diffusivity as well as the strength of the gradient pulse. Figure adapted from [11].

## 5.4 Experimental Methods

### *5.4.1 General Information*

The synthesis of SP1 is presented in Chapter 3 and the synthesis of SP4 is presented in Chapter 4. 5-methoxy-2,3,3-trimethyl-3H-indole was purchased from Biosynth. Cobalt bis(trifluoromethylsulfonyl)imide ($Co(nTf)_{2)}$ and copper bis(trifluoromethylsulfonyl)imide ($Cu(nTf)_2$) were purchased from TCI Chemicals. Sodium bis(trifluoromethylsulfonyl)imide was purchased from Alfa Aesar. All other chemicals and solvents were purchased from either Sigma Aldrich or Alfa Aesar. All chemicals and solvents were used without further purification. $^1$H and $^{13}$C 1D NMR spectra reported for the as-synthesized compounds were taken on a 500 MHz Carver B500 spectrometer. All 1D and 2D NMR experiments were measured on a Varian 750 MHz spectrometer. All $^1$H NMR data are reported in δ units, in parts per million (ppm), and were measured relative to the signals of residual acetone (2.05 ppm), DMSO (2.50 ppm), or chloroform (7.24 ppm) in deuterated S3 solvent. All $^{13}$C NMR spectra were measured in deuterated solvents and are reported in ppm relative to the signals for residual acetone (206.26 and 29.84 ppm), DMSO (39.52 ppm), or chloroform (77.23 ppm).

### *5.4.2 Synthetic procedures*

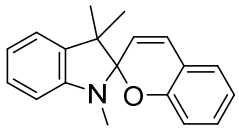


***SP2:*** *1',3',3'-trimethylspiro[chromene-2,2'-indoline]:* 1.09 g (8.926 mmol) of salicylaldehyde, 2.889 g (9.593 mmol) of 1,2,3,3-tetramethyl-3H-indol-1-ium iodide, and 1.13 g (11.167 mmol) of trimethylamine were dissolved in 43 ml of anhydrous ethanol. The solution was refluxed at 100 °C for 6 hours. Solvent was evaporated *in vacuo* and the mixture was re-dissolved in 30 ml of dichloromethane. Combined organics were washed with 0.1 M HCl (3 x 10 ml), 0.15 M

NaOH (1 x 30 ml) and brine (1 x 30 ml). The organic layer was dried over $MgSO_4$ and purified via flash chromatography over silica (3% EtOAc/hexanes). Solution was concentrated *in vacuo* to obtain the title product as a yellow solid (1.75 g, 6.31 mmol, 70.7%). $^1$H NMR (500 MHz, Acetone-$d_6$) δ 7.17 – 7.06 (m, 4H), 6.99 (d, $J$ = 10.2 Hz, 1H), 6.81 (dtd, $J$ = 19.1, 7.5, 1.0 Hz, 2H), 6.63 (d, $J$ = 8.1 Hz, 1H), 6.55 (d, $J$ = 7.7 Hz, 1H), 5.77 (d, $J$ = 10.2 Hz, 1H), 2.71 (s, 3H), 1.28 (s, 3H), 1.15 (s, 3H). $^{13}$C NMR (126 MHz, Acetone-$d_6$) δ 155.56, 149.37, 137.74, 130.76, 130.48, 128.50, 127.91, 122.40, 121.18, 120.38, 120.10, 120.06, 115.52, 107.81, 105.29, 52.55, 29.26, 26.37, 20.58.

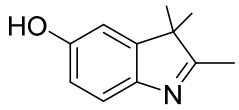


*2,3,3-trimethyl-3H-indol-5-ol:* 25 g (132 mmol) of 5-methoxy-2,3,3-trimethyl-3H-indole was dissolved in 450 ml of 48% aqueous HBr and refluxed at 120 °C for 4 hours under argon. After cooling to room temperature, the solution was added to 600 ml of DI water, partially neutralized with $Na_2CO_3$ and brought to pH ~7-8 with $NaHCO_3$. The precipitated solid was filtered and washed with DI water to yield the title product as an off-white solid (23.1 g, 131.8 mmoles, 99.8%). $^1$H NMR (500 MHz, DMSO-$d_6$) δ 9.27 (s, 1H), 7.18 (d, $J$ = 8.2 Hz, 1H), 6.77 (d, $J$ = 2.4 Hz, 1H), 6.64 (dd, $J$ = 8.2, 2.4 Hz, 1H), 2.12 (s, 3H), 1.18 (s, 6H). $^{13}$C NMR (126 MHz, DMSO-$d_6$) δ 183.93, 155.31, 147.48, 145.85, 119.49, 113.45, 109.17, 53.02, 22.76, 14.81.

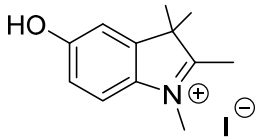


*5-hydroxy-1,2,3,3-tetramethyl-3H-indol-1-ium iodide*. 16.39 g (93.52 mmol) of 2,3,3-trimethyl-3H-indol-5-ol was dissolved in 400 ml of 1:1 toluene/acetonitrile in a one-necked

round bottom flask. 26.5 g (186.7 mmol, 2 equiv) of iodomethane was added and the solution was refluxed at 90 °C for 14 hours. The precipitated solid was filtered and washed copiously with ethanol and diethyl ether to yield **1** as a white, sand-textured powder (28.914 g, 91.16 mmol, 97.48%). $^{1}$H NMR (500 MHz, DMSO-$d_6$) δ 7.69 (d, $J$ = 8.7 Hz, 1H), 7.12 (d, $J$ = 2.4 Hz, 1H), 6.93 (dd, $J$ = 8.7, 2.4 Hz, 1H), 3.91 (d, $J$ = 1.2 Hz, 3H), 2.70 (d, $J$ = 1.3 Hz, 3H), 1.47 (s, 6H). $^{13}$C NMR (126 MHz, DMSO-$d_6$) δ 191.89, 158.94, 143.72, 134.15, 116.14, 115.01, 110.31, 53.47, 34.79, 21.91, 13.98.

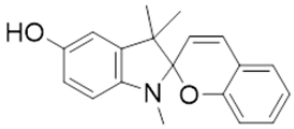


*1',3',3'-trimethylspiro[chromene-2,2'-indolin]-5'-ol.* 6.024 g (19 mmol) of 5-hydroxy-1,2,3,3-tetramethyl-3H-indol-1-ium iodide, 2.651 g (21.7 mmol) of salicylaldehyde and 2.48 g (24.5 mmol) of trimethylamine were dissolved in 76 ml of anhydrous ethanol. Argon was bubbled through the solution for 15 minutes and the solution was refluxed at 100 °C for 10 hours. Solution was concentrated *in vacuo* and dry loaded onto a silica column, which was then washed with hexanes. Product was purified using a gradient of 100% dichloromethane to 1% methanol/dichloromethane as eluent to obtain the title product as a pale yellow solid (3.209 g, 10.94 mmol, 57.5%). $^{1}$H NMR (500 MHz, DMSO-$d_6$) δ 8.65 (s, 1H), 7.14 (dd, $J$ = 7.5, 1.7 Hz, 1H), 7.08 (ddd, $J$ = 8.2, 7.4, 1.7 Hz, 1H), 6.97 (dd, $J$ = 10.3, 0.7 Hz, 1H), 6.81 (td, $J$ = 7.4, 1.2 Hz, 1H), 6.65 (dt, $J$ = 8.2, 0.9 Hz, 1H), 6.56 (d, $J$ = 2.4 Hz, 1H), 6.50 (dd, $J$ = 8.1, 2.5 Hz, 1H), 6.34 (d, $J$ = 8.2 Hz, 1H), 5.72 (d, 1H), 2.55 (s, 3H), 1.12 (d, $J$ = 42.5 Hz, 6H). $^{13}$C NMR (126 MHz, DMSO-$d_6$) δ 154.11, 150.94, 140.64, 137.55, 129.68, 129.08, 126.84, 120.00, 119.36, 118.67, 114.25, 112.75, 109.79, 107.23, 104.23, 51.44, 28.99, 25.56, 19.85.

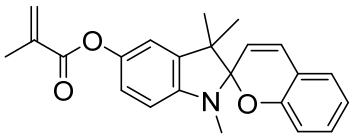

***SP3****: 1',3',3'-trimethylspiro[chromene-2,2'-indolin]-5'-yl methacrylate.* 3.209 g (10.94 mmol) of 1',3',3'-trimethylspiro[chromene-2,2'-indolin]-5'-ol and 0.668 g (5.47 mmol) of DMAP were dissolved in 22 ml of anhydrous dichloromethane. 3.37 g (21.86 mmol) of methacrylic anhydride was added dropwise and the reaction proceeded at room temperature for 12 hours. Solution was washed with concentrated $Na_2CO_3$ (3 x 20 ml) and brine (3 x 20 ml) to obtain the crude product as a yellow oil. Crude product was purified by chromatography over silica (0.3-0.8% EtOAc/hexanes). Solution was concentrated *in vacuo* to obtain a pale yellow solid 1.13 g (3.13 mmol, 28.6%). *Note, we suspect we would have obtained much higher yield if we had used a fresh bottle of methacrylic anhydride. δ 7.11 (td, *J* = 7.7, 1.7 Hz, 1H), 7.06 (dd, *J* = 7.5, 1.7 Hz, 1H), 6.92 (ddt, *J* = 8.2, 2.4, 1.2 Hz, 1H), 6.89 – 6.80 (m, 3H), 6.73 (d, *J* = 8.2 Hz, 1H), 6.49 (dd, *J* = 8.3, 1.7 Hz, 1H), 6.39 – 6.31 (m, 1H), 5.74 (p, *J* = 1.5 Hz, 1H), 5.68 (dd, *J* = 10.2, 1.5 Hz, 1H), 2.73 (d, *J* = 1.5 Hz, 3H), 2.09 (t, *J* = 1.3 Hz, 3H), 1.30 (d, *J* = 1.8 Hz, 3H), 1.20 (d, *J* = 1.7 Hz, 3H). $^{13}$C NMR (126 MHz, Chloroform-*d*) δ 166.65, 154.48, 146.08, 144.00, 138.04, 136.32, 129.87, 129.60, 126.80, 126.78, 120.17, 120.03, 119.16, 118.81, 115.54, 115.08, 106.79, 104.55, 51.87, 29.22, 25.83, 20.22, 18.59.

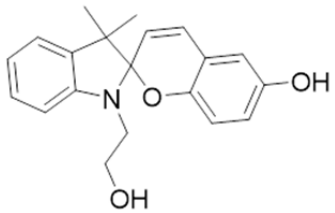

*1'-(2-hydroxyethyl)-3',3'-dimethylspiro[chromene-2,2'-indolin]-6-ol*. 11.293 g (33.6 mmol) of 1-(2-hydroxyethyl)-2,3,3-trimethyl-3H-indol-1-ium iodide, 4.8936 g (35.43 mmol) of 2,5-hydroxybenzaldehyde, and 4.8 g (47.4 mmol) of trimethylamine were dissolved in 110 ml of

anhydrous ethanol. The solution was bubbled with argon for 15 minutes and refluxed at 100 °C for 6 hours. The solution was concentrated *in vacuo* and redissolved in 100 ml of chloroform. Combined organics were was with DI water (3 x 100 ml), saturated sodium bicarbonate (3 x 100 ml), saturated aqueous ammonium chloride (3 x 100 ml), brine (1 x 1100 ml), dried over anhydrous $Na_2SO_4$, filtered and concentrated *in vacuo* to obtain the title compound as a pinkish-pale yellow powder (5.25 g, 16.2 mmol, 48.3%).

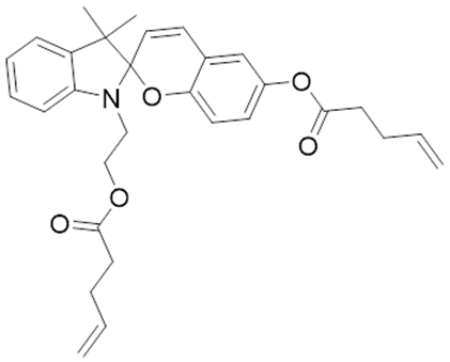


***SP5:*** *3',3'-dimethyl-1'-(2-(pent-4-enoyloxy)ethyl)spiro[chromene-2,2'-indolin]-6-yl pent-4-enoate.* 2.0486 g (6.34 mmol) of 1'-(2-hydroxyethyl)-3',3'-dimethylspiro[chromene-2,2'-indolin]-6-ol and 0.775 g (6.34 mmol) of DMAP were dissolved in 60 ml of chloroform. 3 g (16.28 mmol) of pentenoic anhydride was added dropwise and the reaction proceeded for 2 hours at room temperature (at which point TLC shows reaction is nearly complete). Solution was concentrated *in vacuo* and purified by column chromatography over silica (10% EtOAc/hexanes) to obtain the title compound as a transparent, pale yellow oil (1.743 g, 56.4%). *Note, an old bottle of pentenoic anhydride was used for this reaction. In general, with fresher pentenoic anhydride (< 12 months old), less excess is required and higher yields are likely obtainable (see synthesis of "SP0" in Chapter 4. $^1$H NMR (500 MHz, Acetone-$d_6$) δ 7.16 – 7.08 (m, 2H), 6.98 (dd, $J$ = 10.3, 0.7 Hz, 1H), 6.93 (d, $J$ = 2.8 Hz, 1H), 6.85 (dd, $J$ = 8.7, 2.8 Hz, 1H), 6.81 (td, $J$ = 7.4, 1.0 Hz, 1H), 6.72 (dd, $J$ = 7.8, 0.8 Hz, 1H), 6.64 (dd, $J$ = 8.7, 0.6 Hz, 1H), 5.98 – 5.86 (m,

2H), 5.80 (ddt, $J$ = 16.6, 10.2, 6.3 Hz, 1H), 5.13 (dq, $J$ = 17.2, 1.7 Hz, 1H), 5.05 – 4.98 (m, 2H), 4.96 – 4.89 (m, 1H), 4.30 – 4.17 (m, 2H), 3.55 (dt, $J$ = 15.1, 6.5 Hz, 1H), 3.39 (dt, $J$ = 15.1, 6.0 Hz, 1H), 2.64 (t, $J$ = 7.3 Hz, 2H), 2.51 – 2.39 (m, 2H), 2.42 – 2.33 (m, 2H), 2.35 – 2.24 (m, 2H), 1.28 (s, 3H), 1.14 (s, 3H). $^{13}$C NMR (126 MHz, Acetone-$d_6$) δ 173.16, 172.18, 148.33, 138.09, 137.88, 137.28, 129.90, 128.50, 123.79, 122.67, 121.72, 120.82, 120.24, 120.12, 116.16, 116.09, 115.84, 107.47, 105.80, 63.27, 53.20, 43.38, 34.11, 34.07, 29.77, 29.70, 26.38, 20.53.

*5.4.3 Diffusion ordered spectroscopy (DOSY)*

DOSY experiments were performed on a Varian Unity Inova 750 MHz spectrometer capable of performing pulsed field gradient (PFG) spin-echo diffusion measurements. Solutions were prepared in acetone-$d_6$, methanol-$d_4$, THF-$d_8$ or DMSO-$d_6$ and thermally equilibrated at 25 ºC for 48 hours prior to data collection. Experiments were performed at 25 ºC. 90 degree pulse widths were set using the 1D $^1$H FID prior to performing experiments. DOSY was performed using a convection compensated gradient stimulated echo pulse sequence with a spectral width of 8992.8 Hz, d1 value of 2 s, diffusion gradient length of 2 ms, diffusion delay of 30.0 ms, and an either a 15 step array or 18 step array of gradients varying from 2.79-42.88 or 2.79-55.74 G/cm, respectively. The baselines and phases of all spectra were corrected prior to data processing. The data were processed and the diffusion coefficients extracted by fitting the arrayed data using the VNMR software.

## 5.5 $^1$H NMR and 2D DOSY results

Prior to performing DOSY, we performed 1D NOESY to ensure there was no exchange between SP and MC during the diffusion delay of the DOSY experiments. If exchange was

measured this would significantly complicate our DOSY analysis. In all of our samples NOESY spectra showed no exchange for a mixing time of 500 ms. Because a diffusion delay of only 30 ms is used in our DOSY experiments, our measurements are guaranteed not to be complicated by exchange between SP and MC isomers. A representative example of a DOSY array of a solution of 150 mM SP2 with a 10:1 ratio of SP2:Cu(nTf)$_2$ in acetone-$d_6$ is shown in Figure 5.5a. This spectrum contains peaks from both SP and MC. Figure 5.5b plots the N-methyl peaks of SP2 and MC2 as a function of gradient strength. At quick glance, the signal from SP attenuates faster than that of MC, suggesting that SP diffuses faster in its ring-closed state. By analyzing all the $^1$H NMR signals and fitting their DOSY plots with equation 5.3, we obtain a 2D DOSY spectrum, which plots the diffusion coefficient of each resonance peak (Figure 5.6).

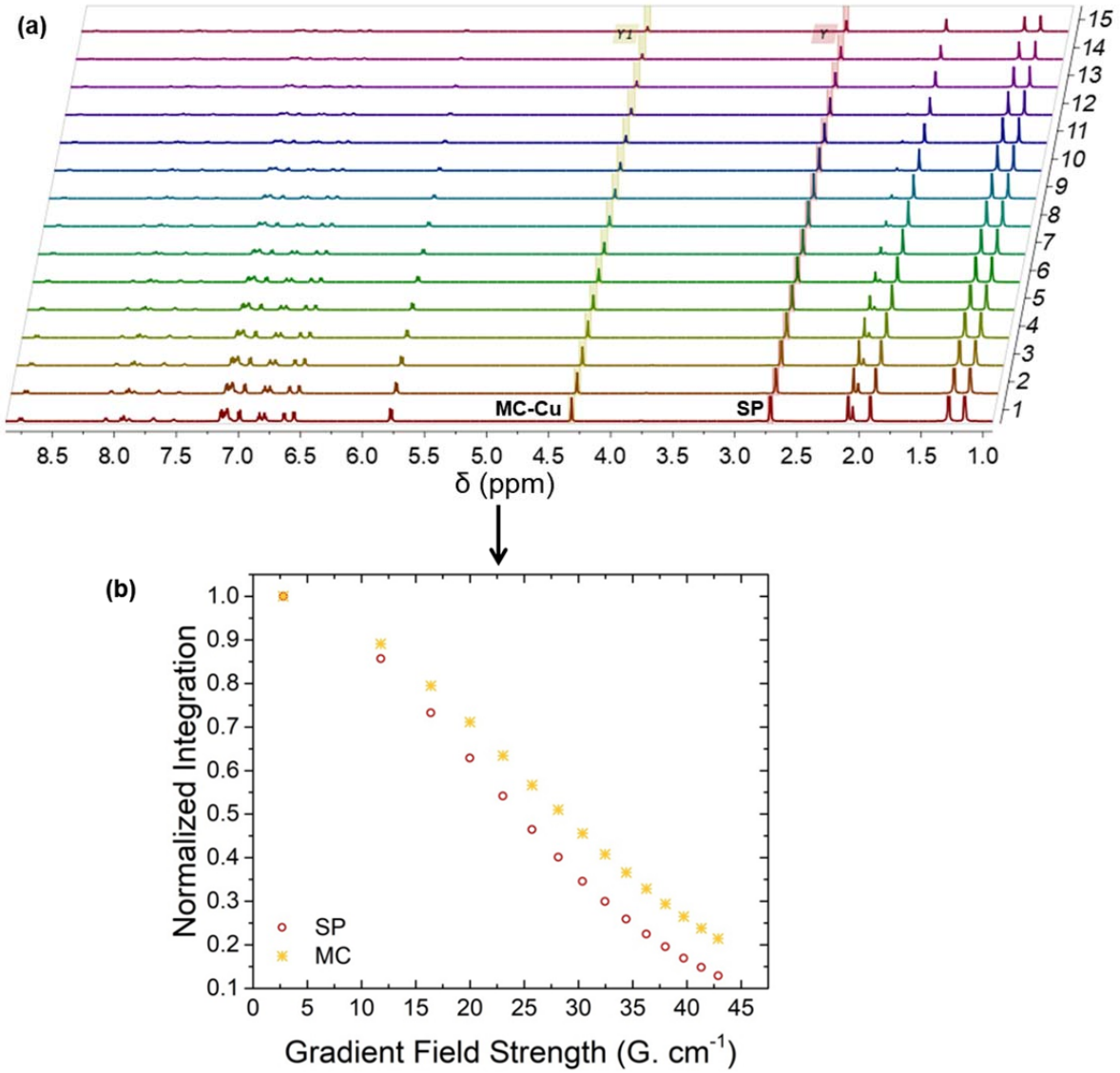


**Figure 5.5.** (a) DOSY array of 150 mM SP2 containing 2:1 SP:Cu($NTf_2$)$_2$ in acetone-$d_6$. (b) Plot of the integrated intensities of the N-methyl peaks of SP2 (red circles) and MC2 (yellow stars) as a function of gradient field strength. Experimental details are provided in Section 5.4.3.

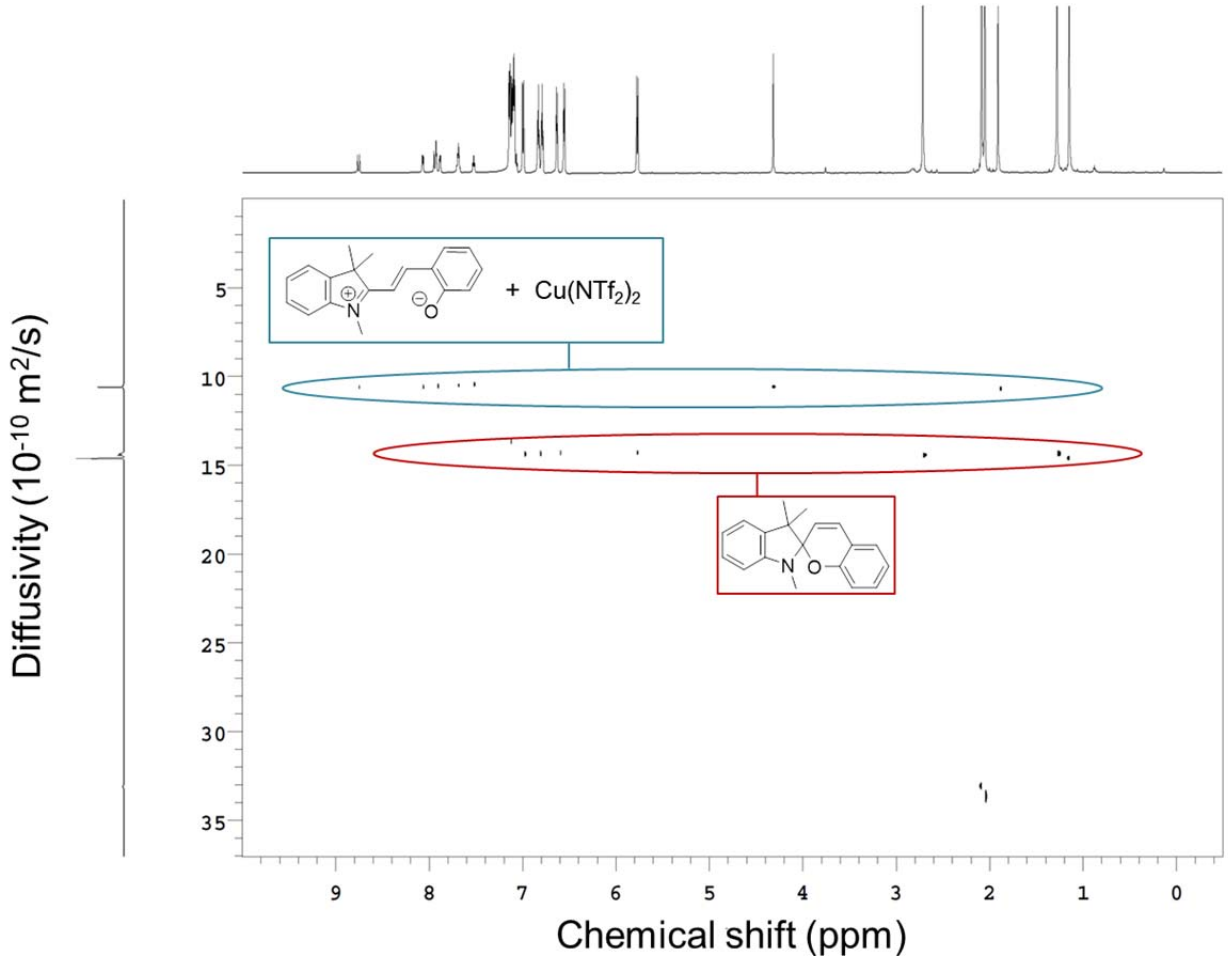


**Figure 5.6.** DOSY spectrum of 150 mM SP2 containing 2:1 SP:$Cu(NTf_2)_2$ in acetone-$d_6$. Peaks circled in red correspond to the ring-closed SP state. Peaks circled in blue correspond to the ring-open MC state. $Cu(NTf_2)_2$ is grouped with the MC peaks only to indicate that the presence of Cu(II) ions is what produces the MC state. The fast diffusing species at 2.05 ppm is acetone. Experimental details are provided in Section 5.4.3.

To elucidate the stoichiometry of MC-metal complexes, we look at two key pieces of information: the relative concentration of MC with respect to metal ions (MC:ion in Table 5.1), and the ratio of diffusion coefficients $D_{SP}/D_{MC}$. We compare the data for $Na(NTf_2)$ and $H^+$, which are expected to only form monomeric MC-Na and $MCH^+$ species, to $Cu(NTf_2)_2$ and $Co(NTf_2)_2$, which may bridge two or more MC molecules. The $^1$H NMR and 2D DOSY data are summarized in Table 5.1.

**Table 5.1.** DOSY results. SP:ion is the ratio of SP to salt or acid in each sample. MC:ion ratio was measured by integrating the $^1$H peaks of SP and MC. $D_{SP}$ and $D_{MC}$ are the average diffusion coefficients of SP and MC, respectively. And $D_{SP}/D_{MC}$ is the ratio of diffusion coefficients.

| SP Type | Solvent | SP conc. | Ion | SP:ion | MC:ion | $D_{SP}$ ($10^{-10}$ m/s$^2$) | $D_{MC}$ ($10^{-10}$ m/s$^2$) | $D_{SP}/D_{MC}$ |
|---|---|---|---|---|---|---|---|---|
| SP2 | Acetone-$d_6$ | 150 mM | Cu(II) | 11:1 | 1.87:1 | 14.42 | 10.59 | 1.36 |
| | Acetone-$d_6$ | 150 mM | Co(II) | 10:1* | 1.52:1* | 14.20 | 10.72 | 1.32 |
| | Acetone-$d_6$ | 150 mM | Na(I) | 2:1 | 0.062:1 | 13.17 | 9.89 | 1.33 |
| | Acetone-$d_6$ | 150 mM | $H^+$ (TFA) | ~10:1 | ~1:1 | 14.55 | 10.79 | 1.35 |
| | Acetone-$d_6$ | 20 mM | Cu(II) | 2:1 | 1.44:1 | 15.62 | 11.51 | 1.36 |
| | Acetone-$d_6$ | 20 mM | Na(I) | 1:1 | 0.039:1 | 15.46 | 11.45 | 1.35 |
| | Acetone-$d_6$ | 20 mM | $H^+$ (TFA) | 2:1 | 0.724:1 | 15.70 | 11.70 | 1.34 |
| | Methanol-$d_4$ | 20 mM | Cu(II) | 2:1 | 0.640:1 | 10.05 | 7.39 | 1.36 |
| | Methanol-$d_4$ | 20 mM | Na(I) | 1:1 | 0.042:1 | 10.38 | 7.75 | 1.34 |
| SP3 | THF-$d_8$ | 20 mM | Cu(II) | 2:1 | 1.16:1 | 8.20 | 5.86 | 1.40 |
| | THF-$d_8$ | 20 mM | Na(I) | 1:1 | 0.036:1 | 8.27 | 6.20 | 1.33 |
| | DMSO-$d_6$ | 20 mM | Cu(II) | 2:1 | 0 | - | - | - |
| | DMSO-$d_6$ | 20 mM | Na(I) | 1:1 | 0.036:1 | 2.08 | 1.74 | 1.20 |
| SP4 | Acetone-$d_6$ | 150 mM | Cu(II) | 2:1 | 0.210:1 | 10.10 | 8.40 | 1.20 |
| | Acetone-$d_6$ | 80 mM | $H^+$ (TFA) | ~2:1 | ~0.22:1 | 11.21 | 9.43 | 1.19 |
| SP5 | Acetone-$d_6$ | 150 mM | Cu(II) | 2:1 | 0.305:1 | 9.30 | 8.26 | 1.13 |

*Some solids precipitated after adding $Co(NTf_2)_2$ stock solution to the SP stock solution

The first five columns of Table 5.1 show the conditions used for each sample (type of SP, solvent, concentration of SP, the type of ions introduced to the solution, and the ratio of SP to ions in solution. Here, we note the primary solvent of choice for our studies was acetone-$d_6$; however, with SP3 we used THF-$d_8$ because we found SP3 to be insoluble in acetone. The last five columns include the ratio of MC to ions in solution (MC:ion), as determined by integrating the $^1$H NMR peaks of MC, and summarize the results from DOSY measurements.

The MC:ion ratios indicate that SP2 and SP3 interact only very weakly with Na(I), as the degree of activation is quite low. In addition, the degree of MC-Na activation is similar between SP2 and SP3, and appears to have little dependence on the polarity or electron donor character of the solvent. Because Na(I) ions typically bind to ligands (e.g. carboxylates) with 1:1 stoichiometry, we assume that MC-Na is a 1:1 complex. Based on several studies on the acidochromism of spiropyrans [13, 14], we also expect 1:1 binding between MC and protons. A nearly 1:1 MC:$H^+$ ratio is observed when mixing trifluoroacetic acid with SP2 in acetone., indicating that SP interacts with protons much more strongly than with Na(I) ions.

When using NMR to studying MC complexation with paramagnetic metal ions such as Cu(II) and Co(II), we found that the concentration of metal ions had to be kept relatively low (≤ 20 mM) in order to avoid significant distortion of the NMR signals. Here, we study two cases: in one, we have a 150 mM solution of SP and a large excess (~10:1 ratio) of SP with respect to the transition metal salt. In the other, we have a 20 mM solution of SP with a 2:1 ratio of SP to metal salt. Evidently, the activation of MC is drastically different with transition metal salts than with Na(I) and $H^+$ ions. With $Cu(NTf_2)_2$ we find that nearly 2 MC molecules are generated for every Cu(II) ion in the 150 mM acetone solution. In the 20 mM acetone solution a bit less MC is activated, but nevertheless, the MC to Cu(II) ratio is significantly greater than 1:1. This suggests

that some form of higher order (e.g. 2:1) complexes are produced with Cu(II) in acetone. Unlike with Na(I), the degree of MC activation with Cu(II) is highly dependent on the nature of the solvent. When acetone is replaced with methanol, which has both greater polarity ($\varepsilon_{methanol\text{-}d4}$ = 32.7 vs. $\varepsilon_{acetone\text{-}d6}$ = 20.7) and electron donor character, the degree of MC activation with Cu(II) is significantly reduced. In the case of DMSO, which has the highest polarity ($\varepsilon_{DMSO\text{-}d6}$ = 46.7) and electron donor character, virtually no MC is observed in solutions of either SP2 or SP3. $Co(NTf_2)_2$ also appears to activate a much higher concentration of MC, but unlike with Cu(II), we find that MC precipitates out of solution upon adding $Co(NTf_2)_2$. This happens both with SP2 in acetone and SP3 in THF (Figure 5.7). It's important to note that $Co(NTf_2)_2$ on its own is highly soluble in both THF and acetone, so the precipitate is likely some form of an MC-Co complex. The behavior of SP2 and SP3 with Co(II) in acetone and THF absolutely warrants further investigation, as it is possible that under better controlled conditions, MC complex crystals may be obtained, which then can be analyzed by X-ray crystallography.

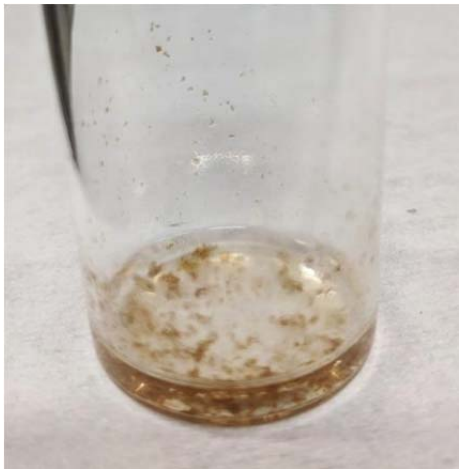

**Figure 5.7.** Precipitate formed in solution of 20 mM SP3 in THF containing 2:1 SP3: $Co(NTf_2)_2$. Bright orange solution formed upon heating, and solid precipitated along with decoloration of the solution within several minutes upon cooling to room temperature.

Despite the large variation in concentration of MC with different ions, the ratios of diffusivities, $D_{SP}/ D_{MC}$, are nearly identical in all samples, regardless of the solvent or valence of the ion. Therefore, we conclude that the MC-complexes in all samples have roughly the same molecular shape and size. Because $MCH^+$ and MC-Na almost certainly do not form dimers, we conclude that MC-Cu and MC-Co also are not dimeric species, and therefore, the MC-cation stoichiometry in all samples must be 1:1. This, unfortunately, opposes our theory in Chapter 3 that transition metal ions bridge multiple MC molecules. However, these results do not disprove our theory either, as the conditions here are different than in Chapter 3. The following section sheds more light on why transition-metal-ion bridging of MC is not observed in these DOSY experiments.

**5.6 2D correlation NMR reveals a surprising explanation for the DOSY results**

The $^1H$ NMR spectra of most of the samples shown in Table 5.1 were recorded with a 7860.5 Hz spectral width spanning from -0.49 to 9.99 ppm. It wasn't until we expanded the spectral window to 8223.6 Hz (spanning 0.13 to 10.98 ppm) that we discovered a singlet at about 10 ppm in the $^1H$ spectra of samples containing $Cu(NTf_2)_2$ and $Co(NTf_2)_2$ metal salts (Figure 5.8 and Figure 5.14, respectively). A full 2D NMR analysis, including homonuclear correlation spectroscopy (COSY), heteronuclear single quantum coherence spectroscopy (HSQC), heteronuclear multiple bond correlation spectroscopy (HMBC), and nuclear Overhauser effect spectroscopy (NOESY) (Figures 5.9-5.13) of the SP3/ $Cu(NTf_2)_2$ sample unequivocally reveals that the singlet at ~10 ppm corresponds to the phenolic proton of protonated MC-$H^+$. This is an unfortunate discovery because it greatly complicates our understanding of thermal complexation of SP with transition metal salts.

First, where do the protons come from? Acetone-$d_6$ and THF-$d_8$ are both aprotic solvents. The most likely source of protons is residual water coordinating to the transition metal salts; however, hexa-aqua complexes of Co(II) and Cu(II) are only weakly acidic (pKa = 9.65 and 8, respectively [15, 16]). It is worth noting here that a 100 mM solution of acetic acid (pKa = 4.75 in water) in acetone does not activate any observable MC-$H^+$. Therefore, the acidity of transition metals alone cannot explain the high concentrations of protonated merocyanine (~10 mM) with Co(II) and Cu(II). This revelation prompted us to look back at our results in chapter 4 with SP4 (which we referred to as "SP0" in the previous chapter). Fortunately, no protonated MC was detected in SP4 solutions containing $Mg(NTf_2)_2$, $Ca(NTf_2)_2$ or $Li(NTf_2)$ in acetone-$d_6$ (Figure 5.15 shows the extended $^1$H NMR spectral window with $Mg(NTf_2)_2$). Evidently, significant concentrations of $H^+$ are introduced only with Co(II) and Cu(II). It is unclear at this time whether protonation of MC competes with metal coordination or whether metal coordination and protonation are somehow coupled.

Though we do not understand the underlying mechanism, the transition-metal-assisted protonation of MC explains why the diffusivities of MC2 and MC3 in the presence of Co(II) and Cu(II) are roughly identical to the diffusivities with trifluoroacetic acid–in both cases we produce protonated MC-$H^+$! We conclude from these results that Co(II) and Cu(II) does not bridge MC2 and MC3 into dimeric or higher coordination number clusters like we originally expected. This suggests that all MC2 and MC3 species reported in Table 5.1 are monomeric; however, this doesn't take into account that greater than one MC is activated for each Cu(II) ion (according to $^1$H peak integrations). Thus, further studies are required to fully understand the mechanism of thermal activation of MC2 and MC3 with transition metal ions in acetone and THF.

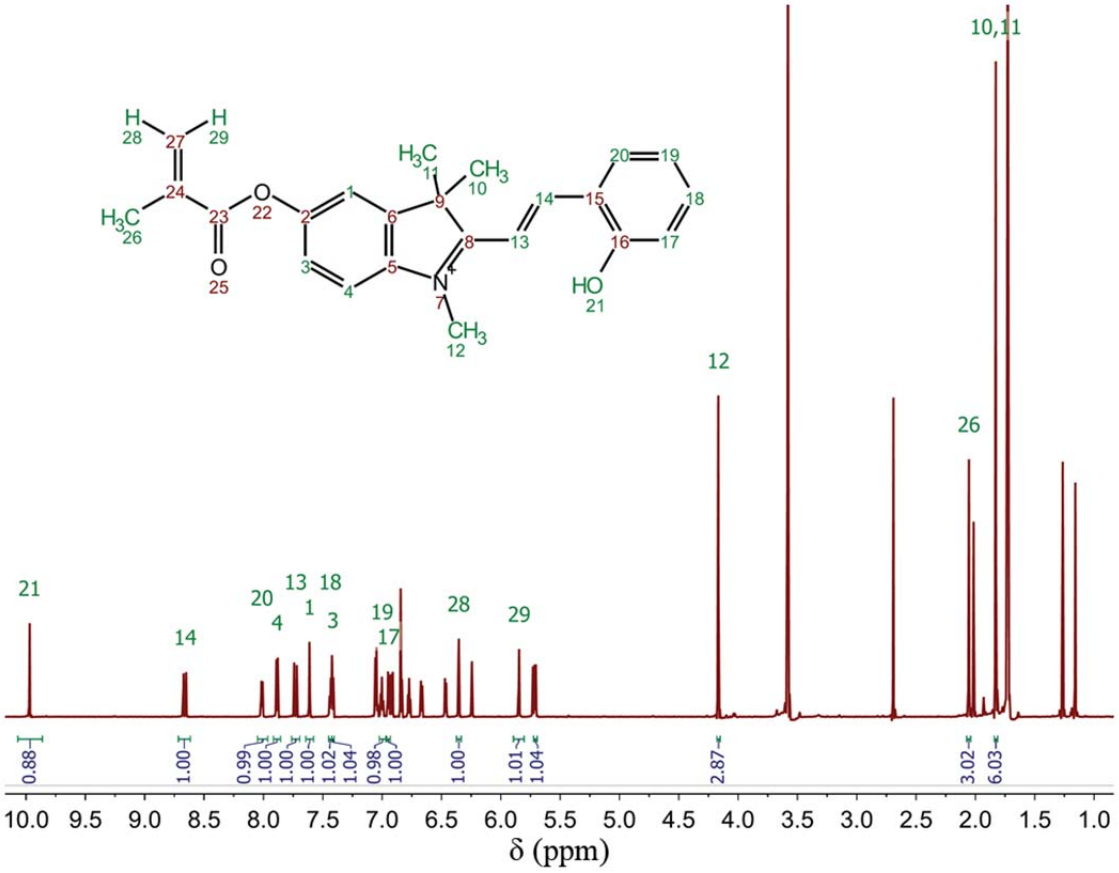


**Figure 5.8.** $^{1}$H NMR spectrum (749 MHz, THF-$d_8$) of 20 mM solution of SP3 with 2:1 SP3: $Cu(NTf_2)_2$. MC peaks were assigned according to the 2D spectra of Figures 5.11-5.15. Singlet peak at 9.97 ppm is confirmed to be a phenolic proton. MC-$H^+$ peaks are as follows:

$^{1}$H NMR (749 MHz, THF-$d_8$) δ 9.97 (s, 1H), 8.66 (d, $J$ = 16.4 Hz, 1H), 8.01 (dd, $J$ = 7.9, 1.6 Hz, 1H), 7.88 (d, $J$ = 8.7 Hz, 1H), 7.73 (d, $J$ = 16.4 Hz, 1H), 7.61 (d, $J$ = 2.2 Hz, 1H), 7.44 (t, 1H), 7.42 (dd, $J$ = 8.6, 2.2 Hz, 1H), 7.00 (t, $J$ = 7.5 Hz, 1H), 6.94 (d, $J$ = 8.2 Hz, 1H), 6.35 (s, 1H), 5.85 (s, 1H), 4.17 (s, 3H), 2.06 (s, 3H), 1.83 (s, 6H).

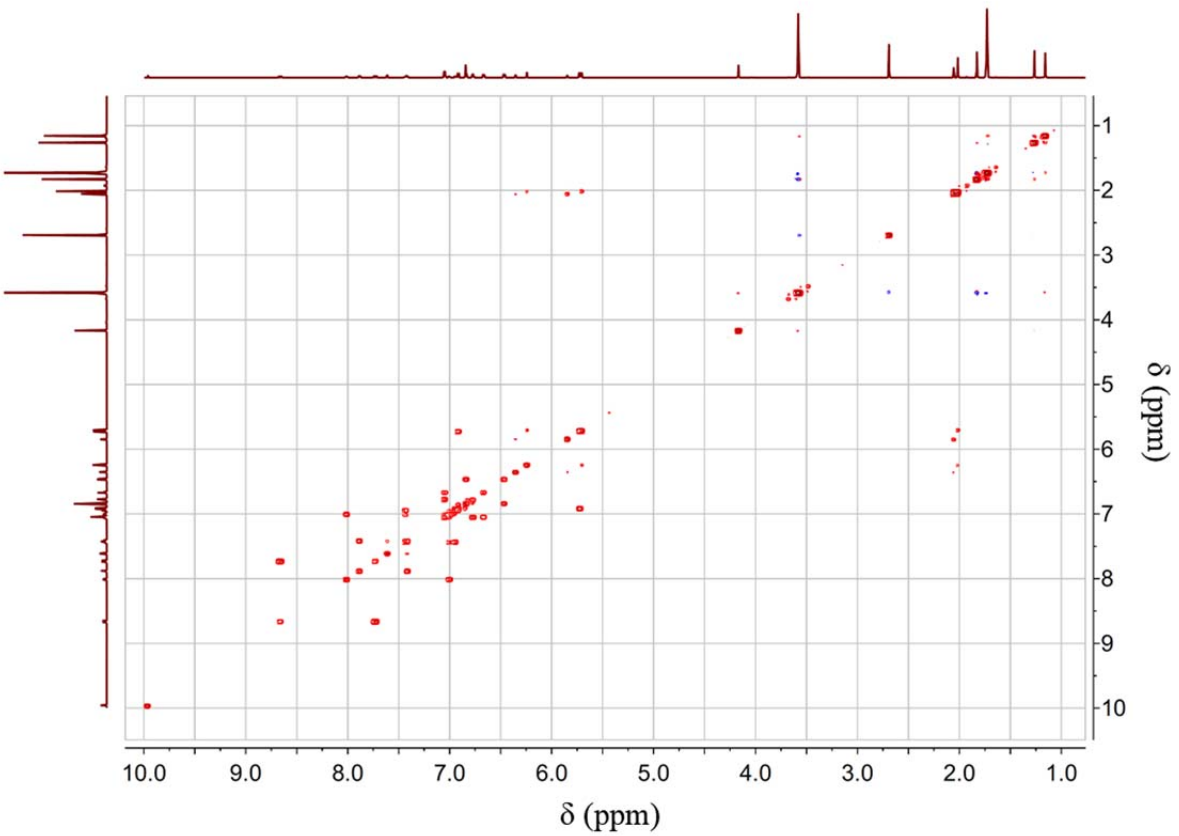


**Figure 5.9.** COSY spectrum of 20 mM solution of SP3 in THF-$d_8$ containing 2:1 SP3: $Cu(NTf_2)_2$ aided the assignments of the protons in the $^1H$ spectrum of Figure 5.8. The singlet at 9.97 ppm shows no cross peaks, indicating this proton is not immediately adjacent to any other proton in either SP3 or MC3.

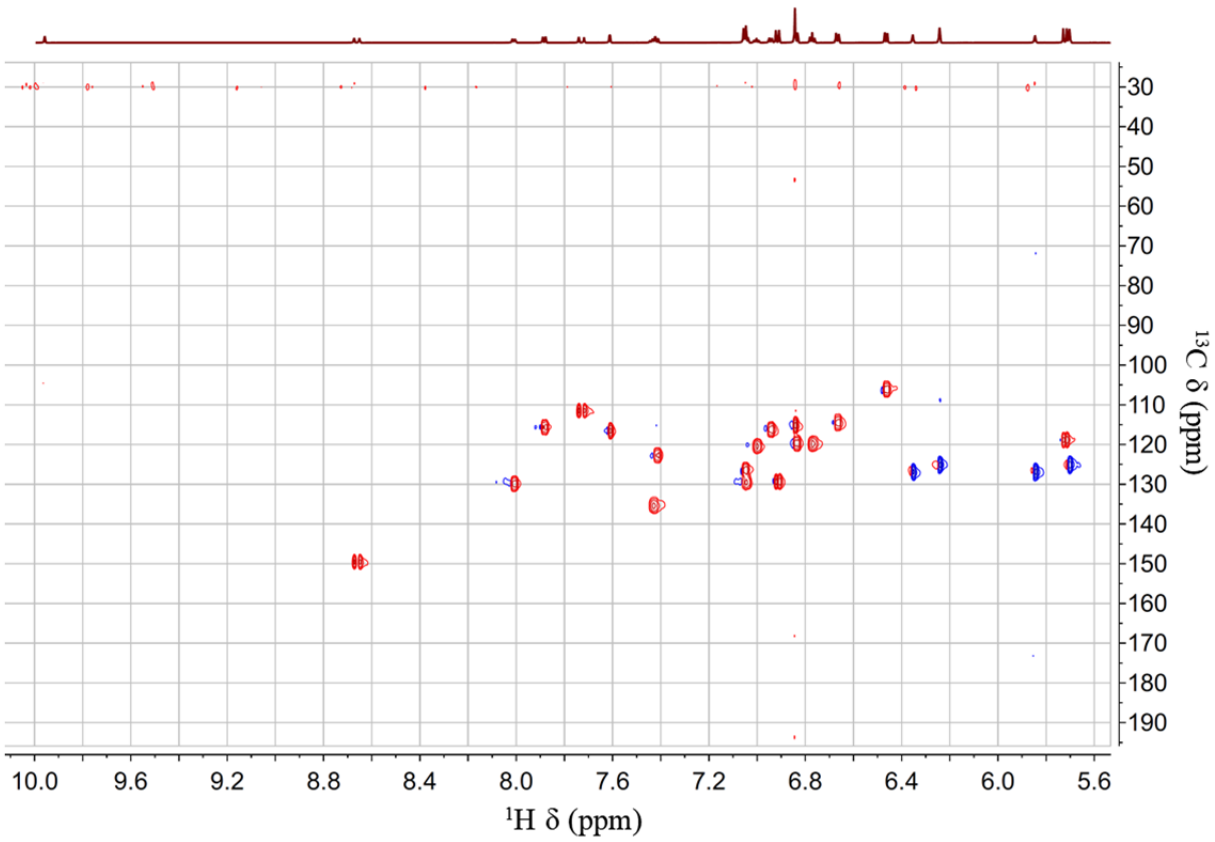


**Figure 5.10.** HSQC spectrum (optimized for $J_{H\text{-}C}$ = 146 Hz) of 20 mM solution of SP3 in THF-$d_8$ containing 2:1 SP3: $Cu(NTf_2)_2$ aided the assignments of the protons in the $^{1}$H spectrum of Figure 5.8. The $^{1}$H peak at 9.97 ppm is not directly coupled to any *aliphatic* carbons in SP3 or MC3.

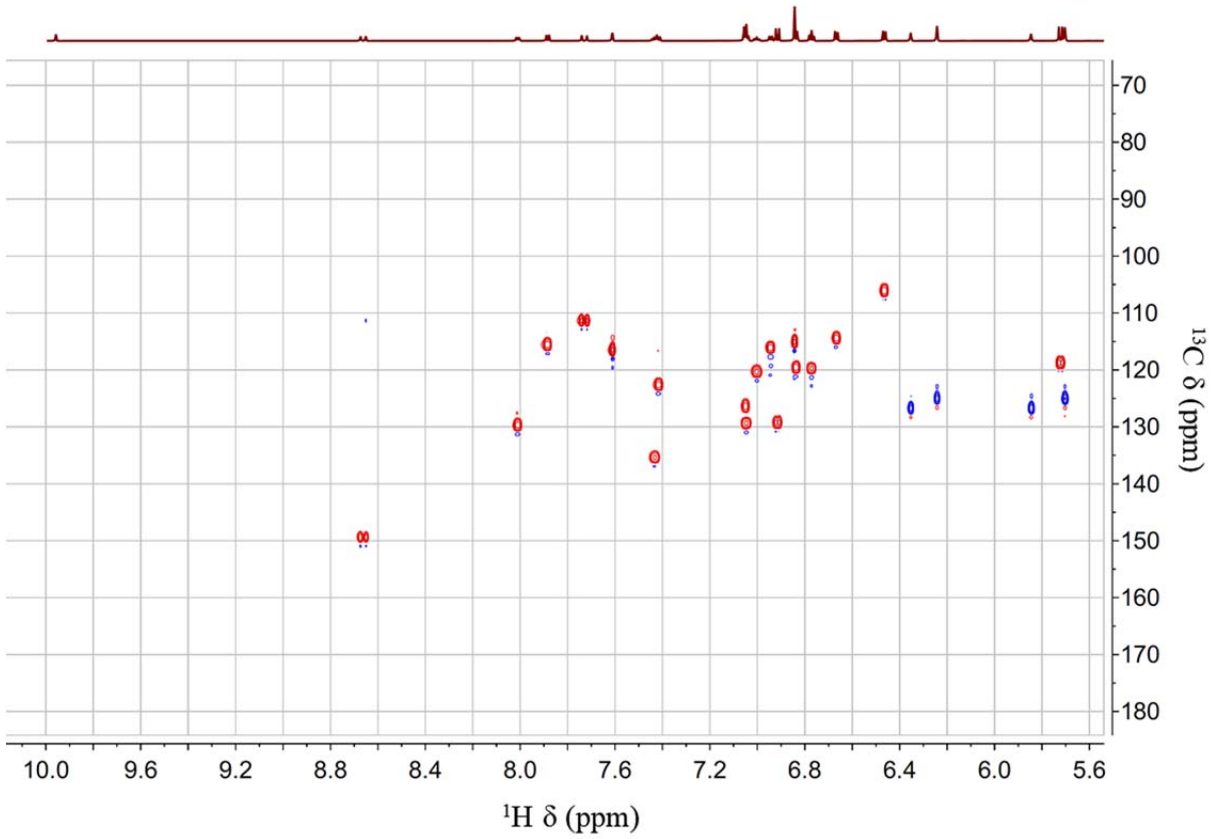


**Figure 5.11.** HSQC spectrum (optimized for $J_{H\text{-}C}$ = 170 Hz) of 20 mM solution of SP3 in THF-$d_8$ containing 2:1 SP3: $Cu(NTf_2)_2$ aided the assignments of the protons in the $^{1}$H spectrum of Figure 5.8. The $^{1}$H peak at 9.97 is not directly coupled to any *aromatic* carbons in SP3 or MC3.

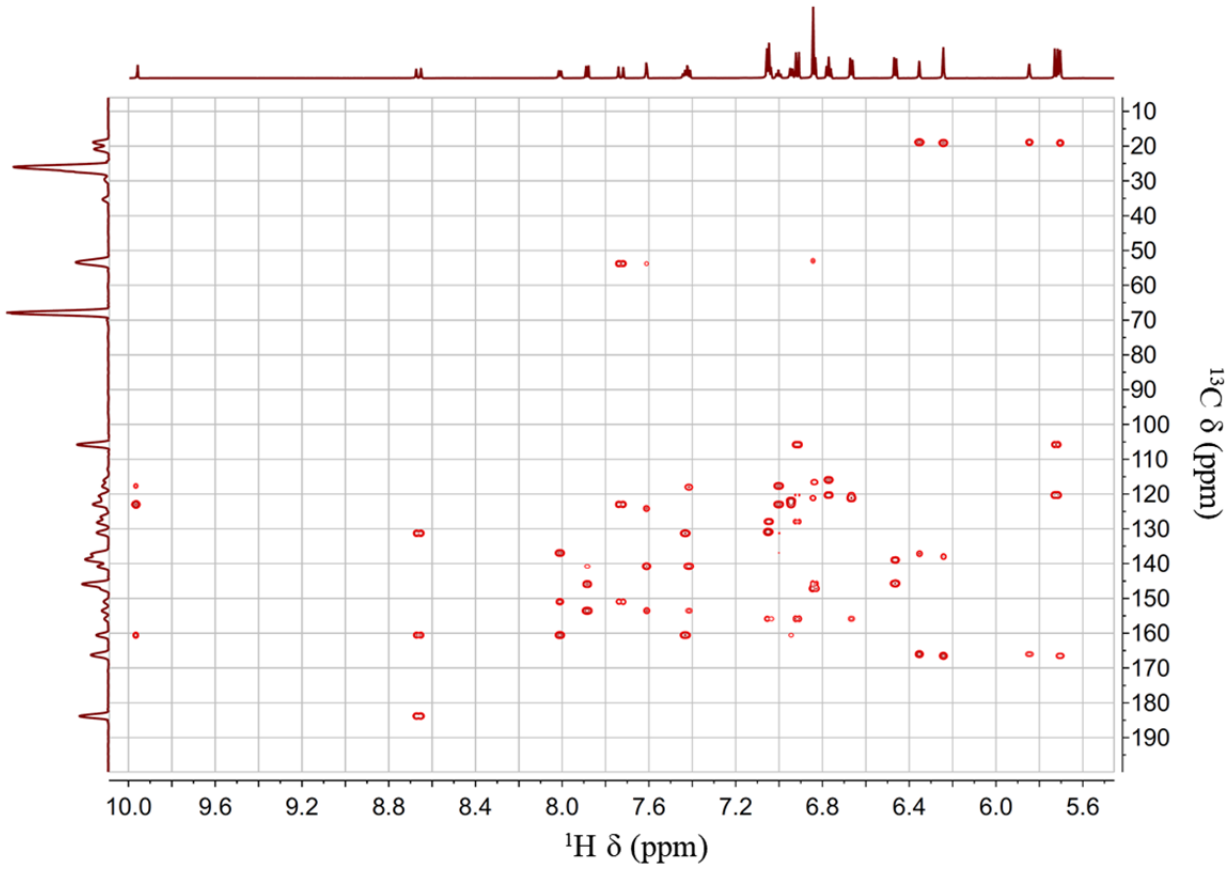


**Figure 5.12.** HMBC spectrum (optimized for $J_{H\text{-}C}$ = 8 Hz) of 20 mM solution of SP3 in THF-$d_8$ containing 2:1 SP3: $Cu(NTf_2)_2$ aided the assignments of the protons in the $^{1}$H spectrum of Figure 5.8. The $^{1}$H peak at 9.97 shows long-range coupling to three carbons in MC3, thus showing that this proton is part of the ring-open MC isomer.

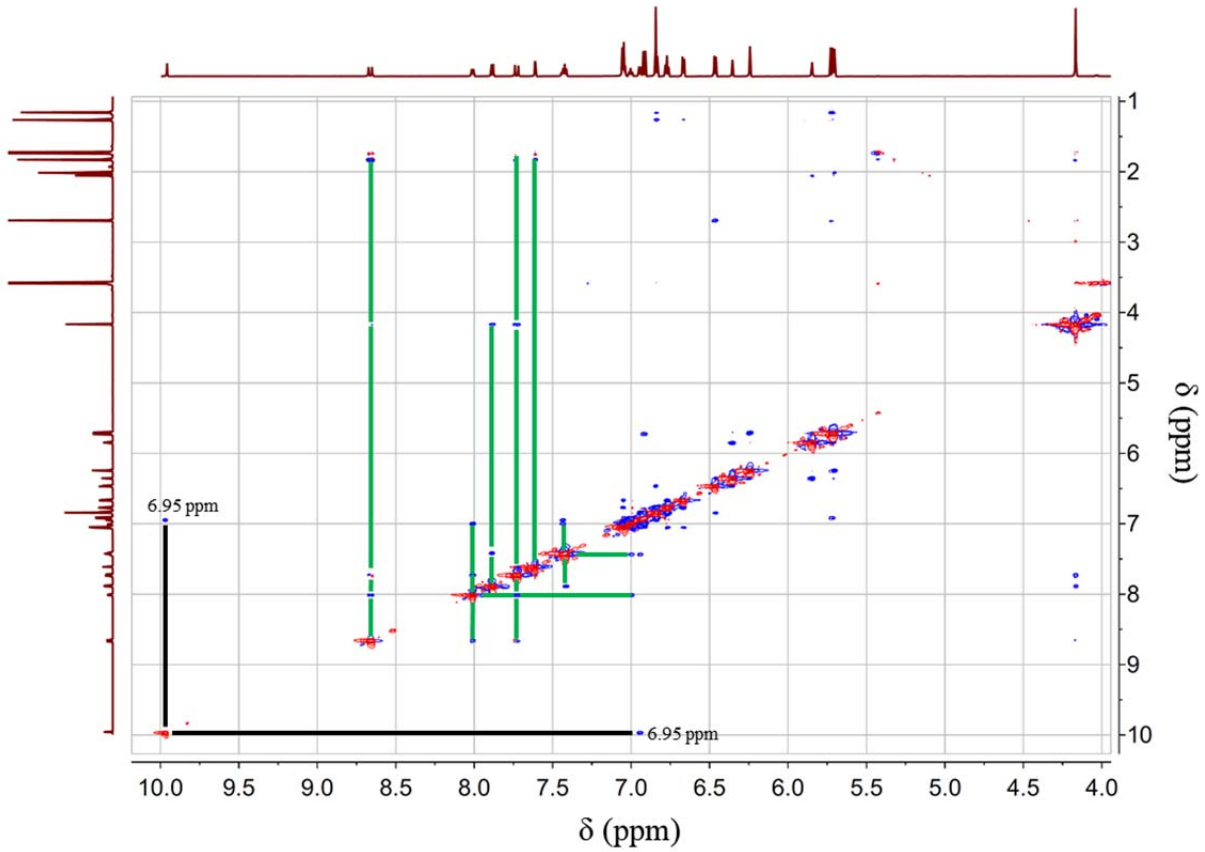


**Figure 5.13.** NOESY/EXSY spectrum ($\Delta_{mix}$ = 700 ms) of 20 mM solution of SP3 in THF-$d_8$ containing 2:1 SP3: $Cu(NTf_2)_2$ aided the assignments of the protons of MC3 shown in Figure 5.8.The $^1$H peak at 9.97 shows through-space correlation with the $^1$H peak of MC3 at 6.95 ppm, which is directly adjacent to the phenolic oxygen of MC3 (see Figure 5.8). This unequivocally shows that the $^1$H peak at 9.97 ppm is a phenolic proton of a protonated merocyanine isomer. In addition, this NOESY spectrum was taken with a relatively long mixing time (700 ms) and recorded over many (n = 1028) scans in attempt to detect intermolecular associations between MC molecules (e.g. dimerization through molecular stacking or bridging by Cu(II) ions). This spectrum shows no exchange correlations between molecules of SP3 or MC3; however, this only rules out the possibility of intermolecular exchange within a distance of ~5 Å. It is still possible that there are long range associations between molecules that can't be detected.

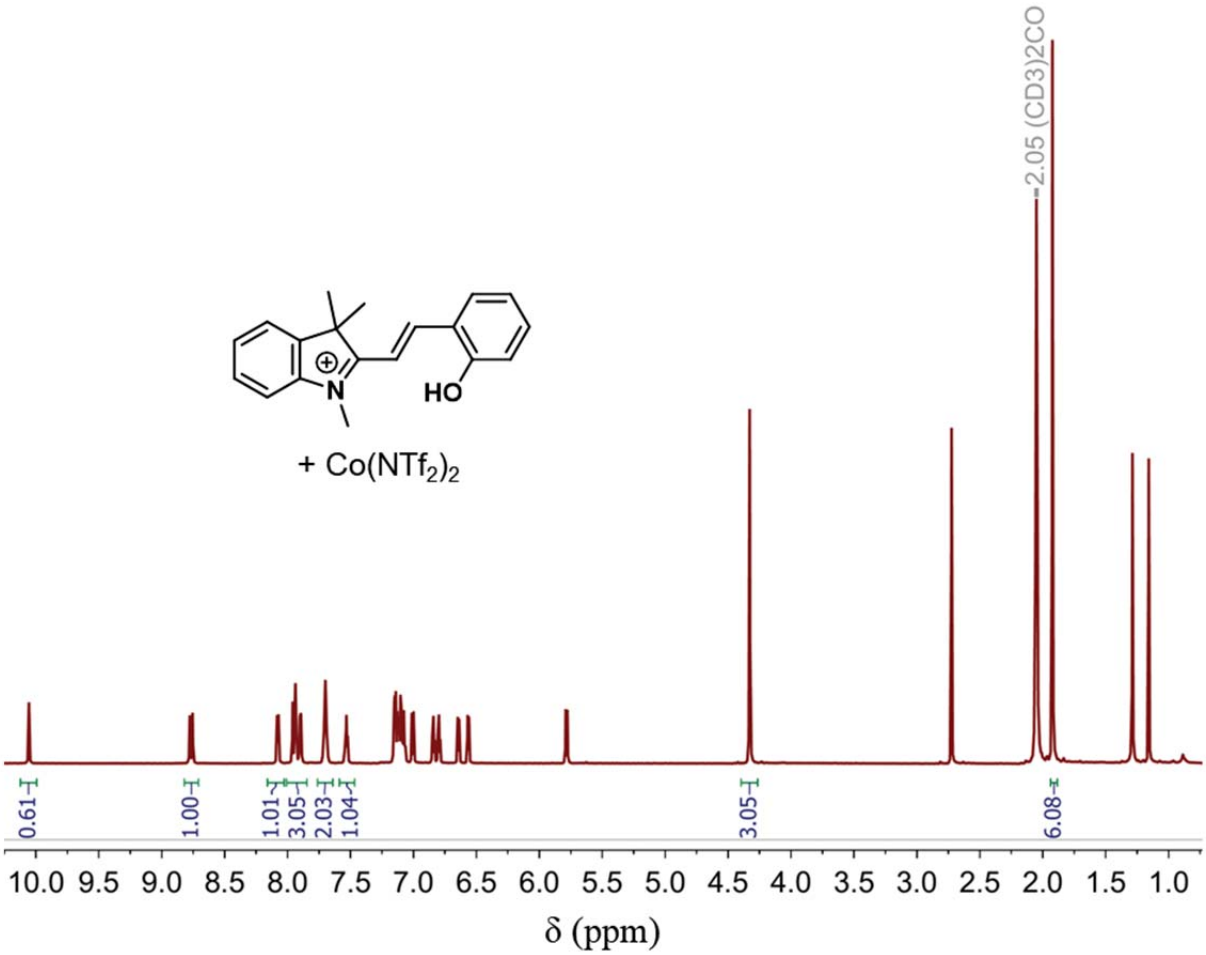


**Figure 5.14.** $^{1}$H NMR spectrum of 20 mM solution of SP2 in acetone-$d_6$ containing 2:1 SP2: $Co(NTf_2)_2$. Protonated MC2-$H^+$ is also detected in solutions containing Co(II).

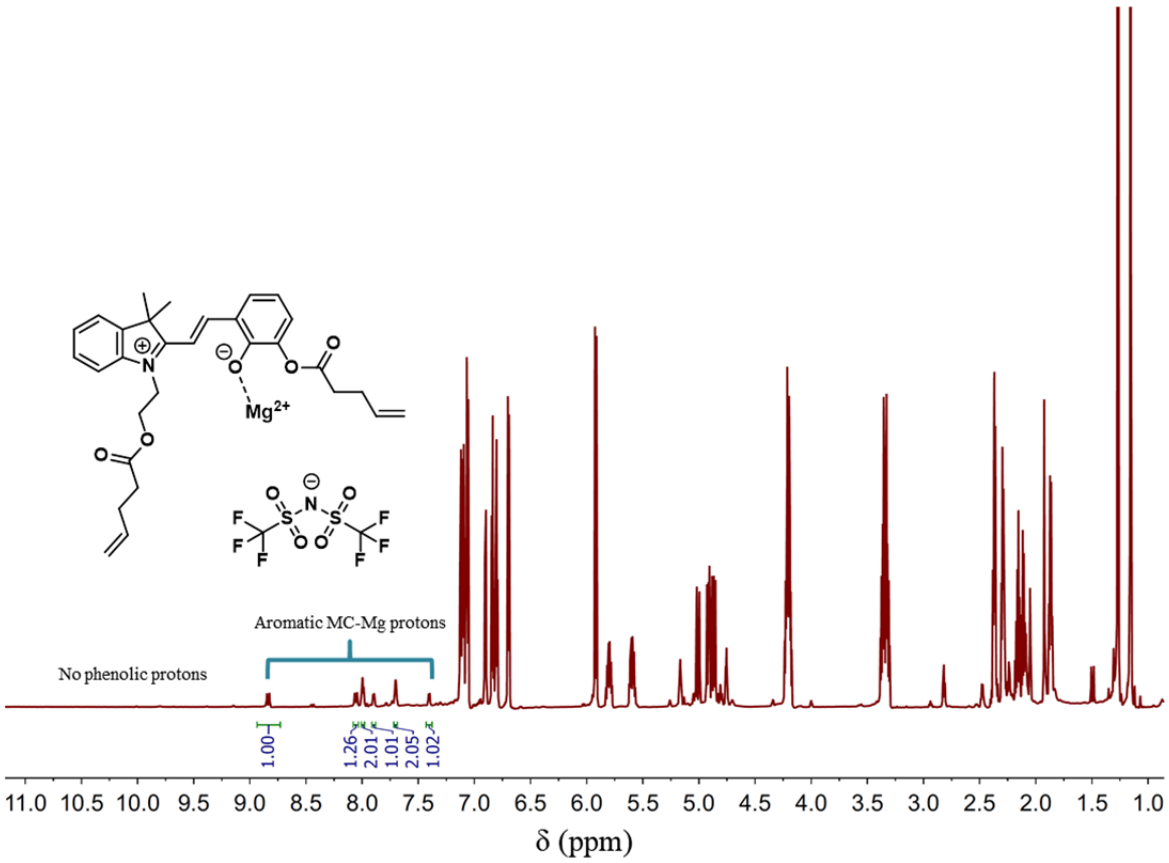


**Figure 5.15.** $^{1}$H NMR spectrum of 80 mM solution of SP4 in acetone-$d_6$ containing 2:1 SP4: $Mg(NTf_2)_2$. No protonated MC4 is detected in samples containing Mg(II), Ca(II) or Li(II). Therefore, we conclude that our NMR analysis in Chapter 4 indeed shows MC-metal complexes.

### 5.7 Rationalizing the slow diffusion of merocyanines

According to the hard sphere approximation (equation 5.3), $MW_{MC}/MW_{SP}$ suggests that MC2 and MC3 are ~2.5x the size of SP2 and SP3 (respectively) in all acetone and THF (see Table 5.1). This seemingly contradicts our hypothesis that the MC species are all monomeric. We attempted to detect intermolecular associations between MC3 molecules by performing an EXSY experiment with a long mixing time (Figure 5.13). No intermolecular exchange was detected, indicating that MC3 molecules must be farther than ~5 Å (the spatial detection limit of a typical NOESY/EXSY experiment) from one another. Evidently, MC2 and MC3 diffuse much more slowly than their ring-closed conformations in acetone and THF; however, we suspect the

hard sphere approximation does not accurately describe the relative diffusivities of SP and MC. The Stokes-Einstein equation considers only the spherical volume of a species and the viscosity of its surrounding medium. To understand why MC2 and MC3 diffuse so much more slowly than their ring-closed isomers, a number of factors have to be considered.

First we ask: how does the true (i.e. aspherical) volume occupied by SP change when it switches to MC? DFT simulations indicate that the unsolvated MC molecule occupies *less* volume than SP (Figure 5.8b), which would actually *increase* the diffusivity of MC. Therefore, MC must either increase in molecular weight via increased solvation, coordination to ions, and/or dimerization, or other factors must account for its significantly reduced diffusion coefficient.

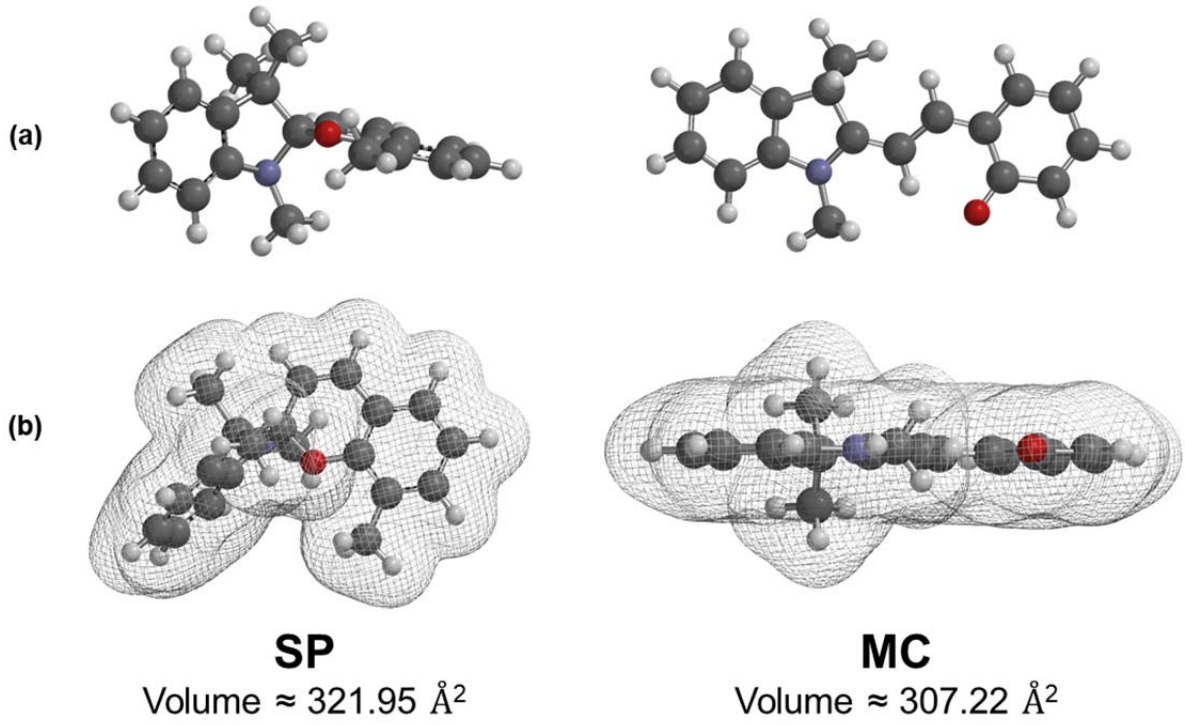


**Figure 5.16.** Molecular volumes of SP2 and MC2 computed by DFT. (a) Optimized geometries of SP and one of the most common isomers of MC (trans-trans-cis). (b) Electron density surfaces of SP and MC. Molecular volume taken as the volume contained within the electron density surface. Calculations performed in the gas state at the B3LYP/6-31G* level of theory.

A second factor to consider is the change in shape when SP switches to its more flattened and outstretched MC conformation (see Figure 5.16). Stalke and coworkers have derived external calibration curves for molecules of different shapes in order to accurately account for shape effects when estimating molecular weights diffusion coefficients [17]. Their methodology is based on the following empirical power law:

$$D = K(MW)^{\alpha} \qquad 5.5$$

where $K$ and $\alpha$ are empirical coefficients that depend on the solvent and the shape of the molecule. In a series of papers, Stalke and coworkers derived $K$ and $\alpha$ values for small molecules of spherical, ellipsoidal and pancake (or what they refer to as "expanded disc") shapes [17-20]. The ring-closed SP conformation is more or less ellipsoidally shaped, whereas MC is best described as an expanded disc/pancake. For comparison, Figure 5.17a shows similar examples of these two shapes classified by Stalke [18]. To understand what might happen to the diffusion coefficient of a molecule if it switches from an ellipsoid to a pancake shape (i.e. SP➔MC), we plot $D_{Pancake}/D_{Ellipsoid}$ as a function of molecular weight using $K$ and $\alpha$ values empirically derived by Stalke and coworkers (Table 5.2) [17, 18].

Evidently, the effect of molecular shape depends heavily on the solvent (Figure 5.17b). In DMSO, switching shape has a negligible effect on compounds regardless of their molecular weight. In THF, the effect of shape depends on the molecular weight of the species. SP2 and SP3 are ~277 g/mol and ~361 g/mol, respectively. According to Figure 5.17b, at these molecular weights we should expect only a modest decrease in diffusivity due to switching from an ellipsoidal to a pancake conformation. But at molecular weights greater than ~360 g/mol, we should expect the diffusion coefficient of the pancake shaped species to diminish more noticeably. Hence, if MC were to increase in molecular weight with respect to SP (e.g. due to

coordination to metal ions and/or by forming a larger solvation shell), we should expect its concomitant decrease in diffusivity to be compounded by its flattened shape.

**Table 5.2** *K* and *α* values for different molecular shapes in THF-$d_8$ [17] and DMSO-$d_6$ [18]

| Shape | Log *K* | *α* |
|---|---|---|
| **Ellipsoid (THF-$d_8$)** | -7.5360 | -0.5824 |
| **Pancake (THF-$d_8$)** | -7.1205 | -0.7519 |
| **Ellipsoid (DMSO-$d_6$)** | -7.78 | -0.709 |
| **Pancake (DMSO-$d_6$)** | -7.45 | -0.846 |

Unfortunately, Stalke's *K* and *α* values do not accurately predict the MW of SP3 in THF-$d_8$ or DMSO-$d_6$ containing metal salts, and therefore, we refrain from using their methodology to predict the relative MWs of MC to SP. However, we can use the empirical trends depicted in Figure 5.17b to better understand the relative diffusivity of MC and SP in salt containing solutions. Interestingly, the ratio of $D_{SP}/D_{MC}$ is significantly larger in THF-$d_8$ than DMSO-$d_6$ (see Table 5.1). Of the four solvents used in our studies (THF, acetone, methanol, and DMSO), DMSO is be the only solvent that significantly reduces the difference in diffusion coefficients of SP and MC. This result correlates well with the shape effect revealed in Figure 5.17. In DMSO, switching shape should have negligible effect, whereas in THF, the diffusivity of MC should decrease, especially if its MW increases due to coordination with a metal ion.

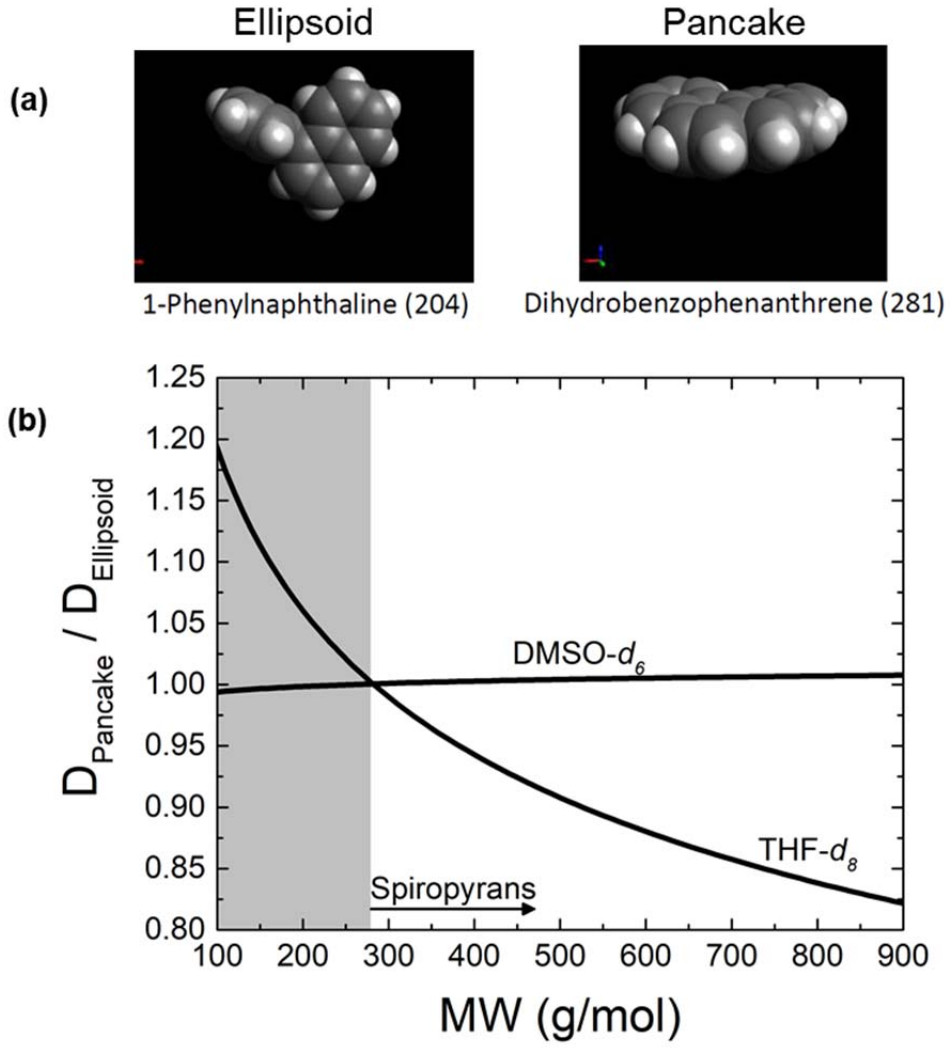


**Figure 5.17.** Plot of the empirically derived relationship (a) Examples of ellipsoids and expanded discs/pancakes according to Stalke and coworkers [18]. (b) Relative diffusivity of pancake vs. ellipsoidal shaped molecule as a function of molecular weight according to equation 5.5 using $K$ and $\alpha$ values derived by Stalke and coworkers for molecules in THF-$d_8$ [17] and DMSO-$d_6$ [18] (Table 5.2). Grey region represents space below the molecular weights of spiropyrans.

It is possible that other factors, such as a significant change in dipole moment and/or change from a neutral to a cationic state accounts for the large discrepancy in diffusion coefficients of SP and ion-coordinated MC. It's possible that DMSO could suppress this effect through electrostatic screening, however, this is unlikely because no differences in diffusion ratios are observe in methanol, acetone and THF, which have very different dielectric constants. Finally,

we note that the diffusion ratios of SP4 and SP5 with $Cu(NTf_2)_2$ in acetone-$d_6$ are significantly reduced compared to SP2 and SP3. These molecules include flexible alkyl chains that are not present in SP2 and SP3. Due to flexibility of these chains, it's probable that the flattened pancake representation of MC2 and MC3 does not apply to MC4 and MC5. Thus, changes in shape have a much smaller effect. Additionally, if MC were to form an expanded solvation shell or increase its molecular weight due to coordination with ions, this effect would be dampened for SP4 and SP5, which have larger molecular weights to begin with.

### 5.8 Summary and suggestions for continuing this work

In this chapter we used DOSY in attempt to elucidate the stoichiometry of MC-metal complexes. Our methodology compares the relative diffusion coefficients, $D_{SP}/D_{MC}$, in cases were 1:1 complexes are expected (e.g. in solutions containing $H^+$ and Na(I)) to cases where divalent Cu(II) or Co(II) ions were hypothesized to form 2:1 MC-metal dimers. Surprisingly, we discovered that in deuterated acetone, THF and methanol, SP2 and SP3 share the same $D_{SP}/D_{MC}$ ratios regardless of the valance of ion in solution. By expanding the spectral window of $^1H$ NMR spectra, we discovered that MC activated by Co(II) and Cu(II) are in fact protonated, despite being in aprotic solvents. The protonation of the phenolic oxygen of MC was confirmed by 2D NMR. Formation of $MCH^+$ explains why Co(II) and Cu(II) produces identical $D_{SP}/D_{MC}$ ratios as with the addition of $H^+$ and Na(I). We proposed that in all of our DOSY experiments, MC exists as monomers, and transition metal ions do not form intermolecular MC bridges like we expected.

However, the Stokes-Einstein equation (hard-sphere approximation) predicts suspiciously high molecular weights for the MC-complexes, on the order of what we might expect if MC formed dimers. Therefore, we pursued alternative explanations for the significantly reduced

diffusivities of protonated/complexed MC. By scrutinizing an empirical model put forth by Stalke and coworkers, we proposed that changes in shape significantly reduce the diffusion coefficients of SP2 and SP3 when they form MC-complexes. According to our analysis this effect would be amplified if MC were to gain any mass through formation of a larger solvation shell or by coordinating to ions. Our data suggest that the extended alkyl chains of SP4 and SP5 partially mask these effects, and diminish the gap in diffusivity between the ring-open and ring-closed states.

DOSY produces clean and very well differentiated data between SP and MC, and this technique should not be discounted based on the complexities uncovered in this initial study. In particular, our data suggest that modifying SP with large alkyl chains can mask the effects from shape changes and increased mass of MC via coordination with ions or solvent molecules. Scheme 5.3 illustrates a relatively simple scheme that may enable easier detection intermolecular bridging of MC. In this scheme the diffusion coefficient should be dominated by the size of the alkyl tail. Bridging between MC isomers should effectively double the size of the oligomer/polymer chain, which would effectively decrease the diffusion coefficient by a factor of $\sim\sqrt[3]{2} = 1.26$.

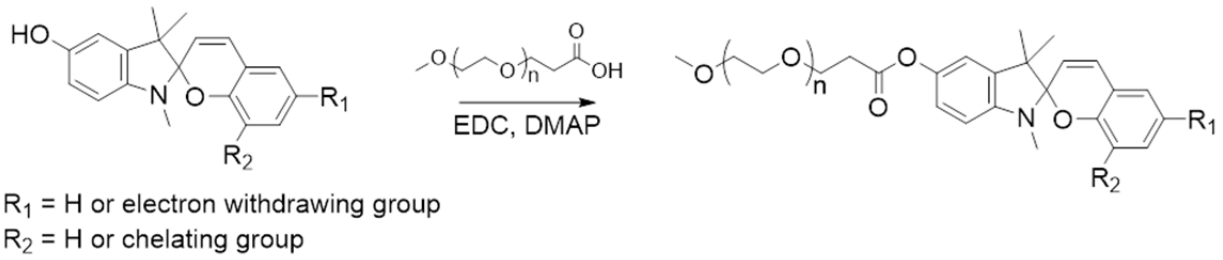


**Scheme 5.3.** Suggested functionalization of SP that may simplify DOSY analysis and enable easier detection of intermolecular bridging between MC.

## 5.9 REFERENCES


1. Shao, N., Zhang, Y., Cheung, S., Yang, R., Chan, W., Mo, T., Li, K. and Liu, F. *Analytical Chemistry* **2005**, *77*, 7294.
2. Chernyshev, A. V., Voloshin, N. A., Metelitsa, A. V., Tkachev, V. V., Aldoshin, S. M., Solov'eva, E., Rostovtseva, I. A. and Minkin, V. I. *Journal of Photochemistry and Photobiology A: Chemistry* **2013**, *265*, 1.
3. Zakharova, M. I., Coudret, C., Pimienta, V., Micheau, J. C., Delbaere, S., Vermeersch, G., Metelitsa, A. V., Voloshin, N. and Minkin, V. I. *Photochemical & Photobiological Sciences* **2010**, *9*, 199.
4. Kundu, P. K., Olsen, G. L., Kiss, V. and Klajn, R. *Nat Commun* **2014**, *5*, 3588.
5. Byrne, R. J., Stitzel, S. E. and Diamond, D. *Journal of Materials Chemistry* **2006**, *16*, 1332.
6. Klajn, R. *Chem Soc Rev* **2014**, *43*, 148.
7. Aleksandar, R., Silvia, S., Robert, B., Conor, S., King Tong, L. and Dermot, D. *Journal of Physics D: Applied Physics* **2007**, *40*, 7238.
8. Renny, J. S., Tomasevich, L. L., Tallmadge, E. H. and Collum, D. B. *Angewandte Chemie International Edition* **2013**, *52*, 11998.
9. Avram, L. and Cohen, Y. *Chemical Society Reviews* **2015**, *44*, 586.
10. Waldeck, A. R., Kuchel, P. W., Lennon, A. J. and Chapman, B. E. *Progress in Nuclear Magnetic Resonance Spectroscopy* **1997**, *30*, 39.
11. Groves, P. *Polymer Chemistry* **2017**, *8*, 6700.
12. Stejskal, E. O. and Tanner, J. E. *The Journal of Chemical Physics* **1965**, *42*, 288.
13. Stumpel, J. E., Ziolkowski, B., Florea, L., Diamond, D., Broer, D. J. and Schenning, A. P. *ACS Appl Mater Interfaces* **2014**, *6*, 7268.
14. Ganesan, R. and Remacle, F. In *Theoretical Chemistry in Belgium: A Topical Collection from Theoretical Chemistry Accounts*; Champagne, B., et al., Eds.; Springer Berlin Heidelberg: Berlin, Heidelberg, 2014, p 167.
15. Galstyan, G. and Knapp, E. W. *Journal of Computational Chemistry* **2014**, *36*, 69.
16. Jackson, V. E., Felmy, A. R. and Dixon, D. A. *The Journal of Physical Chemistry A* **2015**, *119*, 2926.
17. Neufeld, R. and Stalke, D. *Chemical Science* **2015**, *6*, 3354.
18. Bachmann, S., Neufeld, R., Dzemski, M. and Stalke, D. *Chemistry – A European Journal* **2016**, *22*, 8462.
19. Bachmann, S., Gernert, B. and Stalke, D. *Chemical Communications* **2016**, *52*, 12861.
20. Kreyenschmidt, A. K., Bachmann, S., Niklas, T. and Stalke, D. *ChemistrySelect* **2017**, *2*, 6957.

# CHAPTER 6: SUMMARY, ONGOING WORK AND STRATEGIES FOR CONTINUING THIS PROJECT

## 6.1 Summary of thesis

The work presented in this dissertation began with a vision of designing polymers that reversibly crosslink in response to mechanical force. As a first step towards achieving this vision, two critical questions were addressed. First, can spiropyran molecules reversibly crosslink polymer chains? In Chapter 3, we provide compelling evidence that SP forms metal-ion-mediated MC-crosslinks, and that this process is reversible. First, a SP-functionalized methacrylate based copolymer, poly(DEGMEMA-SPMA), was synthesized. UV-Vis spectroscopy showed that when poly(DEGMEMA–SPMA) is mixed with Co(II) ions, MC-metal complexes form spontaneously at room temperature in the dark, a process which was accelerated by applying heat. Exposure to visible light resulted in the rapid release of metal ions and ring closure of SP. The viscoelastic properties of SP-linked polymer solutions were probed under small-amplitude oscillatory shear. It was shown that 2:1 and 3:1 ratios of SP to $Co(NTf_2)_2$ switched polymer solutions from a viscous fluid to a viscoelastic gel. Exposure to visible light transformed the gel back to a fluid state, thereby demonstrating reversibility. When a 1:1 ratio of SP to $Co(NTf_2)_2$ was used, gelation was suppressed and the polymer solution remained a viscous fluid after thermal activation of MC-Co complexes. Based on these results as well as previous reports of 2:1 MC-transition metal complexes, we inferred that reversible gelation was indeed due to metal-ion-mediated crosslinking; however, this was not confirmed spectroscopically. This set of experiments provided a proof-of-concept using light/thermally active SP, but this mechanism has not yet been demonstrated with SP mechanophores or in a dry polymer.

The second critical question we addressed is: can mechanical force be used as an effective stimulus for generating MC-metal coordination bonds? In Chapter 4 we engineered a SP-PDMS/metal ion composite and found that mechanical force can indeed be used to generate MC-metal complexes, but measures must be taken to prevent excessive spontaneous activation in order for mechanical force to be an effective stimulus. In this study we used alkali and alkaline metal salts because we anticipated that the driving force for spontaneous complexation would be too strong with transition metals. On its own, the PDMS matrix did not sufficiently screen SP/metal ion interactions and the degree of spontaneous complexation was unacceptably high. Furthermore, we showed that SP mechanophores with a nitro moiety on the chromene ring are too labile, which also results in unacceptably high degrees of merocyanine activation in the absence of mechanical stress. Spontaneous MC-metal complexation was effectively mitigated by selecting a SP mechanophore that is very stable in its ring-closed state, and by incorporating hexyl acetate in the PDMS matrix, which screened the interactions between SP and metal ions. By effectively controlling the thermal equilibrium, we demonstrated tensile force-triggered MC-metal complexation, followed by thermal decay of the complexes back to their equilibrium concentration after release of the mechanical stress. This process was repeated for multiple cycles with no evidence of degradation and low variability. An inverse relationship between the thermodynamic stability of the MC-metal complexes in solution and the ratio of mechanochemical to thermal activation in the PDMS elastomers was also revealed. Finally, DFT CoGEF computations provided mechanistic insights into the behavior of SP mechanophores with and without an electron withdrawing group, as well as in the presence and absence of metal ions.

In Chapter 5 we addressed the challenges of characterizing the stoichiometry of weak MC-metal complexes by introducing diffusion NMR as a technique to characterize MC-ion

associations. Unfortunately, the DOSY and 2D correlation NMR data presented in Chapter 5 led to more questions than answers, but careful analysis led to important insights on how to precisely pinpoint the mechanisms we wish to reveal using these techniques moving forward.

*6.1.1. Summary of spiropyrans*

When SP is used as a mechanochromic dye, only a few milligrams of SP per gram of polymer are required to observe significant coloration under mechanical stress. However, our goal is to use spiropyran as a primary component in bulk polymers so they can have a substantial impact on the polymer mechanics. A significant challenge in pursuing our objectives was to develop spiropyran synthesis schemes that yield at the very least gram-scale quantities of material. Figure 6.1 highlights the spiropyrans that were synthesized for this dissertation. All procedures are scalable to at least several grams or more. SP1 is the "conventional" nitro-functionalized photochromic dye with an added methacrylate functionality enabling it to be polymerized. SP2 is the most basic form of SP with no additional functional groups. Without the nitro group SP2 is not photochromic (at least not on practical timescales), and is much more stable in the ring-closed conformation. SP3 is the methacrylate functionalized version of SP2. SP4 contains a carboxylic acid on the indoline ring. Discussed further in Section 6.3, this moiety is meant to destabilize MC, and could perhaps further reduce spontaneous activation of MC-metal complexes. SP5 (which we refer to as "SP-NO2" in Chapter 4) contains a nitro moiety which enables UV activation of MC and also kinetically stabilizes the MC state. SP6 is mechanophore with the same polymer chain connectivity as SP5, but is very unstable in the ring-open state, and thus very rapidly switches back to the ring-closed state after mechanical stress is removed. As shown in Chapter 4, metal ions are very effective at slowing the rate of ring-closure of SP6 after mechanochemical activation. SP7 is also a mechanophore, though interestingly, DFT CoGEF

calculations (performed at the B3LYP/6-31G* level of theory) do not predict this (data not shown). Finally, SP8 is a mechanochemically inactive experimental control, as it can be incorporated into a polymer backbone in the same way as SPs 4-6, but does not switch to MC under mechanical stress.

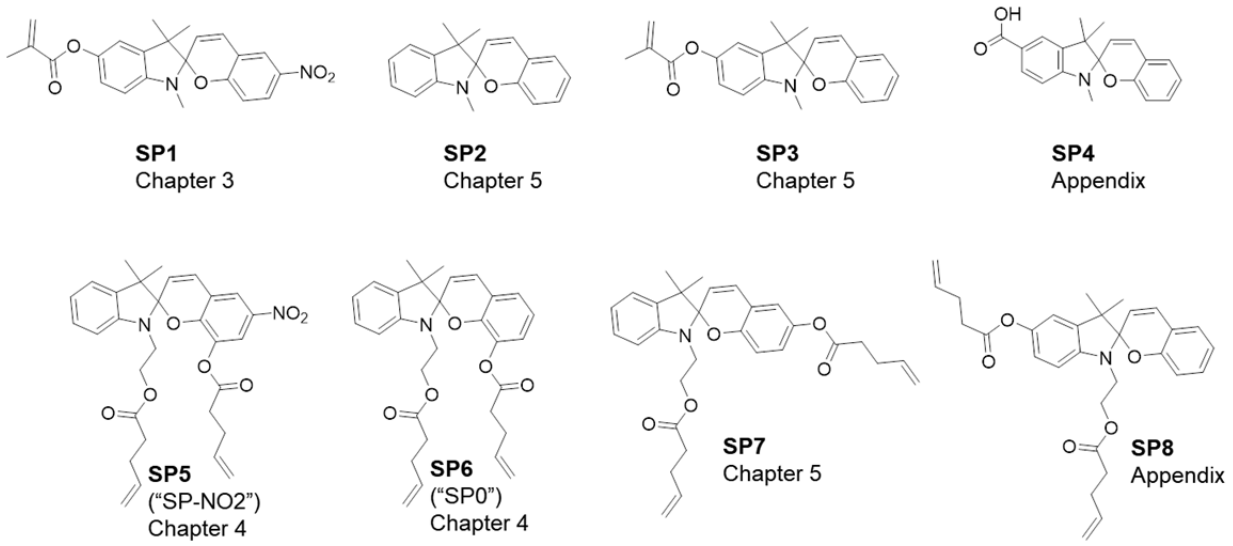


**Figure 6.1.** Spiropyrans synthesized for this dissertation.

One of the major challenges of this project is its massive design space. There are many possible mechanophores, polymer chemistries, and metal ions to incorporate. When I started this project, I made the mistake of trying to make everything work at once, resulting in little progress. The next sections outline two rational strategies for pushing this project forward and produce meaningful results.

## 6.2 The polymer engineer's approach to continuing this project

The immediate objective of "the polymer engineer's approach" is to formulate polymers with high mechanophore loadings (e.g. ≥10 wt%) using mechanophores that we have already developed. We propose that at high loadings, SP mechanophores can dissipate mechanical energy, thereby enhancing material toughness. Because SP to MC isomerization is reversible, SP mechanophores can act as dissipative sacrificial bonds, which can subsequently self-heal after broken (Figure 6.2).

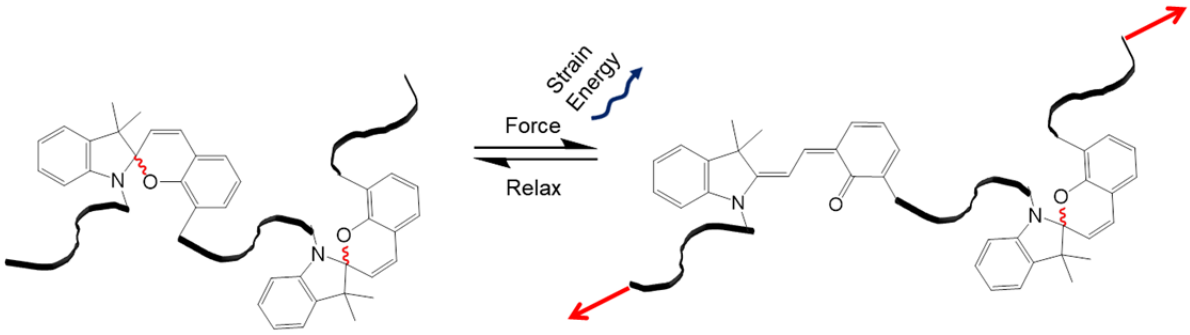


**Figure 6.2.** SP mechanophores may act as sacrificial bonds that dissipate mechanical energy. Mechanochemical activation is reversible, thus enabling sacrificial bonds to heal after rupture.

The work presented in Chapter 4 provides an excellent springboard for designing such a system. We have already developed a multi-gram scale synthesis procedure for SP6, which can be further scaled up if need be, and the extreme stability of SP6 in its ring-closed state suggests that kinetic trapping of the MC state won't be a problem, even at very high concentrations (we have long suspected that this is a problem with nitro-functionalized SP4). Moreover, the rapid kinetics of ring closure of SP6 could lead to some interesting, non-monotonic mechanical responses.

Work towards developing high SP content PDMS elastomers is currently underway. We have preliminary results showing that we can produce PDMS containing ~10 wt% SP6; however, we find that incorporating high concentrations of SP in PDMS using the same procedure described

in Chapter 4, SP solubility becomes an issue. Moreover, even if the solubility issue is solved, the conventional procedure of simply mixing di-alkene functionalized SP with Sylgard PDMS evidently leads to poor mechanical properties at high SP loadings, because the more SP, the higher the crosslink density and the more unbalanced the Si-H/vinyl stoichiometry (Figure 6.3).

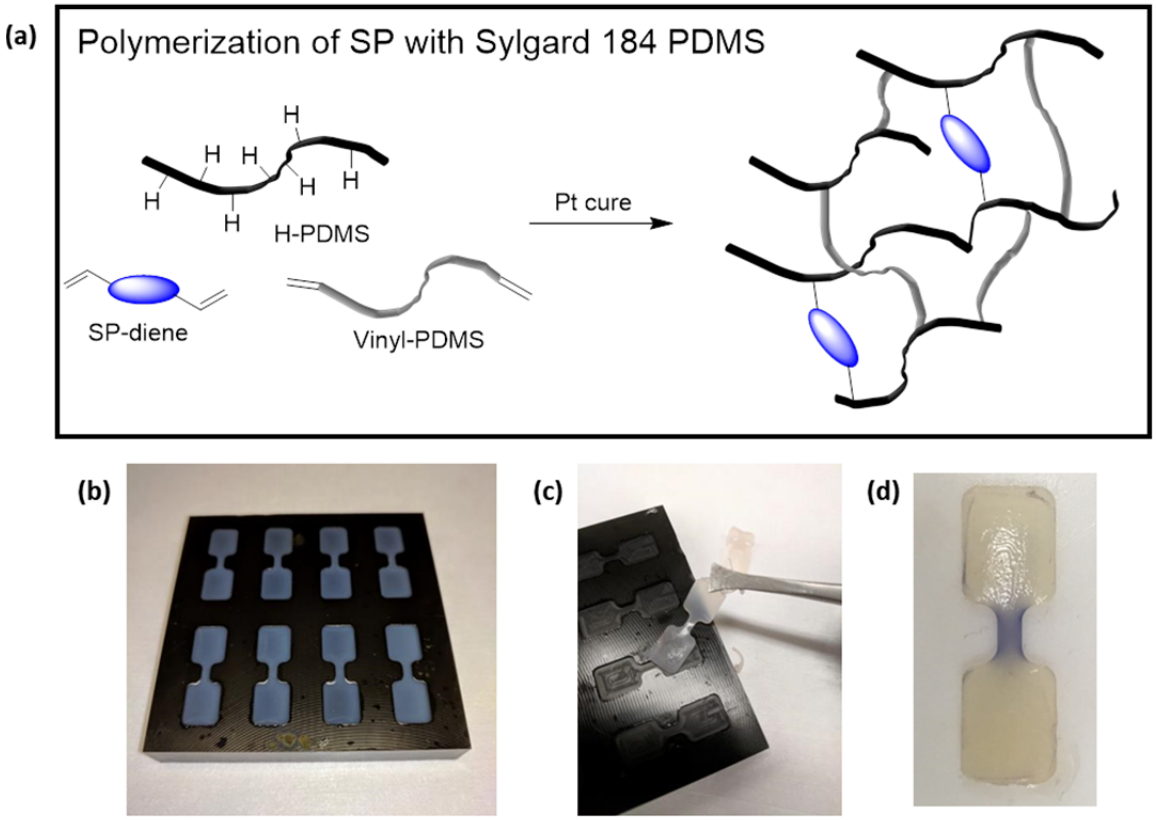


**Figure 6.3.** (a) Typical scheme for incorporating SP mechanophores into PDMS using a standard Sylgard elastomer kit. This scheme works well for relatively low (≤ 1wt%) loadings of mechanophore. (b) At ~10 wt% SP loading, the solubility of SP becomes an issue, producing milky prepolymer solutions. (c) A combination of incomplete solubility and unbalanced Si-H/vinyl stoichiometry results in severely weakened and optically diffuse SP-crosslinked PDMS. (d) Despite these issues, the elastomer is still mechanochromic, suggesting that favorable results may be attained by more careful tuning of the chemistry.

To solve these issues, a 2-step procedure is proposed, whereby di-alkene functionalized SP and di-SiH are first reacted to form a prepolymer, followed by mixing of this pre-polymer with the Sylgard elastomer components. Precisely tuning the stoichiometric ratio of SP to Si-H in the

prepolymer will ensure the prepolymer is alkene terminated (or Si-H terminated if preferred), and that the overall stoichiometry of the reaction remains well-balanced in the second curing step. The proposed procedure is illustrated in Figure 6.4.

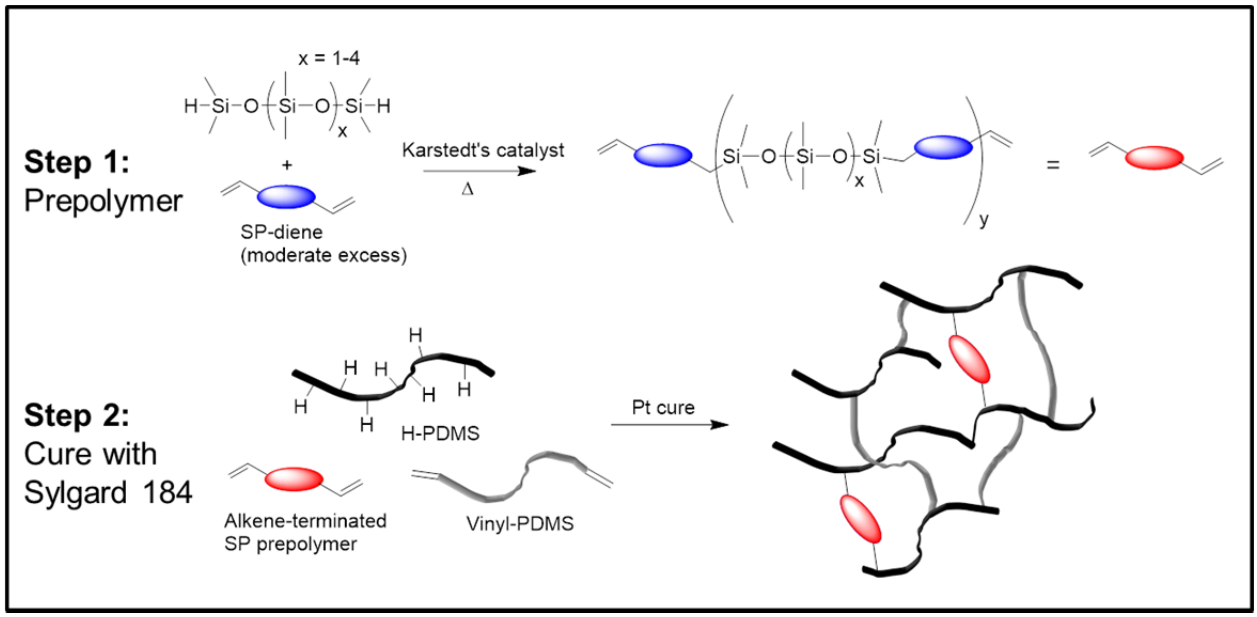


**Figure 6.4.** Proposed 2-step scheme to ensure the vinyl/SiH stoichiometry and crosslink density remains well balanced at high loadings of SP into Sylgard PDMS.

Once control over the polymer formulation is attained, polymers containing high loadings of SP mechanophore can be synthesized. In order to determine if SP has a substantial impact on the polymer's mechanical properties, it will be critical to compare the mechanochemically active polymer to a mechanochemically inactive control. The synthesis of a di-alkene functionalized, mechanochemically inactive control SP (SP8) is included in Appendix A.

If the mechanochemical activity of SP is found to have a significant impact on the stress-strain behavior of the polymer, these properties may be further tuned by incorporating metal cations into the polymer matrix. In Chapter 4, we experimentally demonstrated that even very weak MC-metal ion interactions significantly reduce the rate of ring-closure after force-triggered activation of MC in PDMS. It is possible that different kinetics may lead to very different mechanical responses at high SP loadings. Furthermore, our DFT simulations suggest that the

energy and force of mechanophore bond rupture may be tuned by incorporating ions with different interaction strengths. Thus, there's potential to tune the dissipative mechanics of polymer composites by altering the energy landscape of the constituent mechanophores via non-covalent interactions. These two characteristics are absolutely worth exploring at high mechanophore loadings.

However, in Chapter 4 we also showed that incorporating metal ions results in undesirable spontaneous activation of MC. Addition of hexyl acetate partially suppressed this spontaneous activation by competing with metal complexation. These results may be further improved by exploring other additives that competitively bind or solvate metal ions. The propensity of an additive to solvate ions may be evaluated by the compound's polarity, Lewis basicity and polarizability. The latter two features can be inferred from Kamlet-Taft parameters [1]. In cases where extreme competition is required, one may introduce chelating additives, such as diglyme. Table 6.1 suggests some potentially useful additives along with some predictions of their effectiveness at screening metal ion interactions.

**Table 6.1.** Kamlet-Taft acidity (α), basicity (β) and polarizability (π*) parameters, along with the dielectric constant (ε) of various high boiling point solvents. Higher basicity, polarizability and polarity should result in greater screening of metal cations from SP in PDMS. Based on these values, and the known ability of diglyme to chelate metal ions, the following trend in screening power is predicted: Diglyme >> ethyl benzoate ≈ 2-heptanone > hexyl acetate >> dimethylsiloxane.

| Name | BP (°C) | α | β | π* | ε |
|---|---|---|---|---|---|
| **Dimethylsiloxane**[a] | - | 0 | 0.09 | 0.65 | 2.4 |
| **Hexyl acetate** | 171.5 | 0 | 0.45 | 0.46 | 4.42 |
| **2-Heptanone** | 151 | 0.05 | 0.48 | 0.61 | 11.95 |
| **Ethyl benzoate** | 213 | 0 | 0.41 | 0.74 | 6 |
| **Diglyme**[b] | 162 | 0 | 0.4 | 0.64 | 7.23 |

[a] Kamlet-Taft values taken from reference [2].
[b] Diglyme will likely compete for ion coordination the most, by far, due to its well-known ability to chelate metal ions.

### 6.3 The synthetic chemist's approach to continuing this project

For the daring chemist who isn't afraid to get his or her hands dirty, there remains much potential to fully actualize the original vision of this project: reversible, mechanochemically-triggered metal-ligand crosslinking. Using rheology we have demonstrated compelling evidence that SP1 (see Figure 6.1) forms transition-metal-ion mediated crosslinks; however, we were unable to spectroscopically verify the ≥2:1 MC:metal coordination required for crosslinking. Moreover, our discovery in Chapter 5 that SP2 amd SP3 form protonated $MCH^+$ in the presence of Co(II) and Cu(II) adds an unanticipated and undesirable level of complexity to analyzing the molecular mechanisms of metal complexation.

Therefore, the immediate challenge is to synthesize a polymerizable spiropyran that forms ≥2:1 MC:metal coordination complexes in solution, and provide hard evidence of the stoichiometry. The DOSY method presented in Chapter 5 may be an excellent way to deduce MC-metal stoichiometry *if* measures are taken to ensure the differences in diffusivity between SP and MC are dominated by differences in molecular size rather than differences in shape, solvation or charge. As outlined in Scheme 5.3, one way to do this is to functionalize the SP molecule with long alkyl chains.

If obtaining 2:1 complexes in dry films is the ultimate goal, I highly recommend basing the synthesizing a SP molecule that has unequivocally been proven to form 2:1 complexes. Adding certain nitrogenous chelating groups adjacent to the spirocyclic oxygen of SP has been proven to produce 2:1 MC-metal complexes in solution (see Figure 2.8 and references). When I started this project, synthesizing a SP mechanophore containing similar types of chelating groups was in fact what I set out to do; however, for me, this turned out to be a mistake, as the schemes I originally

designed were quite complicated, and I did not yet possess the necessary skills to successfully carry out the synthesis. Figure 6.5 suggests a rational scheme for synthesizing a chelating SP mechanophore, by adapting a published procedure for an amine functionalized SP.

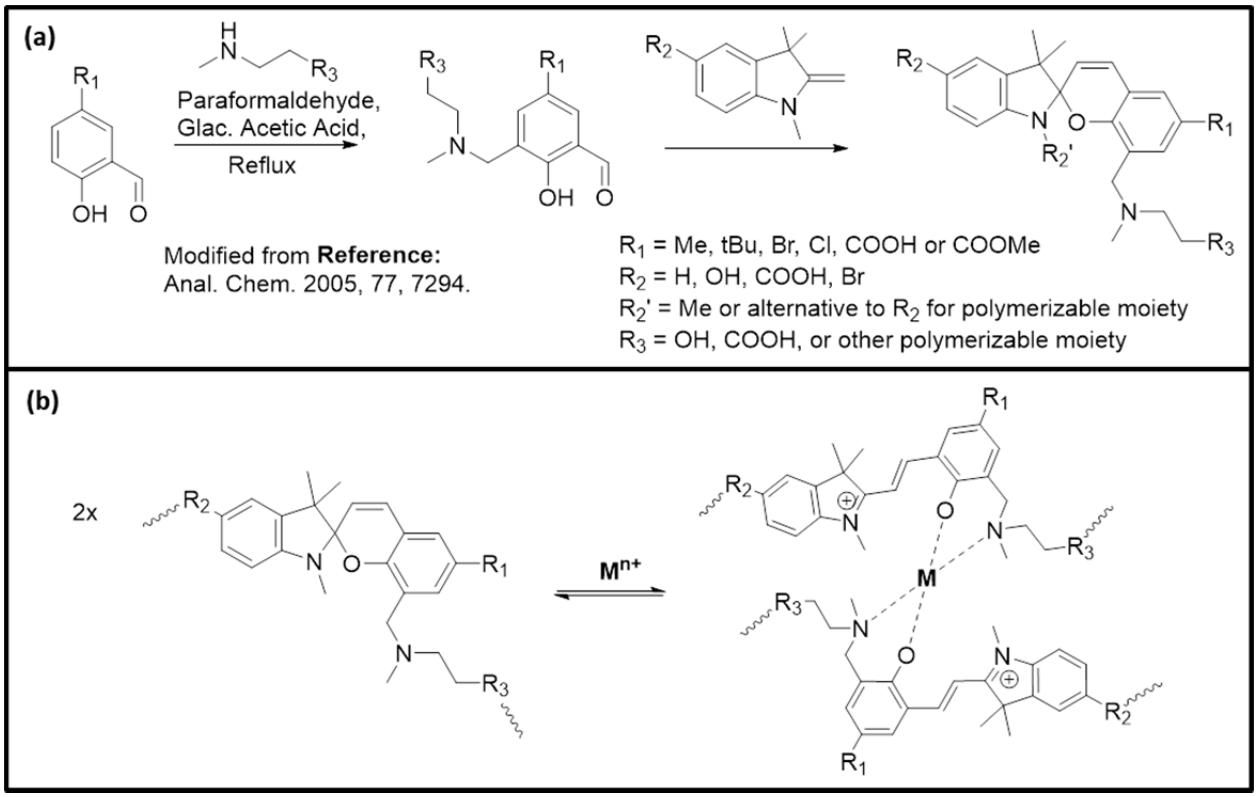


**Figure 6.5.** (a) Proposed scheme for synthesizing a chelating SP mechanophore. SP requires two polymerizable moieties at specific positions to be a mechanophore. $R_3$ is the best position on the chromene ring. On the indoline side, the polymerizable group can be located at $R_2$ or $R_2$'. Positioning at $R_2$' greatly simplifies the synthesis procedure of the indolinium precursor (not shown), but may sterically hinder 2:1 MC-metal coordination. Therefore, $R_2$ is the preferred choice, but limited functionalities are available for purchase. (b) Illustration of predicted 2:1 metal coordination of chelating SP mechanophores.

Though SPs with nitrogen-containing chelating groups will more predictably bind metal cations with 2:1 stoichiometry, they will also form much more stable complexes with metal cations. Therefore, after ≥2:1 MC-metal coordination has been spectroscopically verified (either using UV-Vis or DOSY), measures will then need to be taken to weaken the stability of the complexes without sacrificing their stoichiometry. For example, Cu(II) complexes of amine-containing SPs similar to the one shown in Figure 6.5 are completely irreversible, but Ca(II)

complexes of the same SP were found to be much less stable much less stable [3]. Therefore, reversibility may be possible simply by avoid transition metals and using alkaline metal salts. In addition, as described in Section 6.2, strongly coordinating solvents may be utilized as additives to weaken the MC-metal interaction.

In cases where complexation is too favorable, it may be necessary to alter the electronic structure of the SP rings. Balmond and coworkers have demonstrated that adding an electron withdrawing substituent to the indoline ring of SP destabilizes the merocyanine isomer [4]. Therefore, if MC-metal chelates are too stable, addition of electron withdrawing substituents to the indoline ring may be worth exploring as a means to inhibit spontaneous metal complexation and enhance reversibility. CoGEF calculations suggest that a carboxylate electron withdrawing group has little effect on the amount of force required to rupture the spirocyclic oxygen bond (Figure 6.6). This is a good thing, as it suggests that the electron withdrawing substituent does not affect mechanochemical activity itself. However, a significantly shortened indoline nitrogen bond suggests that the carboxylate has a substantial impact on the electronic structure of the indoline ring. We hypothesize that this altered electronic structure will destabilize MC after bond rupture, thereby leading to a more favorable transformation back to the ring-closed state. Thus far we have synthesized a carboxylic acid functionalized SP (SP4) with decent yield. Procedures are included in Appendix A.

Finally, it is worth noting that SPs containing nitrogenous chelating groups will likely poison the Pt catalyst used to synthesize PDMS. Therefore, alternative formulations may be required. The polyurethane formulation used by Sagara and coworkers may be a good place to start [5].

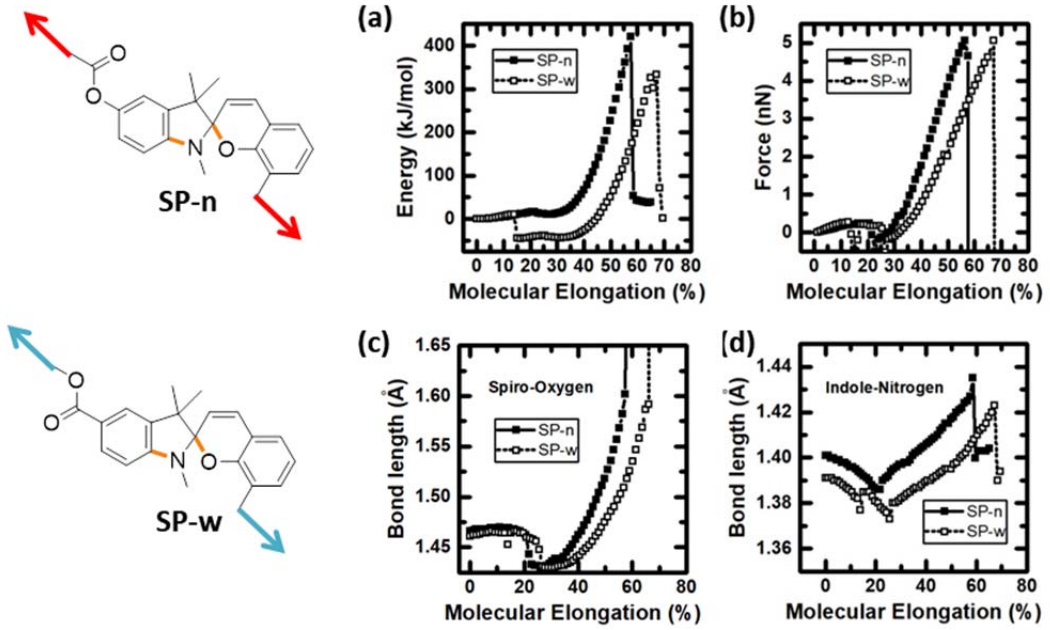


**Figure 6.6.** DFT CoGEF calculations predict that SP mechanophores with a carboxylate electron withdrawing substituent (SP-w) has similar mechanochemical behavior as the SP mechanophore that does not have an electron withdrawing group directly conjugated to the indoline ring (SP-n). (b) Both mechanophores rupture at roughly the same force, and (c) the spirocyclic bond lengths remain roughly the same in the unconstrained states as well as immediately prior to rupture, indicating that the electron withdrawing group has little effect on the mechanochemically active bond. (d) The electron withdrawing carboxylate has a significant effect on the indoline nitrogen bond length (shortened by ~0.01 Å). We hypothesize that this will destabilize the mechanophore in its ring-open state, thereby favorably shifting the equilibrium back to the ring-closed state. Indoline and spirocyclic oxygen bonds are bolded in orange in the SP structures. Calculations performed in the gas state at the B3LYP/6-31G* level of theory.

## 6.4 REFERENCES


1. Kamlet, M. J., Abboud, J. L. and Taft, R. W. *Journal of the American Chemical Society* **1977**, *99*, 6027.
2. Prause, S., Spange, S. and Barthel, H. *Macromolecular Chemistry and Physics* **2005**, *206*, 364.
3. Shao, N., Zhang, Y., Cheung, S., Yang, R., Chan, W., Mo, T., Li, K. and Liu, F. *Analytical Chemistry* **2005**, *77*, 7294.
4. Balmond, E. I., Tautges, B. K., Faulkner, A. L., Or, V. W., Hodur, B. M., Shaw, J. T. and Louie, A. Y. *The Journal of Organic Chemistry* **2016**, *81*, 8744.
5. Sagara, Y., Karman, M., Verde-Sesto, E., Matsuo, K., Kim, Y., Tamaoki, N. and Weder, C. *Journal of the American Chemical Society* **2018**, *140*, 1584.

## APPENDIX A: Additional synthesis procedures and supplementary $^{1}$H NMR data

### A.1 Additional synthesis procedures

*A.1.1 General information:*

5-methoxy-2,3,3-trimethyl-3H-indole was purchased from Biosynth. 4-(Hydrazinocarbonyl) benzoic acid was purchased from Ark Pharm. All other reagents were purchased from either Sigma Aldrich or Alfa Aesar.

*A.1.2 Synthesis of di-alkene functionalized, mechanochemically inactive control SP*

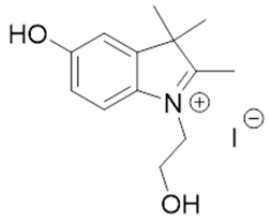


*5-hydroxy-1-(2-hydroxyethyl)-2,3,3-trimethyl-3H-indol-1-ium iodide*. 15.87 g (90.6 mmol) of 2,3,3-trimethyl-3H-indol-5-ol was dissolved in 50 ml of THF and 50 ml of 2-butanone in a one-necked round bottom flask. 30 g (174.4 mmol, 1.9 equiv) of iodoethanol was added and the solution was refluxed at 80 °C for 24 hours. The precipitated solid was filtered and washed with THF and ethanol, yielding an off-white powder (24.2 g, 69.7 mmol, 77%). Product was used without further purification. $^{1}$H NMR (500 MHz, DMSO-$d_6$) δ 7.72 (d, J = 8.7 Hz, 1H), 7.15 (d, J = 2.4 Hz, 1H), 6.93 (dd, J = 8.7, 2.4 Hz, 1H), 4.51 (t, J = 5.1 Hz, 2H), 3.92 – 3.76 (m, 2H), 2.72 (s, 3H), 1.49 (s, 6H). $^{13}$C NMR (126 MHz, DMSO-$d_6$) δ 193.55, 158.98, 143.96, 133.04, 116.52, 115.08, 110.40, 57.85, 53.75, 50.16, 22.17, 13.96.

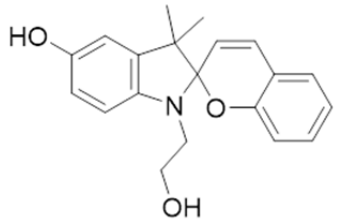


*1'-(2-hydroxyethyl)-3',3'-dimethylspiro[chromene-2,2'-indolin]-5'-ol*. 12 g (34.6 mmol) of 5-hydroxy-1-(2-hydroxyethyl)-2,3,3-trimethyl-3H-indol-1-ium iodide, 4.74 g (38.8 mmol) of salicylaldehyde and 5.36 g (53 mmol) of trimethylamine were dissolved in 130 ml of anhydrous ethanol. Argon was bubbled through the solution for 15 minutes and the solution was refluxed at 100 °C for 12 hours. Solution was concentrated in vacuo and dissolved in a 100 ml of 1:1 (by volume) solution of chloroform and ethyl acetate. The solution was washed with 10% aqueous ammonium chloride (3 x 50 ml), saturated sodium bicarbonate (3 x 50 ml) and brine (1 x 50 ml). Organic layer was dried over $Na_2SO_4$. Crude product was purified by column chromatography using silica (1-3% MeOH/DCM) yielding the title compound as a pale, transparent yellow oil (6.6 g, 20.4 mmol, 59%).

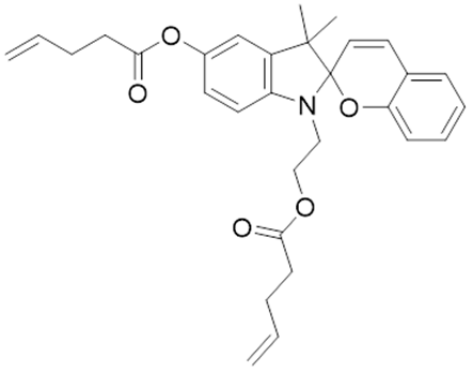


*3',3'-dimethyl-1'-(2-(pent-4-enoyloxy)ethyl)spiro[chromene-2,2'-indolin]-5'-yl pent-4-enoate*. 2.0 g (6.2 mmol) of 1'-(2-hydroxyethyl)-3',3'-dimethylspiro[chromene-2,2'-indolin]-5'-ol, 0.08 g (0.65 mmol) of DMAP, and 1.88 g (18.6 mmol) of trimethylamine were dissolved in 80 ml of dichloromethane. 3.4 g (18.6 mmol) of pentenoic anhydride was added dropwise at room temperature and the reaction proceeded for 4 hours. The solution was concentrated in vacuo and

purified by column chromatography using silica (1-3% EtOAc/hexanes) to yield the title compound as a pale, transparent yellow oil (1.3 g, 2.67 mmol, 29%). This poor yield is attributed to using an older bottle of pentenoic anhydride, and some careless errors on purification. Higher *yields using the described procedure should be attainable*. $^{1}$H NMR (500 MHz, Chloroform-d) δ 7.10 (td, J = 7.8, 1.7 Hz, 1H), 7.05 (dd, J = 7.5, 1.7 Hz, 1H), 6.90 – 6.79 (m, 4H), 6.70 (d, J = 8.1 Hz, 1H), 6.62 (d, J = 8.3 Hz, 1H), 5.93 (ddt, J = 16.8, 10.3, 6.4 Hz, 1H), 5.87 – 5.73 (m, 1H), 5.69 (d, J = 10.2 Hz, 1H), 5.17 (dq, J = 17.1, 1.7 Hz, 1H), 5.13 – 4.95 (m, 3H), 4.26 (dt, J = 11.1, 6.5 Hz, 1H), 4.19 (dt, J = 11.1, 6.3 Hz, 1H), 3.53 (dt, J = 15.1, 6.4 Hz, 1H), 3.45 (s, 0H), 3.35 (dt, J = 15.1, 6.4 Hz, 1H), 2.66 (t, J = 7.2 Hz, 2H), 2.57 – 2.48 (m, 2H), 2.49 – 2.29 (m, 4H), 2.17 (s, 1H), 1.28 (s, 3H), 1.17 (s, 3H). $^{13}$C NMR (126 MHz, Chloroform-d) δ 172.86, 172.18, 154.00, 145.00, 143.86, 137.51, 136.57, 136.52, 129.94, 129.63, 126.84, 120.32, 119.94, 119.21, 118.39, 115.84, 115.67, 115.59, 115.06, 106.34, 104.72, 62.75, 52.30, 42.58, 33.67, 33.44, 29.00, 28.77, 25.76, 20.03.

*A.1.3. Synthesis of carboxylic acid functionalized SP mechanophore*

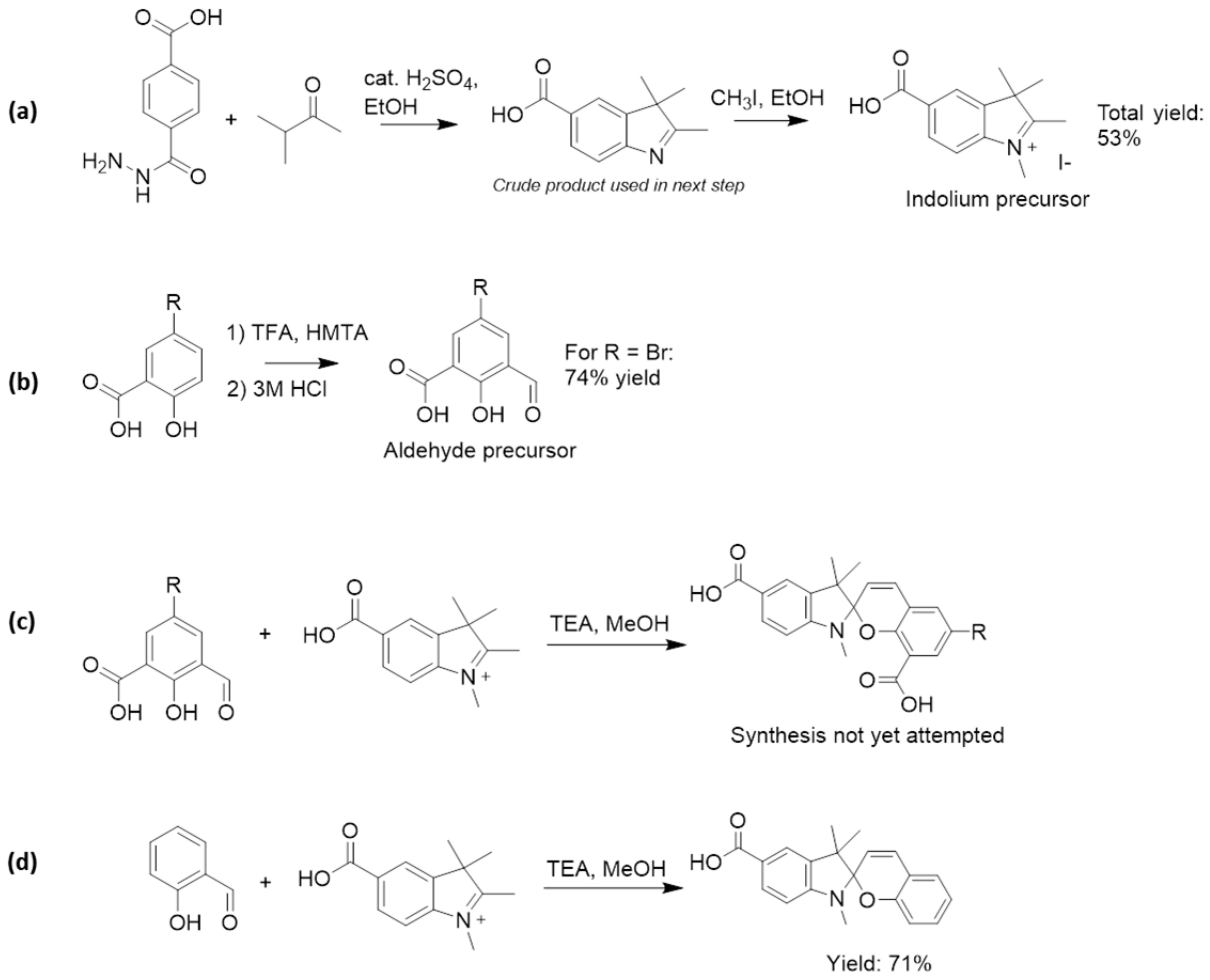


**Scheme A.1.** (a) and (b) Synthesis of precursors for carboxylic acid mechanophore shown in (c). (d) Monofunctional carboxylic acid SP shows reasonably high yield.

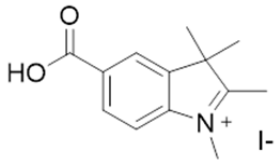

*5-carboxy-1,2,3,3-tetramethyl-3H-indol-1-ium iodide*. 15.68 g (103.56 mmol) of 4-(hydrazinocarbonyl) benzoic acid and 14.25 g (165.45 mmol) of 3-methyl-2-butanone were dissolved in 325 ml of anhydrous ethanol. 3.2 ml of concentrated sulfuric acid was added and the

solution was refluxed at 100 °C for 20 hours under a blanket of nitrogen gas. Upon cooling, some white precipitate formed – this was filtered off. EtOH was evaporated and the crude mixture was redissolved in 150 ml of dichloromethane and was twice with 100 ml of deionized water. DCM was evaporated to yield 2,3,3-trimethyl-3H-indole-5-carboxylic acid as a red solid. This crude product was immediately dispersed in 2:1 toluene/acetonitrile. 30 g (211 mmol) of iodomethane was added and the solution was refluxed for 18 hours. Vigorous stirring was required to break up large clumps of undissolved material and fully dissolve the precursor. The precipitated product was filtered and washed with ethanol. The crude product was recrystallized in boiling ethanol to yield the title compound as white crystals (18.733 g, 54.25 mmol, 52.7%). $^{1}$H NMR (500 MHz, DMSO-$d_6$) δ 8.37 (s, 1H), 8.21 – 8.15 (m, 1H), 8.03 (d, $J$ = 8.4 Hz, 1H), 4.00 (s, 3H), 2.82 (s, 3H), 1.57 (s, 5H). $^{13}$C NMR (126 MHz, DMSO-$d_6$) δ 198.98, 166.45, 145.24, 141.93, 131.56, 130.33, 124.18, 115.37, 54.25, 35.08, 21.49, 14.69.

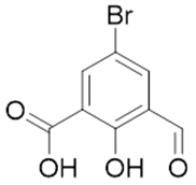


*5-bromo-3-formyl-2-hydroxybenzoic acid*. 10.385 g (47.85 mmol) of 5-bromosalicylaldehyde and 17.834 g (127.2 mmol) of hexamethylenetetramine were dissolved in 82 ml of trifluoroacetic acid. The solution was refluxed for 36 hours. The solution was cooled to room temperature and 435 ml of 3 M HCl was added and the solution was stirred for 6 hours until a substantial amount of solid precipitated. The solid was filtered and washed copiously with water to yield the title compound as a faint yellow solid (8.65 g, 35.3 mmol, 73.8%). $^{1}$H NMR (500 MHz, DMSO-$d_6$) δ 10.27 (s, 1H), 8.12 (d, $J$ = 2.7 Hz, 1H), 7.94 (d, $J$ = 2.7 Hz, 1H). $^{13}$C NMR (126 MHz, DMSO-$d_6$) δ 187.53, 170.21, 162.39, 138.21, 135.49, 125.56, 117.54, 110.07.

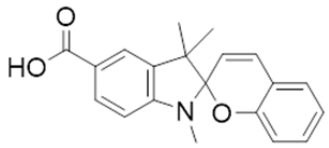


*1',3',3'-trimethylspiro[chromene-2,2'-indoline]-5'-carboxylic acid*. 1.705 g (4.94 mmol) of *5*-carboxy-1,2,3,3-tetramethyl-3H-indol-1-ium iodide, 0.636 g (5.2 mmol) of salicylaldehyde, and 1.04 g (10.28 mmol) of trimethylamine were dissolved in 30 ml of anhydrous methanol. Argon was bubbled through the solution for 15 minutes to displace dissolved oxygen and the solution was refluxed at 100 °C for 8 hours. The solution was concentrated *in vacuo* and the product was precipitated by boiling in ~10 ml of ethanol and slowly cooling to room temperature. The title product precipitated as small white crystals. This precipitation was repeated several times to obtain multiple crops of pure product (1.123 g, 3.5 mmol, 70.8%). $^{1}$H NMR (500 MHz, DMSO-$d_6$) δ 8.37 (s, 1H), 8.18 (d, 1H), 8.03 (d, $J$ = 8.4 Hz, 1H), 4.00 (s, 3H), 2.82 (s, 3H), 1.57 (s, 6H). $^{13}$C NMR (126 MHz, DMSO-$d_6$) δ 167.47, 153.59, 151.52, 136.25, 130.69, 129.89, 129.56, 127.00, 122.83, 121.15, 120.47, 118.63, 118.44, 114.39, 105.92, 103.83, 51.03, 28.41, 25.50, 19.78.

## A.2 $^{1}$H NMR Spectra

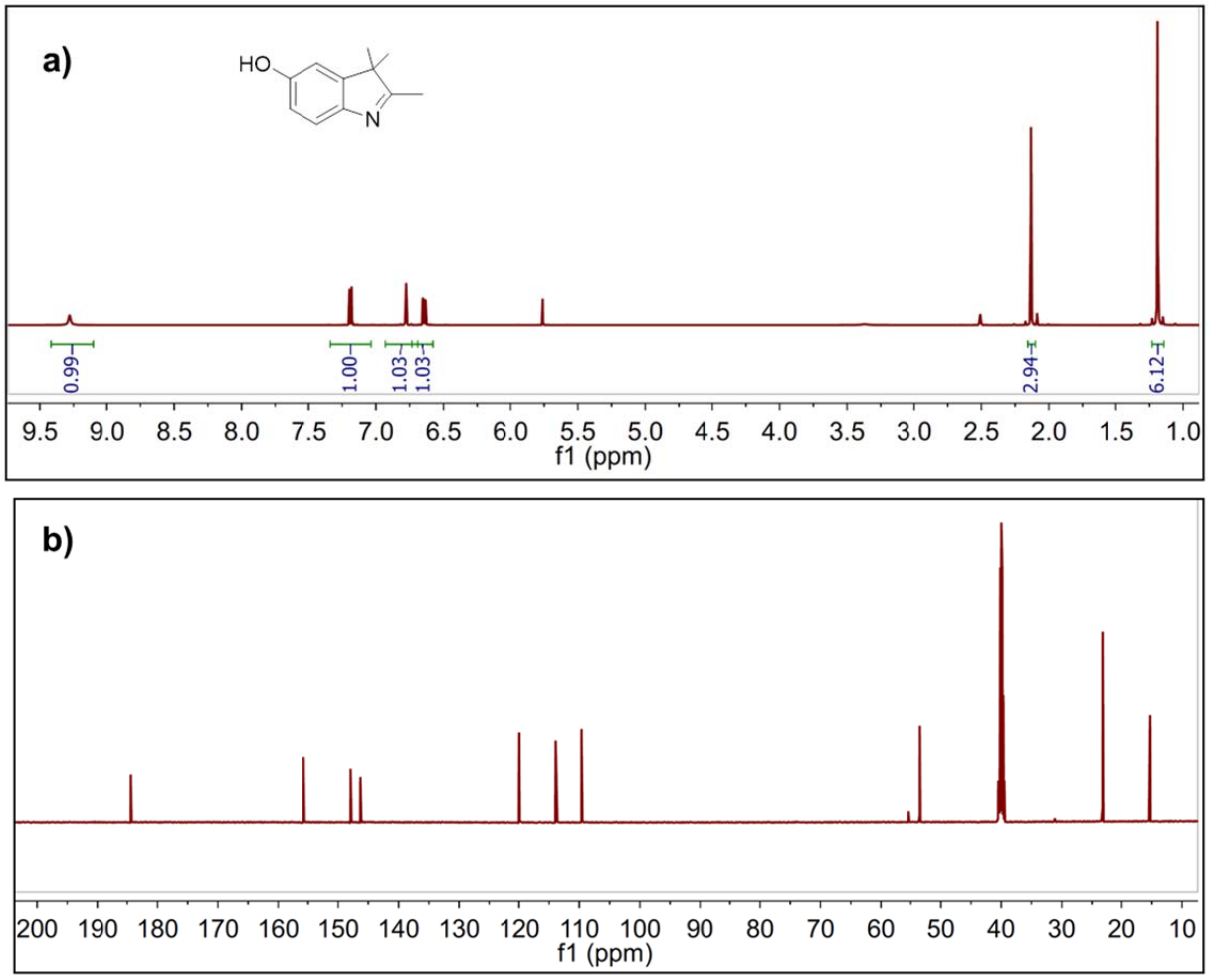


**Figure A.1.** a) 1H NMR and b) 13C NMR spectra of 5-hydroxy-1,2,3,3-tetramethyl-3H-indol-1-ium iodide in DMSO-$d_6$.

.

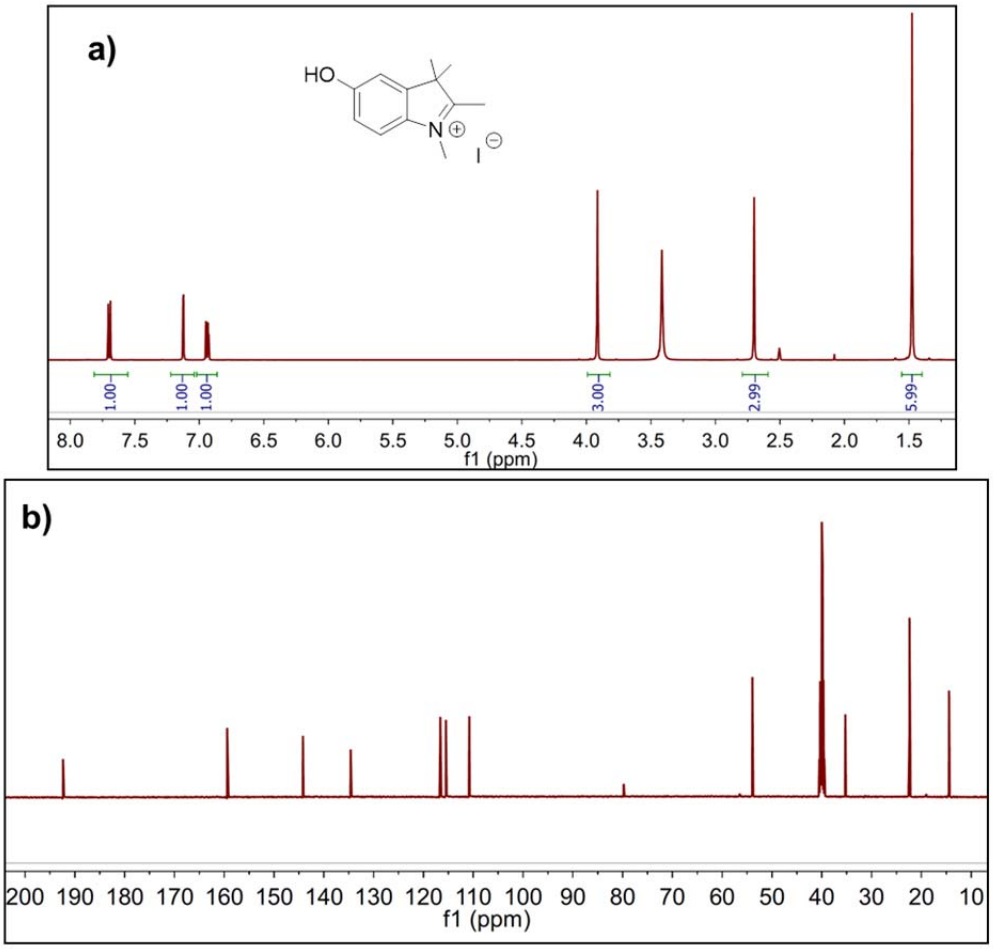


**Figure A.2.** a) 1H NMR and b) 13C NMR spectra of 5-hydroxy-1,2,3,3-tetramethyl-3H-indol-1-ium iodide in DMSO-$d_6$.

.

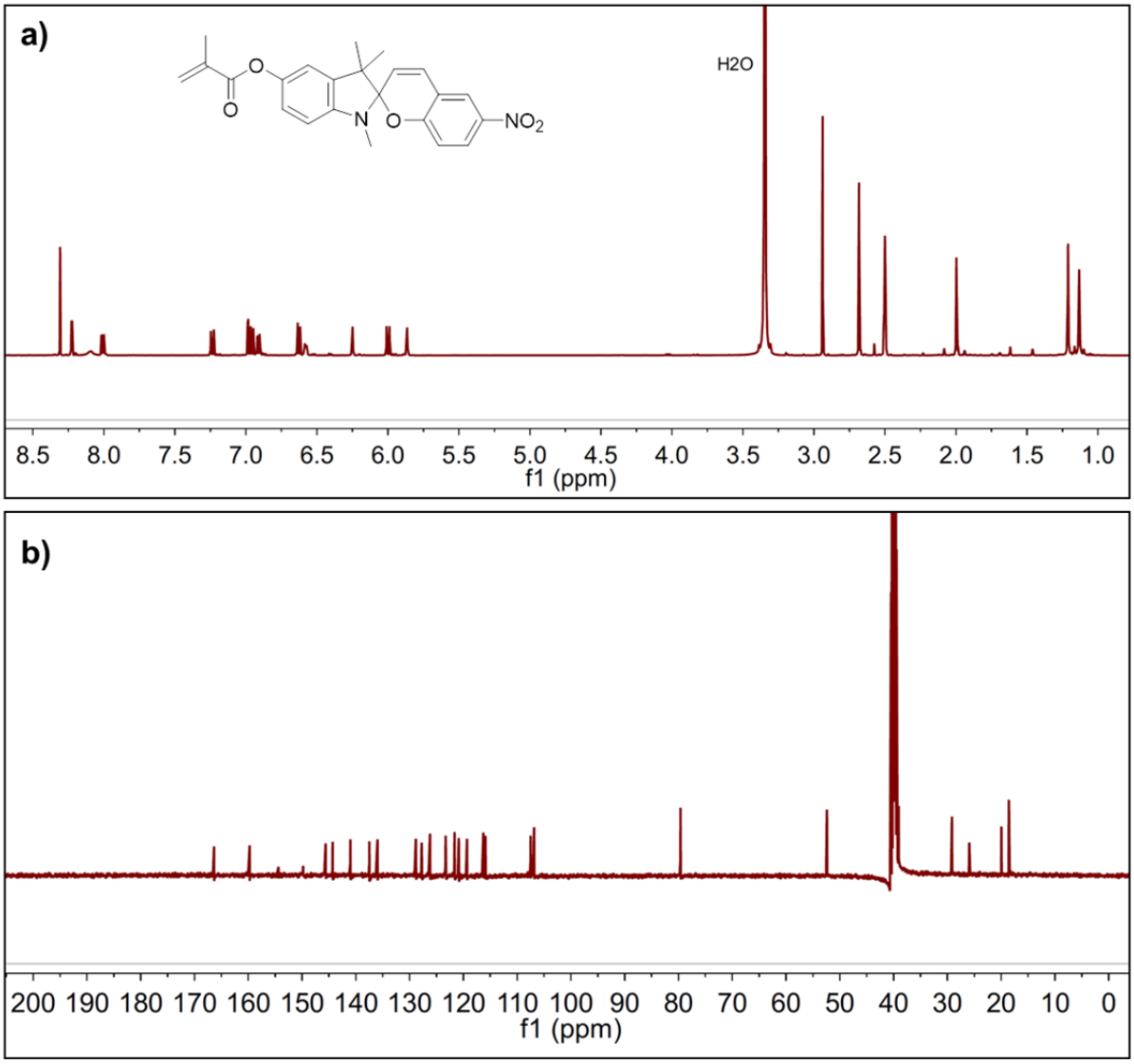


**Figure A.3.** a) 1H NMR and b) 13C NMR of 1-(2-hydroxyethyl)-2,3,3-trimethyl-3H-indol-1-ium iodide in DMSO-$d_6$.

.

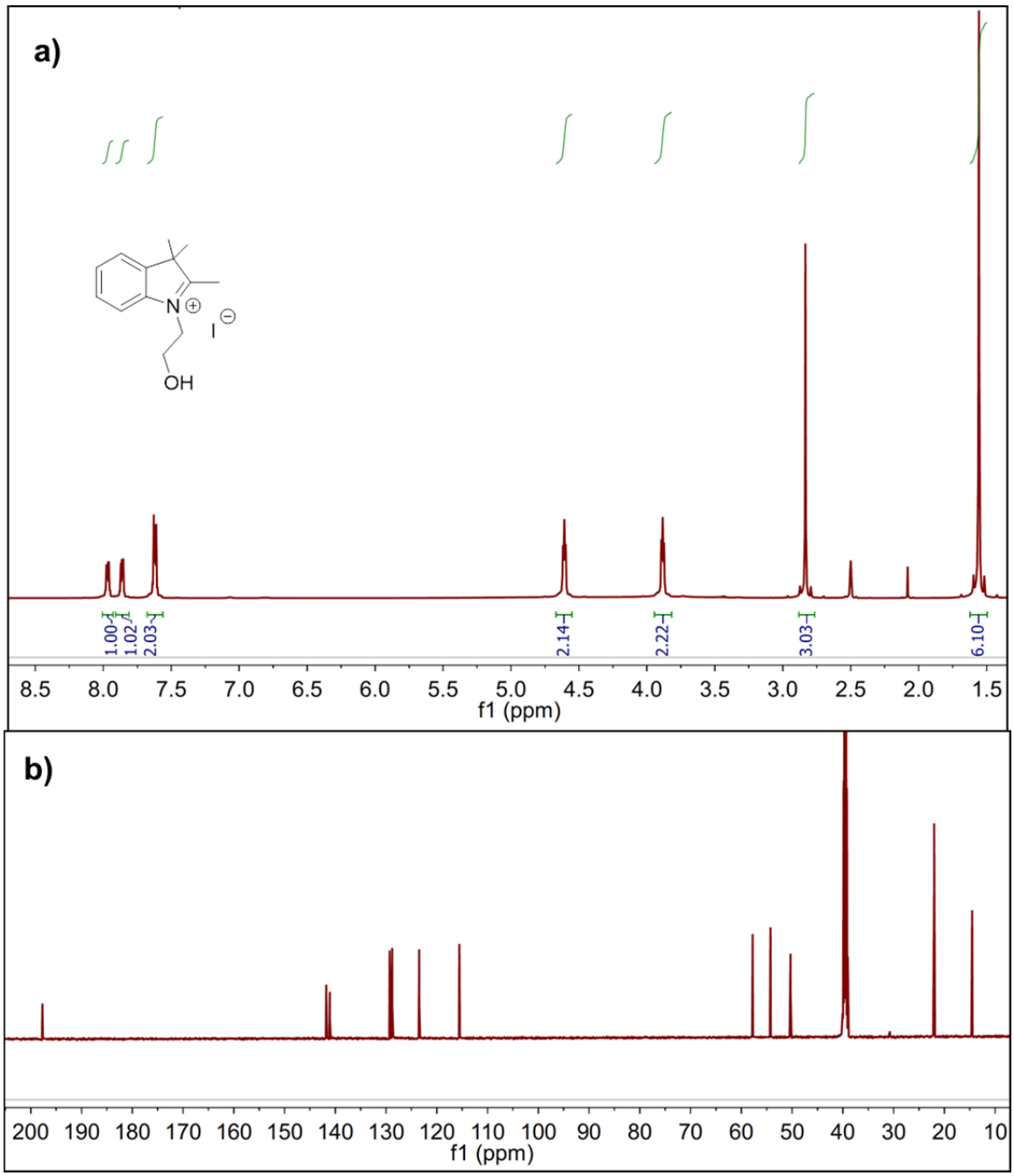


**Figure A.4.** a) 1H NMR and b) 13C NMR of 1-(2-hydroxyethyl)-2,3,3-trimethyl-3H-indol-1-ium iodide in DMSO-$d_6$.

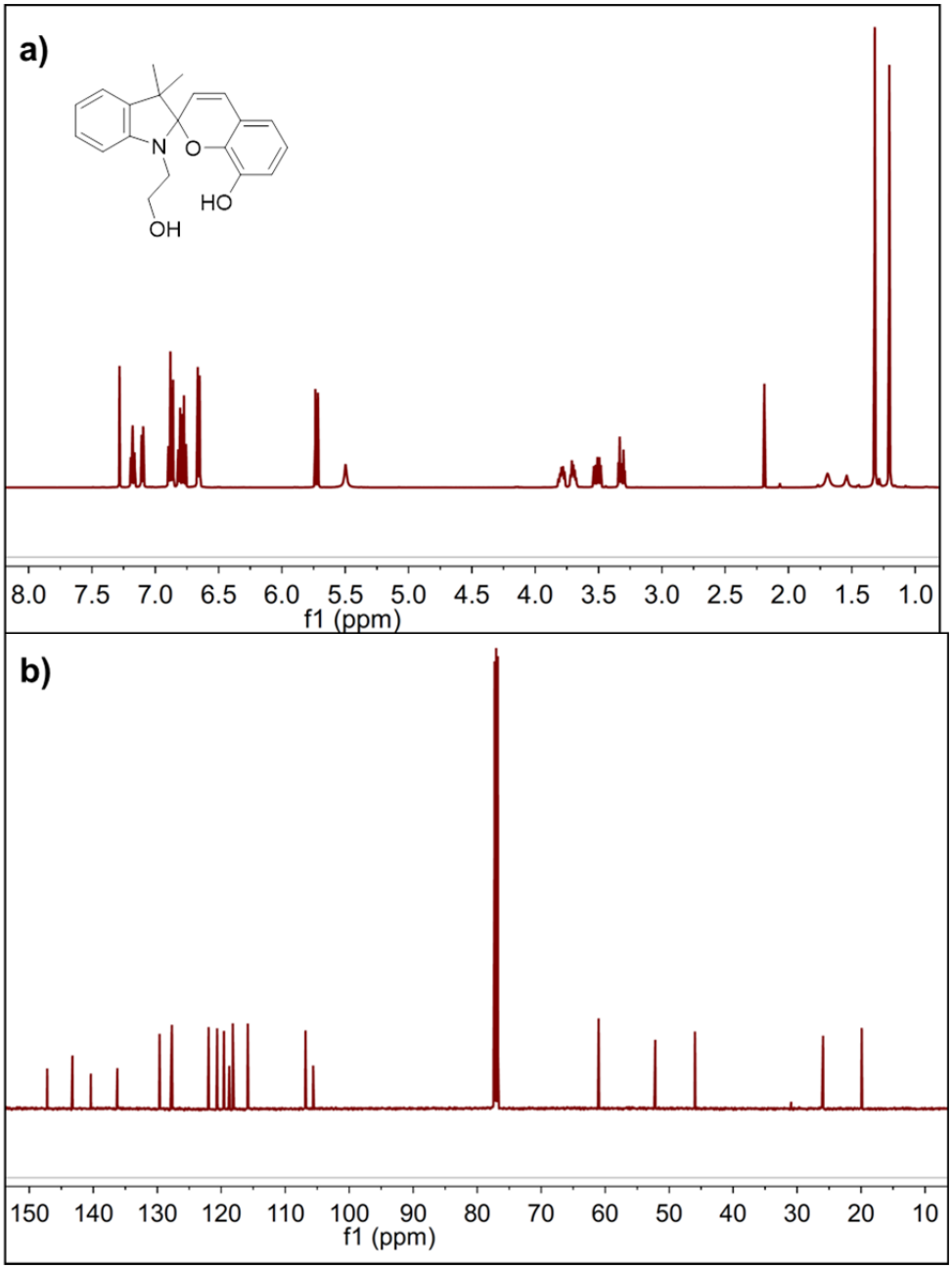


**Figure A.5.** a) 1H NMR and b) 13C NMR of 1'-(2-hydroxyethyl)-3',3'-dimethylspiro[chromene-2,2'-indolin]-8-ol in $CdCl_3$.

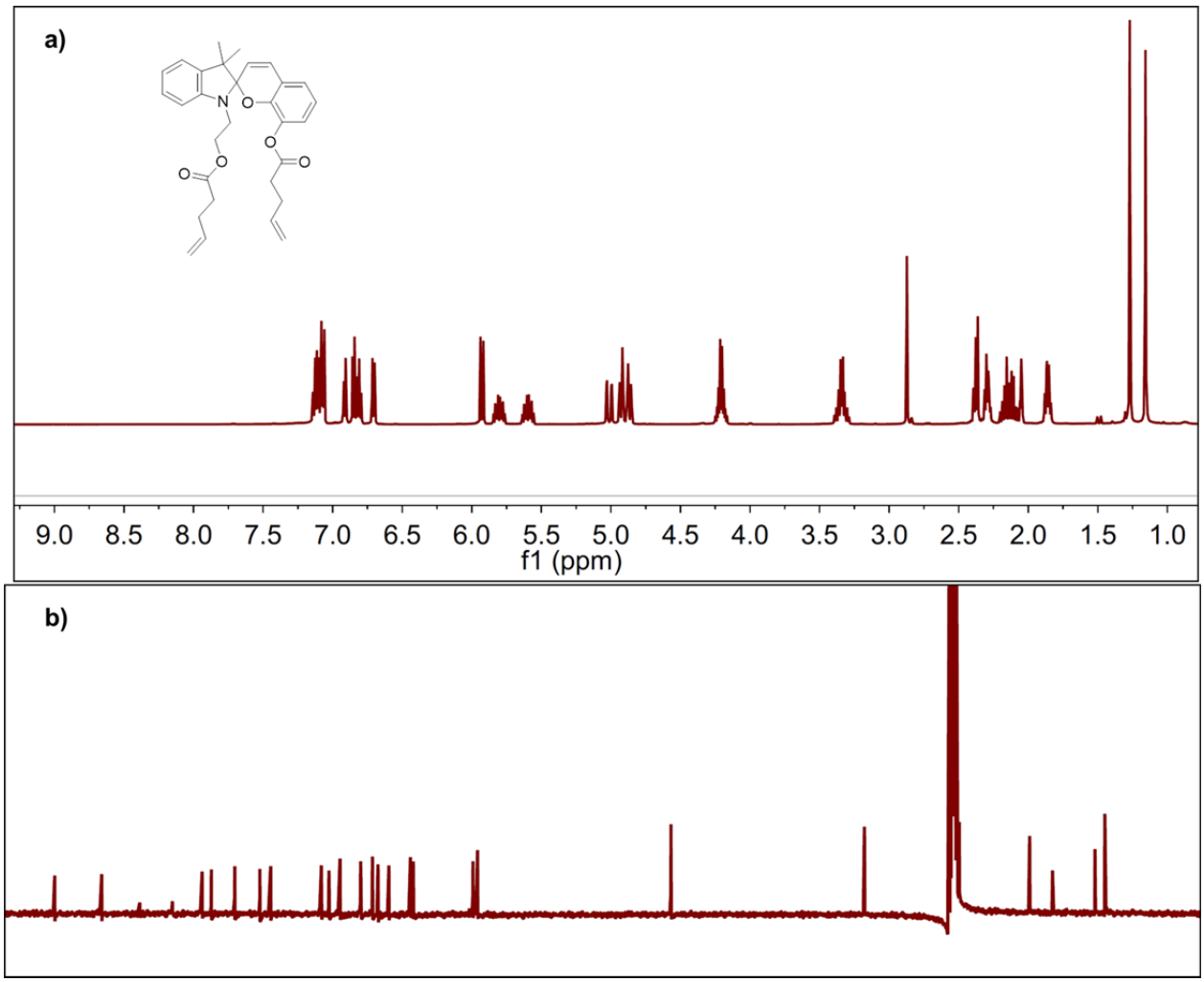


**Figure A.6.** a) 1H NMR and b) 13C NMR of 3',3'-dimethyl-1'-(2-(pent-4-enoyloxy)ethyl)spiro[chromene-2,2'-indolin]-8-yl pent-4-enoate in $CdCl_3$.

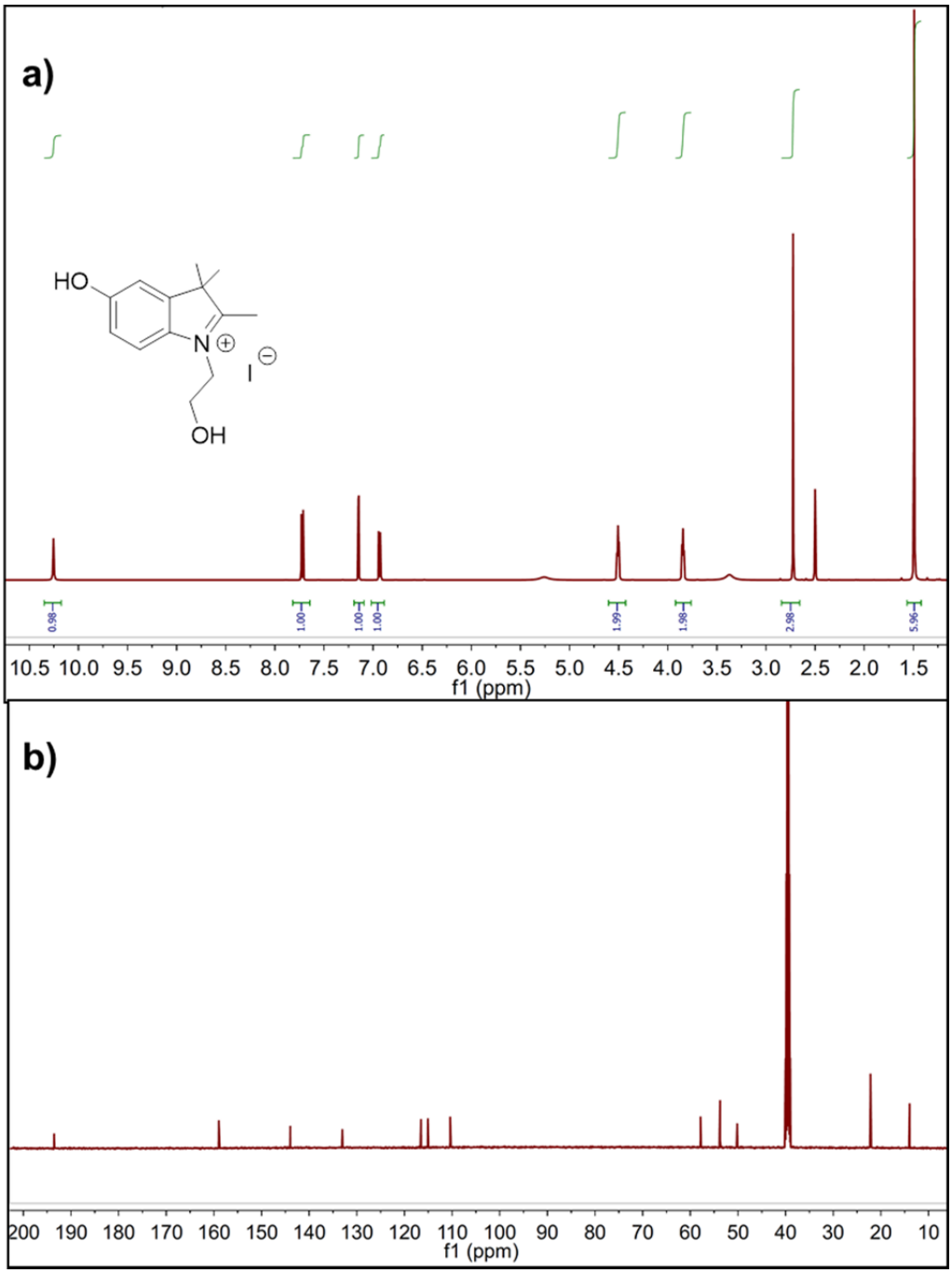


**Figure A.7.** a) 1H NMR and b) 13C NMR of 5-hydroxy-1-(2-hydroxyethyl)-2,3,3-trimethyl-3H-indol-1-ium iodide in DMSO-$d_6$.

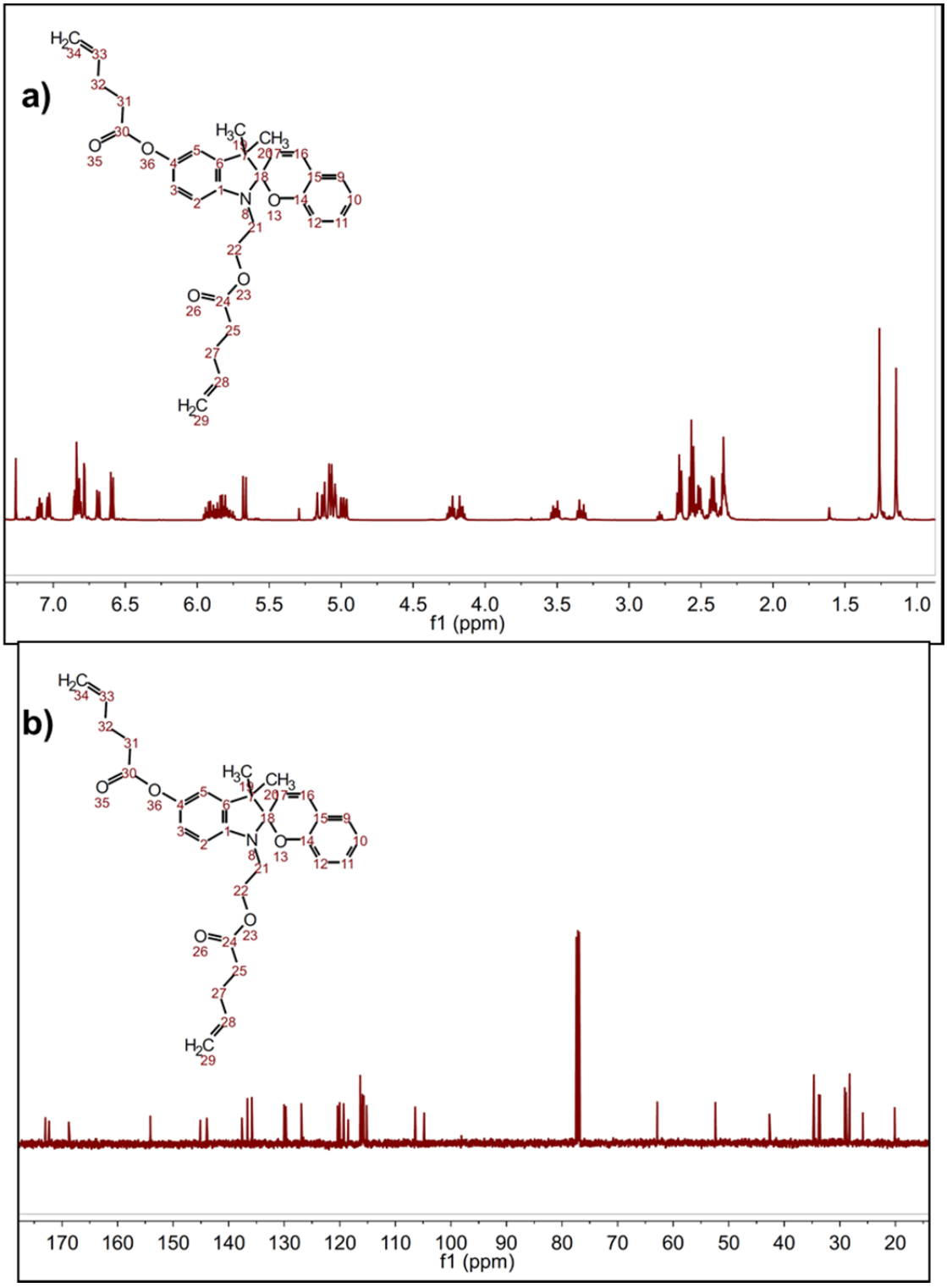


**Figure A.8.** a) 1H NMR and b) 13C NMR of 3',3'-dimethyl-1'-(2-(pent-4-enoyloxy)ethyl)spiro[chromene-2,2'-indolin]-5'-yl pent-4-enoate in $CdCl_3$.

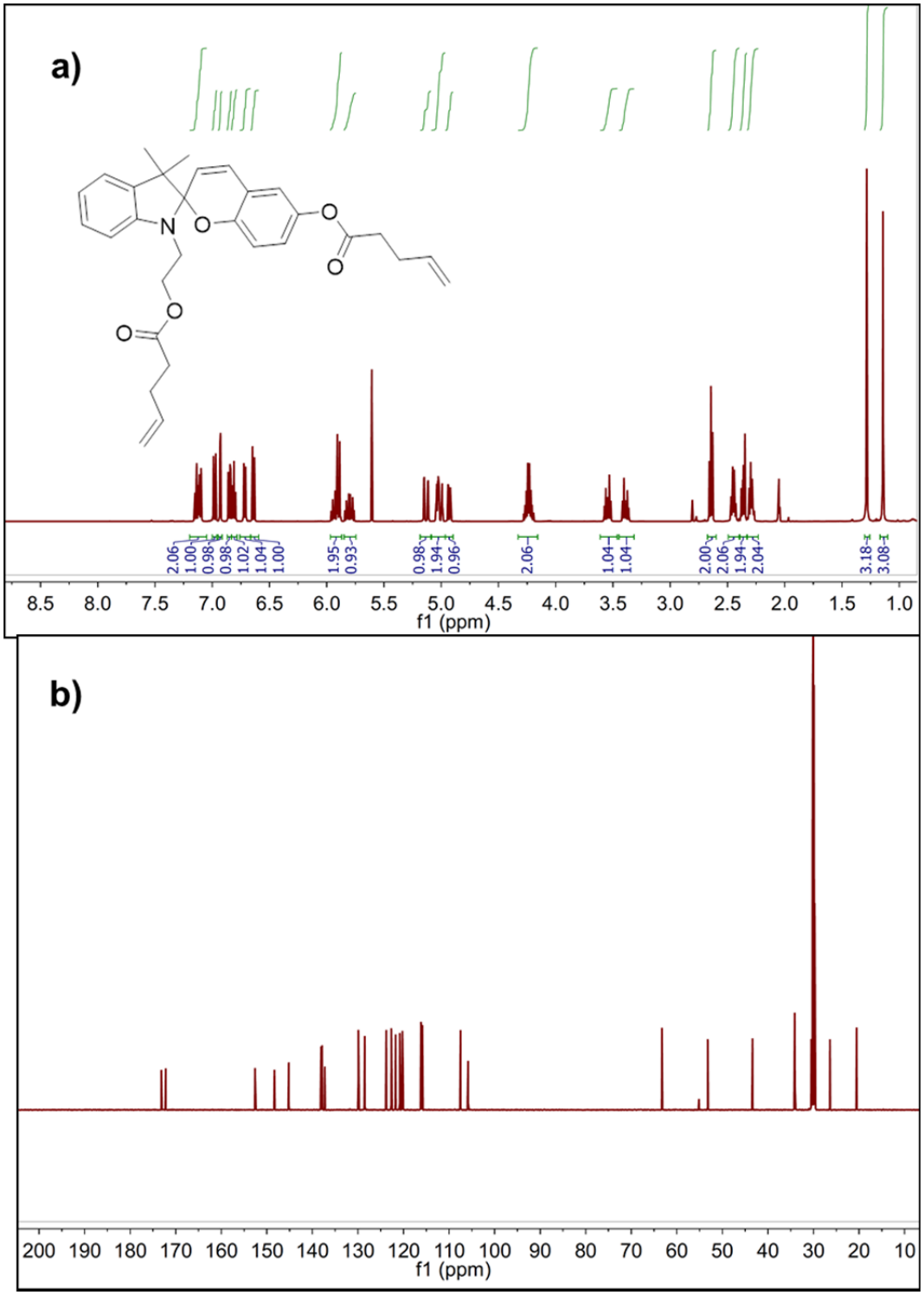


**Figure A.9.** a) 1H NMR and b) 13C NMR of 3',3'-dimethyl-1'-(2-(pent-4-enoyloxy)ethyl)spiro[chromene-2,2'-indolin]-6-yl pent-4-enoate in acetone-$d_6$.

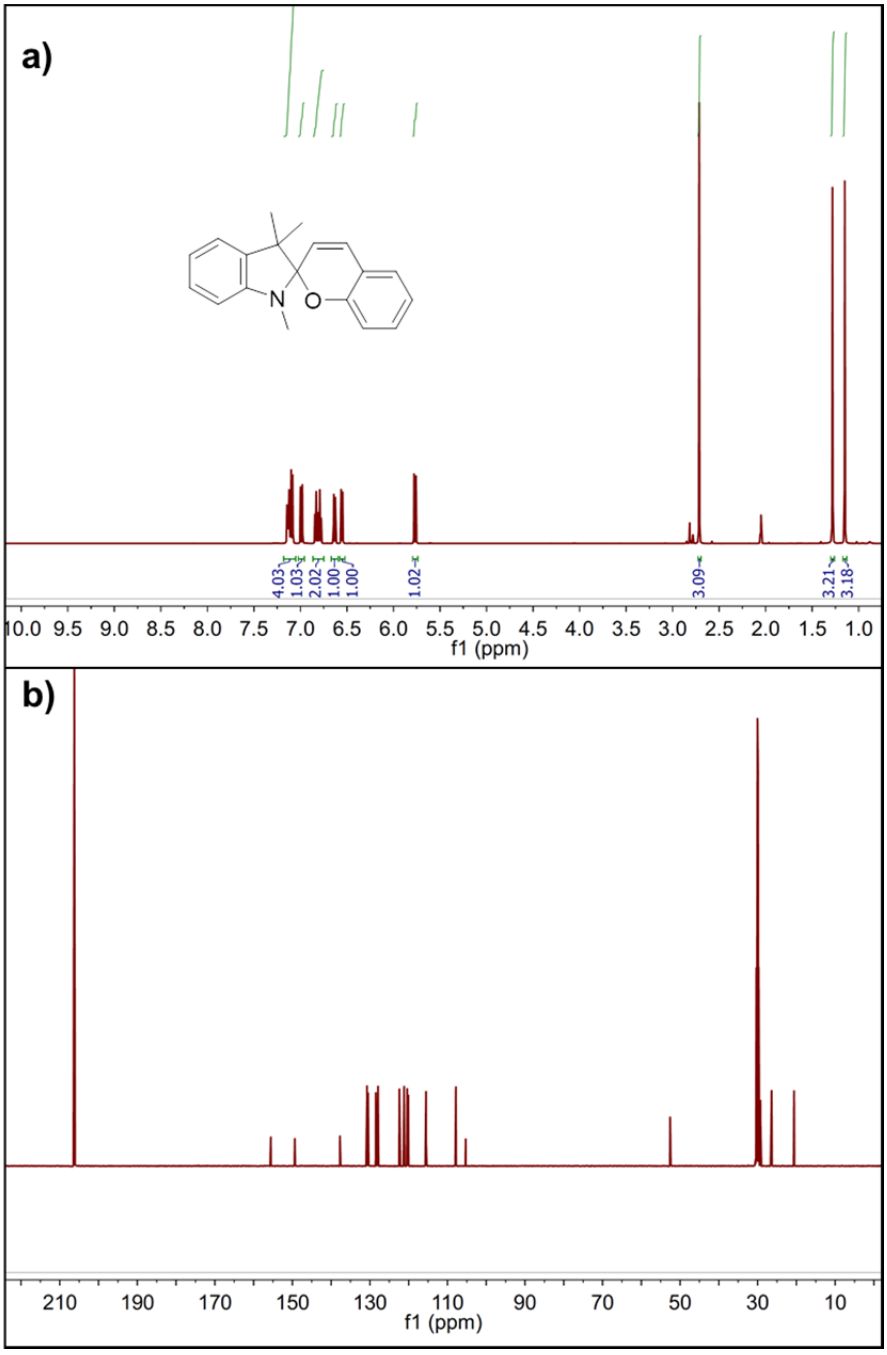


**Figure A.10.** a) 1H NMR and b) 13C NMR of 1',3',3'-trimethylspiro[chromene-2,2'-indoline] acetone-$d_6$.

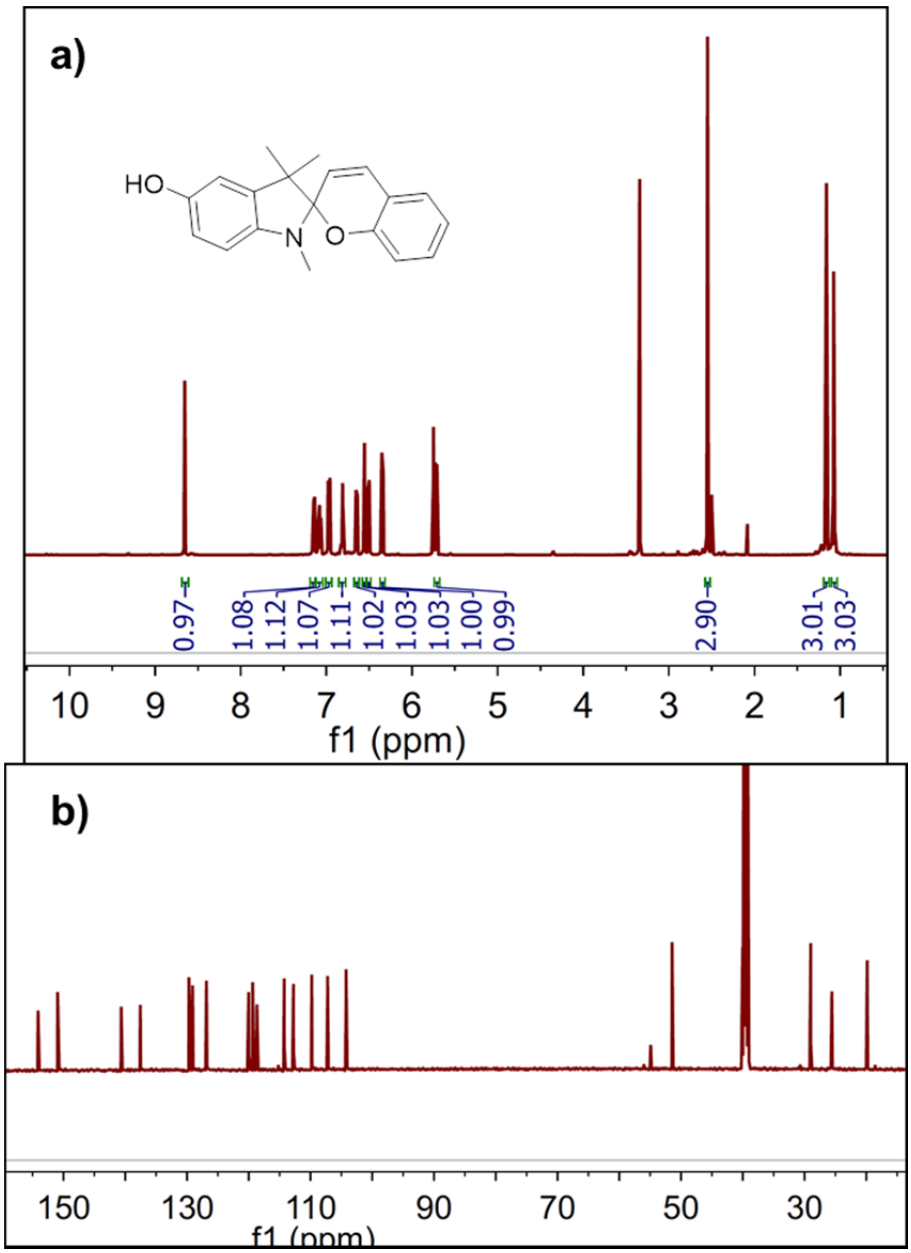


**Figure A11.** a)1H and b) 13C NMR spectra of 1',3',3'-trimethylspiro[chromene-2,2'-indolin]-5'-ol in DMSO-$d_6$.

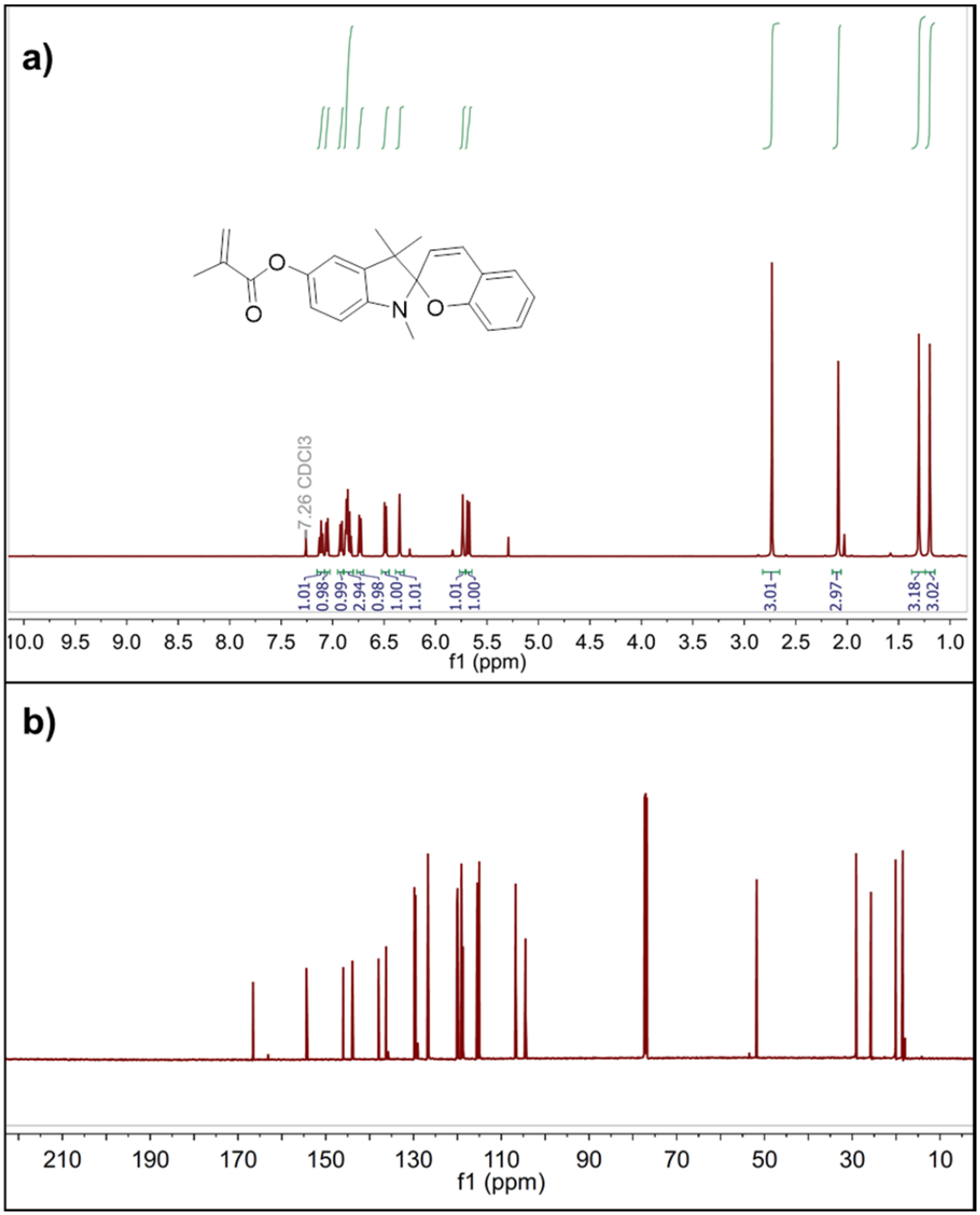


**Figure A12.** a) 1H and b) 13C NMR spectra of 1',3',3'-trimethylspiro[chromene-2,2'-indolin]-5'-yl methacrylate in CdCl3.

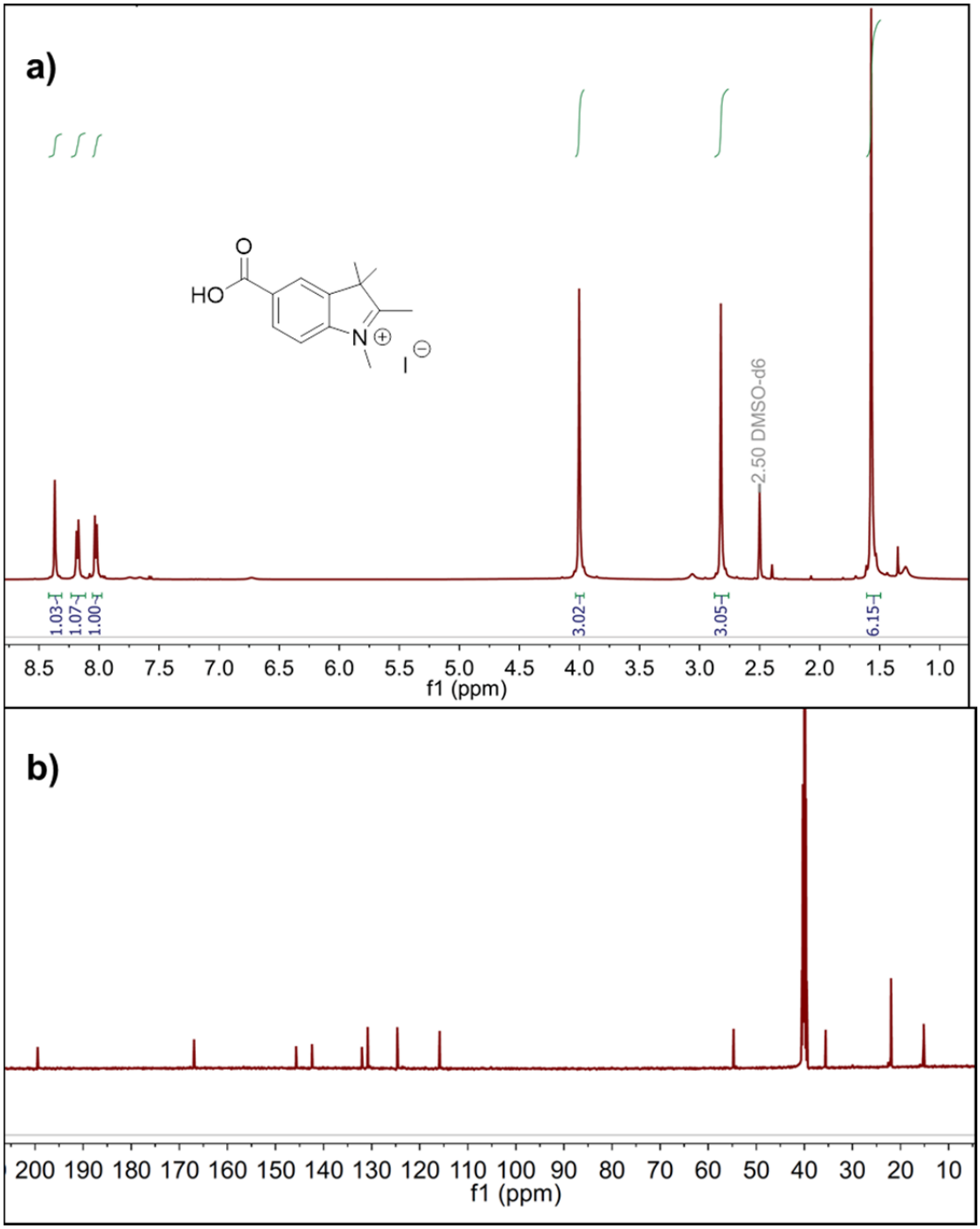


**Figure A13.** a) 1H and b) 13C NMR spectra of 5-carboxy-1,2,3,3-tetramethyl-3H-indol-1-ium iodide in DMSO-$d_6$.

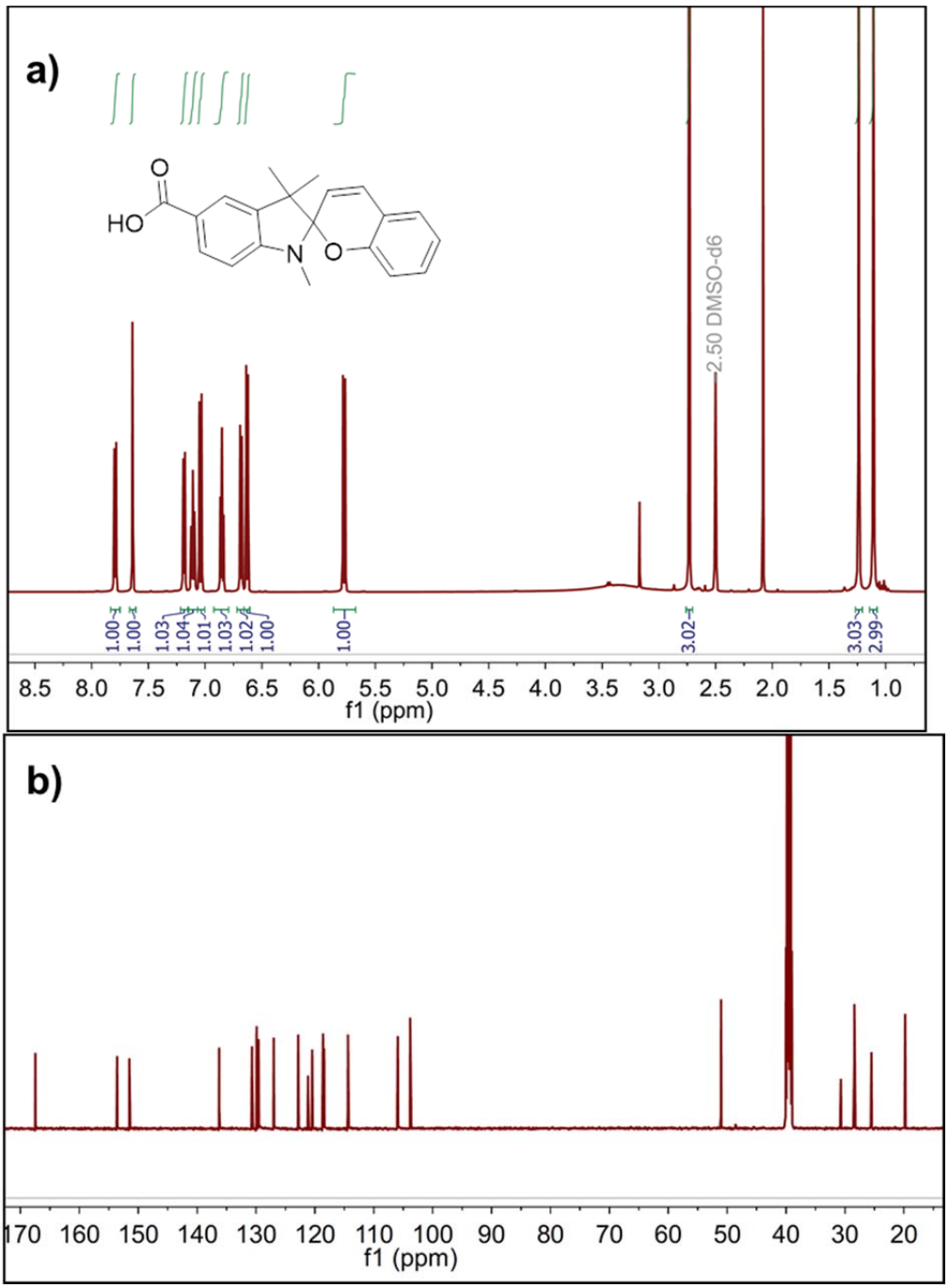


**Figure A14.** a) 1H and b) 13C NMR spectra of 1',3',3'-trimethylspiro[chromene-2,2'-indoline]-5'-carboxylic acid in DMSO-$d_6$.

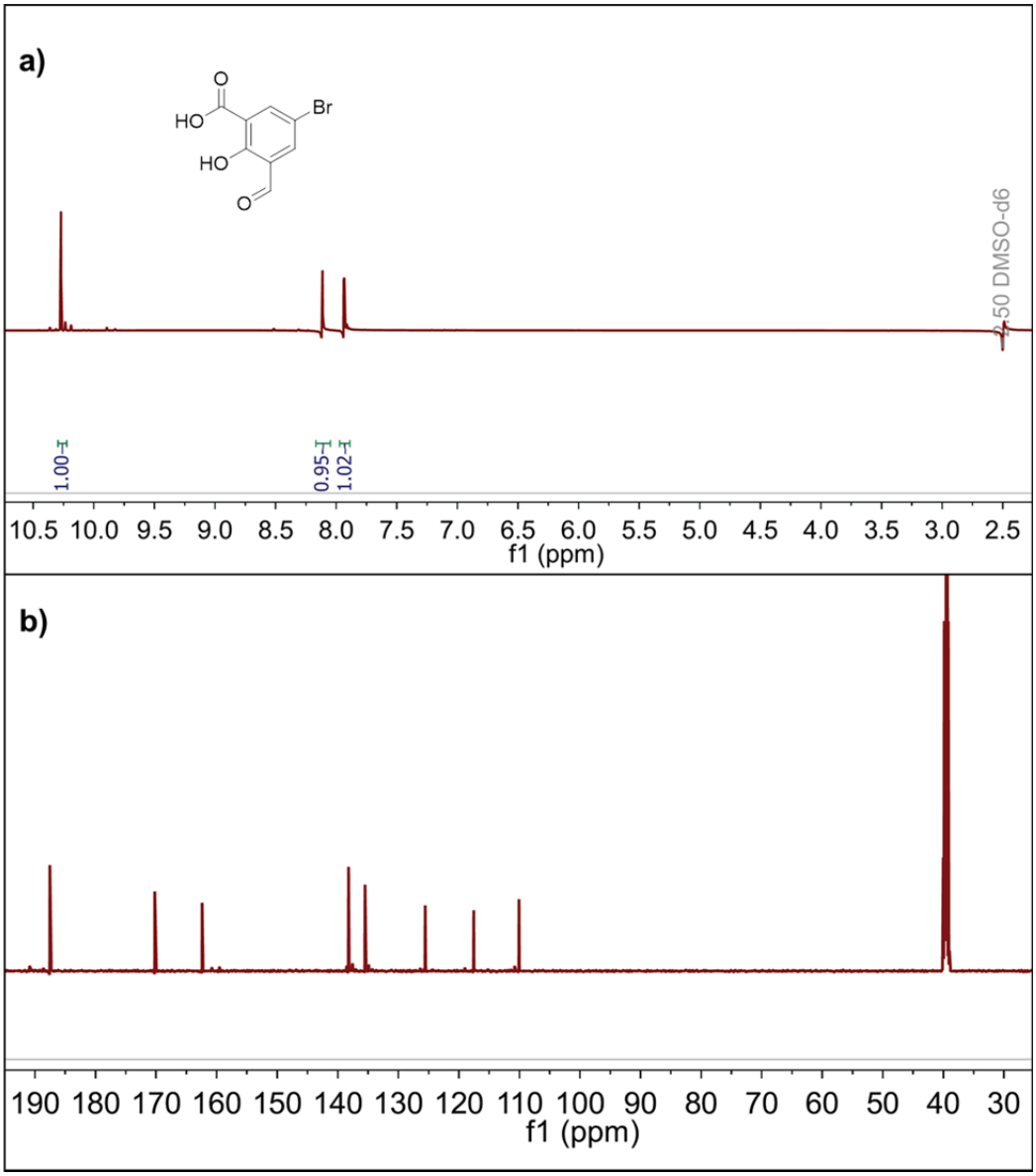


**Figure A15.** a) 1H and b) 13C NMR spectra of 5-bromo-3-formyl-2-hydroxybenzoic acid in DMSO-$d_6$.